SHVALYA VASYL

"Influence of Isovalent Dopants on Critical Behavior and Dynamic Thermal Properties of Sn(Pb)$_2$P$_2$S(Se)$_6$ Ferroelectric Crystals"

Presented for obtaining the degree of Doctor of Physical Sciences

Tutors:

Dr. Yulian Vysochanskii

Uzhgorod National University

Institute for Solid State Physics and Chemistry

Dr. Alberto Oleaga

University of the Basque Country UPV/EHU

Department of Applied Physics

Ukraine, Uzhgorod - 2016

ACKNOWLEDGMENTS

This PhD thesis is a complex project which has been contributed by many people. I am honored to say a few good words to some of them.

First of all, to my dear tutors Dr. Yulian Vysochanskii and Dr. Alberto Oleaga who gave me a ticket in a real scientific life. I am sincerely grateful to you for your daily support during my PhD study.

I would also like to thank Dr. Volodymyr Lazur who convinced me nine years ago to choose the Department of Physics at Uzhgorod National University and for his valuable advice that helped me while being a student.

I am very grateful to all the staff of the Department of Applied Physics at the UPV/EHU especially, again to Dr. Alberto Oleaga, Dr. Agustin Salazar, Dr. Arantza Mendioroz and to my colleagues in the office (Macarena, Arrate and Itxaso) for a wonderful working environment from one day to another.

In Bilbao I have made a lot of new friends but two Mexican fellows were just amazing persons. Nelson and Angel, I am really glad for our friendship. Hope you will achieve all you wish.

This project would not have been possible without funding from Erasmus Mundus ACTIVE program that provided my comfortable living during my study in Bilbao.

Lastly, my sweetheart Natalia, I cannot find the way to express how you have changed my life. Thank you for your inspiration and for the all time you have been waiting for me, while I was far from home. Thank you for 02.03.2015.

This PhD thesis I want to dedicate to my daughter Angelina. Love you so much, darling.

INDEX

INTRODUCTION

Interest of the study. Phase transitions in ferroelectric crystals is a quite interesting phenomenon, which has been actively studied along the previous decades, as the mechanisms responsible for these transitions are of great importance from the solid state physics point of view. So far, more than thousand ferroelectric crystal compounds are known. The most extensively studied among them are several representatives of perovskite ferroelectrics (Lead Titanate, Lithium Tantalate, Lithium Niobate, Barium Strontium Titanat...), triglycine sulphate TGS and chalcogenide crystals $Sn(Pb)_2P_2S(Se)_6$. The description of their different physical properties and some practical applications can be found in different monographs [1-3]. The ferroelectric materials are attractive for application in microwave technology [4]. In present time, the special attention is also paid for studying the properties of the nanoscale ferroelectrics [5, 6]. Thermodynamic properties stand out among the rest as they play a fundamental role because they give a wide spectrum of data needed to describe phonon-phonon processes taking place in the crystal lattice. For example, the temperature evolution of the specific heat provides information about the harmonic lattice vibration processes while, on the other hand, data about thermal expansion and thermal conductivity is useful to interpret anharmonic processes. Thermal diffusivity, in general, reflects the group velocity of the short-waves phonons while phase velocity can be characterized by acoustic data. Thus, the study of the temperature evolution of the thermal properties gives a quite complete picture about the phonon-phonon interactions inside the crystal and about heat propagation phenomena. Thus, this kind of studies gives a better understanding of the dynamics of the crystal lattice vibrations and defines their role at the phase transition.

$(Sn_{1-y}Pb_y)_2P_2(S_{1-x}Se_x)_6$-like crystals are a quite interesting and complex system, providing a continuous stable series of these solid ferroelectrics with attractive physical properties. The origin of the ferroelectricity in these materials is related to an spontaneous polarization appearance caused by intrinsic electronic properties. One of the most important features of this ferroelectric family is that the isovalent atom substitution of Sn by Pb in the cation sublattice or S by Se in the anion one has a strong

effect on the ferroelectric properties, shifting the temperature of the phase transition along the state diagram. Moreover, such replacing complicates the aforementioned diagram provoking the appearance of a modulated incommensurate phase and different multicritical points (Lifshitz point, Tricritical point, Lifshitz Tricritical point) as well as altering other physical properties of the crystals. A very important aspect is that multicritical points can be easily reached on the phase diagram. This allows to perform a comprehensive study under relatively simple experimental conditions, which cannot be achieved with any other materials. Also, these ferroelectrics can be used as a model example for different theoretical predictions developed for this type of materials, in order to properly describe the nature of the physical phenomena which take place in them. In particular, critical behavior theory is a very powerful tool to discriminate among the different possible physical mechanisms responsible for continuous phase transitions; either from the classical point of view of Landau mean field model or from the more powerful insight of renormalization group theory, the comparison of the experimental curves with the theoretical models and universality classes (with their different critical exponents) provides a means to go deeply into the physics of the transitions and their characterization.

$Sn_2P_2S_6$ crystals also possess a promising combination of electrooptical, acoustooptical and photorefractive parameters, which could find application in the nonlinear optical field. Another feature which makes these chalcogenide semiconductor crystals attractive for researchers comes from the possibility of changing their electrooptical, thermal and other properties by introducing isovalent alien dopants into the crystal lattice. This ability has a practical value, which allows obtaining crystals with predetermined characteristics. The impact of dopants on the ferroelectricity of the crystals is another field of interest as they can improve or worsen it, introducing changes in the position and shape of the transitions.

All the facts aforementioned have defined the interest of the study. Thus, the scope of this thesis is the thermal characterization of $Sn(Pb)_2P_2S(Se)_6$ mixed ferroelectric family in a wide temperature range and the study of the critical behavior of the second order phase transitions in the phase diagram, for which a detailed study of

the corresponding temperature regions must be performed. The technique used is high resolution *ac* photopyroelectric calorimetry with which thermal diffusivity measurements will be carried out. The critical behavior analysis of the inverse of this physical variable will allow us to analyze in depth the physical mechanisms playing a predominant role at the phase transitions. The first point of interest is how the replacement of Sn by Pb or the introduction of other kind of dopants (Ge, Te, Sb) affects the thermal properties and especially the critical behavior in $(Sn_{1-y}Pb_y)_2P_2(S_{1-x}Se_x)_6$ series. What is more relevant at the transition: long-range dipolar interactions, fluctuations of the order parameter, influence of the charged defects or closeness of the system to a certain multicritical point (Lifshitz, Tricritical, Tricritical Lifshitz)? When is it necessary to take into account one or two-components of the order parameter to properly describe the dynamics of the system? Which universality class is appropriate for a particular phase transition and thus which is the correct physical description? To answer these questions we have considered, depending on the situations, the classical Landau theory based on the mean-field approach together with several corrections accounting for the fluctuations of the order parameter, or the universality classes predicted by renormalization group theory. In this way, many different physical scenarios have been contemplated: the importance of fluctuations of the order parameter, their possible attenuation due to strong dipolar forces, possible contribution of charged defects, the closeness to a Lifshitz point… At the same time, the evolution of the stereoactivity of the doped crystals will be interpreted.

Lastly, a very intriguing question is related to the possible location of a unique Lifshitz Tricritical point on the temperature-concentration phase diagram in $(Sn_{1-y}Pb_y)_2P_2(S_{1-x}Se_x)_6$ taking into account simultaneous changes of *x* and *y*. This subject is also covered in this report.

Relationship with academic programs, plans, themes

This thesis has been performed in a frame of a special cotutelle PhD agreement between Spain (The University of the Basque Country, Bilbao) and Ukraine (Uzhgorod National University, Uzhgorod). The European Union, through the ERASMUS MUNDUS ACTIVE programme, has provided a generous grant to cover the 2-year stay

of the PhD candidate at Bilbao (Spain). The research study has been supported by different Spanish funding programmes: Ministerio de Ciencia e Innovación with FEDER support (MAT2011-23811), Gobierno Vasco (IT619-13), and UPV/EHU (UFI11/55).

Purpose and objectives of the study

Object: Family of the mixed ferroelectric crystals $Sn(Pb)_2P_2S(Se)_6$.

Subject: Thermal properties and critical behavior of the $Sn(Pb)_2P_2S(Se)_6$ mixed ferroelectrics.

Purpose: Investigate the temperature evolution of the thermal properties of $Sn(Pb)_2P_2S(Se)_6$ covering a wide temperature range and study the critical behavior of the second order phase transitions in the phase diagram, mainly focusing on the study of the influence of Sn by Pb substitution in $(Sn_{1-y}Pb_y)_2P_2S_6$ and $(Sn_{1-y}Pb_y)_2P_2Se_6$ solid solutions. Investigate the influence of dopants (Ge, Sb, Te) on the ferroelectric and thermal properties of the uniaxial $Sn_2P_2S_6$ crystal, studying possible changes in the critical behavior. And, lastly, analyze the influence of Pb and Ge dopants in the crystal with a Lifshitz point $Sn_2P_2(S_{0.72}Se_{0.28})_6$, in order to define the possible location of the Lifshitz tricritical point. In agreement with these purposes, the following tasks were formulated:

• Experimentally measure the thermal diffusivity in $(Sn_{1-y}Pb_y)_2P_2S_6$ mixed crystal in a wide temperature range, studying the influence of Pb atoms on the character of the phase transition. Perform a critical behavior study of the anomalies considering a classical mean-field theory, possible deviation from a classical behavior taking into account fluctuation of the order parameter, possible attenuation due to strong dipolar forces or possible contribution of charged defects and consider the appropriateness of different universality classes. Investigate the thermal anisotropy in $Pb_2P_2S_6$ monoclinic paraelectric crystal.

• Investigate the thermal diffusivity in $(Sn_{1-y}Pb_y)_2P_2Se_6$ ferroelectrics in a wide temperature range, studying the influence of Pb atoms on the position and shape of the first and second order phase transition. Perform theoretical data treatment of the

paraelectric-incommensurate transition in order to check the possible appropriateness of a particular universality class predicted by renormalization group theory.

• Investigate the influence of Ge, Sb and Te dopants on the ferroelectric and thermal properties of the uniaxial $Sn_2P_2S_6$ crystal measuring thermal diffusivity around a critical point. Use all the theoretical approaches mentioned above to understand the role of each dopant in the critical behavior of the transition.

• Study the influence of Pb and Ge isovalent dopants in the $Sn_2P_2(S_{0.72}Se_{0.28})_6$ ferroelectric, which is considered a Lifshitz point. Consider the possible appearance of a Lifshitz tricritical point on the state diagram, studying the evolution of the critical behavior, from a non tricritical universality class to a tricritical one, comparing the experimental data with the theoretical predictions.

• Perform a general analysis of the thermal properties in a wide temperature range and consider the role of phonons in the heat propagation taking into account all the experimental data obtained for $Sn(Pb)_2P_2S(Se)_6$ solid solutions during the research.

Methods: Photopyroelectric calorimeter has been employed to investigate ferroelectric crystals studied. Data treatment of the experimental results has been carried out by using the appropriate critical behavior analysis.

Scientific novelty of the results

• Thermal diffusivity has been measured for the first time for $Sn_2P_2S_6$, $Sn_2P_2Se_6$, $Pb_2P_2S_6$ and $Pb_2P_2Se_6$ parent compounds as well for their solid solutions ($Sn_{1-y}Pb_y)_2P_2S(Se)_6$ covering a wide temperature range (30-350K). This has provided a unique opportunity to carry out a great quality critical behavior study for the complete system ($Sn_{1-y}Pb_y)_2P_2S(Se)_6$ across the different types of the continuous phase transition.

• Up to now, nobody had done a complex critical analysis study for $Sn_2P_2S_6$ doped with Ge, Sb and Te, where each dopant takes the place of a particular atom in a crystal lattice. Thus, Ge, Sb and Te atoms substitute Sn, P and S, respectively.

• So far, there are no published works in literature where a Lifshitz Tricritical point has been experimentally confirmed. We are the first who found it in the family ($Sn_{1-y}Pb_y)_2P_2(S_{1-x}Se_x)_6$ with coordinates $T = 259.12$ K, $x = 0.28$, $y = 0.05$.

• Also, a complete analysis of the thermal conductivity dependencies in a wide temperature range has been undertaken for $Sn(Pb)_2P_2S(Se)_6$ and correlated with the features occurring on their state diagram.

Practical interest of the study

The whole set of experimental results together with the theoretical data treatment give a clear picture about the influence of isovalent atom substitutions in $Sn(Pb)_2P_2S(Se)$, which can serve as a basement for further theoretical developments. In particular, thermal diffusivity measurements for $Sn_2P_2S_6$, $Sn_2P_2Se_6$, $Pb_2P_2S_6$ and $Pb_2P_2Se_6$ extreme compounds can help to understand the heat propagation phenomena in uniaxial ferroelectrics. Also, such a study can give a new impulse and a possibility to properly describe the variety of the physical phenomena which take place in these ferroelectric materials.

On the other hand, studying the influence of the different types of dopants can be used at a crystal manufacturing stage, in order to obtain samples with predetermined properties, which is important for both practical and theoretical standpoints. This has been the case when foreseeing the possible location of the Lifshitz tricritical point on the phase diagram of the $(Sn_{1-y}Pb_y)_2P_2(S_{1-x}Se_x)_6$ chemical compounds.

Contribution of the PhD candidate

The full experimental work concerning thermal diffusivity measurements has been performed by PhD candidate personally in the Photothermal Techniques Laboratory of the Department of Applied Physics I at the University of the Basque Country (Bilbao, Spain). The PhD candidate has also been working on the sample preparation (cutting, polishing). All the crystals have been grown in the Institute for Solid State Physics and Chemistry of the Uzhgorod National University. The author participated in the formulation of research tasks, novelty of the study, discussions and interpretations of the results. Also, the PhD student has performed a complete critical behavior analysis of the all experimental data and formulated the conclusions of the thesis.

Publications and contribution to the conferences

The results of the thesis have been presented on the following conferences:

1. R. Bilanych, A. Molnar, M. Medulych, V. Shvalia, A. Kohutych, R. Yevych, A. Dziaugys, V. Samulionis, J. Banys, Yu. Vysochanskii. *Tricritical Point and Virtual Ferroelectricity in $(Pb_ySn_{1-y})_2P_2S_6$.* 12th Russian/CIS/Baltic/Japanese Symposium on Ferroelectricity & Functional Materials and NanoTechnologies (Riga, Latvia, September 29 - October 2, 2014).

2. V. Haborets, M. Medulych, V. Shvalya, A. Molnar, R. Yevych, A. Kohutych, A. Dziaugys, J. Banys, Yu. Vysochanskii. *Quantum Paraelectric $Pb_2P_2S_6$ With Charge Instability.* International Meeting "Clusters and Nanostructured Materials", CNM'4 (Ukraine, Uzhgorod, October 12-16, 2015).

3. V. Shvalya, A. Oleaga, A. Salazar, A. Kohutych, Yu. Vysochanskii. *Thermal Diffusivity and Critical Behaviour Study of Ferroelectrics $(Pb_xSn_{1-X})_2P_2S_6$.* 18th International Conference on Photoacoustic and Photothermal Phenomena (Serbia, Novi Sad, September 6-10, 2015).

4. A. Oleaga, V. Shvalya, A. Salazar. *Transport Thermal Properties of Photopyroelectric Sensor $LiTaO_3$ from 10 to 400 K.* 18th International Conference on Photoacoustic and Photothermal Phenomena (Serbia, Novi Sad, Serbia, September 6-10, 2015).

5. V. Shvalya, A. Oleaga, A. Salazar, A. Kohutych, Yu. Vysochanskii. *Thermal Characterization and Critical Behavior Study of $(Pb_xSn_{1-x})_2P_2Se_6$.* 13th Russia/CIS/Baltic/Japan Symposium on Ferroelectricity & 8th International Workshop on Relaxor Ferroelectrics (Japan, Shimane, June 19-23, 2016).

6. V. Shvalya, A. Oleaga, A. Salazar, A. Kohutych, Yu. Vysochanskii. *Doping Effects on the Thermal Properties of $Sn_2P_2S_6$ Ferroelectrics.* 13th Russia/CIS/Baltic/Japan Symposium on Ferroelectricity & 8th International Workshop on Relaxor Ferroelectrics (Japan, Shimane, June 19-23, 2016).

7. V. Shvalya, A. Oleaga, A. Salazar, I. Stoika, Yu. Vysochanskii. *Influence of Ge, Pb, Sb and Te dopants on ferroelectricity and critical behavior of $Sn_2P_2S_6$ semiconductor crystal.* I Jornadas Doctorales de la UPV/EHU (Spain, Bilbao, July 11-12, 2016).

8. A. Oleaga, V. Shvalya, A. Salazar, A. Kohutych, I. Stoika, Yu. Vysochanskii. *Critical Behavior Study of Ferroelectrics $Sn_2P_2(S_{1-x}Se_x)_6$ Doped with Pb and Ge by Means of ac Photopyroelectric Calorimetry*. Fourth Mediterranean International Workshop on Photoacoustic & Photothermal Phenomena (Sicily, Erice, October 19-26, 2016).

The realization of this thesis has led to publications in following journals:

1. A. Salazar, A. Oleaga, V. Shvalya, E. Apinaniz / *Improved thermal effusivity measurements of solids using the photopyroelectric technique in the front configuration* // International Journal of Thermal Sciences, – 2016. – V. 100. – P. 60-65.

2. V. Shvalya, A. Oleaga, A. Salazar, A. Kohutych, Yu. Vysochanskii / *Critical behavior study of ferroelectric semiconductors $(Pb_xSn_{1-x})_2P_2S_6$ from thermal diffusivity measurements* // Thermochimica Acta, – 2015. – V. 617. – P. 136-143.

3. A. Oleaga, V. Shvalya, A. Salazar / *Transport thermal properties of $LiTaO_3$ pyroelectric sensor from 15K to 400K and its application to the study of critical behavior in $EuCo_2As_2$* // International Journal of Thermophysics, – 2016. – V. 37. – P. 4.

4. V. Shvalya, A. Oleaga, A. Salazar, A. Kohutych, Yu. Vysochanskii / *Thermal diffusivity and 3D-XY critical behavior of ferroelectric semiconductors $(Pb_xSn_{1-x})_2P_2Se_6$* // Journal of Physics and Chemistry of Solids, – 2016. – V. 88. – P. 78-84.

5. V. Shvalya, A. Oleaga, A. Salazar, I. Stoika, Yu. Vysochanskii / *Influence of dopants on the thermal properties and critical behavior of the ferroelectric transition in uniaxial ferroelectric $Sn_2P_2S_6$* // Journal of Materials Science, – 2016. – V. 51. – P. 8156-8167.

6. V. Shvalya, A. Oleaga, A. Salazar, A. Kohutych, Yu. Vysochanskii / *Thermal characterization and critical behavior study of $(Pb_xSn_{1-x})_2P_2Se_6$* / Ferroelectrics (accepted for publication 2016).

7. A. Oleaga, V. Shvalya, A. Salazar, I. Stoika, Yu. Vysochanskii / *In search of a tricritical Lifshitz point in $Sn_2P_2(S_{1-x}Se_x)_6$ doped with Pb, Ge: a critical behavior study* // Journal of Alloys and Compounds, – 2017. – V. 694. – P. 808-814.

8. V. Shvalya, A. Oleaga, A. Salazar, A. Kohutych and Yu. Vysochanskii / *Electron-phonon anharmonicity and ultra-low thermal conductivity in phosphorous chalcogenide ferroelectrics*// (in publishing).

Structure of the thesis

The PhD thesis includes an introduction, nine chapters, general conclusions, bibliography, where 228 references are listed summary written in Spanish. The total volume is 206 pages; the thesis contains 88 figures and 14 tables.

The **first chapter** is devoted to a general theoretical review of heat transfer phenomena and related heat exchange processes. In the first place, we explain which the heat transfer mechanisms are and how heat is transmitted in homogeneous, isotropic or anisotropic materials. Secondly, the mathematical description of the heat propagation will be shown through the parabolic and hyperbolic heat diffusion equations. Also the description of the heat carriers in solid semiconductors (the materials studied in this work) will be considered. In the end of the chapter a brief view of the main thermophysical properties (specific heat, thermal diffusivity, thermal effusivity and thermal conductivity) is given, in order to distinguish the fundamental differences among them.

The second chapter contains general information about the *ac* photopyroelectric (PPE) calorimetry technique, its physical background and the advantages of this technique in respect to other ones. The chapter contains a mathematical description of the Back-detection configuration setup BPPE, which serve as the foundations for our further experimental investigations. This model is one of the most widely used in PPE calorimetry and allows extracting directly the thermal diffusivity of the sample studied. This method accompanied together with a cryostat is a powerful tool while monitoring transport thermal properties of the solid semiconductor materials. Descriptions of the cryostats used and the relevant thermal properties of the $LiTaO_3$ sensor are also presented in the chapter. Also, a new development of the PPE technique is presented. This method allows measuring thermal effusivity of solids at a fixed temperature as well as in a continuous temperature run using a photopyroelectric calorimetry in a front-configuration setup.

The third chapter is completely devoted to the description of the $Sn(Pb)_2P_2S(Se)_6$ mixed ferroelectrics considering their different physical properties. In the first place, the crystal structure of four parent compounds will be described in detail.

After that, step by step, a general review of the phase diagram of $Sn_2P_2(S_{1-x}Se_x)_6$, $(Pb_ySn_{1-y})_2P_2S_6$ and $(Pb_ySn_{1-y})_2P_2Se_6$ will be considered highlighting the features that appears when Se substitutes S. In this case, the most interesting aspect is a true Lifshitz point location on the state diagram and the existence of a modulated incommensurate phase. We further discuss the influence of Pb atoms on the phase transition temperature position and on the critical anomalies shape in the $Sn_2P_2S_6$ and $Sn_2P_2Se_6$ compounds. Lastly, according to the scope of the thesis we will introduce a brief survey about the thermal properties of $Sn(Pb)_2P_2S(Se)_6$ that have been done before.

According to the general aim of the thesis the relevant theoretical models related to critical behavior are collected in **chapter four**. In the first place, a classical Landau theory based on a mean-field approach is considered. After that, different physical mechanisms (fluctuations of the order parameter, attenuation of the order parameter fluctuations due to a long-range interaction, influence of the charged defect), which can provoke a deviation from the mean-field behavior are considered. Additionally, we present renormalization group theory developments and give information about the different universality classes which can appear while studying $(Sn_{1-y}Pb_y)_2P_2(S_{1-x}Se_x)_6$ ferroelectric family. Besides, due to the physical properties of the material studied in this work, the critical behavior of a special commensurate-incommensurate phase transition will be described. At the end of the chapter a review of the experimental results related to the critical behavior analysis of $Sn(Pb)_2P_2S(Se)_6$ will be presented.

The next four chapters are fully devoted to the interpretation of the data obtained in this work. Thus, in **chapter five** we study the influence of the Pb atoms on the thermal properties and critical behavior of the continuous para-ferroelectric transition in uniaxial $(Pb_ySn_{1-y})_2P_2S_6$ crystals at y=0.1 0.2, 0.3, 0.45, 0.8 and 1. We show that Pb atoms provoke a crossover from a clear non-mean-field model at y=0.1 (where the first-order fluctuations as well as the presence of defects must be taken into account) to a mean-field one at Pb content of y=0.3.

In **chapter six** a similar study is performed for $(Pb_ySn_{1-y})_2P_2Se_6$ mixed ferroelectrics for y=0, 0.05, 0.1, 0.2, 0.47, 0.8 and 1. This system reveals two phase transitions at y=0: the continuous one from the paraelectric to the incommensurate

phase and a discontinuous one from the incommensurate to the ferroelectric phase. The results of thermal diffusivity measurements as well as the critical behavior study are presented. The analysis of the second order transitions has been carried out within the frame of renormalization group theory, seeking the model which can properly describe the dynamics of the system at the critical point.

The influence of Ge, Sb, Te atoms on the ferroelectricity and thermal properties of $Sn_2P_2S_6$ is studied in **chapter seven**. We discuss how the chemical substitution alters the total electronic levels hybridization of the material affecting the ferroelectric properties. Additionally, we perform a full theoretical data treatment of the continuous para-ferroelectric phase transition, considering all the critical models described in the thesis, in order to distinguish the predominant physical mechanism contributing to the critical anomaly.

In **chapter eight** a complete research on the crystal with a Lifshitz point $Sn_2P_2(S_{0.72}Se_{0.28})_6$ independently doped with Pb and Ge is presented. The chapter contains high-resolution thermal hysteresis curves and a detailed critical behavior study performed within the frame of renormalization group theory. Special attention has been devoted to testing the different universality classes, where Tricritical behavior takes place. It has been performed in order to ascertain what kind of tricritical point appears there. The results obtained have been compared with the proposed Blue-Emery-Griffiths BEG model with random field influence. All these manipulations have been undertaken in order to explain a possible location of a Lifshitz tricritical point on the temperature-concentration state diagram of $(Sn_{1-y}Pb_y)_2P_2(S_{1-x}Se_x)_6$ solid solutions.

Chapter nine contains experimental data of the thermal conductivity obtained for $Sn(Pb)_2P_2S(Se)_6$ system. An analysis of *k(T)* evolution is discussed in detail taking into account the features of the phase diagram. The origin of ultra-low thermal conductivity in phosphorous chalcogenide crystals is discussed considering the influence of several possible mechanisms (strong optic and acoustic phonon branches interaction, fluctuation of mass in the crystal lattice, electron lone pair relaxations) that can lead to the growth of the lattice anharmonicity in the investigated materials.

CHAPTER 1

Heat transfer phenomena and thermal properties

In solid state physics the thermal properties play an important role. It is a powerful tool, which lets understand better the nature of a high number of intrinsic phenomena in a medium, ranging from a general temperature characterization of a whole medium up to nano-scale effects compared with the crystal lattice size.

This chapter is devoted to a general theoretical review of the heat transfer phenomena and the related heat exchange processes. In the first place, we will explain which the heat transfer mechanisms are, and how heat is transmitted in homogeneous, isotropic or anisotropic materials. Secondly, the mathematical description of the heat propagation will be shown through the parabolic and hyperbolic heat diffusion equations. Also the description of the heat carriers in solid semiconductors (the materials studied in this work) will be considered.

The chapter concludes with a general, brief view of the main thermophysical properties (specific heat, thermal diffusivity, thermal effusivity and thermal conductivity).

1.1. Heat transfer phenomena: conduction, convection and radiation

The presence of any temperature difference in a medium or between bodies provides heat transfer. Heat can be transferred by several mechanisms: *conduction, convection* and *radiation* (fig 1.1). In most real processes the above three mechanisms are present in varying degrees. In all cases there is a quantitative relation between the heat flow $\vec{q}$ and the temperature gradient $\vec{\nabla} T$.

1.1.1. Conduction is the mechanism by which heat is exchanged between bodies in direct contact in the presence of a temperature gradient; different particles can be responsible for this exchange: electrons, molecules, phonons ... The basic law that gives the relationship between the heat flow and the temperature gradient is generally named Fourier's law. For a homogeneous, isotropic solid body (material in which thermal conductivity is independent of direction) it is given in the form [7]

$$\vec{q}_{con} = -K\vec{\nabla}T \,, \tag{1.1}$$

where $\vec{q}_{con}$ is heat flow, K the heat conductive coefficient (thermal conductivity). K is an intrinsic characteristic of the material and is temperature dependent. In this case the conductivity is presented as a scalar and indicates the ability of material to conduct heat. The heat transfer is proportional to the temperature gradient and the sign "−" in equation (1.1) implies that heat flows in the direction of decreasing temperature.

1.1.2. Convection. This process mainly takes place in gases and liquids or in the case when a surface of a solid body is surrounded by a fluid. Here, heat exchange occurs due to the motion of the medium particles. The appropriate equation which describes convective heat flow is known as Newton's cooling law and is written below in the form [7]:

$$q_{conv} = h(T_s - T_\infty) \,. \tag{1.2}$$

From equation (1.2) we can see that q_{conv} (heat flow), is proportional to the temperature gradient between a body surface T_s and a fluid T_∞. The constant h (known as the convection coefficient of heat transfer), depends in its turn on the flow velocity and the sample properties.

1.1.3. Thermal radiation occurs in all bodies without exceptions, due to its non-zero temperature. In this case, the thermal energy is transported by photons (electromagnetic waves) and the process requires no conduction medium in contrast to the two mechanisms above mentioned. The maximum heat flux that a perfect black body can emit is expressed by the well known Stefan-Boltzmann's law:

$$q_{rad} = \sigma_{SB} T_S^{\;4} \,, \tag{1.3}$$

where $\sigma_{SB} = 5{,}67 \cdot 10^{-8} Wm^{-2} K^{-4}$ is the Stefan-Boltzmann's constant. For real bodies the emitted heat flow from its surface changes slightly from (1.3) and writes

$$q_{rad} = \varepsilon \sigma_{SB} T_S^{\;4} \,, \tag{1.4}$$

where ε is the emissivity, which characterizes the radiative features of the body surface. In general it is difficult to compute the energy exchange produced by radiation between two bodies. Nevertheless, to simplify this situation one can consider the case in which heat is exchanged by radiation between two close surfaces which satisfy the condition

$S_1 \ll S_2$, which is the most frequent case in practice. To calculate a radiative heat transfer in this case, the equation below is of application [7]

$$q_{rad} = \varepsilon \sigma_{SB} S_1 (T_1^4 - T_2^4),$$
(1.5)

S_1 being the area of the body surface, T_1 the surface temperature and T_2 the temperature of the surrounding, respectively.

It is important to emphasize that we will only take into account in what follows the heat transported by conduction, due to the experimental conditions we will be working with and which will be described in Chapter 2. The main reason is that the convection and radiation mechanisms are negligible in comparison with conduction in our experimental systems, because the temperature gradients we are producing are very small (see chapter 2).
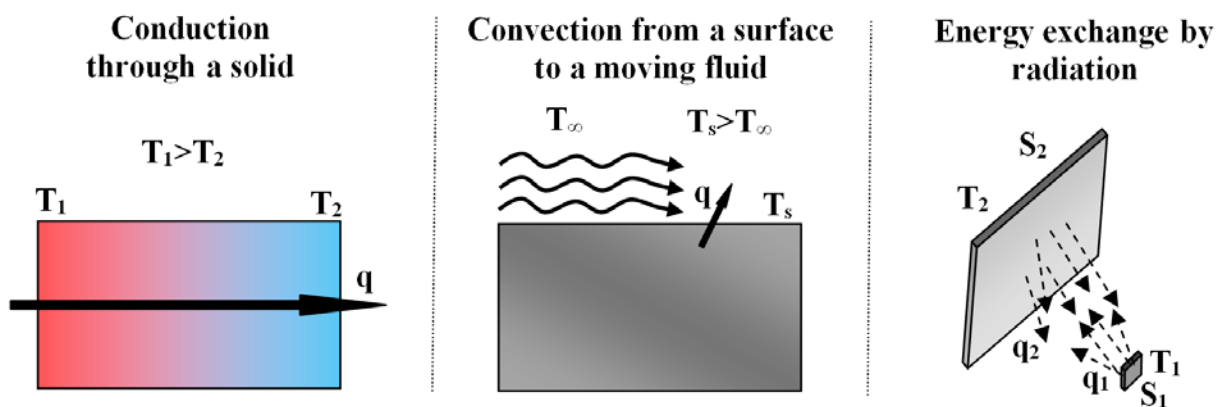
Fig. 1.1. Illustration of the heat transport mechanisms.

1.2. Heat conduction equation for the homogeneous isotropic and anisotropic cases

1.2.1. Differential heat conduction equation

One of the most important aims in an analysis of photothermal phenomena is to find a temperature distribution field in a medium. Let's pay attention to the *Fourier's law* in more detail. The spatial and temporal distribution of a temperature can be determined by applying the proper boundary conditions for the energy conversation principle to the heat flux, which flows into or out of a homogeneous differential element

of a body volume of thermal conductivity k, specific heat c and density ρ. The equation we use is as follows [8]:

$$Q_{in} + Q_g - Q_{out} = Q_{st}, \qquad (1.6)$$

where $Q_{in} = q_x + q_y + q_z$ contains the heat fluxes entering a volume dV; $Q_g = \dot{g}\, dxdydz$ the energy generated in dV; $Q_{out} = q_{x+dx} + q_{y+dy} + q_{z+dz}$ the heat fluxes exiting the volume dV.

Q_{st} is the rate of energy storage in the differential volume $Q_{st} = \rho c \dfrac{\partial T}{\partial t} dxdydz$.

The heat fluxes entering the volume q_x, q_y, q_z can be evaluated using Eq (1.1).

$$q_x = -k\, dydz \left.\frac{\partial T}{\partial x}\right|_x, \quad q_y = -k\, dxdz \left.\frac{\partial T}{\partial y}\right|_y, \quad q_z = -k\, dxdy \left.\frac{\partial T}{\partial z}\right|_z.$$

And the heat fluxes exiting it via a Taylor expansion

$$q_{x+dx} = q_x + \frac{\partial q_x}{\partial x} dx, \quad q_{y+dy} = q_y + \frac{\partial q_y}{\partial y} dy, \quad q_{z+dz} = q_z + \frac{\partial q_z}{\partial z} dz.$$

Introducing all this into equation (1.6), we obtain

$$-\frac{\partial q_x}{\partial x} dx - \frac{\partial q_y}{\partial y} dy - \frac{\partial q_z}{\partial z} dz + \dot{g}\, dxdydz = \rho c \frac{\partial T}{\partial t} dxdydz. \qquad (1.7)$$

Which leads to:

$$\frac{\partial}{\partial x}\left(k\, dydz \frac{\partial T}{\partial x}\right)dx + \frac{\partial}{\partial y}\left(k\, dxdz \frac{\partial T}{\partial y}\right)dy + \frac{\partial}{\partial z}\left(k\, dydx \frac{\partial T}{\partial z}\right)dz + \dot{g}\, dxdydz = \rho c \frac{\partial T}{\partial t} dxdydz. \quad (1.8)$$

This is the general form of the heat diffusion equation in cartesian coordinates. By solving equation (1.8) we can compute a distribution of temperature as a function of time. Its physical interpretation is as follows: at any point in a medium the sum of heat conduction rate into a volume and the rate of heat generation within the volume must be equal to the rate of change of the thermal energy stored at the same point.

In practice it is a complex task to find a solution for (1.8); it can be simplified by assuming that the thermal conductivity of the material is **isotropic** and introducing a new thermophysical parameter, the ***thermal diffusivity*** $D = k / \rho C$ (m^2/s). It is an important thermophysical coefficient whose physical meaning is: it indicates the rate at which heat is distributed in a material. Therefore, we can write these special cases:

a) Non-steady state with the presence of an internal heat source

$$\frac{\partial^2 T}{\partial x^2} + \frac{\partial^2 T}{\partial y^2} + \frac{\partial^2 T}{\partial z^2} + \frac{\dot{g}}{k} = \frac{1}{D}\frac{\partial T}{\partial t}, \tag{1.9}$$

or in a shortened form $\qquad \nabla^2 T + \dfrac{\dot{g}}{k} = \dfrac{1}{D}\dfrac{\partial T}{\partial t}$

b) Non-steady state without internal generation of heat

$$\frac{\partial^2 T}{\partial x^2} + \frac{\partial^2 T}{\partial y^2} + \frac{\partial^2 T}{\partial z^2} = \frac{1}{D}\frac{\partial T}{\partial t}, \quad \nabla^2 T = \frac{1}{D}\frac{\partial T}{\partial t} \tag{1.10}$$

c) Steady-state with internal heat generation

$$\frac{\partial^2 T}{\partial x^2} + \frac{\partial^2 T}{\partial y^2} + \frac{\partial^2 T}{\partial z^2} + \frac{\dot{g}(x,y,z)}{k} = 0, \quad \nabla^2 T + \frac{\dot{g}}{k} = 0 \tag{1.11}$$

d) Steady-state without internal generation of heat

$$\frac{\partial^2 T}{\partial x^2} + \frac{\partial^2 T}{\partial y^2} + \frac{\partial^2 T}{\partial z^2} = 0, \quad \nabla^2 T = 0 \tag{1.12}$$

which is the Laplace equation

1.2.2. Anisotropic cases

In order to take into account crystalline anisotropic media, we can rewrite the general equations (1.6)-(1.8) in the form [9]:

$$-\nabla \cdot \vec{q}(r,t) + \dot{g}(r,t) = \rho c \frac{\partial T(r,t)}{\partial t}. \tag{1.13}$$

And the thermal conductivity as a tensor of second rank

$$k = \begin{pmatrix} k_{11} & k_{12} & k_{13} \\ k_{21} & k_{22} & k_{23} \\ k_{31} & k_{32} & k_{33} \end{pmatrix}; \quad k_{ij}, \; i,j = 1,2,3 \tag{1.14}$$

so that the components of the heat flux will read:

$$q_x = -\left(k_{11}\frac{\partial T}{\partial x} + k_{12}\frac{\partial T}{\partial x} + k_{13}\frac{\partial T}{\partial x} \right);$$

$$q_x = -\left(k_{21}\frac{\partial T}{\partial y} + k_{22}\frac{\partial T}{\partial y} + k_{23}\frac{\partial T}{\partial y} \right); \tag{1.15}$$

$$q_z = -\left(k_{31}\frac{\partial T}{\partial z} + k_{32}\frac{\partial T}{\partial z} + k_{33}\frac{\partial T}{\partial z} \right);$$

Introducing (1.14) and (1.15) in eq (1.13) and assuming the common situation in which there are no internal heat sources, we obtain:

$$k_{11}\frac{\partial^2 T}{\partial x^2} + k_{22}\frac{\partial^2 T}{\partial y^2} + k_{33}\frac{\partial^2 T}{\partial z^2} + 2k_{12}\frac{\partial^2 T}{\partial x \partial y} + 2k_{13}\frac{\partial^2 T}{\partial x \partial z} + 2k_{23}\frac{\partial^2 T}{\partial y \partial z} = \rho\, c\, \frac{\partial T}{\partial t}, \qquad (1.16)$$

having taken into account that $k_{ij} = k_{ji}$, $(i \neq j)$ by the reciprocity relation. This equation can also be written as a function of the thermal diffusivity tensor of second rank

$$D_{11}\frac{\partial^2 T}{\partial x^2} + D_{22}\frac{\partial^2 T}{\partial y^2} + D_{33}\frac{\partial^2 T}{\partial z^2} + 2D_{12}\frac{\partial^2 T}{\partial x \partial y} + 2D_{13}\frac{\partial^2 T}{\partial x \partial z} + 2D_{23}\frac{\partial^2 T}{\partial y \partial z} = \frac{\partial T}{\partial t}. \qquad (1.17)$$

As thermal conductivity and thermal diffusivity tensors are symmetric and the elements in the diagonal are positive, we can always find a reference system (X, Y, Z) in which they can be written as

$$k = \begin{pmatrix} k_x & 0 & 0 \\ 0 & k_y & 0 \\ 0 & 0 & k_z \end{pmatrix}, \quad D = \begin{pmatrix} D_x & 0 & 0 \\ 0 & D_y & 0 \\ 0 & 0 & D_z \end{pmatrix}, \qquad (1.18)$$

where the components in the tensors are known as the main conductivities and diffusivities.

Let's imagine that we have a sheet of an anisotropic material whose thickness l is much smaller than its surface dimension $x \ll z, y$, and whose faces are cut perpendicularly to a major axis (for example $\perp$ to X). In this situation the temperature gradient between the opposite faces depends only on X, implying that:

$$\frac{\partial T}{\partial z} = \frac{\partial T}{\partial y} = 0. \qquad (1.19)$$

Taking into account (1.19), the equation of heat flux is given as a one-dimensional problem instead of a 3-Dimensional

$$q_x = -k_x \frac{dT}{dx}. \qquad (1.20)$$

The problem in (1.20) is equal to the one that we have in the case of an isotropic medium, when q is expressed through only one thermal conductivity component. Hence, knowing the thermal gradient dT/dx and the component of heat flow q_x it is easy to obtain the thermal conductivity in the same direction. Repeating this procedure with the different cuts of a material, and complying the size condition ($y \ll x, z; z \ll x,$

y), it is possible to calculate the two others conductivity components k_y and k_z, respectively. Or the thermal diffusivities.

1.2.3. Conductivity matrix for crystal systems

With symmetry considerations, the anisotropic crystals can be grouped into the seven distinct systems identified as *triclinic, monoclinic, orthorhombic, hexagonal, tetragonal, trigonal*, and *cubic* systems. Regarding the symmetry groups the thermal conductivity tensors can be summarized as follow:

● *Triclinic*. The system with a lowest symmetry ($a \neq b \neq c$, $\alpha \neq \beta \neq \gamma$), hence all nine components of k_{ij} can be nonzero, and we have

$$k = \begin{pmatrix} k_{11} & k_{12} & k_{13} \\ k_{21} & k_{22} & k_{23} \\ k_{31} & k_{32} & k_{33} \end{pmatrix}. \tag{1.21}$$

● *Monoclinic*. Some of the components become zero with symmetry considerations ($a \neq b \neq c$, $\alpha = \gamma = 90^0 \neq \beta$).

$$k = \begin{pmatrix} k_{11} & k_{12} & 0 \\ k_{21} & k_{22} & 0 \\ 0 & 0 & k_{33} \end{pmatrix}. \tag{1.22}$$

● *Orthorhombic*. The thermal conductivity coefficients ($a \neq b \neq c$, $\alpha = \beta = \gamma = 90^0$) are given by

$$k = \begin{pmatrix} k_{11} & 0 & 0 \\ 0 & k_{22} & 0 \\ 0 & 0 & k_{33} \end{pmatrix}. \tag{1.23}$$

● *Cubic*. In this system all the main conductivities are equal $k_{11} = k_{22} = k_{33}$ ($a = b = c$, $\alpha = \beta = \gamma = 90^0$)

$$k = \begin{pmatrix} k_{11} & 0 & 0 \\ 0 & k_{11} & 0 \\ 0 & 0 & k_{11} \end{pmatrix}. \tag{1.24}$$

● *Hexagonal* ($a = b \neq c$, $\alpha = \beta = 90^0$ $\gamma = 120^0$), *Tetragonal* ($a = b \neq c$, $\alpha = \beta = \gamma = 90^0$) *and Trigonal* ($a = b = c$, $\alpha = \beta = \gamma \neq 90^0$)

$$k = \begin{pmatrix} k_{11} & k_{12} & 0 \\ -k_{12} & k_{11} & 0 \\ 0 & 0 & k_{33} \end{pmatrix}. \qquad (1.25)$$

Taking into account $k_{ij} = k_{ji}$, $(i \neq j)$, the maximum number of components will be 6 for the triclinic system while the minimum will be 1 for the cubic one; in the hexagonal, trigonal and tetragonal systems, this implies that $k_{12}=0$. All these considerations are also applicable to the thermal diffusivity tensor.

1.3. Heat propagation in a medium. Thermal waves

Huge theoretical efforts have been done along the years by the different research groups which work in the physics of photothermal phenomena. Due to this a lot of papers have been published in order to explain the propagation of thermal energy in a medium, making it impossible to account for all of them in this work; nevertheless, they have the same physical background [10-17]. In the following, we are going to discuss how heat propagation in a medium can be described, including the consideration of heat waves.

1.3.1. Parabolic heat diffusion equation. To explain this phenomenon and to understand the physical sense of the term "thermal wave", we will show the mathematical description for the ***parabolic*** and ***hyperbolic*** heat diffusion equations. To do this, we refer in the first place to the well established classical approach [8], whose physical meaning can be interpreted as follows: whenever there is a temperature gradient $\vec{\nabla} T$ in a solid material or in a stationary liquid, the heat flow $\vec{q}$ occurs from the warmer part to the colder one, this is known as the *Fourier's law* (1.1). Secondly, we apply the energy conversation law as proposed in [7]. Together they lead to

$$\nabla^2 T(\vec{r},t) - \frac{1}{D}\frac{\partial T(\vec{r},t)}{\partial t} = 0, \qquad (1.26)$$

Where D is the thermal diffusivity of the material. Again it must be pointed out that the relation between the thermal conductivity and diffusivity is expressed though an equation $D = k/\rho c$, where ρ is the density and c is the heat capacity of the material. The expression (1.26) written above is called the *parabolic heat diffusion equation*, which contains the spatial $\vec{r}$ and temporal t parts. Note that (1.26) assumes no internal heat

sources. It is one of the four special cases described in the section 1.1.2, in particular equation (1.10).

Let's consider a material, which is isotropic, homogeneous and semi-infinite along its *x*-axis, and whose surface is uniformly illuminated by a light beam as a harmonic heat source with the modulated intensity $I = \dfrac{I_0}{2}\left(1+\cos(\omega t)\right) = \mathrm{Re}\left[\dfrac{I_0\left(1+\exp\left[i\omega t\right]\right)}{2}\right]$, where I_0 is the source intensity, $\omega = 2\pi f$ is the angular modulation frequency (fig.1.2). The symbol "Re" means real part [11].
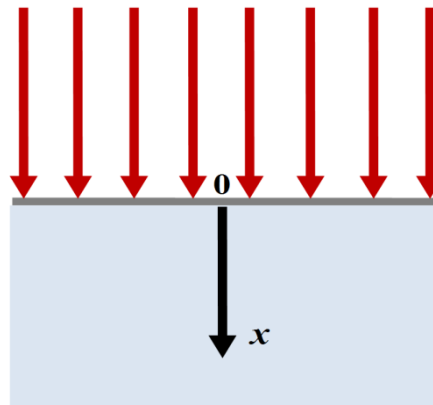
Fig. 1.2. The opaque, semi-infinite material illuminated by a modulated light beam.

As this is a one-dimensional problem, equation (1.26) reduces to

$$\frac{\partial^2 T}{\partial x^2} - \frac{1}{D}\frac{\partial T}{\partial t} = 0, \text{ with} \qquad x>0,\ t>0 \tag{1.27}$$

The temperature distribution at any point of the material is then given by

$$T(x,t) = T_{amb} + T_{dc}(x) + T_{ac}(x,t), \tag{1.28}$$

where T_{amb} is the ambient temperature, T_{dc} is a time-independent increase above T_{amb}, T_{ac} is a periodic thermal oscillation which has the same frequency as the light beam. We are interested in the time-dependent component of T_{ac}, which can be written as the real part of

$$T_{ac}(x,t) = T_{ac}(x)e^{i\omega t}. \tag{1.29}$$

Substituting (1.29) into (1.27), the spatial component of T_{ac} satisfies Helmholtz's equation.

$$\frac{d^2 T_{ac}(x)}{dx^2} - \sigma^2 \, \mathrm{T}_{ac}(x) = 0; \quad \sigma = \sqrt{i\omega / \mathrm{D}}, \tag{1.30}$$

whose general solution has the form

$$T_{ac}(x) = A \exp[-\sigma x] + B \exp[\sigma x], \tag{1.31}$$

where *A* and *B* are constant. In our case when $x \to \infty$, $T(x)$ must be finite, hence, *B*=0. Constant *A* can be evaluated by applying the flux continuity boundary conditions, when *x*=0

$$-k \frac{dT_{ac}}{dx}\bigg|_{x=0} = k \, \sigma \, A e^{-\sigma x}\big|_{x=0} = \frac{I_0}{2}, \tag{1.32}$$

from (1.32) we obtain $A = I_0 / 2k\sigma$, thus, the full solution of (1.29) is

$$\frac{I_0}{2k\sigma} \exp[-\sigma x] \exp[i\omega t], \tag{1.33}$$

whose real part is

$$T_{ac}(x,t) = \frac{I_0}{2\varepsilon\sqrt{\omega}} \exp[-x/\mu] \cos\left[\frac{x}{\mu} - \omega t + \pi / 4\right]. \tag{1.34}$$

The equation (1.34) represents a highly damped planar harmonic wave propagating along *x*-axis, with the same frequency *f* as the modulated heat source. Here $\varepsilon = k / \sqrt{D}$ is the thermal effusivity of the material (also known as *e* but we don't use this form here in order not to mistake it for the exponentials). $\mu = \sqrt{2D / \omega}$ is the thermal diffusion length, the parameter whose physical meaning is as follows: it shows the penetration depth travelled by the wave at which the amplitude of the temperature is reduced by a factor *e* (fig. 1.3). This thermal wave approximation is found to be convenient in the description of the majority of the photothermal experiments [1, 11, 12].
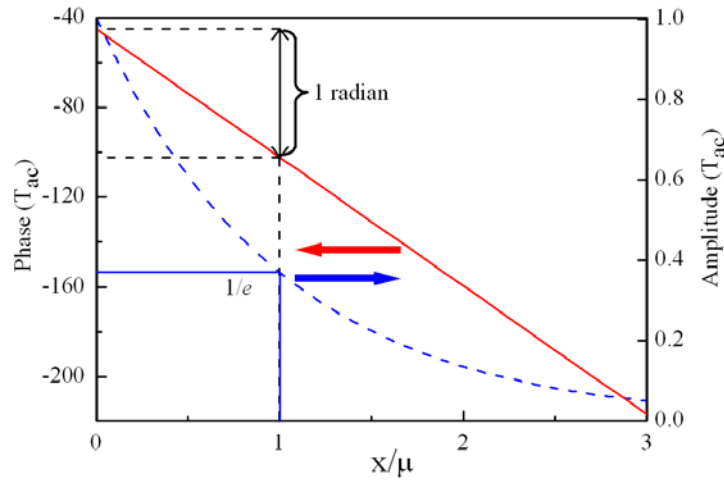
Fig.1.3. The normalized phase and amplitude of the time-dependent component T_{ac} as a function of the reduced depth x/μ.

1.3.2. Hyperbolic heat diffusion equation.

Even though the parabolic heat diffusion equation is a powerful tool in photothermal science, it cannot be a fundamental description of heat transport because it does not account for a propagation speed [5]. Let´s introduce in (1.1) a new parameter τ, a delay between the heat flux and the temperature gradient, as it has been done in [12]; therefore, (1.26) becomes

$$\nabla^2 T(\vec{r},t) - \frac{1}{D}\frac{\partial T(\vec{r},t)}{\partial t} - \frac{\tau}{D}\frac{\partial T(\vec{r},t)}{\partial t} = 0, \tag{1.35}$$

Where it is obvious that if $\tau = 0$, (1.35) becomes (1.27). Following with same procedure as in 1.3.1, the Helmholtz equation will be

$$\frac{d^2 T'_{ac}(x)}{dx^2} - \sigma'^2\, T'_{ac}(x) = 0; \quad \sigma' = \sqrt{\frac{i\omega}{D} - \frac{\tau\omega^2}{D}} = \frac{i\omega}{D}(1+i\omega\tau). \tag{1.36}$$

The real part of the time-dependent component T'_{ac} has a solution of the form

$$
\begin{aligned}
T'_{ac}(x,t) = {} & \frac{I_0\sqrt{\tau}}{2e}\sqrt[4]{\frac{1+(\omega\tau)^2}{(\omega\tau)^2}}\exp\left(-x\sqrt{\frac{\omega}{2D}}\sqrt{\sqrt{1+(\omega\tau)^2}-\omega\tau}\right)\times \\
& \times\cos\left(x\sqrt{\frac{\omega}{2D}}\sqrt{\sqrt{1+(\omega\tau)^2}-\omega\tau}-\omega\tau-\frac{arctg(\omega\tau)}{2}+\pi/4\right)
\end{aligned} \tag{1.37}
$$

Consider two regimes for (1.37): the *low* and ***high*** frequencies:

● If $\omega\tau \ll 1$, therefore we have that (1.37) becomes (1.34). Then, both solutions for the parabolic and the hyperbolic cases coincide.

● If $\omega\tau \gg 1$, equation (1.37) can be modified to:

$$T'_{ac}(x,t) = \frac{I_0\sqrt{\tau}}{2e}\exp\left(-x\sqrt{\frac{\omega}{2D\tau}}\right)\cos\left(\sqrt{\frac{\tau}{D}}\omega x - \omega t\right). \qquad (1.38)$$

Which means that this hyperbolic description is appropriate or not depending on the time scale. The upper limit of this time delay is small enough and can be observed only in a high frequency regime so as not to have any influence in measurements performed under our experimental conditions.

1.3.3. Physical analysis of the thermal wave

Analyzing the solutions of the time-dependent component of the temperature distribution (1.34) and (1.37), several facts can be established.

● Mathematically they are described as ordinary electromagnetic waves, with the important difference that the thermal waves do not transport energy [11].

● Thermal waves have an oscillatory spatial dependence $\exp[ikx]$, whose wave vector is written $\text{Re}(\sigma) = 1/\mu = \sqrt{\omega/2D}$, were μ is the thermal diffusion length.

● If $\mu < l$, where l is the thickness, a material is thermally thick while it is considered thermally thin when $\mu > l$.

● Thermal waves are heavily damped with a decay constant equal to μ. Thermal waves will propagate deeper into a solid if it has high diffusivity or if the frequency of the thermal wave is low.

● Thermal waves are highly dispersive $\upsilon = \omega\mu = \sqrt{2D\omega}$.

● At the surface when $x=0$, there is a phase lag between the excitation and the surface temperature equal to 45^0, as this phase lag is in general $\varphi = -\frac{x}{\mu} - \frac{\pi}{4}$.

● Similarly to the electrical impedance, thermal wave impedance is defined as $Z = \frac{1}{k\sigma} = \frac{1}{\sqrt{i\omega\rho c k}} = \frac{1}{\varepsilon\sqrt{i\omega}}$, were ε is the thermal effusivity and determines the magnitude of the thermal wave at the sample surface. If the value of effusivity is low it leads to a high value of the surface temperature [7].

Another interesting detail that can be pointed out from (1.35) is that thermal waves have an intrinsic diffusive character, because D appears in both derivatives; as a consequence the thermal diffusivity controls both the damping and the wave velocity at the same time.

1.3.4. Reflection and refraction of thermal waves

Similarly to the electromagnetic and acoustic waves the thermal waves can also be reflected and refracted. As consequence, they can be used to obtain the reflection and transmission coefficients at a thermal boundary. Suppose we have media 1 and media 2, separated by a boundary plane at $x=0$ (fig.1.4), where θ_i, θ_r and θ_t are the angles for the incidence T_i, the reflected T_r and the transmitted T_t thermal waves, respectively. Let the expression for these three waves has the form [7]

$$T_i = A\exp(-\sigma_1 x\cos\theta_i - \sigma_1 y sin\theta_i + i\omega\, t);$$
$$T_r = AR\,\exp(\sigma_1 x\cos\theta_r - \sigma_1 y sin\theta_r + i\omega\, t); \qquad (1.39)$$
$$T_t = AT\exp(-\sigma_2 x\cos\theta_t - \sigma_2 y sin\theta_t + i\omega\, t);$$

where A is the amplitude of the incident wave, R and T, accordingly, are the reflection and transmission coefficients at $x=0$ and $y=0$.

Considering the continuity of temperature at interface $(X=0)$ we can determinate the values of these coefficients:

$$A\exp(-\sigma_1 y sin\theta_i) + AR\,\exp(-\sigma_1 y sin\theta_r) = AT\exp(-\sigma_2 y sin\theta_t), \qquad (1.40\ a)$$

or using $\sigma = \sqrt{\omega/2D}$

$$A\exp(-\sqrt{\frac{\omega}{2D_1}}y sin\theta_i) + AR\,\exp(-\sqrt{\frac{\omega}{2D_1}}y sin\theta_r) = AT\exp(-\sqrt{\frac{\omega}{2D_2}}y sin\theta_t), \qquad (1.40\ b)$$
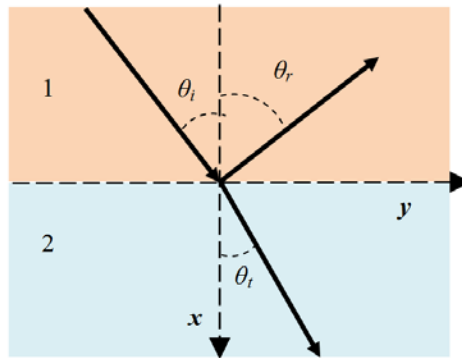
Fig. 1.4. Reflection and refraction of the thermal waves at interfaces.

For all y position across $x=0$ this condition must be maintained, hence, in (1.40 a) the exponents must be equal. In turn, we can rewrite it in the form

$$\sigma_1 y sin\theta_i = \sigma_1 y sin\theta_r = \sigma_2 y sin\theta_t, \qquad (1.41)$$

From (1.41) the reflection and refraction laws follow

$\theta_i = \theta_r$ the reflection law; $\qquad\qquad \sigma_1 \sin(\theta_i) = \sigma_2 \sin(\theta_t)$ the refraction law.

In case of continuity of flux at $x=0$, by differentiating the equation (1.40 a) we will obtain

$$k_1\sigma_1 \cos(\theta_i) - Rk_1\sigma_1 \cos(\theta_i) = Tk_2\sigma_2 \cos(\theta_t), \qquad (1.42)$$

applying the condition written above $\theta_i = \theta_r$ and $T = 1 + R$ at $y = 0$, from (1.40a) the coefficients R and T can be found as

$$R = \frac{\cos(\theta_i) - b\cos(\theta_t)}{\cos(\theta_i) + b\cos(\theta_t)}, \quad \text{and} \quad T = \frac{2\cos(\theta_i)}{\cos(\theta_i) + b\cos(\theta_t)}, \qquad (1.43)$$

here, $b = \dfrac{k_2\sigma_2}{k_1\sigma_1} = \dfrac{\sqrt{k_2\rho_2 c_2}}{\sqrt{k_1\rho_1 c_1}} = \dfrac{e_2}{e_1}$, where $e = \sqrt{k\rho c}$ is the thermal effusivity. As it can be seen,

b is the effusivity ratio of the two media, thus it provides a measure of the thermal mismatch between them.

For a normal incidence beam $\theta_i = \theta_r = 0$, therefore, the equations (1.43) are reduced to

$$R = \frac{1-b}{1+b} = \frac{e_1 - e_2}{e_1 + e_2}, \quad \text{and} \quad T = \frac{2}{1+b} = \frac{2e_1}{e_1 + e_2}. \qquad (1.44)$$

Both coefficients R and T depend on the thermal effusivity. To explain the role which plays the thermal effusivity, suppose we have medium 1 and medium 2 with effusivities e_1 and e_2, respectively, in perfect thermal contact (see figure 1.5). A thermal waves propagates along medium 1 from left to right and arrives at the interface of both media at $x=0$. Let's consider two cases in which the thermal effusivities and conductivities are very different:

a) $e_1 \gg e_2$, $T_1 > T_2$ and $k_1 \gg k_2$. Under these conditions, $b \sim 0$. Substituting it into (1.44) gives us $R \sim 1$ and $T \sim 2$. Introducing these values in equation (1.39) gives that $T_t \neq 0$ meaning that the thermal wave propagates into medium 2, fig. 1.5 *a*.

b) $e_1 \ll e_2$, $T_1 > T_2$ and $k_1 \ll k_2$. In this case $b \sim \infty$ that, in turn, modifies the reflection and transition coefficients $R \sim -1$, $T \sim 0$. Substituting these R and T into the equation (1.39) gives $T_t \sim 0$, which means that the thermal wave does not propagate along medium 2 [19]. It is important to emphasize one detail here, the phase of the reflected wave is shifted on 180^0 in respect to incidence one (fig.1.5 *b*). This effect is known as ***a thermal mirror***.
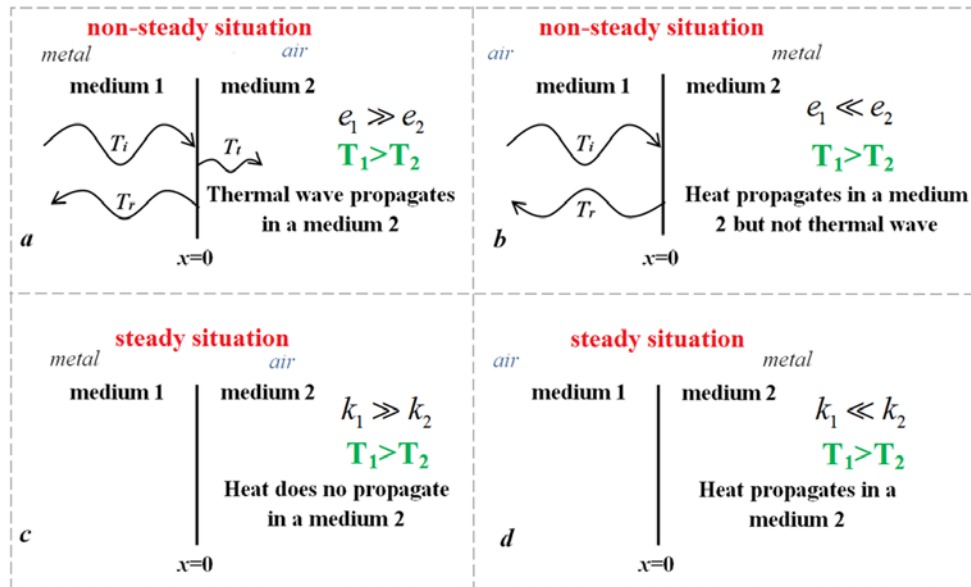
Fig.1.5. Thermal wave propagation through the two media.

Let's compare this situation with what happens in a steady situation and a thermal gradient is maintained between both media which are characterized by the same extreme conditions.

c) $e_1 \gg e_2$, $T_1 > T_2$ and $k_1 \gg k_2$. As the thermal conductivity of the second medium is so low compared to the first one, nearly no heat will be transferred from medium1 to medium 2 (Fig. 1.5 c).

d) $e_1 \ll e_2$, $T_1 > T_2$ and $k_1 \ll k_2$. Heat will be efficiently transferred to medium 2 (Fig. 1.5 d).

This might be considered as a paradox (in one case thermal wave is transmitted but no heat is transferred while in the other one it is just the opposite) but it is not. Two different regimes are being taken into account: *non-steady and steady*. In the first case, thermal effusivity governs what happens in the interface, while in the steady case

thermal conductivity tells us what will happen. This is related to the fact that thermal waves lack an important wave-like feature: they do not transport energy, as already mentioned in the previous section. This is why both thermal magnitudes are equally important when dealing with the physics of thermal sciences.

1.4. Heat carriers in solid semiconductors

1.4.1. Phonons as heat carriers. In a solid system a thermal resistance is caused by the anharmonicity of the lattice vibrations known as phonons. The consideration of these vibrations only through a harmonic approximation leads to the absence of thermal resistance [20]. This statement is a quite obvious: for the harmonic waves a linear superposition principle is of application. As a consequence the phonons do not interact, hence, the thermal resistance tends to 0, because the heat flux propagates with the velocity of sound.

This situation can be overcome by introducing the terms of power three for the displacement of atoms into an expansion of the potential energy [20]. Therefore, it makes possible to imagine the collision process for three phonons (fig 1.6).
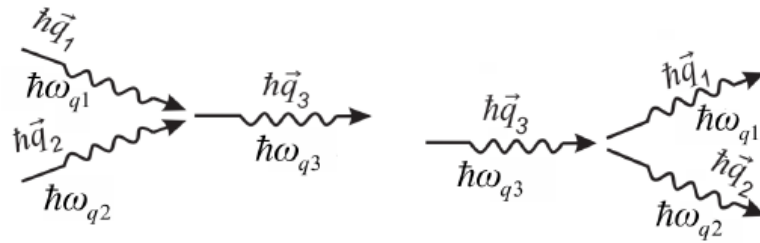
Fig.1.6. Illustration of the phonon-phonon interactions: *a* – two phonons converted into one; *b* – one phonon splits into two [20].

The probability of those processes is nonzero if two conditions are satisfied:

$$\hbar\omega_{q_1} + \hbar\omega_{q_2} = \hbar\omega_{q_3},\tag{1.45}$$

$$\hbar\vec{q}_1 + \hbar\vec{q}_2 = \hbar\vec{q}_3 + \vec{T}_g,\tag{1.46}$$

where $\vec{T}_g = g_1\vec{b}_1 + g_2\vec{b}_2 + g_3\vec{b}_3$ is the reciprocal vector of the crystal lattice.

The phonon-phonon interactions can be separated into two groups: the normal process or "*N-process*" when $\vec{T}_g = 0$, and the Umklapp process "*U-process*" if $\vec{T}_g = 0$ (fig. 1.7). Let's mark the difference between them. Thermal energy propagates in the

direction of the phonon group velocity. In the case of a "*N*-process" the direction of the energy flow with wave vector $\vec{q}_3$ coincides with the direction in which the thermal energy is transmitted by the addition of the modes whose wave vectors are $\vec{q}_1$ and $\vec{q}_2$, respectively (fig. 1.7, *a*). In contrast, for a "*U-process*" the direction of a wave vector $\vec{q}_3$ is different with respect to the direction obtained by adding $\vec{q}_1$ and $\vec{q}_2$. The fact that "U-processes" involve a non perfect conservation of crystal momentum leads to a quick recovery of the equilibrium phonons distribution in a medium, and as a consequence, the thermal conductivity will have a finite value.
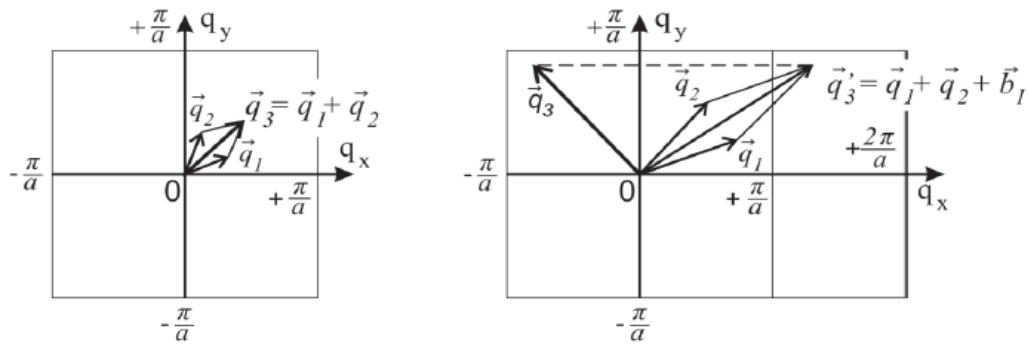
Fig. 1.7. The scheme illustrates the difference between "*N*" and "*U*" processes [20].

According to the classical kinetic theory of the gases, the thermal conductivity of the phonons in a solid material is expressed as

$$k_{ph} = \frac{1}{3} c_V \bar{\upsilon}_{ph} \bar{\lambda}_{ph} = \frac{1}{3} c_V (\bar{\upsilon}_{ph})^2 \langle \tau \rangle, \qquad (1.47)$$

where c_V is the heat capacity of a unit volume; $\bar{\upsilon}_{ph}$ the average phonons velocity in a crystal; $\bar{\lambda}_{ph}$ the phonon mean free path, an average distance travelled by a phonon between the two scattering acts, and depends heavily on temperature; $\langle \tau \rangle = \bar{\lambda}_{ph} / \bar{\upsilon}_{ph}$ is the effective relaxation time of phonons, whose inverse magnitude $\langle \tau \rangle^{-1}$ corresponds to the frequency of the phonons collisions.

Let´s briefly consider the temperature dependence of equation (1.47), were c_V and $\bar{\lambda}_{ph}$ mainly determine the temperature behavior of k_{ph}.

• *High temperature region* $T > \theta_{Debay}$. At these temperatures c_V obeys the *Dulong and Petit's law* ($c_V = 3Nk_B$, k_B being the Boltzmann constant) and leads to a saturation

value; therefore, the temperature dependence of k_{ph} is mainly determined by $\bar{\lambda}_{ph}$. The probability of the "*U*-processes" taking place grows with the number of phonons, which increase with temperature. As a consequence, the frequency of collisions $\langle \tau \rangle^{-1}$ will rise in proportion to *T*. If we account that the phonon mean free path is inversely proportional to temperature, then for the thermal conductivity by phonons we can write:

$$k_{ph} \sim T^{-1}. \tag{1.48}$$

• *Low temperature region* $T < \theta_{Debay}$. The probability of "*U* – processes" decreases exponentially, and only the phonons with energy higher than $\hbar\omega_{ph} > k_B\theta_D / 2$ are able to participate in them. It leads to an exponential increasing of the phonon mean free path $\bar{\lambda}_{ph} \sim \exp(\theta_D / 2T)$. On the other hand, the specific heat in a Debye model decreases as T^3 while lowering the temperature. In spite of this fact, the thermal conductivity will continue rising, due to the strong exponential term.

$$k_{ph} \sim T^3 \exp(\theta_D / 2T). \tag{1.49}$$

• *Temperatures close to* 0K. The probability of the "*U*–processes" is very small; in turn, the phonon mean free path becomes comparable with the sample size and does not depend on temperature. In this case the thermal conductivity of phonons is determined by the heat capacity and behaves as

$$k_{ph} \sim T^3. \tag{1.50}$$

Nevertheless, these regions are not perfectly isolated. In practice, thermal conductivity curves present a maximum for whose description it is necessary to take into account several scattering mechanisms ("*U*-processes", presence of doping, point defects in a crystal lattice, etc.).
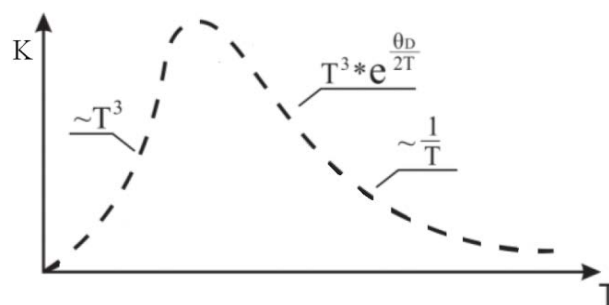
Fig. 1.8. The temperature dependence of the phonon thermal conduction [20].

Regarding the thermal conductivity in crystalline semiconductors is important to emphasize there are several other sources of anharmonicity, which can heavily alter a general shape of the dependence presented above (fig. 1.8). In some particular cases, the thermal conductivity as well a "phonon hump" can be effectively suppressed due to the strong interaction (coupling) between the soft optic and the acoustic phonon branches [21, 22], relaxation of lone pair electrons [23, 24], resonant chemical bounding [25, 26], Jahn-Teller instability of the electronic structure [27] and a complex crystal lattice [28]. Besides, the atomic mass fluctuation in mixed crystals may create additional centers which can favor the phonon scattering processes [29, 30] reducing even more the lattice thermal conductivity. In a last chapter of the thesis we will show the effect of almost all those mechanisms on the thermal conductivity of $Sn(Pb)_2P_2S(Se)_6$-like semiconductor ferroelectrics having summarized a whole set of experimental data obtained in this work.

1.4.2. Electrons as heat carriers. In semiconductors, the contribution of phonons to the thermal conductivity k_{ph} is usually much higher than the electrons contribution k_{el}. However, in cases when the number of the free electrons (or holes) is relatively large (about $10^{18} - 10^{20} cm^{-3}$), k_{ph} and k_{el} could be the same order of magnitude.

To describe the electronic contribution to the thermal conductivity in semiconductors we refer to the kinetic Boltzmann equation for the electrons and to the theoretical analysis performed in [31, 32]. In a semiconductor with monopolar electronic conductivity we get an expression for the thermal energy flow as follows:

$$Q = -n\mu_{el}\left(\frac{2k_B^2 T}{e}\right)\vec{\nabla}T. \qquad (1.51)$$

The term before $\vec{\nabla}T$ in (1.51) plays the role of the thermal conductivity coefficient. Therefore, we can write

$$k_{el} = n\mu_{el}\left(\frac{2k_B^2 T}{e}\right) = 2\left(k_B/e\right)^2 \sigma_{el}T, \qquad (1.52)$$

where μ_{el} is the mobility of electrons, σ_{el} is the electronic conductivity. Accordingly, the thermal conduction caused by the free electrons is determined by the temperature of

a material and its electronic conductivity. The appropriate equation that describes this situation is written below.

$$\frac{k_{el}}{\sigma_{el}} = 2\left(\frac{k_B}{e}\right)^2 T.$$
(1.53)

1.5. Thermal properties of homogeneous materials

In this section we are revising several concepts which have been introduced in the previous sections but whose importance in the development of this work justifies analyzing them as a whole and as a summary of the chapter.

There are four thermal properties which fully characterize a material: specific heat, thermal conductivity, thermal diffusivity and thermal effusivity. If we are in a static situation (the temperature does not depend on position and time) specific heat *c* will be enough to fully describe it. In the analysis of a steady one (temperature does not vary over time but vary over position), thermal conductivity (*k*) characterizes the problem. Concerning the most general situation when temperature varies over position and time, both the thermal diffusivity (*D*) and effusivity (*e*) must be taken into description of the heat propagation in a material [33]. The brief review of these physical properties is written below.

• **Heat capacity.** In a thermally isolated material with mass *m*, the relationship between the heat deposition and the temperature rise is given by equation

$$\Delta Q = mc\Delta T,$$
(1.54)

where ΔQ is an amount of energy (heat) that should be added to a body of mass *m* to produce the intrinsic temperature gradient equal 1K. The specific heat is an ability of the material to store internal energy (thermal energy).

• **Thermal conductivity.** Whenever a temperature gradient is applied to material, a heat flow occurs in it. The appropriate equation has already been shown and is called the Fourier's law

$$\vec{q} = -k\vec{\nabla}T.$$
(1.55)

This quantity characterizes the amount of thermal energy transported through a unit area per unit time, in a material with unit thickness, whose opposite surfaces have the

temperature gradient equal to 1K. The thermal conductivity (W/m·K) is the ability of a material to extract heat from a thermal energy source.

• ***Thermal diffusivity.*** The physical meaning of the thermal diffusivity is associated with the velocity of heat propagation, and characterizes how rapidly a material reaches the thermal equilibrium state. It measures the temperature change created in the unit volume of a material produced by a heat flow transported through a unit area per unit time, in a material with unit thickness, whose opposite surfaces have the temperature gradient equal to 1K.

$$\nabla^2 T(\vec{r},t) - \frac{1}{D}\frac{\partial T(\vec{r},t)}{\partial t} = 0. \tag{1.56}$$

Thermal diffusivity D (m/s^2) defines the rate at which heat is being distributed in a material. This magnitude depends not only on the thermal conductivity of the material, but also on the rate at which the energy can be stored. The conductivity k and diffusivity D are bounded through a constituent relation $D = k/\rho c$, ρ being the density of a material.
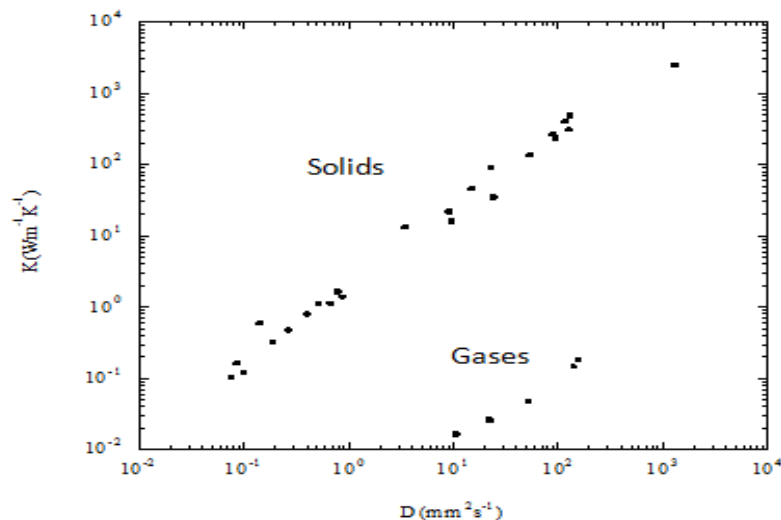
Fig. 1.9. Relation between thermal conductivity and diffusivity in solids and gases [19].

The k/D ratio is the heat capacity per unit volume. For condensed materials this value is practically constant and varies between 1×10^6 and 4×10^6 (Table 1.1). However, the relation that the good (bad) conductor is good (bad) diffuser is not an exact rule. Let's take from the table 1.1 two metals, for instance, Ni and Pb. As seen, nickel is a better heat conductor than lead, hence, we could say that Ni is getting warmer faster in

comparison with Pb, but the reverse situation occurs in their values for thermal diffusivity, heat is being distributed quicker through lead.

It is interesting to point out that gases, due to its low conductivity, extract a small amount of thermal energy from a heat source, but the absorbed energy is rapidly diffused through it.

• **Thermal effusivity.** The last property we describe characterizes the thermal impedance of a material. Effusivity is the ability to exchange thermal energy with the environment.

$$e = \sqrt{\rho c k} = k / \sqrt{D} = \rho c \sqrt{D}. \tag{1.57}$$

To understand the physical sense of it we again refer to table 1.1. Let's consider the materials whose thermal conductivity values are almost the same but whose effusivities are different: Co and K. In steady mode both materials extract from a reservoir the same amount of thermal energy. Nevertheless, under transient condition, Co extracts 2.5 times more heat than K for the same time interval due to its higher effusivity value [33].

Table 1.1.

Thermophysical properties of the some selected materials [33].

Material	ρc, ($\times 10^6$ Jm^{-3}K^{-1})	K, (Wm^{-1}K^{-1})	D, ($\times 10^{-6}$ m^2 s^{-1})	e, (Wm^{-2}K^{-1}s$^{-1/2}$)
Al	2.5	238	93.38	24642
Cr	3.2	93.7	29.15	17356
Cu	3.4	401	116.60	37136
Au	2.5	317	127.32	25093
Ag	2.5	429	173.86	32535
Ni	4.0	90.7	22.95	18931
Ti	2.4	21.9	9.32	7172
K	0.65	102	158	8150
Pb	1.5	35.3	24.13	7186
Co	4.05	100	24.6	20150
Diamond	1.8	2300	1291.05	64011
Silicon	1.7	148	89.21	15669
Quartz glass	1.6	1.4	0.87	1502
Air	0.0012	0.026	22.26	5.51
He	0.0011	0.15	137	12.8
Water	4.18	0.598	0.14	1582

CHAPTER 2

Photopyroelectric calorimetry and experimental devices

2.1. Photopyroelectric calorimetry and Pyroelectricity

2.1.1. Photopyroelectric calorimetry. Calorimetry is a fundamental tool to study the critical evolution of different thermophysical properties in the vicinity of phase transitions. At an around the critical temperature (the one at which the phase transition takes place) many of those physical quantities usually present strong anomalies. To identify such changes in a physical system it is necessary to use a high temperature resolution technique with a high signal to noise ratio. Nowadays several techniques have been developed for monitoring critical behavior in different kind of materials crossing the phase transitions temperatures. The most widely used among them are: Adiabatic Scanning Calorimetry (ASC) [34], Nonadiabatic Scanning Calorimetry (NAS) [35], and several *ac*-Calorimetry [36, 37, 38, 39]. The main experimental requirement for all of them is the possibility to properly work with a small as possible temperature gradient created in the material under study and be of application for a wide temperature range. Due to some limitations not all the techniques can be used complying with the experimental conditions mentioned above. In respect to this, *ac*-Photopyroelectric calorimetry (PPE) [40] in several setup configurations has been proved to be effective in the study of materials with the phase transitions owing to its following advantages [41]:

● it enables to cover a wide temperature range using different sensors;

● high temperature resolution;

● PPE technique is sensitive even to small temperature variations (~mK);

● the possibility to work with a small amount of sample, as a consequence, the thermal equilibrium state in the vicinity of the critical temperature can be achieved more easily;

● simultaneous determination of the parameters are achieved for the thermal transport variables (diffusivity, conductivity, effusivity) as well as for the equilibrium state (heat capacity) by measuring at a fixed frequency.

● it enables to detect the presence of latent hear over first order transition;

● the frequency range used can be almost 6 decades;

● simple setup design and possibility to perform simultaneous studies in combination with other measurements (light scattering, polarization microscopy imaging…).

2.1.2. Pyroelectricity. The physical phenomena underlying the PPE technique is the pyroelectric effect. Pyroelectricity appears when a spontaneous polarization P_s is induced as a result of a temperature change in a noncentrosymmetric, piezoelectric crystal. The equation for pyroelectric coefficient p can be written as

$$p = \frac{dP_s}{dT}.$$ (2.1)

The explanation of this effect is given as follows. The crystalline structure of such kind of materials is divided in sections called domains whose dipolar moment always differ from 0 and are polarized in one distinct direction within each domain. If a temperature field is not applied to a whole material, the total polarization is equal to 0, due to the self-compensated processes caused by the chaotical orientation of domains. To produce polarization in a material we have to align them. In pyroelectric materials this is enabled by applying thermal energy.

Suppose we have a slab of pyroelectric transducer whose permanent orientation is oriented perpendicularly to the surfaces of the sensor. The polarization charges are in an electrical balance due to distribution of opposite free charges in the electrodes (fig.2.1 *a*) and if we connect cables to the electrodes to close a circuit, no current will be flowing. If a small temperature gradient is applied to its faces, it causes the appearance of spontaneous polarization in the slab, consequently the number of free charges decrease. Hence, the redistribution of free charges on the electrodes, to achieve an electrical equilibrium state, leads to a current flow in a connected circuit. (fig. 2.1 *b*).
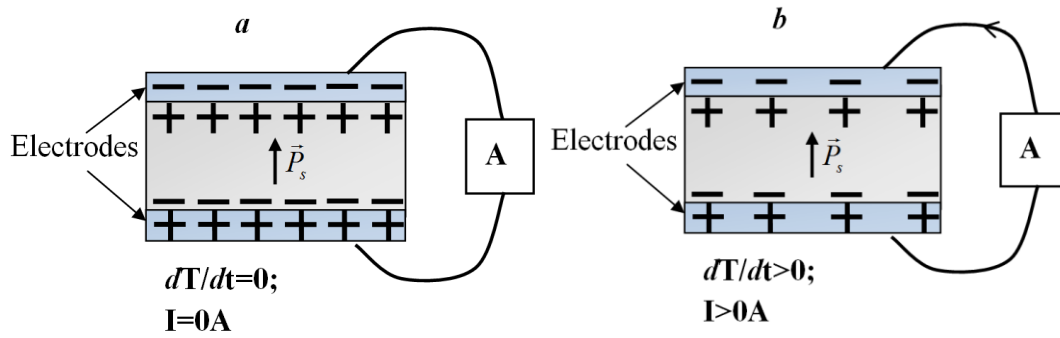
Fig. 2.1. Schematic illustration a nature of pyroelectricity.

The main requirements that make a pyroelectric detector be suitable for practical applications are pointed out below:

● low heat capacity to be able to achieve larger temperature differences between the surfaces of the sensor;

● high pyroelectric coefficient p and small dielectric constant ε_p, which leads to a high value of the figure of merit given by the ratio p/ε_p;

● large Curie temperature value.

Nowadays, among others sensors, in photopyroelectric investigations the most adopted materials are lithium tantalate ($LiTaO_3$), and lithium niobate ($LiNbO_3$). Their main parameters are listed in table 2.1. Due to its higher pyroelectric coefficient, $LiTaO_3$ produces a higher PPE signal than $LiNbO_3$.

As seen, also, they possess a relatively high value of Curie temperature, which allows to use them in a wide temperature range, in contrast to other well known pyroelectric detector β-polyvinylidene (β-PVDF), whose Curie temperature is about 130^0C, which restricts its operating diapason below 100^0C [42].

Table 2.1.

Some properties of lithium tantalate ($LiTaO_3$) and lithium niobate ($LiNbO_3$)

	LiTaO₃	**LiNbO₃**
Symmetry	Trigonal	Trigonal
Point group	*3m*	*3m*
Curie temperature (^0C)	604	1133
Melting temperature (^0C)	1650	1253
Pyroelectric coefficient ($Cm^{-2}/^0C$)	2.3×10^{-4}	0.4×10^{-4}

In practice the detector for PPE technique has a form of slim slab to provide 1-Dimentional experimental conditions. The slab surfaces are coated by an electrical conductive material (depending on the technique configuration the electrodes can be opaque or transparent) and connected to a *lock-in* amplifier. The sample is placed on the sensor, and to provide a good thermal contact between them a thermal grease is generally used for solid materials, which is not necessary if we deal with fluids. A temperature oscillation is maintained on the sample by illuminating the sensor or the sample with a modulated light beam (in what is called the front or back configurations), propagates to the sensor and creates the pyroelectric signal. Simultaneous detecting of its phase and amplitude allows to retrieve the thermal properties of the sample under study.

2.2. Multilayer system resolution

At present, several setups of the PPE technique have been developed, which can be separated in two big groups depending on the position of the incident light beam: *back* detection (BPPE) if the sample is illuminated and *front* detection (FPPE) if it is the sensor. Moreover, the sensors used in them can be: *opaque* or *transparent*, *thermally thick* or *thermally thin*, the detail description of the different photopyroelectric methods for optical and thermal investigation have been considered in [40, 41, 43, 44]. In this chapter we consider the two PPE setups that we have used in our investigations:

● back-detection configuration (with the added conditions that both sample and sensor are thermally thick and opaque);

● front-detection configuration (with the added conditions that both sample and sensor are thermally thick and opaque).

2.2.1. Back-detection configuration BPPE

Let's consider the multilayer system depicted on fig. 2.2. It consists of a gas (g), the opaque sample (s), a coupling fluid (f), the pyroelectric detector (p) and a backing environment. A solid sample is illuminated by a monochromatic modulated light beam with an angular frequency ω, intensity I_0 (W/m^2) and wavelength λ. A thin layer of

grease (f) is used to assure the thermal contact between the sensor (p) and the sample (s). All thicknesses are taken into account.
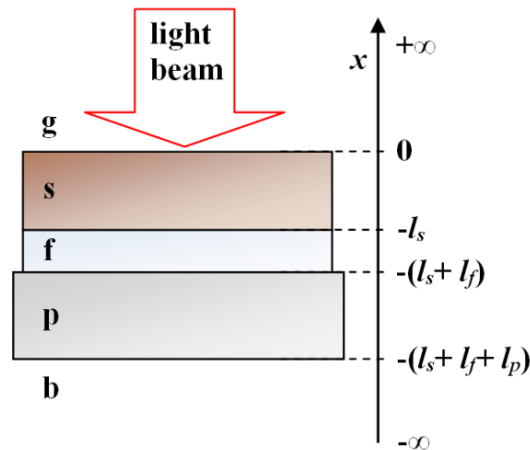
Fig. 2.2. Geometry of the PPE in back–detection configuration with opaque sample.

The light absorbed by the sample is converted into heat. This heat wave propagating from the sample to the pyroelectric detector creates a temperature field distribution in the sensor of the form

$$\langle T_p \rangle = \frac{1}{l_p} \int_{-(ls+lf)}^{-(ls+lf+lp)} T_p(x)\, dx. \tag{2.2}$$

This temperature field produces a potential difference V between the sensor surfaces, and a electrical current in a circuit connected to a *lock-in* amplifier. Considering the sensor as an equivalent resistance-capacitance circuit connected in parallel with the current source, and taking into account the relation between the pyroelectric signal and the temperature field, the pyroelectric output voltage can be expressed by this equation [43]

$$V = \frac{i\omega\tau_\varepsilon\, p\, l_p}{\varepsilon} \langle T_p \rangle, \tag{2.3}$$

where τ_ε is the electrical time constant, p the pyroelectric coefficient and $\varepsilon = \varepsilon_0 \varepsilon_r$ the dielectric constant of the pyroelectric.

As seen from (2.3) to find a photoelectric signal it is necessary to solve the one-dimensional problem of the temperature distribution in a multilayer system (5 layers in this case). To do this we use the heat diffusion equation and solve it for each layer

$$\frac{\partial^2 T_i}{\partial x^2} - \frac{1}{D_i}\frac{\partial T_i}{\partial t} = 0, \tag{2.4}$$

where i = g (gas), s (sample), f (fluid), p (pyroelectric sensor), b (backing environment), D_i the thermal diffusivity of a particular layer corresponding to i. Each of them is characterized by their own spatial range, therefore the general solution for this system is written in the form:

- **gas** $T_g = A \exp\left[-\sigma_g x\right];$ $x \geq 0;$

- **sample** $T_s = B \exp\left[\sigma_s x\right] + C \exp\left[-\sigma_s x\right];$ $-l_s \leq x \leq 0;$

- **fluid** $T_f = D \exp\left[\sigma_f \left(x + l_s\right)\right] + E \exp\left[-\sigma_f \left(x + l_s\right)\right];$ $-(l_s + l_f) \leq x \leq -l_s;$ (2.5)

- **pyro** $T_p = F \exp\left[\sigma_p \left(x + l_s + l_f\right)\right] + G \exp\left[-\sigma_p \left(x + l_s + l_f\right)\right];$ $-(l_p + l_f + l_s) \leq x \leq -(l_s + l_f);$

- **backing** $T_b = H \exp\left[\sigma_b \left(x + l_p + l_f + l_s\right)\right];$ $x \leq -(l_s + l_f + l_p).$

In the system of equations (2.5) A, B, C, D, E, F, G, H are constants. To find them out, we apply the continuity of temperature and of heat flux crossing the boundary between the layers. The illumination with intensity I_0 is completely absorbed by the sample and transformed into heat. This imply an energy input at the sample surface ($x=0$) which will be incorporated to the continuity of heat flux as a term $I_0/2$; thus, the boundary conditions of temperature continuity are given in the form:

$$T_g\big|_{x=0} = T_s\big|_{x=0}; \quad T_s\big|_{x=-ls} = T_f\big|_{x=-ls}; \quad T_f\big|_{x=-(ls+lf)} = T_p\big|_{x=-(ls+lf)}; \quad T_p\big|_{x=-(ls+lf+lp)} = T_b\big|_{x=-(ls+lf+lp)}; \qquad (2.6)$$

and for the heat flux

$$\frac{I_0}{2} + k_g \frac{\partial T_g}{\partial x}\bigg|_{x=0} = k_s \frac{\partial T_s}{\partial x}\bigg|_{x=0}; \qquad\qquad k_s \frac{\partial T_g}{\partial x}\bigg|_{x=-ls} = k_f \frac{\partial T_f}{\partial x}\bigg|_{x=-ls};$$

$$k_f \frac{\partial T_f}{\partial x}\bigg|_{x=-(ls+lf)} = k_p \frac{\partial T_p}{\partial x}\bigg|_{x=-(ls+lf)}; \qquad k_p \frac{\partial T_p}{\partial x}\bigg|_{x=-(ls+lf+lp)} = k_b \frac{\partial T_b}{\partial x}\bigg|_{x=-(ls+lf+lp)}. \qquad (2.7)$$

Substituting (2.6) and (2.7) into (2.2) we get the expression for the temperature distribution $\langle T_p \rangle$

$$\langle T_p \rangle = \frac{4 I_0 (1 - R_s) b_{sg}}{2 k_s l_p} \frac{1}{\sigma_s \sigma_p} \frac{1}{(1 + b_{pf})(1 + b_{fs})(1 + b_{sg})} \left[\frac{e^{\sigma_p l_p} + R_{bp} e^{-\sigma_p l_p} - (1 + R_{bp})}{e^{\sigma_s l_s} \Lambda + R_{gs} e^{-\sigma_s l_s} \Sigma} \right], \qquad (2.8)$$

where $R_{ij} = (b_{ij} - 1)/(b_{ij} + 1)$, and $b_{ij} = e_i / e_j$ are the thermal effusivities ratio of layers, i, j = g, s, f, p, b; R_s is the reflection coefficient of the sample. The constants Λ and Σ are defined as

$$\Lambda = \left(e^{\sigma_p l_p} + R_{bp} R_{pf} e^{-\sigma_p l_p} \right) e^{\sigma_f l_f} + R_{fs} \left(R_{pf} e^{\sigma_p l_p} + R_{bp} e^{-\sigma_p l_p} \right) e^{-\sigma_f l_f},$$

$$\Sigma = R_{fs} \left(e^{\sigma_p l_p} + R_{bp} R_{pf} e^{-\sigma_p l_p} \right) e^{\sigma_f l_f} + \left(R_{pf} e^{\sigma_p l_p} + R_{bp} e^{-\sigma_p l_p} \right) e^{-\sigma_f l_f}.$$

$$(2.9)$$

Now we introduce equation (2.8) into (2.3) to obtain the photopyroelectric signal V produced in the sensor

$$V = \frac{i\omega\tau_\varepsilon p l_p}{\varepsilon} \frac{4I_o(1-R_s)b_{sg}}{2k_s l_p} \frac{1}{\sigma_s \sigma_p} \frac{1}{(1+b_{pf})(1+b_{fs})(1+b_{sg})} \left[\frac{e^{\sigma_p l_p} + R_{bp} e^{-\sigma_p l_p} - (1+R_{bp})}{e^{\sigma_s l_s}\Lambda + R_{gs} e^{-\sigma_s l_s}\Sigma} \right]. \quad (2.10)$$

To avoid the electronic influence in the final result, a normalization procedure is proposed, which consists of dividing the signal obtained by equation (2.10) by the signal of a bare pyroelectric. To do this, it is necessary to find out the temperature field in a sensor without a sample $\langle T_p \rangle_{bare}$. When a detector is directly irradiated, we have $\exp[\sigma_s l_s] \sim \exp[-\sigma_s l_s] \sim 1$. Therefore, the denominator in the square brackets of the equation (2.8) is reduced, hence we have

$$\langle T_p \rangle_{bare} = \frac{4I_o(1-R_p)b_{pg}}{2k_p l_p} \frac{1}{\sigma_p \sigma_p} \frac{1}{(1+b_{pf})(1+b_{fp})(1+b_{pg})} \left[\frac{e^{\sigma_p l_p} + R_{bp} e^{-\sigma_p l_p} - (1+R_{bp})}{\Lambda + R_{gp}\Sigma} \right]. \quad (2.11)$$

The photopyroelectric signal in this case is

$$V_{bare} = \frac{i\omega\tau_\varepsilon p l_p}{\varepsilon} \frac{4I_o(1-R_p)b_{pg}}{2k_p l_p} \frac{1}{\sigma_p \sigma_p} \frac{1}{(1+b_{pf})(1+b_{fp})(1+b_{pg})} \left[\frac{e^{\sigma_p l_p} + R_{bp} e^{-\sigma_p l_p} - (1+R_{bp})}{\Lambda + R_{gp}\Sigma} \right]. \quad (2.12)$$

By dividing (2.10) over (2.12) the normalized PPE signal will have the following form

$$V_n = \frac{V}{V_{p\,bare}} = \frac{(1-R_s)}{(1-R_p)} \frac{(1+b_{fp})(1+b_{pg})}{(1+b_{fs})(1+b_{sg})} \left[\frac{\Lambda + R_{gp}\Sigma}{e^{\sigma_s l_s}\Lambda + R_{gs} e^{-\sigma_s l_s}\Sigma} \right]. \quad (2.13)$$

So far, this expression is valid both for thermally thick or thin sensor, we are now going to particularize it to our particular experimental setup. As was mentioned above, we are going to work with thermally thick detectors, so we can assume $e^{-\sigma_p l_p} \sim 0$. Secondly, the backing environment and the gas are the same thus b=g. In the third place, it is well known that the gases possess low effusivity values so we can consider $R_{gp} \sim R_{gs} \sim -1$ and $(1+b_{pg})/(1+b_{sg}) \sim e_p/e_s$. Taking into account these approximations, after mathematical manipulations (2.13) is modified to give

$$V_n = 4\frac{(1-R_s)}{(1-R_p)}\frac{e_p}{e_s}\frac{1}{(1+b_{pf})(1+b_{fs})}\left[\frac{1}{e^{\sigma_s l_s}(e^{\sigma_f l_f}+R_{fs}R_{pf}e^{-\sigma_f l_f})-e^{-\sigma_s l_s}(R_{fs}e^{\sigma_f l_f}+R_{pf}e^{-\sigma_f l_f})}\right]. \quad (2.14)$$

Let's now study V_n as a function of the illumination frequency for the case study of Ni as sample and LiTaO$_3$ as sensor, for which $D_s=22$ mm^2/s, $e_s=19000$ $Wm^{-2}K^{-1}s^{1/2}$, $e_p=3750$ $Wm^{-2}K^{-1}s^{1/2}$, $l_s=1$ mm, $R_s=R_p=0$, eliminating the fluid layer for simplicity ($l_f=0$, $e^{-\sigma_f l_f}\sim e^{\sigma_f l_f}\sim 1$), and let's represent equation (2.14) as a function of the square root of the modulation frequency (see fig.2.3) [19]. As it is a complex number, we will represent both the natural logarithmic of the amplitude and the phase.
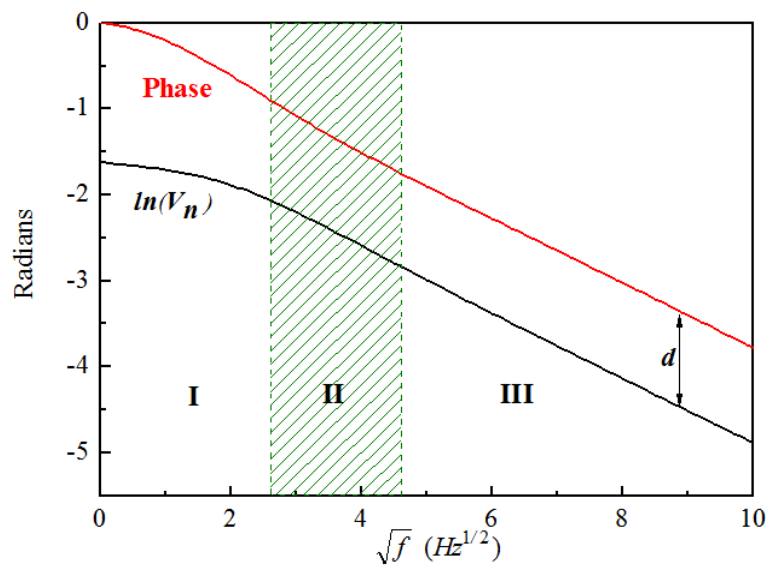
Fig. 2.3. Phase and natural logarithm of PPE signal versus square root of frequency.

As seen from fig. 2.3 three different zones can be distinguished:

● a first one at low frequencies, where the sample is not thermally thick, and there is neither linearity nor parallelism. This is a useless zone.

● the second zone is an intermediate one. The parallelism is being observed between phase and natural logarithm which signals a transition from thermally thin to **thermally thick** mode, but there is still not a complete linearity and parallelism. It produces a significant error in extracting information on the sample properties;

● the third and last one is known as **the linear zone** whose main feature is the presence of a large linear region with good parallelism between both variables (better than 99%), which produces a more than acceptable error in calculating the thermal properties of a sample. To achieve this region, the sample must be thermally thick.

The analytical expression of a normalized PPE voltage (2.14) in the third zone ($e^{-\sigma_s l_s} \sim 0$, the sample is thermally thick) can be obtained in the following form, assuming that the gas contribution can be neglected and that the thickness of the coupling grease l_f is neglectable,

$$V_n = 2\frac{e_p}{e_p + e_s}\exp[-\sigma_s l_s], \qquad (2.15)$$

From which the natural logarithm of the amplitude and the phase can be extracted to get

$$\ln(V_n) = \ln\left(2e_p / \left(e_s + e_p\right)\right) - \sqrt{\pi f / D}l_s;$$
$$phase = -\sqrt{\pi f / D}l_s; \qquad (2.16)$$

As expected, both are linearly depending on $\sqrt{f}$ with the same slope m, from which the thermal diffusivity D of the sample can be retrieved

$$m = \sqrt{\pi l_s^2 / D_s} \quad , \qquad (2.17)$$

moreover, the thermal effusivity e_s can be calculated from the vertical shift d between the two lines on fig. 2.3 using the formula below

$$e_s = e_p\left(\frac{2}{\exp[d]} - 1\right). \qquad (2.18)$$

This is a basic step in thermal characterization of solids – the standard frequency scan at **a fixed temperature**. Nevertheless some details should be emphasized. Here it was assumed that we do not have thermal grease and our multilayer problem has been reduced to a two-layer (sample-sensor). If instead of taking $l_f = 0$, in (2.14) we introduce nonzero thickness for the fluid, we will see that slope on figure 2.3 increases, as consequence, the thermal diffusivity of sample will be underestimated [45]. To overcome this underestimation caused by the coupling grease it has been proposed the use of a transparent pyroelectric sensor and a transparent fluid in combination with a self-normalization procedure. The detailed description of this method is presented in reference [46]. Other effects which might affect the linearity and parallelism of the curves or introduce underestimations/overestimations of the thermal diffusivity have already been studied in detailed: the backing material, possible parasitic light, the

electronic noise, the piezoelectric contribution of the sensor [19]. Our experimental systems are designed to work under conditions in which these effects are minimized.

Measurements as a function of temperature. Since the frequency scan has been performed at a reference temperature T_{ref} and the values of diffusivity and effusivity are extracted using a linear fitting of the experimental data using equations (2.17, 2.18), the second step is to perform a temperature run at a fixed frequency, whose value belongs to the linear region. The appropriative equations which describe a temperature evolution of diffusivity and effusivity under these conditions are written below [47, 48]

$$D(T) = \left[\frac{1}{\sqrt{D_{ref}}} - \frac{\Delta(T)}{l_s \sqrt{\pi f}} \right]^{-2} ; \qquad e(T) = e_p(T) \left(\frac{1 + \left(e_{ref} / e_p(T_{ref}) \right)}{\exp[\Delta''(T)]} - 1 \right), \qquad (2.19)$$

where $\Delta(T) = \psi(T) - \psi(T_{ref})$ is the phase difference; $\Delta'(T) = \ln V(T) - \ln V(T_{ref})$ is the amplitude difference; $\Delta''(T) = \Delta'(T) - \Delta(T)$. Once we have the information about thermal diffusivity and effusivity it is possible to retrieve the temperature behavior of heat capacity $c_p(T)$ and thermal conductivity $k(T)$, using the constituent relationship among them

$$c_p(T) = \frac{e(T)}{\rho \sqrt{D(T)}}, \qquad (2.20)$$

$$k(T) = e(T) \sqrt{D(T)}. \qquad (2.21)$$

where ρ is the density of the sample under study. As seen from these four formulas the diffusivity depends solely on the phase of the PPE signal while the three other quantities conductivity, effusivity and specific heat are obtained by using both the amplitude and the phase of the pyroelectric signal. This is an important advantage, because the performance of a continuous temperature run enables to obtain the temperature evolution of all thermal parameters. In spite of this possibility, at the same time two undesirable problems can appear. From the experimental point of view the phase is always more stable in time than the amplitude of the signal due to laser instabilities or electronic problems; thus, in general, the thermal diffusivity curves are less noisy than the others. A second problem which sometimes arises has to do with the use of equations (2.20 and 2.21) to extract the thermal parameters of a phase transition of a particular material, around a critical point. It might happen that the combination of

amplitude and phase to obtain specific heat and thermal conductivity gives some artifacts in the shape of these last variables in the critical region, making it impossible to retrieve reliable curves of $e(T)$, $c_p(T)$, $k(T)$. In these cases the physics of the transition is more complicated than the model used and, so far, there is no theory developed to cover those cases.

2.2.2. Front-detection configuration FPPE

The theory of PPE technique in front configuration, which is also known as inverse pyroelectric configuration, was developed by Dadarlat and coworkers [44]. In this setup the sensor in thermal contact with a sample is directly illuminated by the light beam and is mainly used to work with fluids, which do not need an additional thermal contact layer. Depending on the electrodes used as coating conductive layer for the pyroelectric sensor the FPPE configuration can be separated in two groups: FPPE *with transparent electrodes* and FPPE *with opaque electrodes* [41]. Moreover a theory for several working regimes has been developed for thermally thin/thick pyroelectric detector and sample [41, 49, 50]. Let's briefly consider the situation depicted on fig.2.4. It is a four-layer system consisting of gas (g), pyrodetector slab (p), sample (s) and backing surrounding (b), where opaque sensor is directly irradiated by a modulated light beam, same as on fig 2.3.
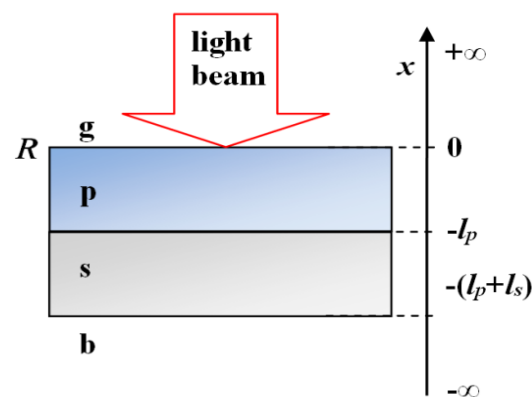
Fig. 2.4. Geometry of the PPE in front–detection configuration with opaque sensor.

The pyroelectric signal for such layer system is given by the following equation [43]

$$V = \frac{i\omega\tau_\varepsilon p l_p}{\varepsilon(1+i\omega\tau_\varepsilon)}\langle T_p \rangle e^{i\omega t}.$$ (2.22)

We follow an analogue procedure to the one for the back configuration and consider an optically opaque sensor so that the illumination is partially absorbed by the pyroelectric surface (this is taken into account through the reflection coefficient R). Under these assumptions, the complex FPPE signal will be expressed as [49]

$$V = \frac{P\tau_\varepsilon}{\varepsilon(1+i\omega\tau_\varepsilon)} \frac{1-R}{2} I_0\Gamma \,, \qquad (2.23)$$

where Γ is defined as

$$\Gamma = C_p^{-1}\left\{1-2b_1\left[S(b_2+1)+S^{-1}(b_2-1)\right]\left[\begin{array}{l} SP(b_1+1)(b_2+1)+SP^{-1}(b_1-1)(b_2+1)+ \\ PS^{-1}(b_1-1)(b_2-1)+P^{-1}S^{-1}(b_1+1)(b_2-1) \end{array}\right]^{-1}\right\}. \qquad (2.24)$$

In equation (2.24) the following notation have been used

$$S = \exp[\sigma_s l_s]; \quad P = \exp[\sigma_p l_p]; \quad b_1 = l_s / e_p; \quad b_1 = e_b / e_s. \qquad (2.25)$$

where $e_i = \sqrt{C_i k_i}$, $i = g, p, s, b$ is the effusivity; $\sigma_i = (1+i)D_i$; $D_i^{-1} = \mu = \sqrt{D_i/\pi f}$, where μ is the thermal diffusion length, and $C = \rho c = k/D$ − the volume heat capacity.

Several special cases can be pointed out for the FPPE signal (2.23):

a) sensor and sample under study are thermally thin: $\sigma_p l_p \ll 1$, $\sigma_s l_s \ll 1$, $\exp[\pm\sigma_p l_p]$ $\sim 1\pm\sigma_p l_p$, $\exp[\pm\sigma_s l_s]\sim 1\pm\sigma_s l_s$. Substituting these approximations in (2.24) gives that $\Gamma = (C_p + C_s l_s / l_p)^{-1}$. It enables a direct calculation of the specific heat of the sample.

b) the pyroelectric is thermally thin and the sample is thermally thick: $\sigma_p l_p \ll 1$, $\sigma_s l_s \gg 1$, for Γ we obtain $\Gamma = C_p^{-1}\sigma_p l_p (b_1+\sigma_p l_p)^{-1}$. As seen Γ depends on diffusivity and effusivity of the sample and, as consequence, both the phase and the amplitude of FPPE signal are sensitive to the thermal properties of sample.

In a further paper, [50] the particular configuration of thermally thick sensor and thermally thick sample was analyzed and it was shown that thermal effusivity and thermal diffusivity could be obtained from the phase of the pyroelectric signal, the amplitude or from the combination of both, being preferable the results obtained from the phase due to its stability compared to the amplitude. The experiments were performed on fluids.

But the extension of these techniques to solid samples is not straightforward, as the frequency scan of the normalized signal is highly sensitive to the thermal effusivity of the backing liquid [56, 57]. And thermal contact between sensor and solid sample is assured by the introduction of a coupling fluid layer, which will importantly modify the normalized PPE signal and the thermal effusivity will not be obtained accurately. We will show on Section 2.5 how we have overcome this situation along the work of this PhD thesis.

2.3. Description of experimental devices

2.3.1. At room temperature. To perform the measurement as a function of the modulation frequency in the back-configuration BPPE we made the following. The sample is in thermal contact with a detector which is connected to a *lock-in* amplifier. Lithium tantalate $LiTaO_3$ has been used as pyroelectric sensor with surfaces covered by metallic electrodes Ni-Cr whose thickness is about ~$1\mu m$. As an electrical conjunction between the amplifier and sensor, thin copper wires have been used. The wires are connected to the electrodes by a high conductive silver paint to provide a good electrical contact. The thermal contact of sample to sensor is guaranteed by a silicon grease whose thickness does not exceed a few microns. The setup is depicted on fig.2.5 schematically.
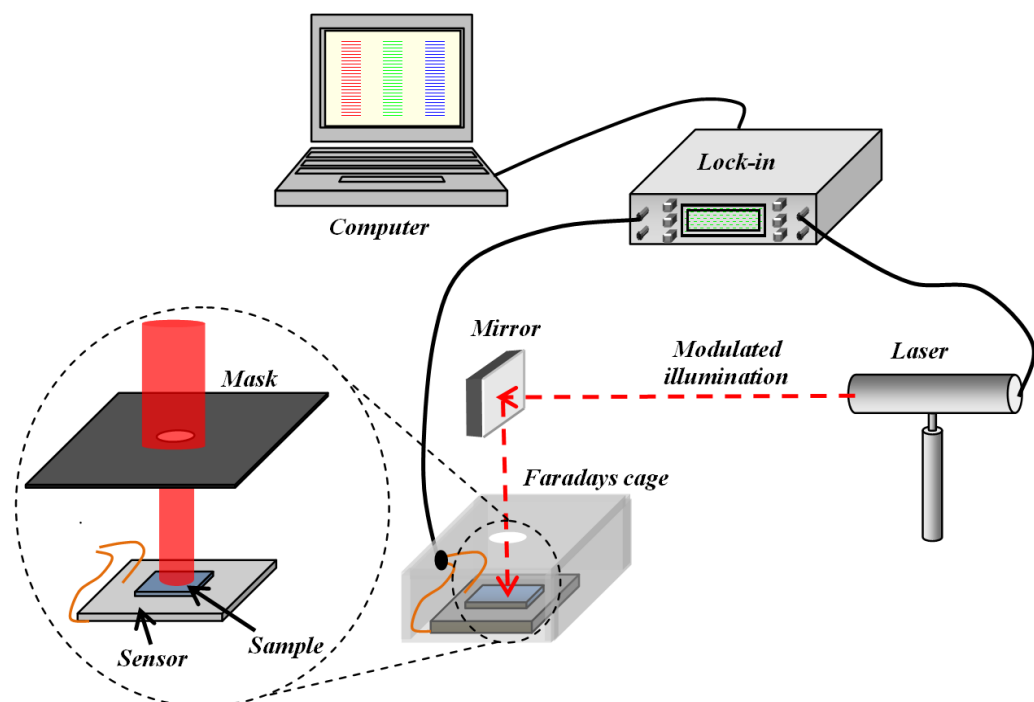
Fig. 2.5. Scheme to perform frequency scans in BPPE configuration at room temperature.

An opaque sample was irradiated by a low power (5mW) modulated He-Ne laser beam (λ=632nm). In that way the thermal energy deposited on the sample is small and also the induced temperature gradient. This will help to quickly achieve thermal equilibrium when the temperature is changed and be able to do very slow temperature runs with a high signal to noise ratio. This is because the temperature oscillations in the sample are of the order of 1 mK, while the dc contribution is estimated at about 2 mK [60].

In case the sample is transparent for the laser wavelength, its surface is coated with a graphite paint in order to increase the absorption, and therefore to have more PPE signal.

The *lock-in* amplifier realizes a double function. It controls the modulation frequency of illumination; on the other hand it amplifies and processes the signal from the detector PPE whose frequency is the same as the modulation of the laser. The working principle of the amplifier is based on a bandpass filter synchronized with the frequency of the PPE signal. This line will make the frequencies outside the bandwidth automatically filtered. Moreover, it provides gain, amplifying the received signal [51].

To eliminate the random electronic noise of the same frequency as the one of the collected signal, the *lock-in* also has a variable integration time. In addition, to minimize the problems associated with noise induced by currents, all components of the measuring system are placed into a Faraday's cage and connected to the earth. Finally, the *lock-in* transmits the amplitude and phase of the PPE to a computer, where they are stored for further analysis. To eliminate possible parasitic light effects (which appear when some amount of radiation falls on the pyroelectric surface), a mask with a hole is placed over the sample so that only the latter is illuminated [19].

In fig. 2.6 a frequency scan at room temperature is shown, for a paraelectric crystal $Pb_2P_2S_6$ cut perpendicularly to [010] direction. As seen, the graph can be separated by two different zones: with linearity (*a*) and without it (*b*):
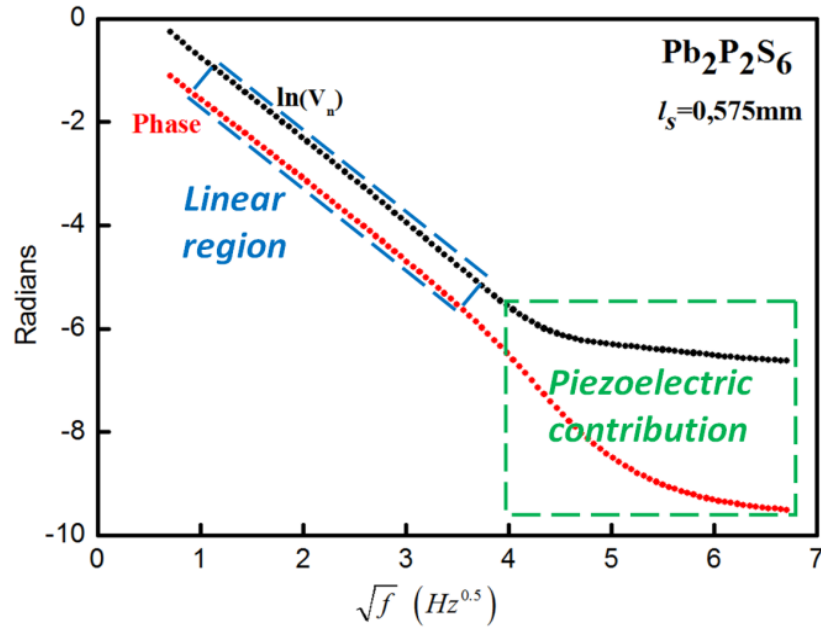
Fig. 2.6. Frequencies scan at room temperature for paraelectric crystal $Pb_2P_2S_6$.

a) with linearity. The typical linear dependence which occurs in a range 1~14Hz, can be used to accurately calculate the thermal properties of sample, it signals that our experimental conditions are in agreement with the theory described above;

b) without linearity. Around 16Hz (for this thickness) the linearity is drastically distorted even if sample is opaque and there is no influence of a parasitic light. The origin of this distortion is related to the fact that both the sensor and the sample are also piezoelectrics. The thermal strain induced in a sample by the thermal wave is transmitted to the detector; consequently, the generated pyroelectric signal also has the contribution of a piezoelectric voltage. When this effect is very important and masks the linear region, a multiparametric fitting should be performed as described in [52] to extract the thermal diffusivity from this kind of curves.

2.3.2. Experimental measurements between 20K and 320K

Once we have measured the thermal diffusivity at room temperature we are interested in investigating the thermal properties of the samples in a wide temperature range, which will allow to study their behavior around phase transitions. In order to perform this kind of studies, the pyroelectric and the sample must be placed in cryostats. Depending on the temperature range of interest, two different cryostat systems have been used: a closed cycle He cryostat and a liquid nitrogen cryostat.

In the first place, we describe the experimental setup which enables to cover the interval 20-320K. To perform such measurements, a conventional closed cycle He cryostat with a vertical configuration has been modified by Janis Research Company to work as an *ac* photopyroelectric calorimeter (fig. 2.7) in collaboration with our research group. The closed cycle refrigerator (CCR) provides a convenient means of cooling samples to temperature down to about 20K. It requires no liquid refrigerant as cooling source. Instead, a closed loop of helium gas is compressed and expanded, based on the Gifford-McMahon (G-M) thermodynamic cycle. The refrigerator operates as follows: the sample holder is suspended from a vibration isolated stage within an exchange gas tube, which in turn is mounted on the refrigerator second stage. Helium exchange gas forms a thermal link between the refrigerator and the adsorber; the exchange gas transfers heat from the sample holder to the refrigerator, cooling the sample holder in process. The cooling system consists of:

- *Compressor*: provides a supply of high-pressure helium gas to the cold head;
- *Cold Head*: expands the helium gas to cool the sample holder;
- *Gas Lines*: these lines are connected between the compressor and cold head supply and return fitting, and transfer the helium gas between the two components;
- *Vacuum Jacket*: this is bolted to the cold head. It includes an evacuation valve, safety pressure relief, electrical feedthroughs, and a clamped vacuum seal for easy access to the sample space;
- *Radiation Shield*: this bolts to the cold head first stage. It is used to intercept room temperature radiation before it reaches the sample, allowing the lowest possible sample temperature to be achieved.;
- *Temperature controller*: this may be provided for use in monitoring and controlling the sample temperature.

A first advantage of this system is that there is no refrigerant consumption. A second one is the vibration isolation system which eliminates mechanical vibrations on the sample holder coming from the engine located at the head of the cryostat and which would introduce a piezoelectric component in the PPE signal [19]. The particular

frequency for the measurements is selected within the linear region described in the previous sections and a double check is performed on the residual noise due to mechanical couplings to obtain a signal as noiseless as possible.
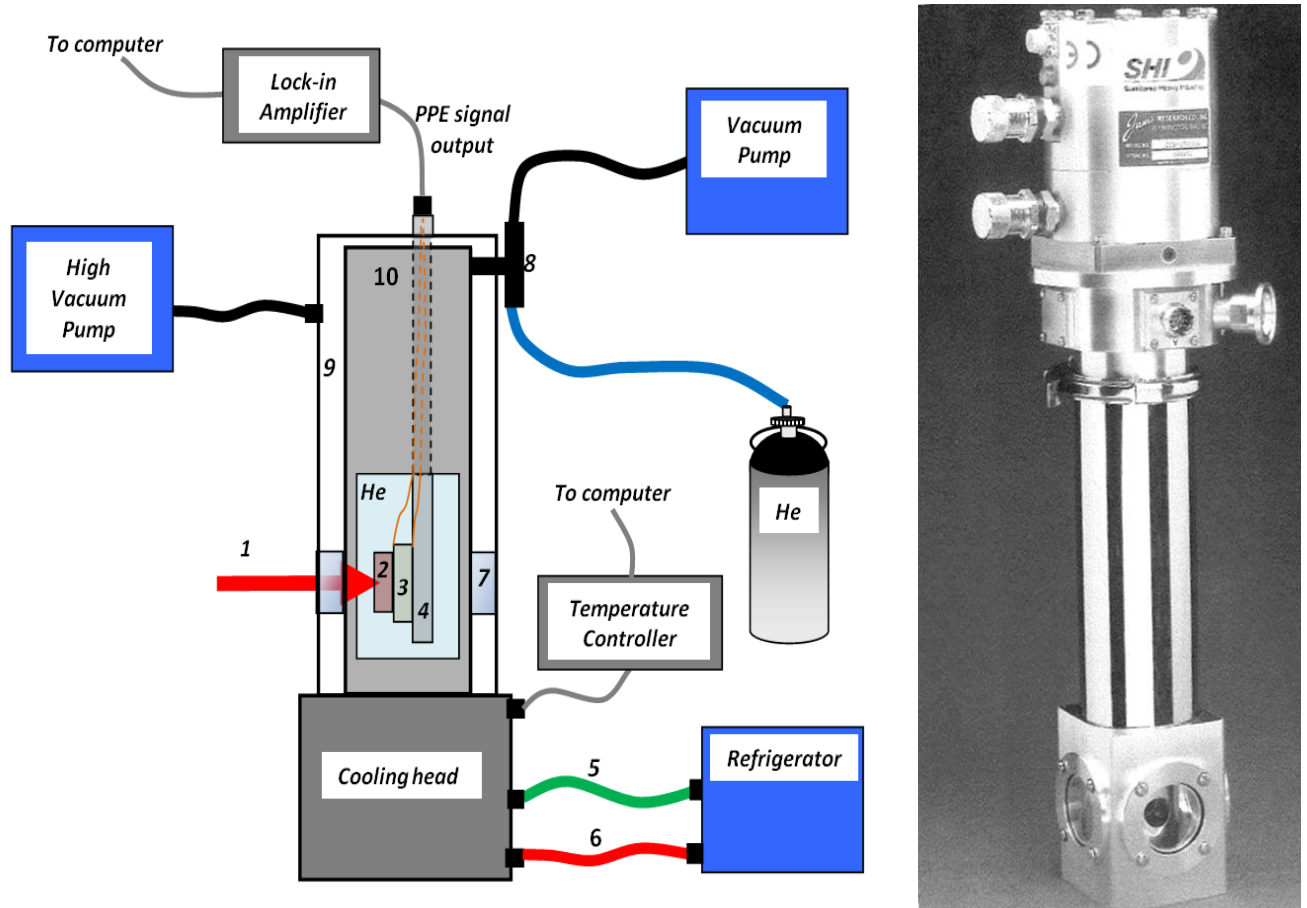
Fig. 2.7. Scheme of the Closed cycle He cryostat in vertical configuration: 1 – modulated heat source; 2 – sample; 3 – pyroelectric detector; 4 – sample holder; 5 – output tube for low-pressure He gas; 6 – input tube for high-pressure He gas; 7 − optical window; 8 – triple position valve for creating a vacuum and introducing a helium gas in an internal chamber; 9 – external chamber; 10 − internal chamber. *Lock-in* – EG & G Instruments, DSP Mod 7265. Temperature Controller: Lake Shore 332.

After the system is adjusted it enables to perform high resolution measurements in the range ~20−320K, with controlled continuous heating and cooling rates down to 5-10mK/min. In this way the system can be used to perform a thorough phase transition study in a particular temperature range or to measure thermal properties in a wide temperature interval.

2.3.3. Experimental measurements between 77K and 400K

Due to the engineering limitations, the CCR cannot work with temperatures higher than 320K. Nevertheless, in some of our samples the phase transitions take place at temperatures that exceed this limit. To overcome this problem we used another cryostat system (fig.2.8) whose working principle is based on liquid nitrogen.
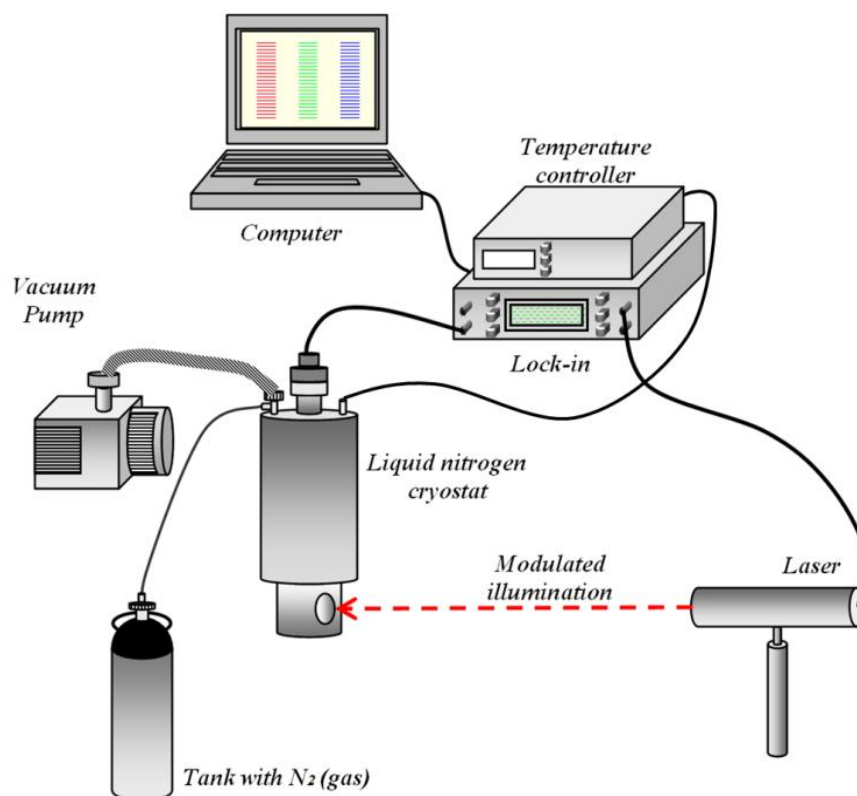
Fig. 2.8. Scheme of experimental setup for measurements as a function of temperature in the range 77-400 K. *Laser*, He-Ne. *Temperature Controller*: Oxford Instruments Mod ITC 502. *Lock-in*. EG & G Instruments, DSP Mod 7265. *Cryostat*: Optistat^{DN}.

The cryostat is designed in a way that the sample holder introduced in an internal chamber has a vertical orientation (fig. 2.9). The cooling process is performed through a reservoir placed on top of a central camera and filled by liquid nitrogen. The nitrogen is being distributed through numerous capillaries promoting heat exchange and cooling the sample. During the measurements it is important to optimize the flow by a controlling valve to obtain a smooth temperature control, for which the PID (proportional-integral-derivative) of the controller has been optimized.

Thermal contact in the cryostat occurs by means of the gas which surrounds the sample and acts as a heat exchanger. The minimum temperature possible to achieve is

77K, due to the use of liquid nitrogen as a refrigerant. The temperature ramps are made via the temperature controller with an accuracy of $\pm$ 0.01K in temperature range between 77K and 200 K and $\pm$ 0.1K if we measure between 200 and 400K. The systems permits to work with rhythms from 100mK/min measuring in a wide temperature range and down to 2mK/min for a high resolution runs. To avoid heat exchange between the inner chamber and the environment it is necessary to make vacuum in the external chamber which acts as a thermal insulator and promotes the optimization of the temperature control. In our case, we perform a vacuum with a rotary pump, reaching approximately 10^{-3} mbar [19].
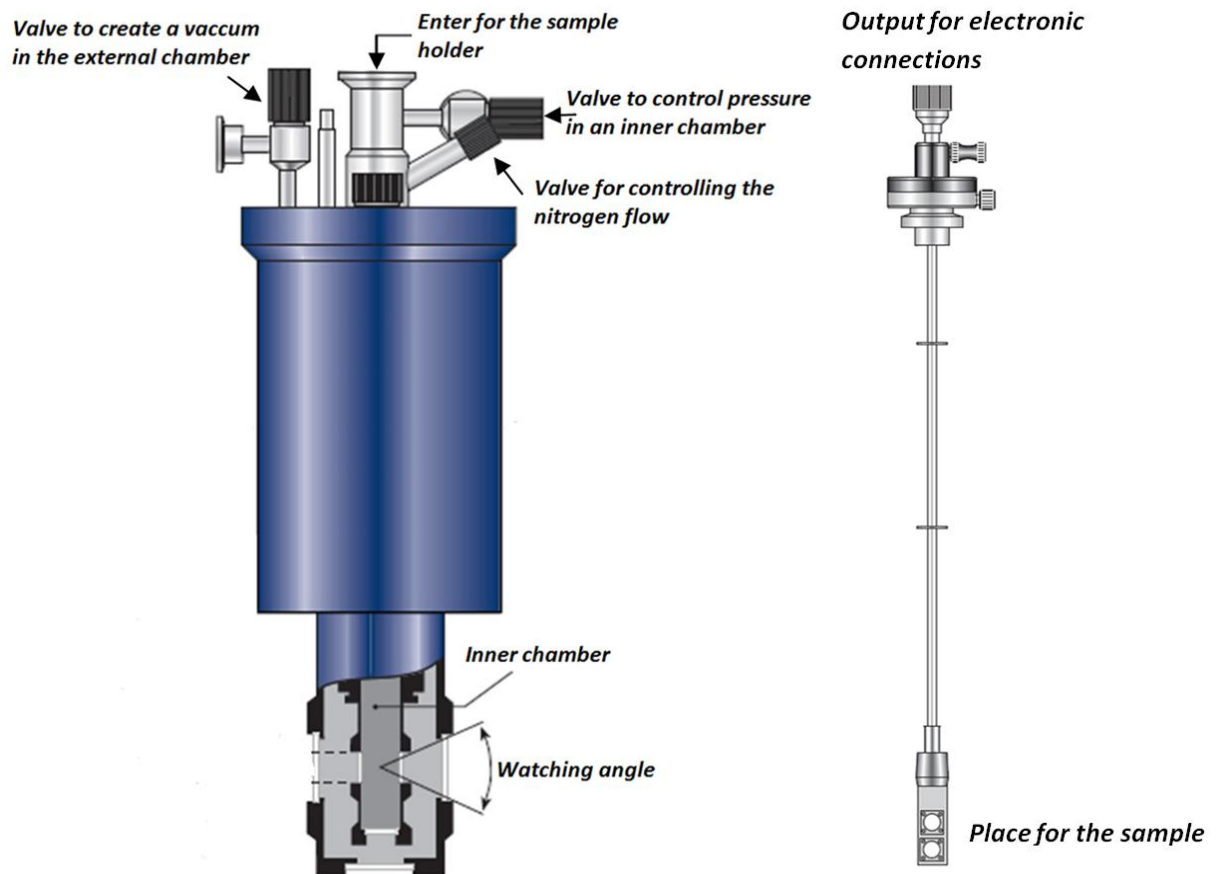
Fig. 2.9. Scheme of a cryostat for investigations between 77-400K.

2.4. Transport thermal properties of lithium tantalate LiTaO₃ pyroelectric sensor

2.4.1. Introduction. As it was mentioned in the beginning of the chapter, $LiTaO_3$ is commonly used as the sensor in many *ac* photopyroelectric calorimeters in the standard back configuration (BPPE), to obtain thermal diffusivity *D(T)* as well as

thermal effusivity *e(T)* of solid and liquid samples, studying their phase transitions. The specific heat *c_p(T)* of those samples is thus obtained by means of the constitutive relation:

$$c_p(T) = \frac{e(T)}{\rho\sqrt{D(T)}},\qquad(2.26)$$

where ρ is the density. In order to measure the thermal effusivity e(T) and as part of a normalization procedure, it is necessary to know the thermal effusivity of the detector as a function of temperature e_p(T). So far, this has been evaluated around room temperature and in the region between 80-150 K [53, 54, 55]. When used as a sensor along other temperature ranges, extrapolations of those results must be used, which is not difficult between 150 and 300 K, as it clearly does not change much, but which is much more difficult for temperatures lower than 80 K; besides, there are no calibrations above 340K. This is why a standard calibration curve is of interest in the full working range, which has never been published before. Our aim was to obtain e_p(T) in a very wide temperature range (15-400 K) independently measuring the specific heat and the thermal diffusivity of LiTaO$_3$ and using Eq. (2.26) to retrieve e_p(T).

2.4.2. Results and discussion. The thermal diffusivity was obtained using our *ac* photopyroelectric calorimeters in the back configuration using LiTaO$_3$ both as sensor and sample. The specific heat was measured using a commercial Physical Properties Measurement System by Quantum design. The measured specific heat and thermal diffusivity are shown in fig. 2.10. For specific heat certain points were taken at particular temperatures to find the trend. In the case of thermal diffusivity, the line is made up of thousands of points. In order to obtain the thermal effusivity of the sensor, analytical expressions were found for the specific heat and for the thermal diffusivity (fitting the experimental points to polynomials of high degree) to mix them using Eq. (2.26) and the result is shown fig. 2.11. In that graph we have also plotted the values found in literature for LiTaO$_3$ [53, 54, 55]. Regarding the values around room temperature, our values are just a little bit higher but this can be do due to the difference of the uncertainties in our measurements and in the published ones, whose relative standard uncertainty seems to be around 5%-6%, where error bars are shown [54, 55].

There was a contradiction between Bentefour *et al.* [54] and Longuemart *et al.* [55] as the conclusion of the first work was that thermal effusivity increased with temperature while the other one said the opposite; in general, an increase of thermal effusivity with temperature is expected in any material (unless there is a phase transition, when some sort of singularity might appear) so the values in [55] where a little bit surprising. Our results support the fact that it is a slowly increasing function, our slope being softer than the one measured in [54]. Concerning the results in the region between 80-150 K, our results differ in the sense that the important change in slope appears at lower temperatures. In the three published cases, the thermal effusivity of $LiTaO_3$ was measured using different photopyroelectric techniques but in all cases they relied on the knowledge of the thermal properties of a reference material as a function of temperature (GaAs in [53], ethylene glycol in [54] and ethanol in [55]) which severely limits the temperature range of study and introduces another factor of uncertainty. In our case we have obtained the thermal diffusivity by only using $LiTaO_3$ both as sensor and sample, so we do not depend on the reliability of the thermal properties of other reference materials. This is the reason why we have been able to evaluate it in a wide temperature range, for the first time. The so obtained curve for $LiTaO_3$ thermal effusivity can be well reproduced by a polynomial of 8th degree, whose coefficients are given in Table 2.2.
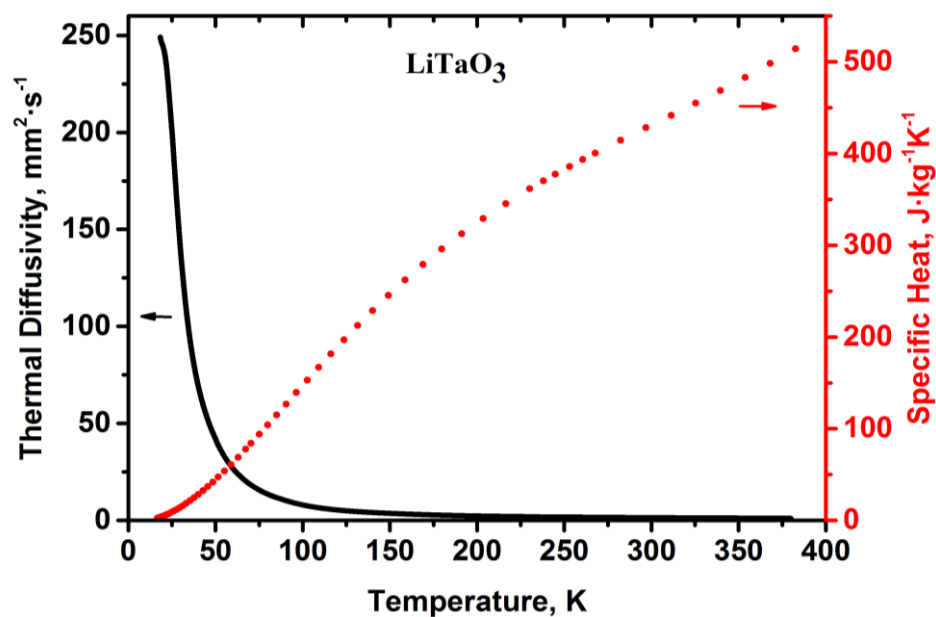
Fig. 2.10. Thermal diffusivity and specific heat of $LiTaO_3$ [56].
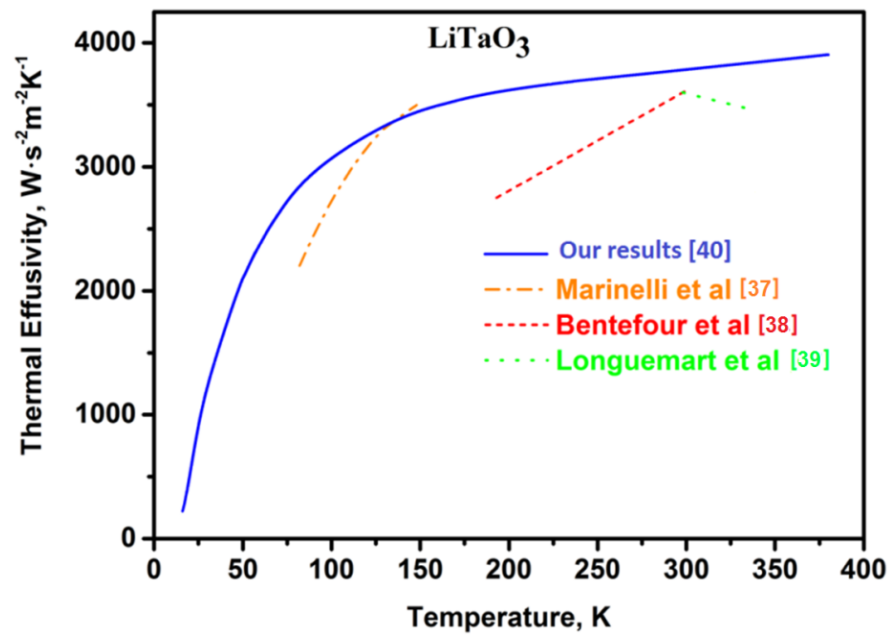
Fig. 2.11 Comparison of the thermal effusivities of LiTaO$_3$ obtained by different authors [56].

Table 2.2.

Coefficients used for the polynomial fit which can reproduce the thermal effusivity result shown in Fig. 2.11. $e_p(T) = a_0 + a_1*T + a_2*T^2 + a_3*T^3 + a_4*T^4 + a_5*T^5 + a_6*T^6 + a_7*T^7 + a_8*T^8$. [56]

Coefficient	Value
a_0	-1564.287039
a_1	137.3189895
a_2	-1.945805029
a_3	0.01748334652
a_4	$-1.008714294 \times 10^{-4}$
a_5	$3.695680593 \times 10^{-7}$
a_6	$-8.283364153 \times 10^{-10}$
a_7	$1.034628129 \times 10^{-12}$
a_8	$-5.514663687 \times 10^{-16}$

2.4.3. Conclusions. The thermal effusivity of the photopyroelectric sensor LiTaO$_3$ has been found in the wide temperature range 15-400 K, an information which is extremely useful when LiTaO$_3$ is used as a sensor in different pyroelectric devices. In particular, its knowledge is necessary when using it as a detector in *ac* photopyroelectric calorimeters in the back configuration to extract the specific heat of samples as a function of temperature. For instance, we have used that curve when obtaining the specific heat of the magnetic system EuCo$_2$As$_2$ around the paramagnetic to antiferromagnetic phase transition which appears when the Eu^{2+} spins order around

41K, having studied its critical behavior. All these results (the ones about the thermal effusivity of the sensor and those on the magnetic transition) have already been published and can be found in [56].

2.5. FPPE technique to measure the thermal effusivity of solids

2.5.1. Introduction. As stated in section 2.2.2, the PPE technique in the front configuration provides an accurate method to measure the thermal effusivity of liquids in the case in which both sample and sensor are thermally thick but it can not be directly applied to solid samples, since the fluid layer that must be introduced to ensure the thermal contact between detector and sample modifies the normalized PPE signal.

An alternative procedure to overcome this issue is to change the frequency scan by a thickness scan of the coupling fluid layer at a fixed frequency [61]. It is shown that this PPE signal is sensitive to the thermal effusivity ratio between coupling fluid and backing solid [62-64]. This method has been used to characterize the thermal effusivity of two families of semiconductors when varying the doping level [65, 66]. However, this method is delicate to manage since it requires the knowledge of the absolute thickness of the coupling fluid layer. Moreover, it is not useful to measure the temperature dependence of the thermal effusivity of solids, which is one of the most relevant applications of PPE calorimetry.

In our research group, we have developed a procedure to measure the thermal effusivity of solids using the FFPE doing a frequency scan, starting with the modeling of the three-layer system (pyroelectric sensor, coupling fluid and test solid), applying it to the evaluation of the thermal effusivity of different solid materials at room temperature and ending with its application to the measurement as a function of temperature, a phase transition in particular.

2.5.2. Resolution of the three layer system. In a three layer system consisting of an opaque pyroelectric slab of thickness L_p, a fluid layer of thickness L_f and a thick solid sample (fig. 2.12), the PPE signal (S) is proportional to the spatially averaged temperature of the pyroelectric slab $\langle T_p \rangle$ [43],

$$S = ab\langle T_p \rangle = ab \frac{1}{L_p} \int_{-L_p}^{0} T_p(z)dz, \qquad (2.27)$$

where a is a frequency-independent factor that depends on the physical properties of the detector (pyroelectric coefficient, dielectric constant and permittivity) and b is a frequency-dependent factor that accounts for the influence of the detection electronics.
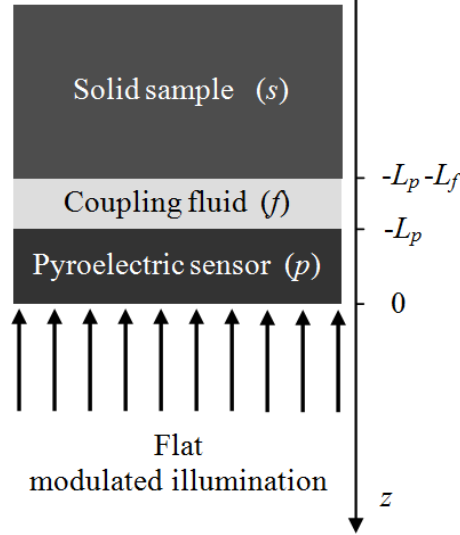
Fig. 2.12. Geometry of the problem [67].

The temperature of the pyroelectric slab is obtained by solving the heat diffusion equation for the three-layer system. If we neglect heat losses at the front surface of the pyroelectric sensor, the temperature at each layer is given by

$$T_p(z) = Ae^{q_p z} + Be^{-q_p z} \qquad (2.28\ a)$$

$$T_f(z) = Ce^{q_f(z+L_p)} + Ee^{-q_f(z+L_p)} \qquad (2.28\ b)$$

$$T_s(z) = Fe^{q_s(z+L_p+L_f)}, \qquad (2.28\ c)$$

where $q = \sqrt{i\omega / D}$ is the thermal wave vector. Subscripts p, f and s stand for pyroelectric detector, coupling fluid and sample respectively. Constants A, B, C, E and F are obtained from the boundary conditions at the interfaces:

• Temperature continuity:

$$T_p\big|_{z=-L_p} = T_f\big|_{z=-L_p} \qquad\qquad T_f\big|_{z=-(L_p+L_f)} = T_s\big|_{z=-(L_p+L_f)} \qquad (2.29\ a)$$

• Heat flux continuity:

$$K_p \frac{dT_p}{dz}\bigg|_{z=-L_p} = K_f \frac{dT_f}{dz}\bigg|_{z=-L_p} \qquad\qquad K_f \frac{dT_f}{dz}\bigg|_{z=-(L_p+L_f)} = K_s \frac{dT_s}{dz}\bigg|_{z=-(L_p+L_f)} \qquad (2.29\ b)$$

• Illumination at the front surface:

$$K_p \left. \frac{dT_p}{dz} \right|_{z=0} = \frac{I_o}{2}. \qquad (2.29\ c)$$

By substituting Eqs. (2.28) into Eqs. (2.29), the temperature of the pyroelectric slab is obtained. Then, from Eq. (2.27), the PPE signal (*S*) is obtained. For normalization purposes, i.e. to eliminate the frequency dependence of the detection electronics, the PPE signal obtained for the three-layer system is divided by the PPE signal obtained for the bare pyroelectric slab. As a consequence, the normalized PPE signal (*S_n*) is

$$S_n = \frac{S_{three-layers}}{S_{pyro}} = \frac{ab\langle T_p \rangle_{three-layers}}{ab\langle T_p \rangle_{pyro}} = \frac{2\sinh\left(q_p L_p / 2\right)\left[M\cosh\left(q_p L_p / 2\right) + N\sinh\left(q_p L_p / 2\right)\right]}{M\sinh\left(q_p L_p\right) + N\cosh\left(q_p L_p\right)}, \quad (2.30)$$

where

$$M = \frac{e_p}{e_f}\left(\cosh\left(q_f L_f\right) + \frac{e_s}{e_f}\sinh\left(q_f L_f\right)\right), \qquad (2.31\ a)$$

$$N = \frac{e_s}{e_f}\cosh\left(q_f L_f\right) + \sinh\left(q_f L_f\right). \qquad (2.31\ b)$$

Note that the normalized signal depends neither on *a* or *b*, indicating that the frequency dependence of the detection electronics is removed. On the other hand, Eq. (2.30) has been written in such a way that the correlation between parameters is clearly seen. Accordingly, S_n depends on four parameters: $L_f / \sqrt{D_f}$, $L_p / \sqrt{D_p}$, e_s/e_f and e_p/e_f (as the sample is thermally thick, S_n does not depend on D_s). Since L_p, D_p, e_p and e_f are known, only two unknown parameters remain: the fluid "thermal thickness" $L_f / \sqrt{D_f}$ and the effusivity ratio e_s/e_f. Therefore, a fitting of the frequency behaviour of normalized PPE signal, S_n, to Eq. (2.30) allows retrieving e_s together with $L_f / \sqrt{D_f}$ as a by-product.

2.5.3. Experimental results

In order to verify the validity of the method we have performed PPE measurements on a set of samples, covering a wide range of effusivities: polymers, glasses, dielectric crystals, alloys, ceramics and metals. These samples, with thicknesses larger than 5 mm in order to satisfy the thermally thick conditions, are placed on top of

a LiTaO$_3$ pyroelectric crystal 0.32 mm thick. A very thin layer of high-conductive silicone grease (Heat sink compound, Dow Corning) is used to ensure the thermal contact. A diode laser (λ = 656 nm) of 50 mW impinges on the free pyroelectric surface. Its intensity is modulated by a periodic current governed by the computer and serving as the lock-in reference. The PPE current produced by the detector has been fed into the digital lock-in amplifier.

Only the phase of the normalized signal will be used in this experimental section to retrieve the thermal effusivity. This is due to the fact that phase of the PPE signal is more stable than its amplitude, since the latter is sensitive to the intensity fluctuations of the laser.

First of all, we have measured the room temperature thermal effusivity of the Heat sink compound that we have used as coupling fluid. We have put a 3 mm thick layer of this paste directly on top of the pyroelectric sensor. Fig. 2.13 shows by dots the frequency dependence of the phase of the normalized PPE signal for Heat sink compound. The continuous line is the fitting to Eq. (2.30) for a thermally thick fluid. The retrieved thermal effusivity for the measurement shown in fig. 2.13 is 968±3 Ws$^{0.5}$m^{-2}K^{-1}. After repeating the same measurement 5 times, the thermal effusivity of the Heat sink compound was found to be e_f = 970±8 Ws$^{0.5}$m^{-2}K^{-1}. This value will be used in the following fittings.
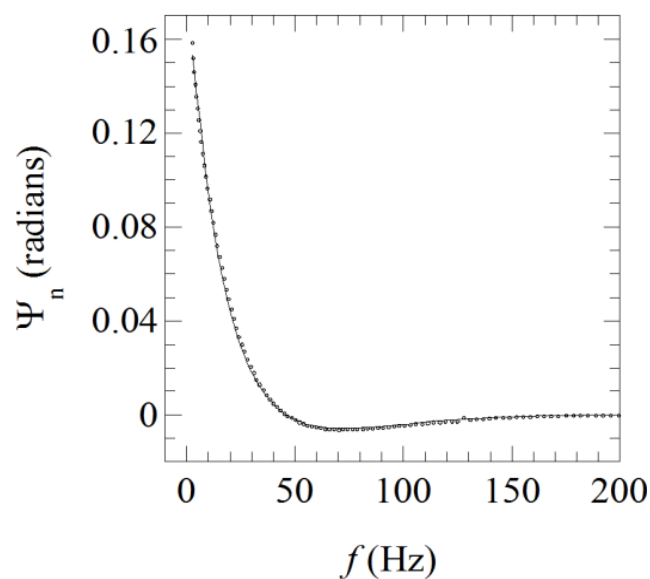
Fig. 2.13. Frequency scan of the phase of the normalized PPE signal for Heat sink compound. Dots are the experimental data and the continuous line is the fitting to Eq. (2.27) [67].

Fig. 2.14 *a* shows the room temperature frequency scan of the phase of the normalized PPE signal for three selected materials: A high effusivity sample (Cu), a low effusivity sample (polyimide, PI) and a sample with effusivity close to the effusivity of the pyroelectric sensor (KCl). The whole frequency range is shown in order to verify that Ψ_n converges to zero at high frequencies. However, the highest sensitivity to the solid effusivity is produced at low frequencies (we have checked this issue doing a whole set of simulations). In fact, all the fittings performed up to 155 Hz are worse that those performed up to 50 Hz, i.e. close to the zero-crossing frequency. Accordingly, to obtain the thermal effusivity of the whole set of calibrated solids only the frequency range 1-50 Hz has been used. Fig. 2.14 *b* shows the room temperature experimental results in such a range for most of the solids measured in this work. Dots are the experimental data and the continuous lines are the fits to equation 2.30. The retrieved values are given in table 2.3 and are in good agreement with the tabulated effusivities. In all measurements $L_f / \sqrt{D_f}$ falls in the range 0.01-0.03 $s^{0.5}$, which corresponds to reasonable grease thicknesses of 5-15 μm.
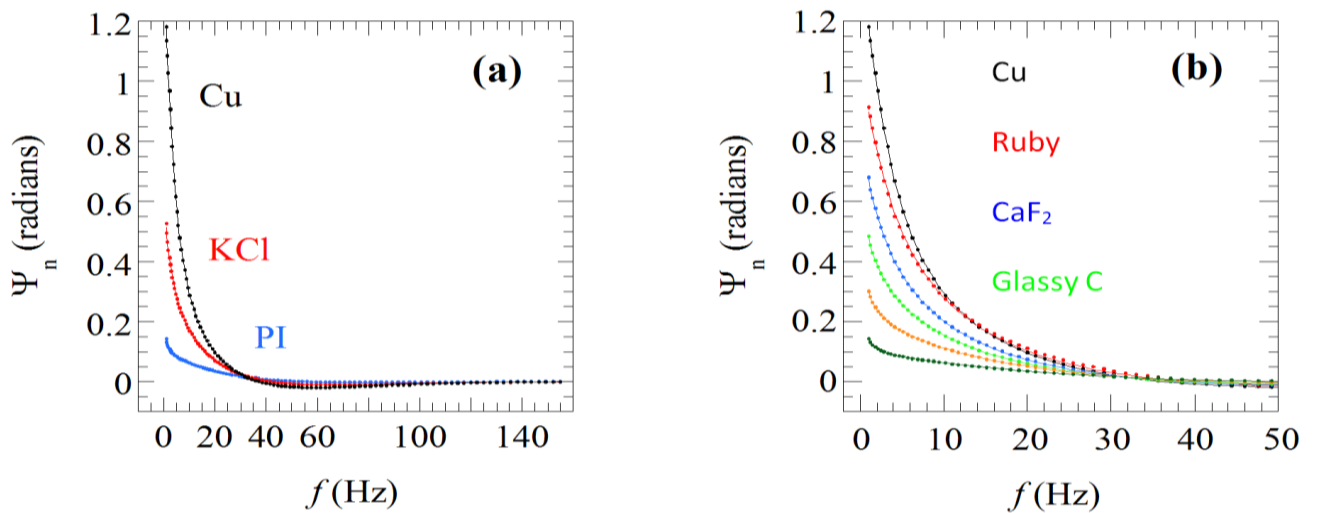
Fig. 2.14. Experimental frequency scans of the phase of the normalized PPE signal: (a) For three selected materials (Cu, KCl and polyimide (PI)) in the whole frequency range and (b) for a wide set of solid samples at low frequencies. Dots are the experimental data and the solid lines are the fits to equation (2.30) [67].
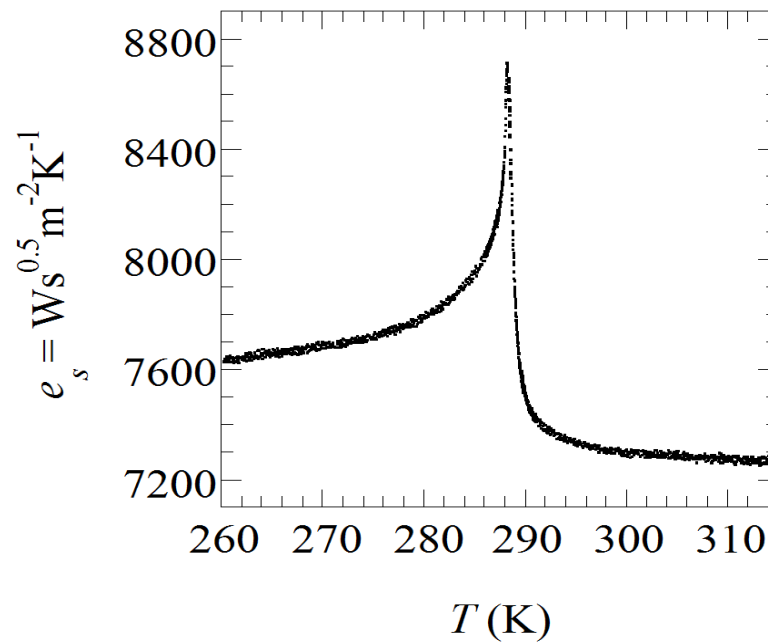
Fig. 2.15. Temperature dependence of the thermal effusivity of CoO around its antiferromagnetic phase transition [67].

The main application of this technique is to measure the temperature dependence of the thermal effusivity of solids from a single heating or cooling run. In particular, we are interested in the characterization of the thermal properties across phase transitions. We proceed as follows. First, at a fixed temperature we measure the thermal thickness of the grease $L_f / \sqrt{D_f}$ from the frequency scan of the normalized phase. Then we choose the frequency at which the normalized phase is insensitive to the thermal thickness of the grease, $f = 1$ Hz in our setup (a LiTaO$_3$ sensor 0.32 mm thick). By keeping this frequency fixed, we vary continuously the temperature while recording the phase of the PPE signal, once for the bare pyroelectric detector and then for the sample. In this way, we obtain Ψ_n as a function of the temperature. Finally, by solving equation (2.30) at each temperature, we retrieve $e_s(T)$. This method requires knowing $e_p(T)$, $D_p(T)$ and $e_f(T)$. The two first properties are known for LiTaO$_3$ whereas the latter, as a first approach, is kept fixed. This assumption is not very restrictive since the characterization of phase transitions involve narrow temperature ranges. In Fig. 2.15 we show the temperature dependence of the thermal effusivity of a CoO single crystal around its antiferromagnetic phase transition at 288 K [68]. This result has been obtained in a continuous heating run at 60 mK/min in order to obtain low noise data and clearly

demonstrates the ability of this method to measure the thermal properties across phase transitions with high resolution.

Table 2.3.

Room temperature thermal effusivity (e_s) of the materials studied in a paper [67]

Material	e_s (Ws$^{0.5}$m^{-2}K^{-1})	e_s literature (Ws$^{0.5}$m^{-2}K^{-1}) [69-74]
Cu	37800±1400	37150
SiC	24300±1100	22000-26000
Ruby	10900±400	11650
Sn	10300±300	10510
Pb	7040±200	7190
CaF$_2$	5180±150	5236
LiTaO$_3$	3860±80	3750
KCl	3040±60	2998
Glassy Carbon	2620±50	2530
PZT	1760±50	1690
Zerodur	1600±40	1719
BK7 glass	1540±40	1549
Low density PE	680±30	759
PEEK	610±20	638
PI (Cirlex)	520±20	513

.

CHAPTER 3

Physical properties of the ferroelectric family Sn(Pb)$_2$P$_2$S(Se)$_6$

The structure of this chapter is aligned as follows: in the beginning a general description of the crystalline structure of this type of materials will be introduced. After that we briefly consider the phase diagrams of $Sn_2P_2S(Se)_6$, $Sn(Pb)_2P_2S_6$ and $Sn(Pb)_2P_2Se_6$ mixed ferroelectrics by means of the investigation of different physical properties. And finally, owing to the main goal of this thesis, a review of the thermophysical properties such as specific heat, thermal diffusivity, thermal expansion and thermal conductivity for $Sn(Pb)_2P_2S(Se)_6$ family will be given in a separate section.

3.1. Crystalline structure of Sn(Pb)$_2$P$_2$S(Se)$_6$ compounds

$Sn(Pb)_2P_2S(Se)_6$ are ion-covalent crystals. They comprise $[P_2S(Se)_6]^{4-}$ anions combined with $Sn(Pb)^{2+}$ cations into a three-dimensional lattice. The crystallographic unit cell comprises two formula units (Z=2). The anions $[P_2S(Se)_6]^{4-}$ are described by the distorted point symmetry group ($\overline{3}m$) and include two deformed trigonal pyramids $PS(Se)_3$ which in turns are interlinked by a P−P bond 2.202 Å long. The P−S bonds in the pyramids have different lengths in the range 2.015-2.035 Å. Tin atoms are located between the ions inside the polyhedron formed by 7 or 8 sulphur or selenium atoms. The lengths of the Sn−S ionic bounds (2.77-3.451 Å) are considerably larger than for P−S and P−P. The parameters for the monoclinic cell at ambient conditions for the $Sn_2P_2S_6$ crystal are as follows: a=9.378 Å, b=7.488 Å c=6.513 Å, and the angle β=91.15° [75, 76]. At room temperature three extreme compounds $Pb_2P_2S_6$, $Pb_2P_2Se_6$ and $Sn_2P_2Se_6$ posses centrosymmetric structure and they are in a paraelectric phase, whereas the crystal $Sn_2P_2S_6$ has an acentric structure and belongs to a ferroelectric phase. In the paraelectric phase the crystalline structure of $Sn(Pb)_2P_2S(Se)_6$may be described by the P2$_1$/c space group [77, 78].

The uniaxial ferroelectric crystal $Sn_2P_2S_6$ undergoes a second order phase transition (PT) at $T_0 \approx 337$ K, having lowered its unit cell symmetry from $P2_1/c$ to Pc [3]. As seen on figure 3.1 only the Sn atoms are shifted significantly in the [100] direction with respect to the locations of the metal atoms in the centrosymmetric state

[76]. This allows considering the Sn cation sublattice as ferroactive. At the transition from the ferroelectric phase to the paraelectric one, all four Sn atoms are shifted by nearly 0.26 Å along the [100] direction, reaching centrosymmetric state. In addition, two tin atoms are also displaced along [01$\bar{0}$] direction by 0.04 Å, while at the same time other two are shifted the same distance along [010] direction. The changes in the position of P and S atoms are extremely small [3]. These tin atoms migrations are the physical realization of the order parameter associated to the ferroelectric phase transition in $Sn_2P_2S_6$.
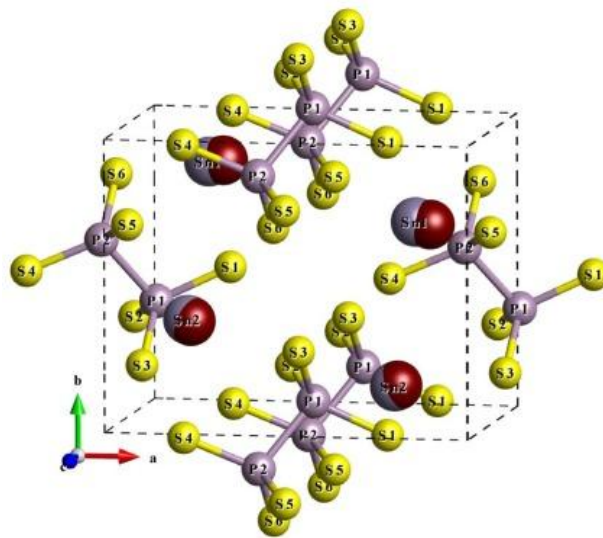
Fig. 3.1. The crystal structure of $Sn_2P_2S_6$ ferroelectric phase [75]. The tin atoms positions in the paraelectric phase [79] are shown by red spheres.

Let's consider the variation of the structural parameters when substituting S by Se and Sn by Pb. The replacement of S by Se leads to an increase in the unit cell volume from 456 Å^3 for $Sn_2P_2S_6$ to 505 Å^3 for $Sn_2P_2Se_6$. The same happens in lead compounds: the unit cell volume is changed from 462 Å^3 to 513 Å^3 for $Pb_2P_2S_6$ and $Pb_2P_2Se_6$, respectively. The difference in volumes for two sulphide and two selenide solid solutions is quite small in view of the difference in the atomic radii of octa-coordinated tin and lead atoms: 1.58 Å and 1.75 Å. Thus, the Sn^{2+} ions are in a less "squeezed" state, which is reflected in their ferroactivity, suggesting that compounds with cation radii bigger than that for Sn^{2+} should possess lower PT temperature [3].

$Sn_2P_2Se_6$ exhibits three phases; at room temperature it is paraelectric ($P2_1/c$) [76], at $T_i \approx 221$ K a second order transition takes place to a modulated incommensurate

phase, and at $T_c \approx 193$ K the crystal shows a first order transition to the ferroelectric phase (Pc) [80, 81]. The period of transverse wave modulation of spontaneous polarization in the IC phase is about 14 unit cells [82]. The structures in paraelectric and ferroelectric phases were accurately determined in references [83, 84]. The projection onto (010) plane of both low temperature (150 K) and room temperature (293 K) structures are depicted on fig. 3.2 a, b. In these figures the difference between them is not clearly seen, but if we put one on top of the other (fig.3.3), it is clear that the metal ions have changed their initial positions. Such a comparison between those two structures shows that tin ions are shifted about 0.13 Å from their individual centrosymmetric sites in the high-temperature phase to the corresponding tin position in the low-temperature phase. The shift, from the average Sn-position in the paraelectric phase with respect to the Sn-positions in the ferroelectric one, is about 0.30 Å and on average 10° off the vector $\vec{a}+\vec{c}$, which is displayed by arrows, thus these ions migrations provoke the appearance of spontaneous polarization. In additional, the average direction of these displacements is perpendicular to the modulation wave vector direction in the incommensurate phase [82, 85], showing the prime importance of such movements on the formation of the incommensurate phase (IC).
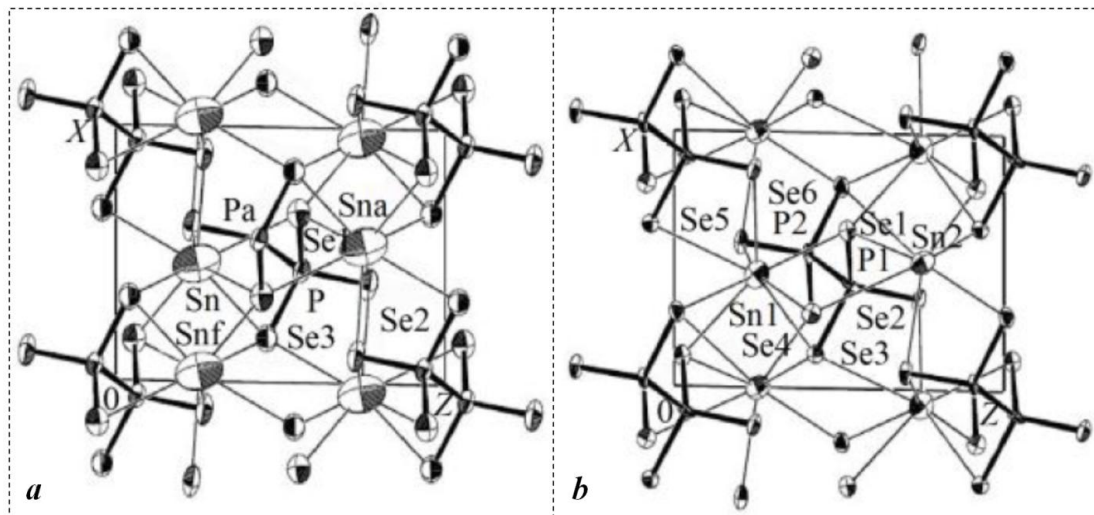
Fig. 3.2. Crystalline structure of $Sn_2P_2Se_6$ (projection onto (010)): a − paraelectric phase (293K); b − ferroelectric phase (150K) [83].
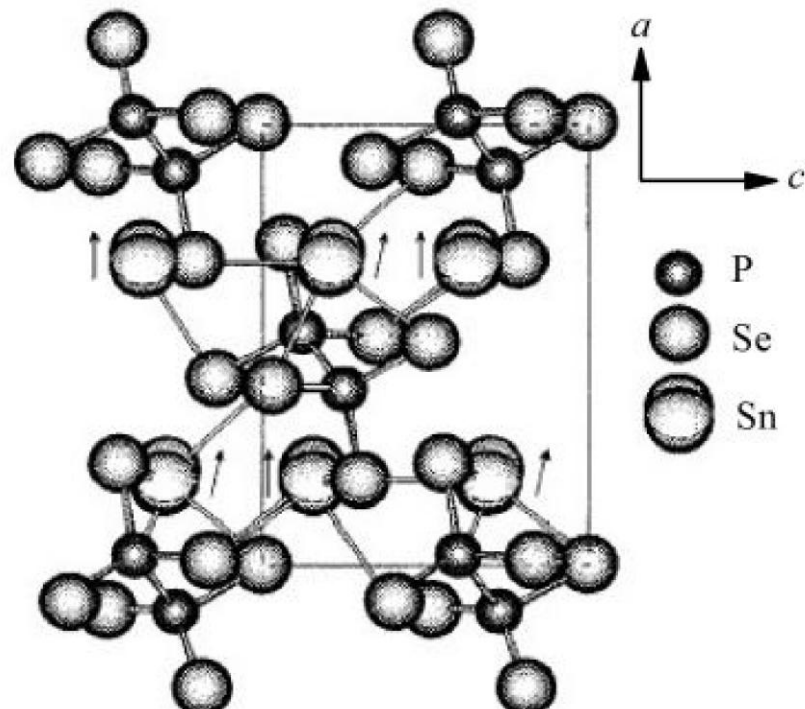
Fig. 3.3. Compared structures of Sn$_2$P$_2$Se$_6$ in the paraelectric and in the ferroelectric phases. Arrows show the Sn^{2+} cations displacements at the transition to the ferroelectric phase [78, 84].

Indeed, direct diffraction data obtained in [81] confirm the existence of a modulated structure for Sn$_2$P$_2$Se$_6$ below 221K. Satellite reflection pairs indicating the appearance of a modulation are detected close to the main reflections in the oscillating crystal X-ray pictures obtained by rotation of the crystal around the [010] axis. The modulation wave vector lies in a plane perpendicular to the [010] direction. As fig. 3.4 shows, the satellites (2 and 3) are seen as separate maxima whose intensities are 5 times smaller than for the central peak (1). The positions of two additional peaks in the crystallographic frame with their origin at the main reflection are given as $\pm 0.082a^* \pm 0.72c^*$. Note that the half-widths of the satellites and the main peak almost coincide. This indicates an incommensurate modulation with period about 12-14 times of the unit cell size in the paraelectric phase. Moreover, a smooth temperature variation of the modulation wave vector q (fig. 3.5) confirms the presence of a truly incommensurate structural modulation [3].
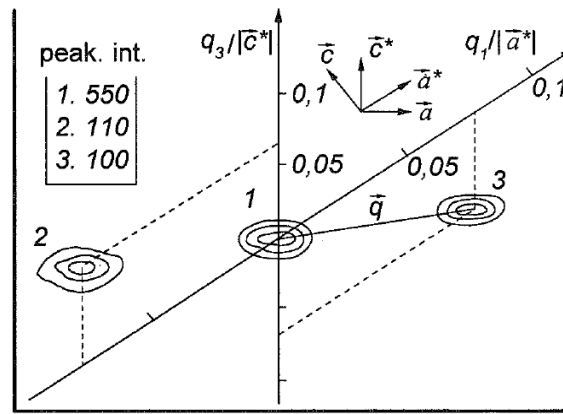
Fig.3.4. Scattering intensity distribution in $Sn_2P_2Se_6$ at 200K: 1 – is the main peak; 2 and 3 are satellites. Isolines represent levels (0.25; 0.50, 0.75) of the peak intensity for each reflection [3].

The satellite reflections appear at T_i (221K) and their intensity increase monotonically below T_i signaling that the transition has a continuous character. At T_c (193K) the diffraction modulation effects vanish abruptly, meaning that $Sn_2P_2Se_6$ undergoes a first-order transition from IC into a polar ferroelectric phase. Such transformations also lead to the lowering of the symmetry down to Pc. In addition, reverse temperature run exhibits an opposite sequence of transitions with an observed hysteresis of about 0.5K for T_c and without it for T_i [3].
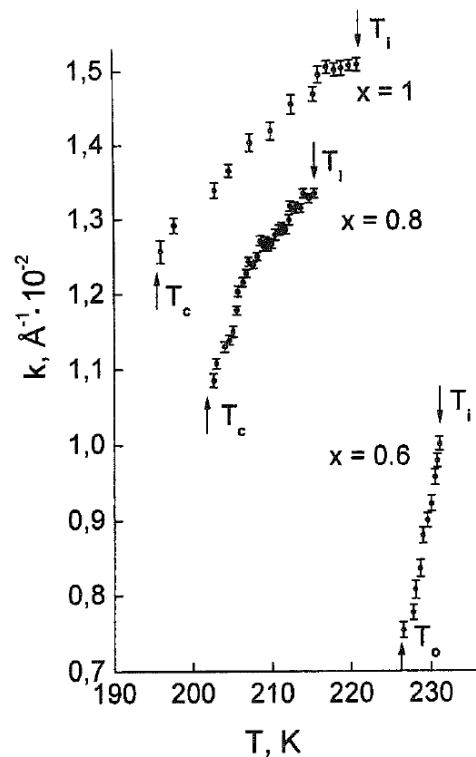
Fig. 3.5. Temperature behavior of the modulation wave vector for $Sn_2P_2(S_{1-x}Se_x)_6$ crystals [3].

$Pb_2P_2S_6$ and $Pb_2P_2Se_6$ crystals remain in the centrosymmetric phase ($P2_1/c$) till 0 K [84]. Their crystalline structures are similar to the one presented above for $Sn_2P_2S_6$ in the paraelectric phase (fig. 3.1). They differ only in the volume of the unit cell, due to the difference in the sizes of the ions which provoke a change in the crystal lattice parameters. The structures of $Pb_2P_2S(Se)_6$ compounds based on data published in [85, 86] are presented on fig.3.6.
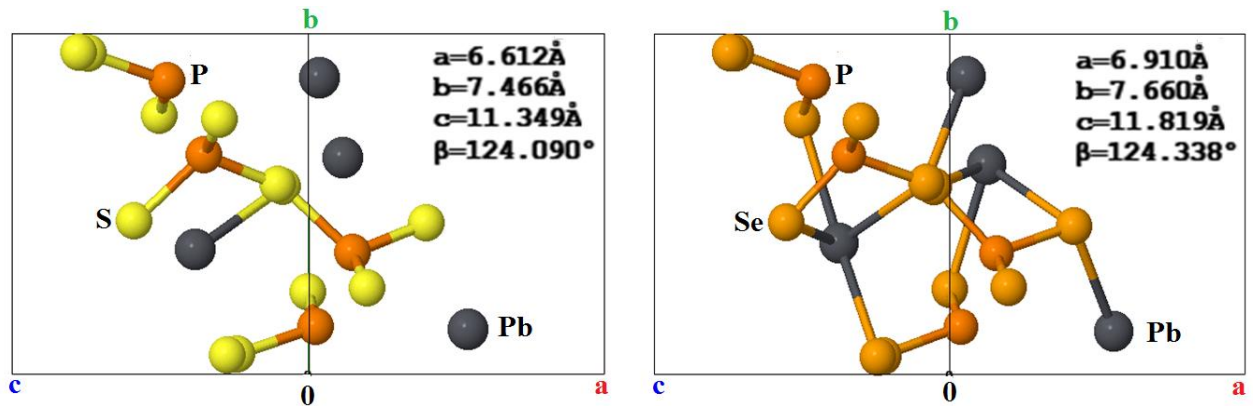
Fig. 3.6. Crystalline structure for $Pb_2P_2S_6$ (on the right) and $Pb_2P_2Se_6$ (on the left) crystals [87, 88].

To quantitatively summarize this section, we introduce table 3.1 contained with main parameters which are characterize the monoclinic crystalline lattice of $Sn(Pb)_2P_2S(Se)_6$ ferroelectric family.

Table 3.1.

Crystalline lattice parameters of $Sn(Pb)_2P_2S(Se)_6$ ferroelectrics [3].

Lattice parameters	$Sn_2P_2S_6$		$Sn_2P_2Se_6$		$Pb_2P_2S_6$	$Pb_2P_2Se_6$
	FerroPhase	ParaPhase	FerroPhase	ParaPhase	ParaPhase	ParaPhase
a, Å	9.378	9.362	9.616	9.626	6.612	6.910
b, Å	7.488	7.493	7.708	7.671	7.466	7.660
c, Å	6.513	6.550	6.805	6.815	11.349	11.819
β, ^{0}	91.15	91.17	91.03	91.01	124.09	124.38
V, Å^3	456		505		462	513

3.2. Phase diagram study of $Sn(Pb)_2P_2S(Se)_6$ mixed compounds

3.2.1. General shape of the phase diagram of $Sn(Pb)_2P_2S(Se)_6$ ferroelectrics.

From 1970, when $Sn(Pb)_2P_2S(Se)_6$ crystals were firstly grown and their structures studied [89], till present days, huge efforts have been devoted to investigate the phase diagram of these solid compounds. Optical [90], thermal [91], elastic [92] and dielectric

[93] measurements indicate that Sn$_2$P$_2$S$_6$ undergoes a second-order PT at 337K from the initial high-temperature paraelectric phase to the low-temperature ferroelectric one accompanied by a symmetry change $P2_1/c \rightarrow Pc$. These structural modifications lead to the appearance of a spontaneous polarization, known as the order parameter in these materials.

Let's discuss the general features of the "temperature-concentration" phase diagram of Sn(Pb)$_2$P$_2$S(Se)$_6$ ferroelectrics by replacing Se ions instead of S in the anion sublattice and Pb instead of Sn in the cation one (fig.3.7) [91, 94]. Substituting S by Se in the Sn$_2$P$_2$(S$_{1-x}$Se$_x$)$_6$ series leads to a smooth splitting of the second order PT line (dashed line on fig. 3.7) into a first order (solid curves) and second order (dashed curves) phase transition lines. As the result, in the crystal Sn$_2$P$_2$Se$_6$ two phase transitions occur: a second-order transition at T$_i$=221K and a first-order one at T$_c$=193K.

Replacing the Pb ions instead of the Sn ions in the cation sublattice of (Sn$_{1-y}$Pb$_y$)$_2$P$_2$S$_6$ compounds sharply reduces the temperature of the paraelectric-ferroelectric transition and at a lead concentration of 0.61, it reaches 4.2K. At concentrations larger than 0.61, PT is frozen, hence, such crystals are being paraelectric till the lowest temperatures. The character of the transition remains to be a continuous one [94].
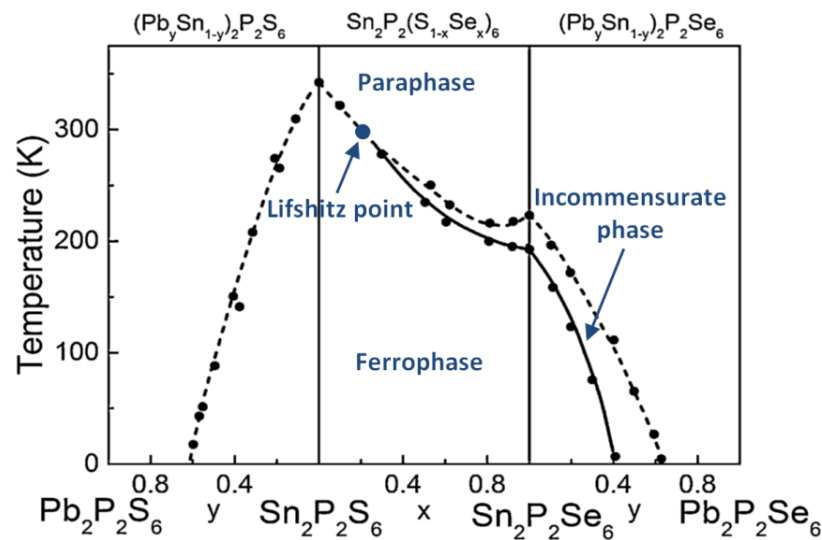
Fig. 3.7. Phase diagram of Sn(Pb)$_2$P$_2$S(Se)$_6$ ferroelectric crystals: The dashed lines indicate the second-order phase transitions: from the paraelectric phase to the ferroelectric one in (Pb$_y$Sn$_{1-y}$)$_2$P$_2$S$_6$ and in Sn$_2$P$_2$(S$_{1-x}$Se$_x$)$_6$ with x<0.28, while in Sn$_2$P$_2$(S$_{1-x}$Se$_x$)$_6$ with x>0.28 and (Pb$_y$Sn$_{1-y}$)P$_2$Se$_6$ it indicates the transition to an incommensurate phase. The continuous lines indicate the first order transition from the incommensurate to the ferroelectric phase [3].

Introducing Pb into $Sn_2P_2Se_6$ has the same effect as in $Sn_2P_2S_6$. Lead ions lower the temperatures of the transitions T_i and T_c. At the same time, replacing Pb by Sn increases the width of the incommensurate phase. For instance, for $y=0.4$ the width exceeds 100K. It should be pointed out that the first-order and second-order transition lines approach 0K at $y=0.40$ and $y=0.61$, respectively.

3.2.2. Phase transitions diagram of the $Sn_2P_2(S_{1-x}Se_x)_6$ crystals. Lifshitz point

Consider the shape and peculiarities of the diagram shown on fig. 3.7 in detail. To do this we will present the results of the different physical properties investigated by means of dielectric, optic, thermal, elastic and other measurements. First, we summarize available data about temperature-concentration phase diagram of the tin-sulfur/selenium compounds. Before this work, the phase transitions in $Sn_2P_2(S_{1-x}Se_x)_6$ have been studied by thermal diffusivity [60, 95], X-ray diffraction [96, 82], dielectric [97, 98], ultrasound [99], and specific heat [100] measurements. All these data lead to the conclusion that the phase transitions line starts to be splitted at $x\sim0.28$ (fig. 3.8).
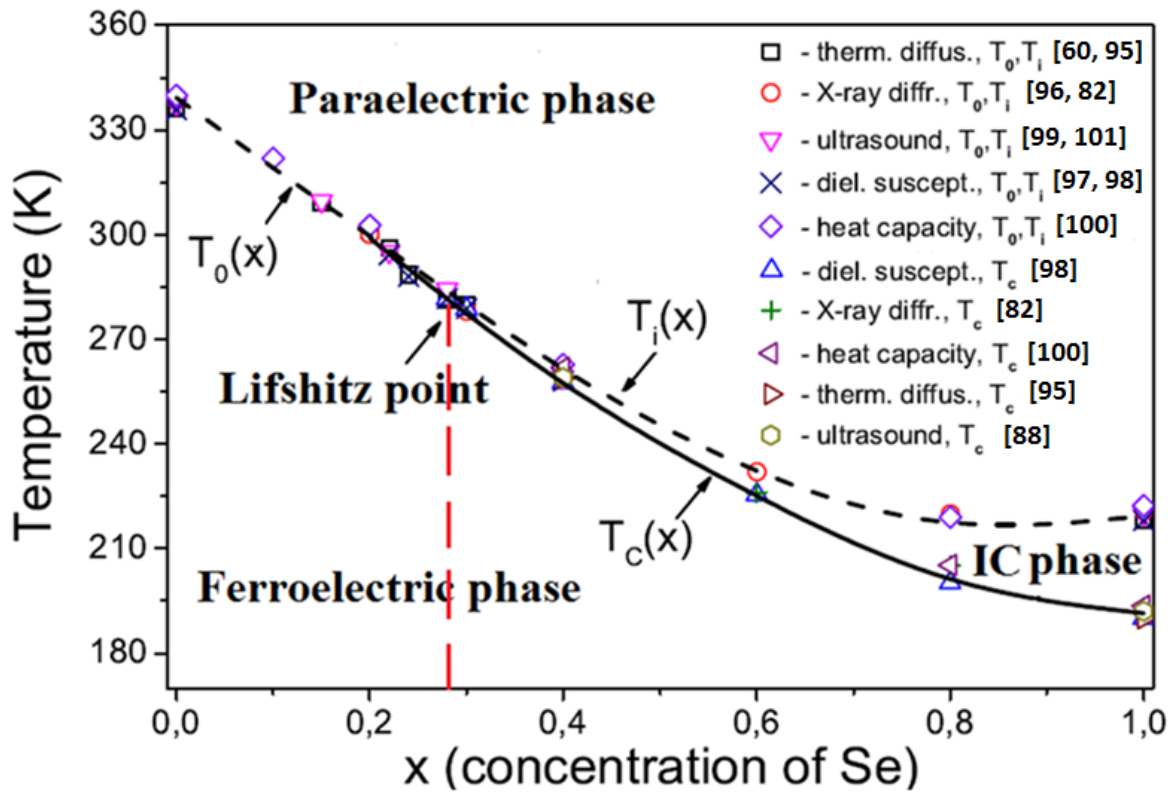
Fig. 3.8. Phase diagram of $Sn_2P_2(S_{1-x}Se_x)_6$ crystals. $T_0(x)$ at $x<0.28$ and $T_i(x)$ at $x>0.28$ are the second order paraelectric-ferroelectric and paraelectric-IC transitions, respectively (dashed line). $T_c(x)$ is the first-order lock-in IC-ferroelectric transition at $x>0.28$ (solid line) [101].

This special splitting point is known as a Lifshitz point (LP), at which the second order transitions line $T_0(x)$ from the paraelectric to ferroelectric states separates into the continuous second order transitions line $T_i(x)$ and the line of first order transitions $T_c(x)$. Between the lines the modulated incommensurate phase (IC) is observed with the same point symmetry as the paraelectric one. When approaching the LP concentration, if selenium content is changed in such a way that $1 > x > x_{LP}$, the wave vector of the incommensurate modulations q_i that appears along the $T_i(x)$ line decreases as well as the temperature width of the region $T_i - T_c$ where IC phase occurs. The concentration dependences of the modulation wave number q_i in the IC phase and the temperature width $T_i - T_c$ satisfy the next interpolations $T_i - T_c \sim (x - x_{LP})^2$ and $q_i \sim (x - x_{LP})^{0.5}$. The dependences are depicted on fig. 3.9 [101].
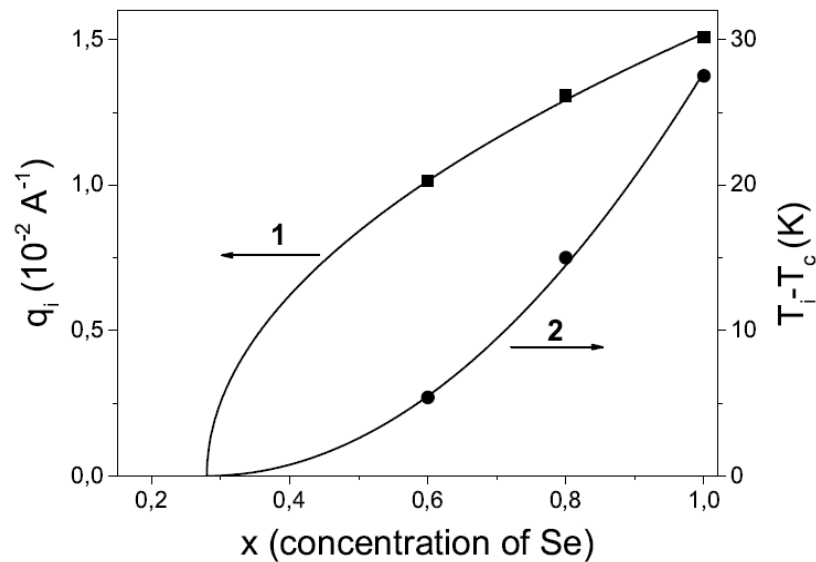
Fig. 3.9. The concentration dependences of the modulation wave number q_i (1) along the $T_i(x)$ line and the temperature width $T_i - T_c$ (2) in Sn$_2$P$_2$(S$_{1-x}$Se$_x$)$_6$ ferroelectrics [101].

Looking at fig. 3.8 more closely, one issue can arise: it is about the "precise" location of the LP on the phase diagram. Its position could be estimated from the evolution of the temperature dependences of the phonon spectra at certain selenium content in Sn$_2$P$_2$(S$_{1-x}$Se$_x$)$_6$ solid solution. To analyze that diagram in detail we refer to thermal diffusivity, ultrasound and hypersound data published in [60, 95, 99]. In general, the thermal diffusivity data gives information on the group velocity of the short-waves phonons; on the other hand, acoustic data can be used to characterize the

phase velocity of the ultrasound and hypersound waves. The position of the LP could be evaluated from the evolution of the temperature dependence of phonon spectra at different concentrations. According to data depicted on fig. 3.10 the thermal diffusivity in paraelectric phase lowers as the amount of Se is increased. Such lowering takes place only until x=0.22, and at higher values the concentration dependence of diffusivity in high symmetric phase becomes almost flat (see inset on fig. 3.10). That concentration of Selenium is smaller than expected in $Sn_2P_2(S_{1-x}Se_x)_6$ mixed ferroelectrics with LP composition about $x_{LP} \sim 0.28$ [101]. This reduction in the thermal diffusivity could be associated with a softening of the acoustic phonon branches, which is expected near the LP (an effect already observed in Brillouin scattering and ultrasound investigations). This could suggest that the LP might be found at a lower concentration than x=0.28.

Another strong fact which can confirm that x_{LP} should be shifted a bit "to the left" on the phase diagram is a high resolution hysteresis study of thermal diffusivity published in [60]. Fig. 3.11 shows the evolution of the difference in the critical temperature in heating and cooling runs as a function of concentration; in x=0.15, 0.20 and 0.22 the linear extrapolation tends to 0 indicating a lack of hysteresis in thermal diffusivity. While for concentrations x=0.26, 0.28 and 0.30 the extrapolations intersect the vertical axis between 0.1 and 0.2K showing the presence of hysteresis. Besides, the shapes of thermal diffusivity curves for slow heating-cooling runs are practically the same at concentrations without hysteresis 3.12 *a*, and differ for samples with hysteresis fig. 3.12, *b.*
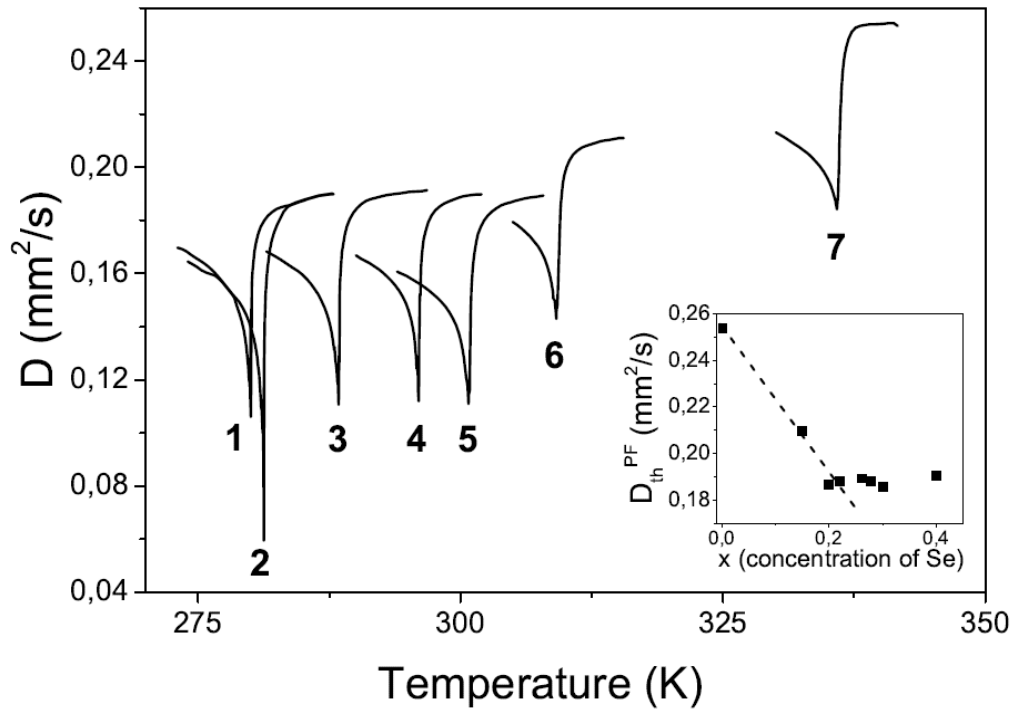
Fig. 3.10. Thermal diffusivity anomalies across the phase transition point of Sn$_2$P$_2$(S$_{1-x}$Se$_x$)$_6$. ferroelectrics: 1 − x=0.30, 2 − x=0.28, 3 − x=0.26, 4 − x=0.22, 5 − x=0.20, 6 − x=0.15, 7 − x=0. Inset represents concentration dependences of thermal diffusivity in a paraelectric state [101].
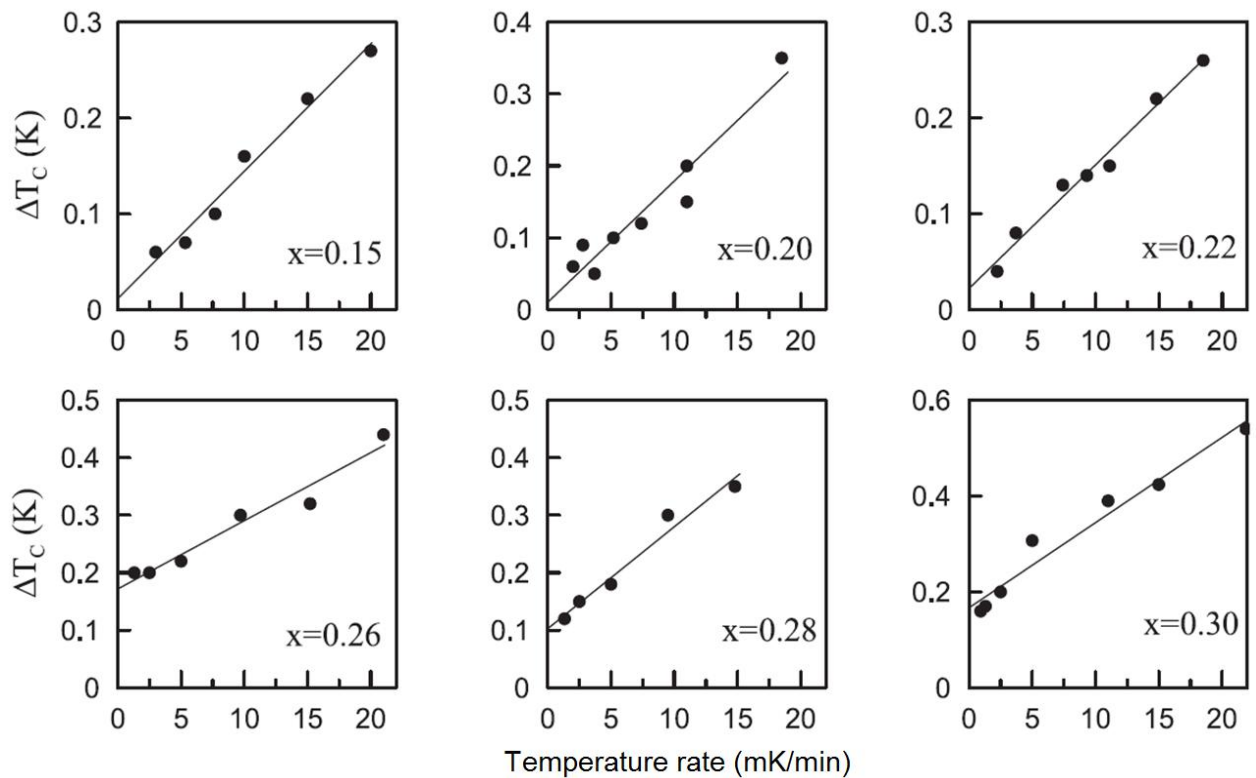
Fig.3.11. Thermal hysteresis of ferroelectric phase transition for certain concentrations of Sn$_2$P$_2$(S$_{1-x}$Se$_x$)$_6$ ferroelectric family [60].
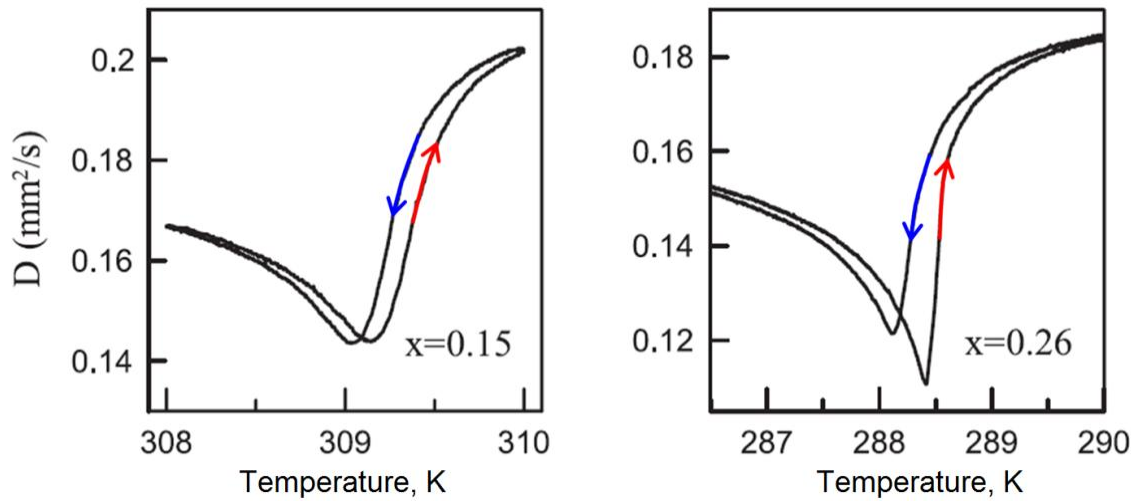
Fig.3.12. Thermal diffusivity performed at slow rate heating-cooling runs for *x*=0.15 (7.7mK/min) and *x*=0.26 (9.7mK/min) [60].

On the other hand, ultrasound and hypersound velocity data show some discrepancy. The temperature dependencies of longitudinal ultrasound velocity (fig.3.13) [99] exhibit the sharpest shape at Se concentration of *x*=0.26 reaching a minimal value of about 3100 m/s (fig.3.13 *d*). The deepest minimum of ultrasound velocity has been observed at the composition *x*=0.28 (fig.3.14, curve 2). Note that a similar behavior has also been found from thermal diffusivity measurements, the sharpest shape has a sample with selenium content of *x*=0.28 (fig.3.10, curve 2).
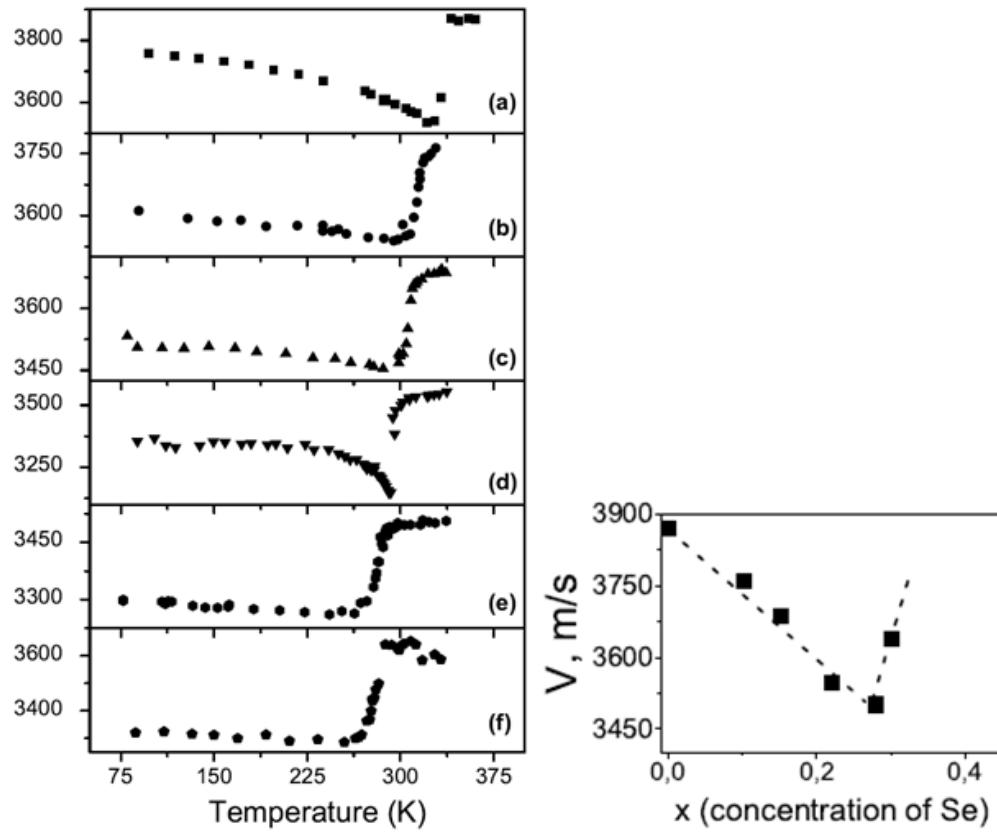
Fig. 3.13. Hypersound velocity data of $Sn_2P_2(S_{1-x}Se_x)_6$ obtained by Brillouin scattering. (a) $-$ x=0, (b) $-$ x=0.10, (c) $-$ x=0.15, (d) $-$ x=0.22, (e) $-$ x=0.28, (f) $-$ x=0.30. The inset illustrates the concentration behavior of hypersound velocity in a paraelectric phase [101].
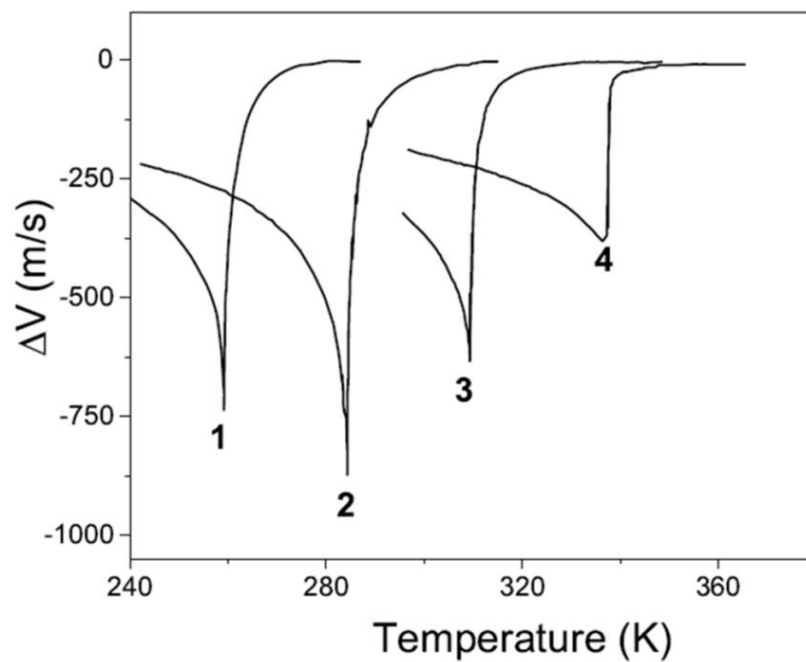
Fig. 3.14. Temperature variation of longitudinal ultrasound velocity at the ferroelectric phase transition of $Sn_2P_2(S_{1-x}Se_x)_6$ solid solutions. 1 $-$ x=0.40, 2 $-$ x=0.28, 3 $-$ x=0.15, 4 $-$ x=0 [103].

To precisely "localize" the LP on the T−x state diagram we refer to high resolution dielectric data [101] which have been performed at slow cooling run for the tin-sulfur/selenium compounds. From the temperature anomalies of reciprocal dielectric susceptibility, the transitions at $T_i(x)$ and $T_c(x)$ are separately seen for x=0.40 indicating the presence of a true IC phase with temperature width of about 0.6K (fig. 3.15 c). In the case of a crystal with x=0.28 the intermediate state is still observed between the paraelectric and the ferroelectric phases. It gives a hint that the position of LP in Sn$_2$P$_2$(S$_{1-x}$Se$_x$)$_6$ mixed crystals should be placed somewhere between $0.22 < x < 0.28$. The IC state is observed in an interval of about 0.2K at a cooling speed of 5mK/min, while at a higher rate 100mK/min the kink in the dielectric susceptibility at T_c is completely smeared and the curve is being similar to the one at Se concentration of x=0.22. Such a smearing is related to the domain wall concentration in the ferroelectric state whose size increases at higher cooling rates. This effect can be explained within the theory of Kibble-Zurek model, where in the case of the uniaxial ferroelectrics the domain walls in a sample could be considered as scalar topological defects [102, 103]. As was estimated by authors in [101], at a cooling rate of 0.1K/min, the biggest value of domain size is about 50nm, which is comparable to the modulation wavelength in the vicinity of LP. However, further high resolution investigations on LP would be desirable and helpful in the discussion of the phenomena which take place at such critical point.
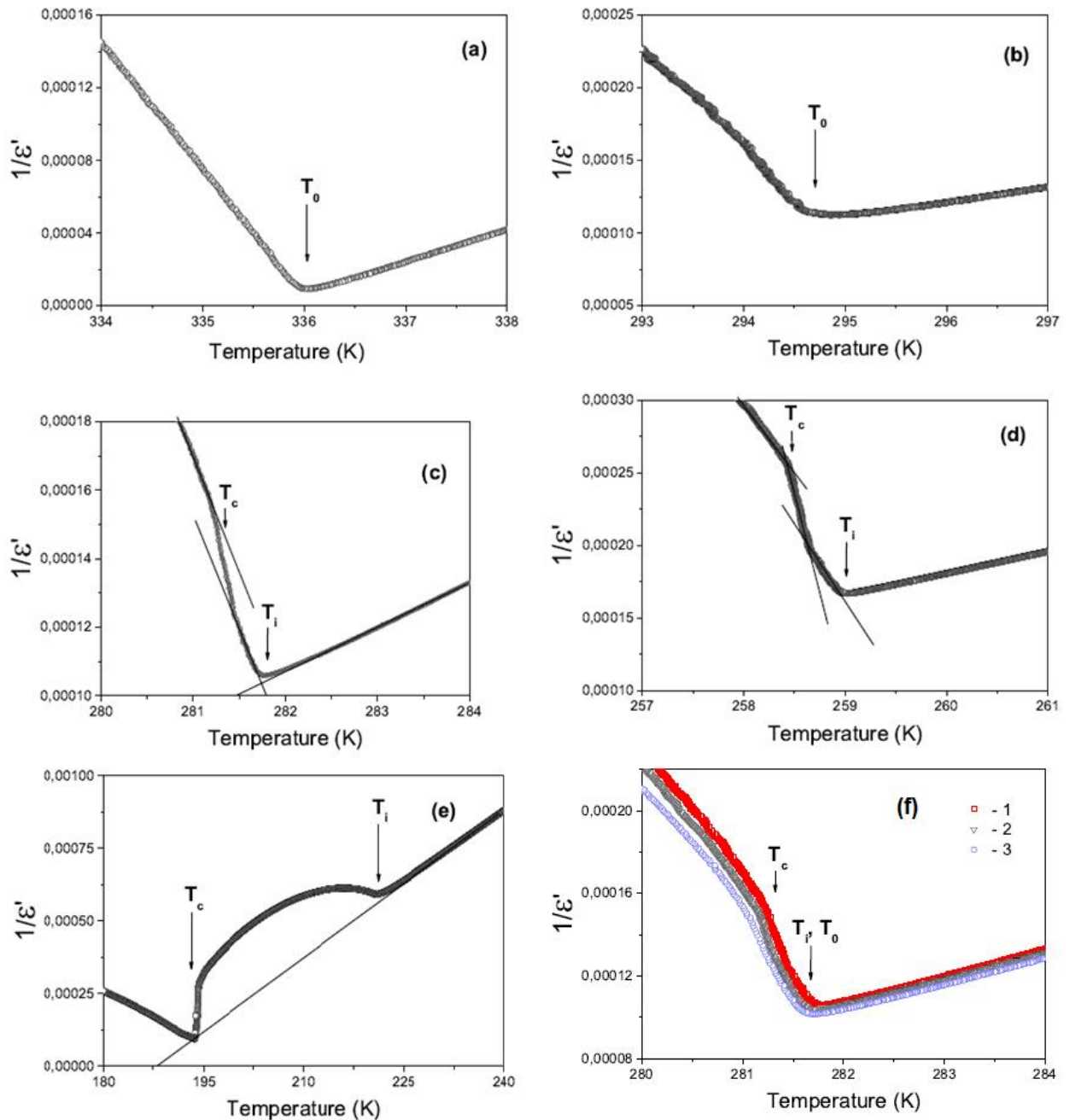
Fig. 3.15. Reciprocal dielectric susceptibility for $Sn_2P_2(S_{1-x}Se_x)_6$ ferroelectrics performed at 5mK/min in a cooling regime. (a) − $x=0$; (b) − $x=0.22$; (c) − $x=0.28$; (d) − $x=0.40$; (e) − $x=1$; (f) − $x=0.28$ at different rates: 0.005K/min (red), 0.05K/min (grey), 0.1K/min (blue) [101].

3.2.3. Phase transitions diagram of $(Sn_{1-y}Pb_y)_2P_2S_6$ crystals

This phase diagram has been first characterized by dielectric measurements performed at low frequencies [82, 106, 109]. The transition temperatures according to those data are plotted on fig. 3.16. With an increase of Pb content in this series the PT temperatures decrease almost linearly from $y=0$ to $y=0.27$. Approximately from $y=0.30$,

the line bends showing an upward curvature and achieves 4.2K at concentrations *y*=0.61 and *y*=0.66. This discrepancy corresponds to the fluctuations in concentrations of a particular sample. The temperature lowering is caused by the weakening of the average bond stiffness in a crystal lattice, when Sn ions are substituted by Pb, as was suggested in reference [108].
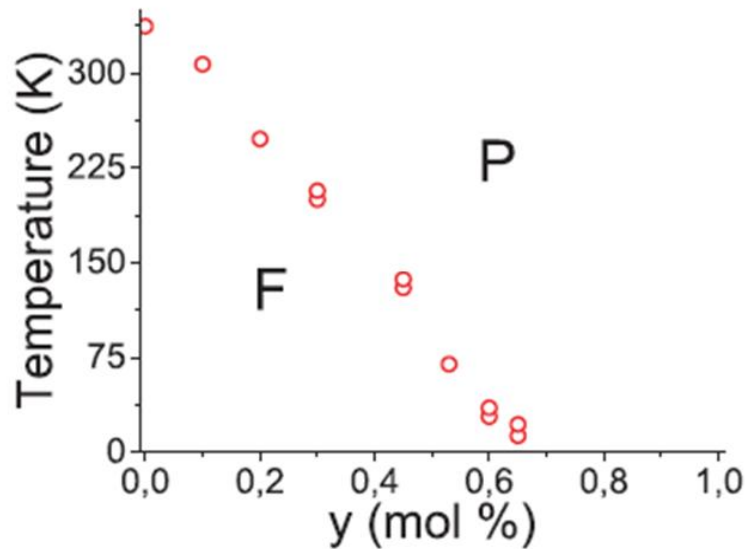
Fig. 3.16. Phase transitions temperatures of (Sn$_{1-y}$Pb$_y$)$_2$P$_2$S$_6$ crystals as a function of the lead concentration; F – ferroelectric phase, P – paraelectric phase [107].

Till recent time the transitions from the high symmetry phase to a low symmetry one in these compounds were suggested to be of a second order type in the range 0<*y*<0.66. In publications [107, 108] the authors have presented low-frequency dielectric, ultrasound, and hypersound studies performed for (Sn$_{1-y}$Pb$_y$)$_2$P$_2$S$_6$ ferroelectric family assessing that the temperature-concentration phase diagram is not so "simple" for these compounds. They showed that TCP could be reached at *y*>0.2 and that some phase coexistence takes place there. According to the dielectric data, for a Pb content of *y*=0.2 the transition "para-ferro" phase which occurs at T≈248K changes its character from second to first order. That can be seen from the changes of real and imaginary parts of dielectric susceptibility anomalies (fig. 3.17, 3.18).
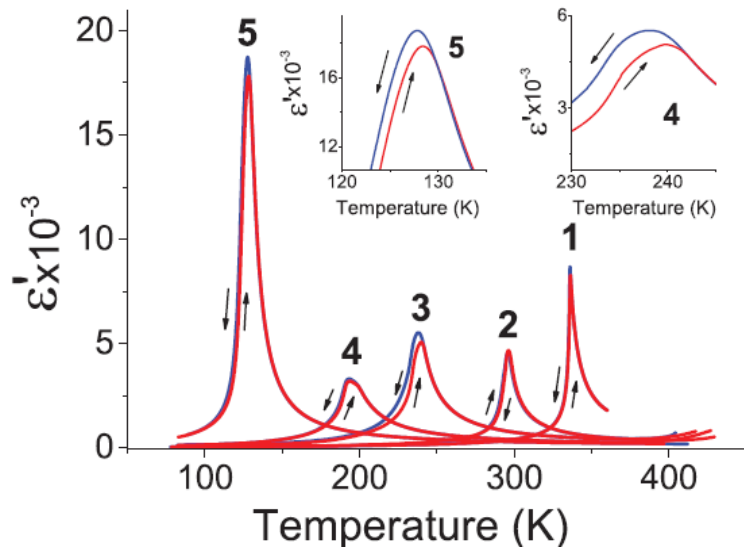
Fig. 3.17. Real part of dielectric susceptibility at 100kHz on heating (red curves) and cooling (blue curves) runs for $(Sn_{1-y}Pb_y)_2P_2S_6$ ferroelectrics: (1) – y=0; (2) – y=0.1; (3) – y=0.2; (4) – y=0.3; (5) – y=0.45. Inset demonstrates the temperature hysteresis for y=0.3 and y=0.45 [107].
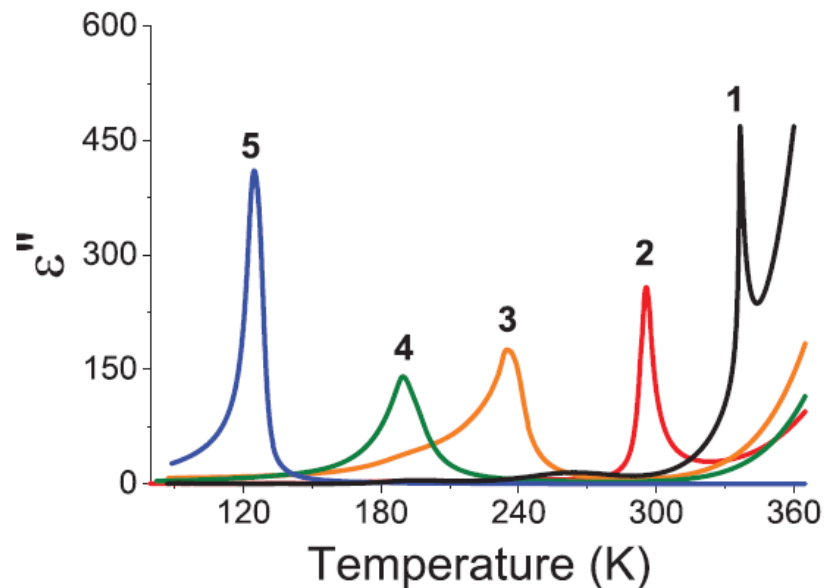
Fig. 3.18. Imaginary part of dielectric susceptibility at 100kHz in cooling runs for $(Sn_{1-y}Pb_y)_2P_2S_6$ ferroelectrics: 1 – y=0; 2 – y=0.1; 3 – y=0.2; 4 – y=0.3; 5 – y=0.45 [107].

As was shown by the authors in ref. [107], for the lead concentration y=0.3, the real and imaginary parts of dielectric susceptibility become broader and with a clearer presence of temperature hysteresis with respect to the anomaly at y=0.2. Moreover, they have shown that for y=0.45 the dielectric losses have the highest value (fig.3.17) and the shape of curve is also different in heating or cooling runs (see the inset on fig.3.17). Such features could usually be expected at a first-order transition.

The reciprocal dielectric susceptibility data for the extreme compounds y=0 demonstrates that the ratio of slopes ferroelectric/paraelectric phases has a value about 4, which confirms it closeness to tricriticality [107]. In the case of mixed compounds the slopes are similar and cannot be explained simply by a continuous phase transition [107].
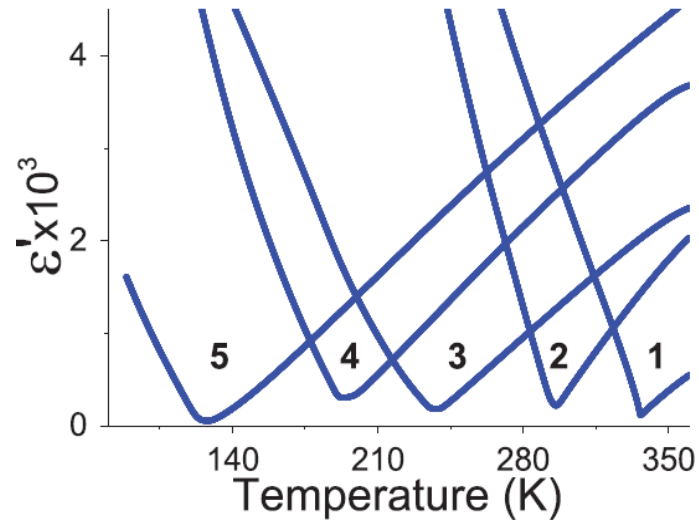
Fig. 3.19. The reciprocal real part of dielectric susceptibility at 100kHz on cooling runs for (Sn$_{1-y}$Pb$_y$)$_2$P$_2$S$_6$ ferroelectrics: 1 – y=0; 2 – y=0.1; 3 – y=0.2; 4 – y=0.3; 5 – y=0.45 [107].

The temperature dependencies of ultrasound velocity data [107] demonstrate that for the sample with y=0.3 the shape of the anomaly is altered, there is an additional contribution on the step of sound velocity (fig.3.20). Such singularities could be explained as follows: a first-order transition is already occuring for y=0.3 and phase coexistence produces those changes and makes the anomaly more complex in shape.
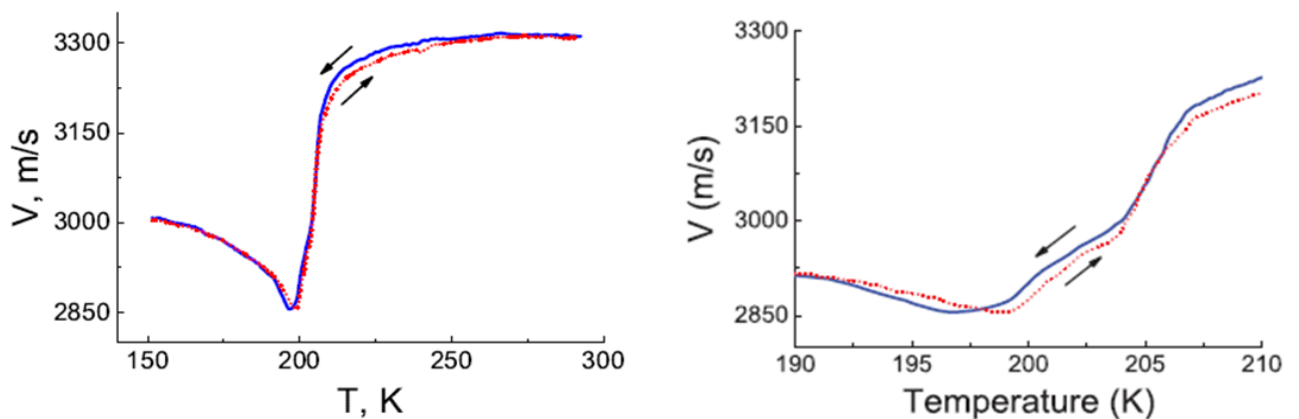
Fig. 3.20. Ultrasound velocity data at cooling (blue) and (heating) runs performed for (Sn$_{0.7}$Pb$_{0.3}$)$_2$P$_2$S$_6$ [107].

In the case of $(Sn_{0.55}Pb_{0.45})_2P_2S_6$, the ultrasound velocity and the attenuation exhibit a huge hysteresis at cooling and heating runs (fig.3.21) that could also be related to the first-order character of transition.
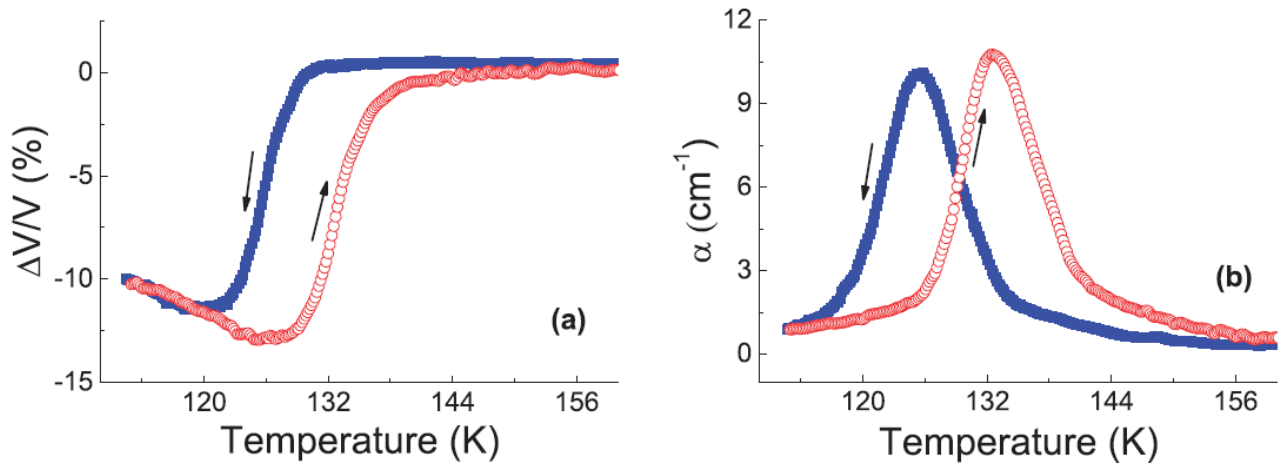
Fig. 3.21. Ultrasound velocity (a) and attenuation (d) for $(Sn_{0.55}Pb_{0.45})_2P_2S_6$ ferroelectric performed at cooling (blue) and heating (red) runs [107].

Finally, we consider the hypersound velocity data [107] and their analysis in terms of the mean field model using the Landau-Khalatnikov approximation (fig.3.22). Phenomenological parameters obtained from this model could also give a hint about the order of transition (see chapter IV for a description of the Landau theory). As seen from the graph below, the coefficients β and γ, indeed, are reduced with the increase of Pb concentration in $(Sn_{1-y}Pb_y)_2P_2S_6$ series. Such trend was also observed for $Sn_2P_2S_6$ (fig.3.15 b) and confirms that the phase transition in $(Sn_{1-y}Pb_y)_2P_2S_6$ can also change its character (β is negative for a first order one). But as the values of β are positive at least till lead content y=0.45, the second order character of the para-ferroelectric transition in the concentration range from y=0 to y=0.45 is confirmed. Probably, TCP could be achieved for $(Sn_{1-y}Pb_y)_2P_2S_6$ series applying an external pressure as has been demonstrated in a previous section for $Sn_2P_2S_6$. Nevertheless, observed trend of possible existence TCPs on the tin/lead-sulfur temperature-concentration phase diagram is of particular interest, and it deserves to be studied in more detail.
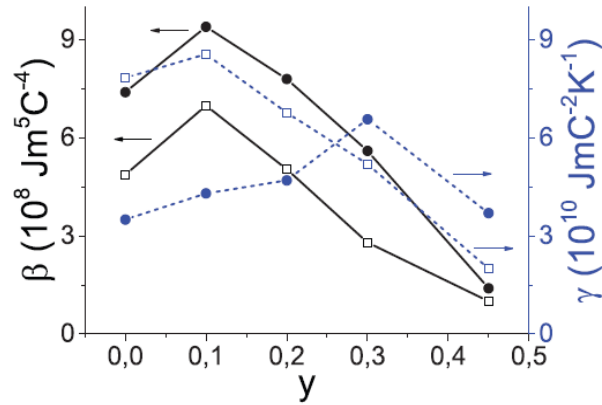
Fig. 3.22. Concentration dependencies of coefficients β and γ in Landau thermodynamic potential. Solid symbols represent hypersound data analysis, open symbols – ultrasound. [107].

3.2.4. Phase transitions diagram of the $(Sn_{1-y}Pb_y)_2P_2Se_6$ crystals.

Phase transition temperatures of $(Sn_{1-y}Pb_y)_2P_2Se_6$ ferroelectric series (fig.3.23) have been obtained by means of heat capacity [110], light transmition and dielectric measurements [94, 111].
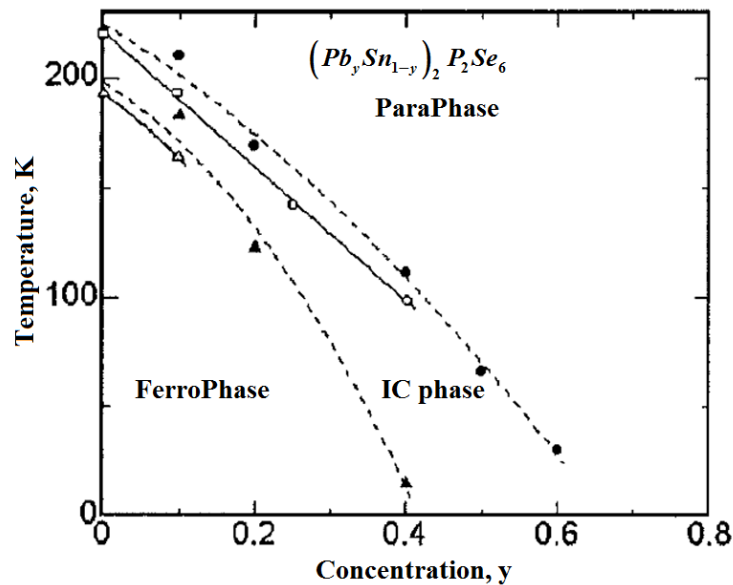
Fig. 3.23. Phase transitions temperatures as a function of lead concentration. Solid symbols represent high-temperature Paraelectric-IC phase transitions (second order) and empty symbols the lock-in IC-ferroelectric phase transitions , which are first order. Circles correspond to data [110] and triangles to [94].

According to the light transmition study [94] substitution Sn by Pb in $(Sn_{1-y}Pb_y)_2P_2Se_6$ series increases the width of IC phase from 28K at y=0 to 65K at y=0.3. Side by side with this increase, the temperature hysteresis of the first-order transition is also increased. For y=0 this hysteresis is 1K and for y=0.3 it is about 12K.

$(Sn_{0.6}Pb_{0.4})_2P_2Se_6$ crystal exhibits maximal width of the IC phase. It occurs in a range exceeding 110K. The second order transition in this case is seen as a smooth change in the slope of the temperature behavior of light transmition coefficient while the first-order one corresponds to an abrupt jump with the presence of hysteresis [94].

As seen from fig.3.23, with increasing Pb content the transitions are shifted to lower temperature. Such a decrease can be interpret as follows: the ionic radius of lead ions is bigger than for tin ions, hence, the addition of Pb increases the space available for Sn in $(Sn_{1-y}Pb_y)_2P_2Se_6$ series. As a result, the motion of the Sn becomes easier and ions can move with smaller thermal energy which leads to the lowering of the phase transition temperatures [110].

Additionally to the lowering of T_i and T_c a smear of the anomalies in physical properties was observed. Low temperature dielectric study performed in [112] exhibits a smear of dielectric permittivity with an increase of Pb fraction. This well correlates with the concentration behavior of light transmition coefficient at T_i in this ferroelectric family [94]. It was also found that thermal hysteresis occurs only for concentration of lead below y=0.45 (fig. 3.24) [112].
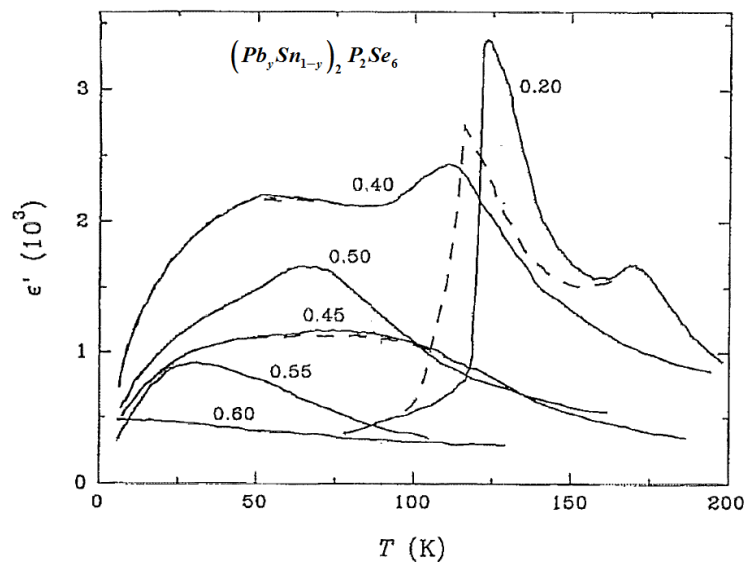
Fig. 3.24. Temperature dependence of the real part of dielectric permittivity for $(Sn_{1-y}Pb_y)_2P_2Se_6$ mixed ferroelectrics with different Pb content. Dashed line – cooling, solid line – heating [112].

The particular interest of this family is caused by the existence of a wide modulated incommensurate phase which gives the possibility to study some rare

phenomena, such as the freezing of the incommensurate modulation dynamics [113] or the glassy behavior of dielectric constant at ultralow temperatures (below 1K) [114], when Sn ions are replaced by Pb in the cation sublattice.

3.2.5. Multicritical points on the (T, p, x, y) phase diagrams of $(Sn_{1-y}Pb_y)_2P_2(S_{1-x}Se_x)_6$

a) Tricritical point TCP in $Sn_2P_2S_6$ crystal

So far we have considered the phase diagram of $(Sn_{1-y}Pb_y)_2P_2(S_{1-x}Se_x)_6$ mixed ferroelectrics using concentration (x or y) as a variable, which is quite complex, as there are three different phases bounded by first and second order phase transition lines as well as a LP. However, if we add pressure p to our variable list or a possibility to simultaneously change x and y in the general formula $(Sn_{1-y}Pb_y)_2P_2(S_{1-x}Se_x)_6$ the picture becomes even more complicated and interesting. Let's start our discussion with the undoped $Sn_2P_2S_6$. As known, this crystal is a uniaxial ferroelectric with a three-well local potential for spontaneous polarization fluctuations [115]. The Hamiltonian of such system could be well described within the frame of the Blue-Emery-Griffiths (BEG) model, where pseudospins can have three different values 0, +1 and −1 [116]. The interesting aspect is that this model predicts the appearance of a tricritical point (TCP) on the phase diagram. TCP is one of the special points on the phase diagram at which the second-order transitions line transforms into a line with transitions of first-order type. Such high order critical point can be realized as the transition temperature decreases in the $(Sn_{1-y}Pb_y)_2P_2(S_{1-x}Se_x)_6$ system from the value that it has for $Sn_2P_2S_6$ [107]. For these ferroelectric crystals the TCP can be achieved by changing x and y, which, in its turn, makes it possible the appearance of the random bonds or random field defects in the anion or cation sublattices. Such defects will heavily alter the phase diagram predicted by the BEG model. Besides, the transition temperature lowering can also be produced by applying an external pressure [107].

There are several studies published in literature which have been devoted to a search of a high order critical point in pure $Sn_2P_2S_6$ measuring different physical quantities under an external pressure [117, 118 119, 120, 105, 121, 122]. There is now

agreement that the continuous paraelectric to ferroelectric phase transition changes its character to first-order at about $T \approx 250K$ and $p \approx 0.4GPa$ [107, 121]. Along the years, there has been some discussion about the type of the critical point, whether it is a LP or a TCP. Neutron diffraction measurements settled down this matter, with the conclusion that this critical point is a simple TCP [120]. The same result was confirmed by means of ultrasound velocity (fig. 3.25) [105] and birefringence [121]. Lastly, high-resolution X-ray diffraction measurements performed under pressure up to 1GPa [122] shown a lack of the incommensurate phase closing all the peculiarities about the type of a critical point, which takes place on the (T, p) diagram of $Sn_2P_2S_6$. That point is a TCP but not a LP.
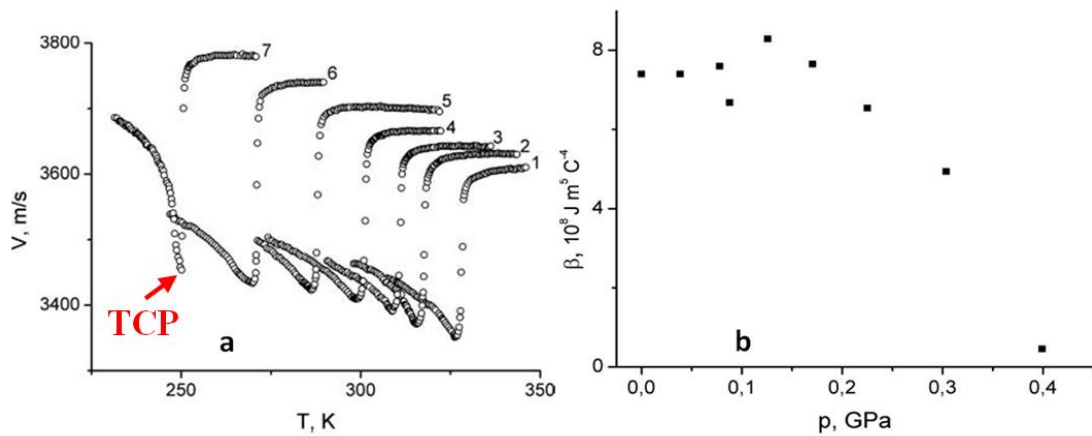
Fig. 3.25. (a) Ultrasound velocity data for $Sn_2P_2S_6$ at different pressures. 1: 0.039GPa; 2: 0.088GPa; 3: 0.126GPa; 4: 0.171GPa; 5: 0.225GPa; 6: 0.304GPa; 7: 0.399GPa; (b) Pressure dependence of the phenomenological coefficient β in the Landau expansion (see chapter 4) for the same crystal [105].

The physical mechanism, which stays behind this phenomenon can be described as follows: for the undoped $Sn_2P_2S_6$ the Sn^{2+} cations stereoactivity decreases when the external pressure is applied (fig.3.25). This effect reduces the depth of the side wells of the local three-well potential. Bear in mind that the intercell interaction remains almost unchanged. Due to the local potential surface flattening the second order phase transition temperature is lowered and shifted to the TCP [107].

b) Tricritical Lifshitz point TCLP in Sn(Pb)₂P₂S(Se)₆ mixed compounds

Since the question about the existence of a TCP in $Sn_2P_2S_6$ crystal has been settled, the researchers have turned their attention to another intriguing problem. Is it

possible to find any other multicritical points on the (T, p, x, y) state diagram of $(Sn_{1-y}Pb_y)_2P_2(S_{1-x}Se_x)_6$ ferroelectric family? A very important question is how the isovalent atom substitution of Sn by Pb in the cation sublattice and the replacement of S by Se in the anion one affects the stereoactivity of these mixed compounds. If Se atoms take the place of S ones, then the covalence of the chemical bounds increases and the intercell interaction becomes weaker. At a basically similar form of the thee-well local potential the temperature of the phase transition is lowered [107]. On the other hand, if Pb atoms, which are less stereoactive and have also a larger ionic radius, substitute the Sn ones, then the total ionicity of the Sn-S bounds increases. In this case the intercell interaction becomes stronger. Both effects lead to the decrease of the phase transition [107].

At the substitution of S by Se the random field effects can appear. Nevertheless, their influence does not play a significant role, because they do not provoke any smearing in the critical anomaly [see for example fig. 3.10]. To properly describe this case the above mentioned BEG model has to be accompanied with the well known ANNNI (axial-next-nearest-neighbor Ising) model [107]. Such model combination predicts the possible existence of a TCP and also an intermediate incommensurate phase existence on the state diagram of $Sn_2P_2(S_{1-x}Se_x)_6$ at $x > x_{LP}$ [107, 3]. On the contrary, the introduction of Pb in the cation sublattice heavily alters the total electronic orbitals hybridization, which provokes the appearance of strong random-field defects. To describe such a complicated case a diluted BEG [123] model has to be considered.

Several interesting papers have been devoted to check the theoretical predictions mentioned above in order to search for a tricritical Lifshitz point TCLP along the (T, p, x, y) state diagram of the ferroelectrics studied [104, 117, 124]. For the solid solutions $Sn_2P_2(S_{1-x}Se_x)_6$ the virtual TCLP (placed inside of the incommensurate phase) has been suggested to be found at $x \approx 0.6$, $y=0$ and $T \approx 240K$ [117, 124, 3]. Moreover, the authors in [104] have theoretically estimated the appearance of a TCLP on the phase diagram of $(Sn_{1-y}Pb_y)_2P_2(S_{1-x}Se_x)_6$ at $x = 0$; $y = 0.12$; $p \approx 0.28GPa$ and $T \approx 225K$ (fig.3.26). One important conclusion which can be emphasized from this analysis is that the baric thermodynamic trajectory of the pure $Sn_2P_2S_6$ passes close to the Tricritical point.
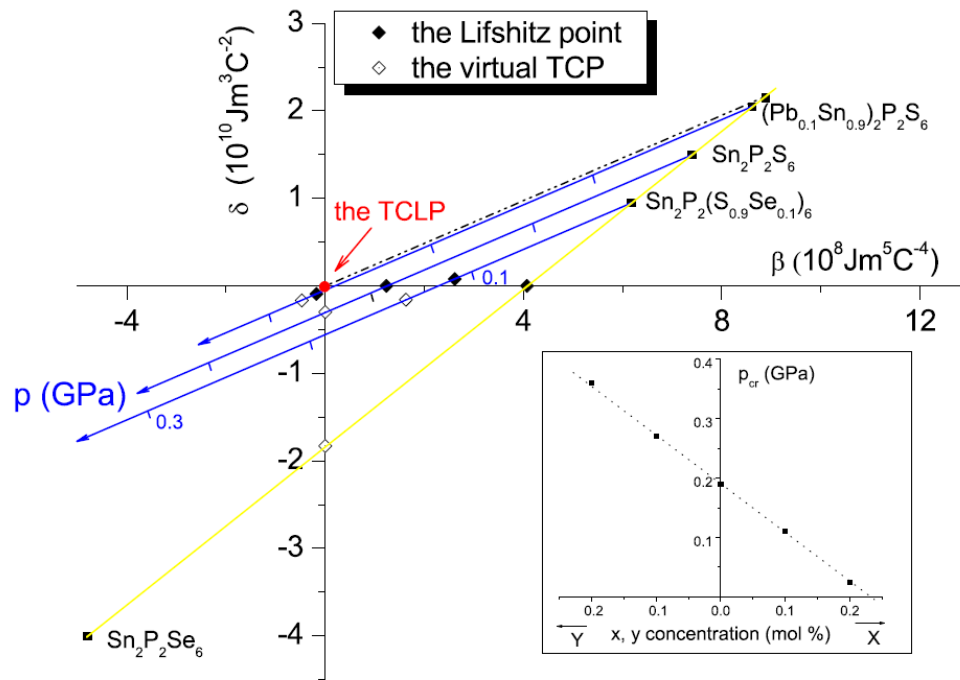
Fig. 3.26. Theoretical prediction of the tricritical Lifshitz point location for $(Sn_{1-y}Pb_y)_2P_2(S_{1-x}Se_x)_6$ mixed ferroelectric crystals [104].

Unfortunately, this high order critical point has not been experimentally proven yet. Thus, we are in situation where we have more questions than answers. Further experimental investigations are needed to better understand the physical background related to this matter.

3.3. Thermal properties of Sn(Pb)₂P₂S(Se)₆ ferroelectrics

3.3.1. Specific heat. The temperature dependence of specific heat c_p for $Sn_2P_2S_6$ exhibits a λ–shape anomaly at about 337K, signaling the presence of a second order transition from a high symmetry state to a low symmetry one. With increasing Pb content the anomaly shifts to lower temperatures. At the same time its shape becomes more smeared and less sharp (fig. 3. 27 a). In case of $Sn_2P_2Se_6$ Pb replacing also alters the shape of the anomalies at first and second order transitions in the same manner as for $Sn_2P_2S_6$ (fig. 3.27 b). One can note that the temperature range of IC phase is enlarged.
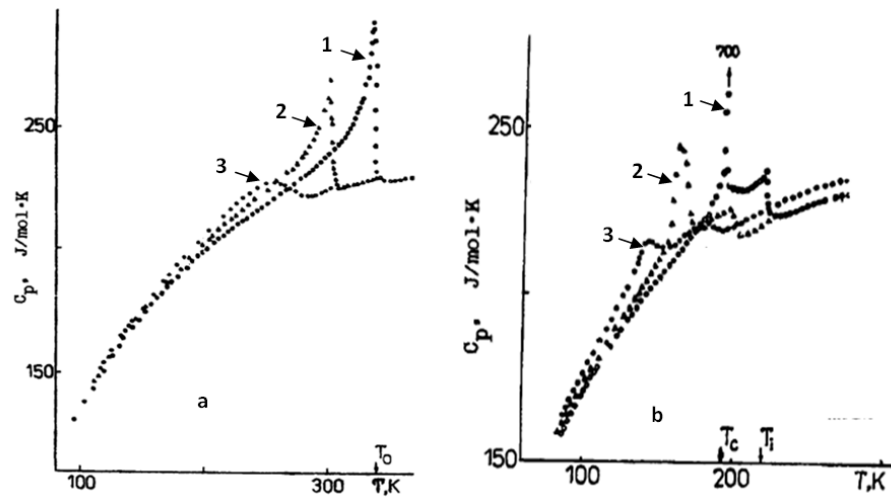
Fig. 3.27. Heat capacity data for $(Sn_{1-y}Pb_y)_2P_2S_6$ and $(Sn_{1-y}Pb_y)_2P_2Se_6$ ferroelectrics with: (a) 1 – y=0.0, 2 – y=0.1, 3 – y=0.2 and (b) 1 – y=0.0, 2 – y=0.1, 3 – y=0.2 [125].

Specific heat has been also measured by others authors [100, 110] in a wide temperature range for $Sn_2P_2S_6$, $Sn_2P_2Se_6$ and $Pb_2P_2Se_6$; those results are depicted on fig. 3.28.
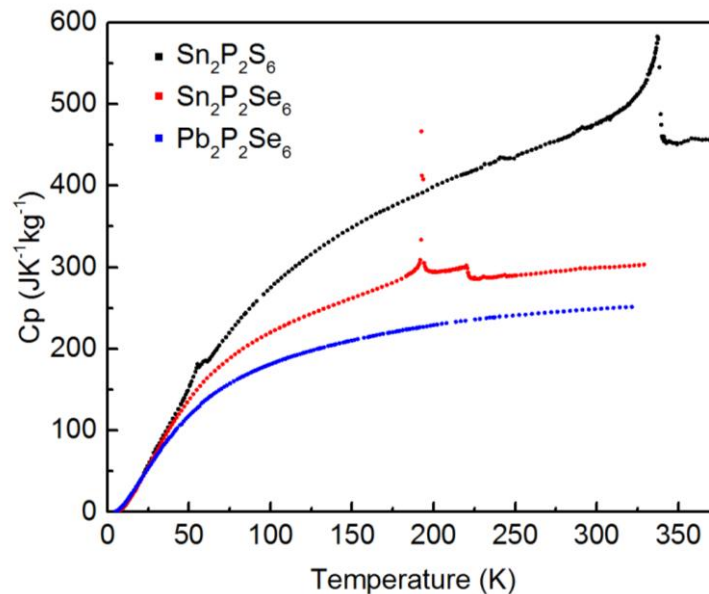
Fig. 3.28. Specific heat data of $Sn_2P_2S_6$, $Sn_2P_2Se_6$ and $Pb_2P_2Se_6$ crystals according to the data in [100, 110].

3.3.2. Thermal diffusivity. Some studies have been performed prior to this work on the thermal diffusivity of $Sn_2P_2(S_{1-x}Se_x)_6$ [60, 95] using ac photopyroelectric calorimetry, specially focusing on the critical behavior of the phase transitions; that's why the regions close to the critical temperatures have been mainly studied and not in

the full temperature range. The results are displayed on fig.3.29. As it can be seen, the phase transitions are shown as dips superimposed on the monotonous background of the thermal diffusivity curve and are in general agreement with the phase diagrams suggested by other techniques, including their first or second order character. As it was mentioned in the first section of the chapter, this type of crystal possesses a monoclinic structure, thus is expected to observe an anisotropic behavior in thermal diffusivity. This was confirmed for Sn$_2$P$_2$S$_6$, where it turned out that heat is more easily transmitted along the [100] direction (fig.3.29 a), in the vicinity of the transition. A full account of the conclusions of the critical behavior studies performed in references [60, 95] is presented in chapter 4, section 4.
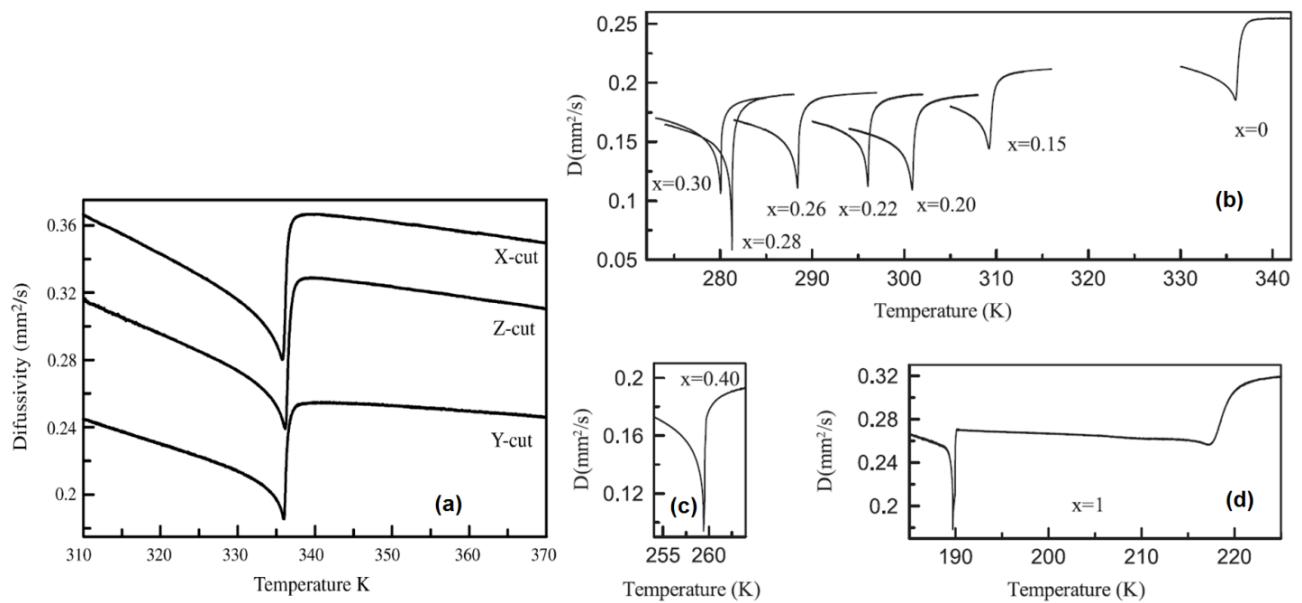
Fig.3.29. Temperature evolution of thermal diffusivity for Sn$_2$P$_2$S$_6$ crystal in different crystallographic directions (a), and for Sn$_2$P$_2$(S$_{1-x}$Se$_x$)$_6$in [010] direction (b, c, d) [60, 95].

3.3.3. Thermal expansion.

Another important property, which provides information on the accuracy of harmonic approximation for the description of atomic vibrations in a medium, is *the thermal expansion coefficient $\alpha_V(T)$*. This thermodynamic quantity for Sn(Pb)$_2$P$_2$S(Se)$_6$ ferroelectrics has been observed by dilatometric measurements [91, 128]. The temperature dependencies of $\alpha_V(T)$. for Sn$_2$P$_2$S$_6$, Sn$_2$P$_2$Se$_6$ and Pb$_2$P$_2$Se$_6$ crystals are shown on fig. 3.30. For the two tin-based compounds the dips

are signaling the PT presence, while in the case of Pb$_2$P$_2$Se$_6$ no anomaly was found; only a slight reduction with temperature was observed.
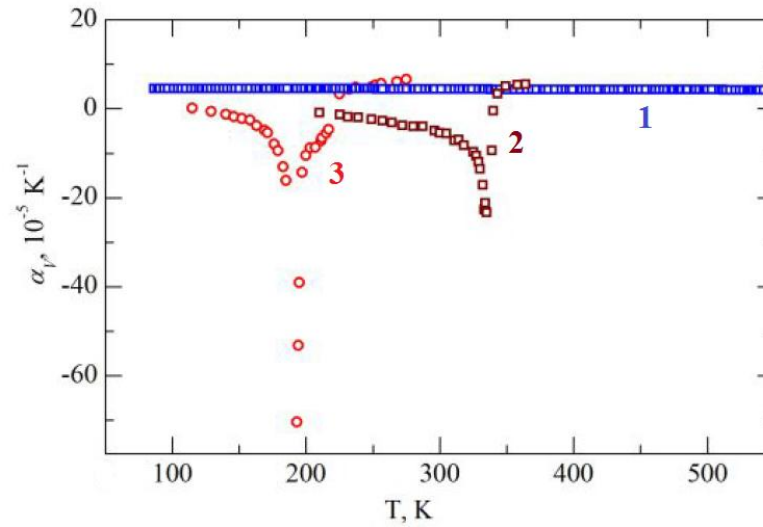
Fig. 3.30. Temperature behavior of the volume thermal expansion coefficient: (1) − Pb$_2$P$_2$Se$_6$ (2) − Sn$_2$P$_2$S$_6$ (3) − Sn$_2$P$_2$Se$_6$ [129].

3.3.4. Thermal conductivity is of great importance when we deal with the description of lattice dynamics. Heat conduction coefficient for Sn(Pb)$_2$P$_2$S(Se)$_6$ ferroelectric family has been measured using stationary longitudinal heat flux method by K. Al'-shoufi, Rizak *et.al* [127, 130, 117]. The results performed for different crystallographic directions [100], [010] and [001] are presented on fig. 3.31 *a*, *b*. A similar general temperature behavior was found with the presence of a maximum at about 11K for all three directions. It should be pointed out that the values at the maximum strongly differ indicating the anisotropy of this thermodynamic property. The lowest value is observed is along the x-direction while the highest one is along z-axis. The small value obtained at room temperature tells us that these materials are poor thermal conductors.

Theoretical analysis performed for these results demonstrates that thermal conductivity of Sn$_2$P$_2$S$_6$ crystal obeys Eiken's law $\lambda \sim T^{-1}$ in the temperature range 12<T<200K. At temperatures above 200K λ is weakly dependent on T. For the other three extreme compounds (Sn$_2$P$_2$Se$_6$, Pb$_2$P$_2$Se, Pb$_2$P$_2$Se$_6$) the Eiken's behavior has been confirmed in the interval 100-190K. Again above 200K, thermal conductivity becomes almost independent of T and deviates from the theoretically predicted evolution [127].

Such behavior and the low conductivity values of Sn$_2$P$_2$S$_6$-like crystals can be explained by a reduction of the phonon mean-free path till the lattice period dimensions at double of the Debye temperature θ_D (Sn$_2$P$_2$S$_6 \approx 83$K, Sn$_2$P$_2$Se$_6 \approx 74$K, Pb$_2$P$_2$S$_6 \approx 85$K, Pb$_2$P$_2$Se$_6$ ≈ 55K [3, 129]).

For Sn(Pb)$_2$P$_2$S(Se)$_6$-like ferroelectrics, thermal conductivity does not exhibit significant singularities across the phase transition temperature as thermal diffusivity or specific heat do. The observed behavior is a step-like behavior [3] or just only a monotonous variation with temperature as has been found in publication [95] (see fig. 3.32).
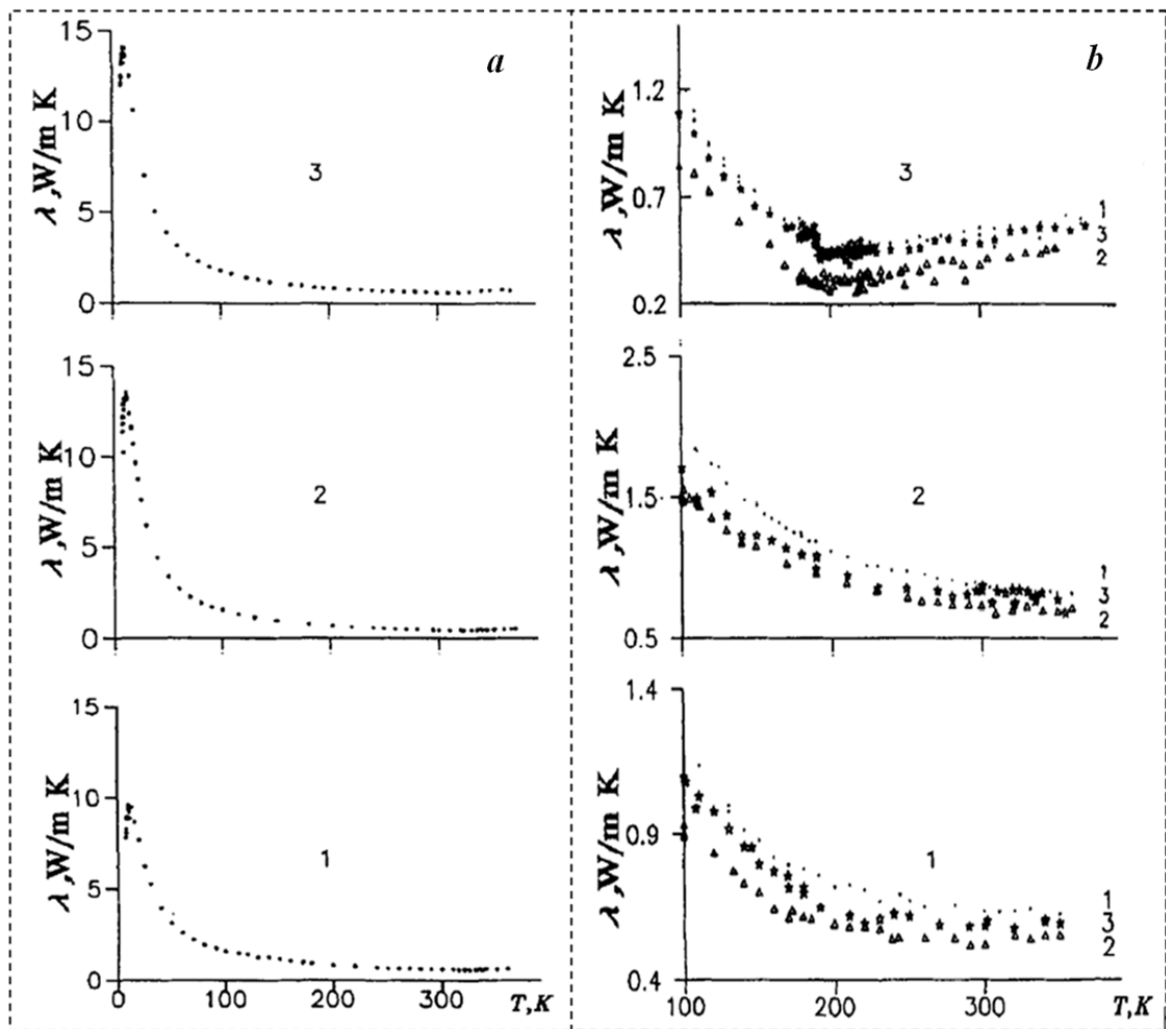
Fig. 3.31. (a) − thermal conduction coefficient for Sn$_2$P$_2$S$_6$: 1 − [100], 2 − [010], 3 − [001]. (b) − thermal conductivity for Pb$_2$P$_2$Se$_6$ (1), Pb$_2$P$_2$S$_6$ (2) and Sn$_2$P$_2$Se$_6$ (3) along crystallographic directions: 1 − [100], 2 − [010], 3 − [001] [128].
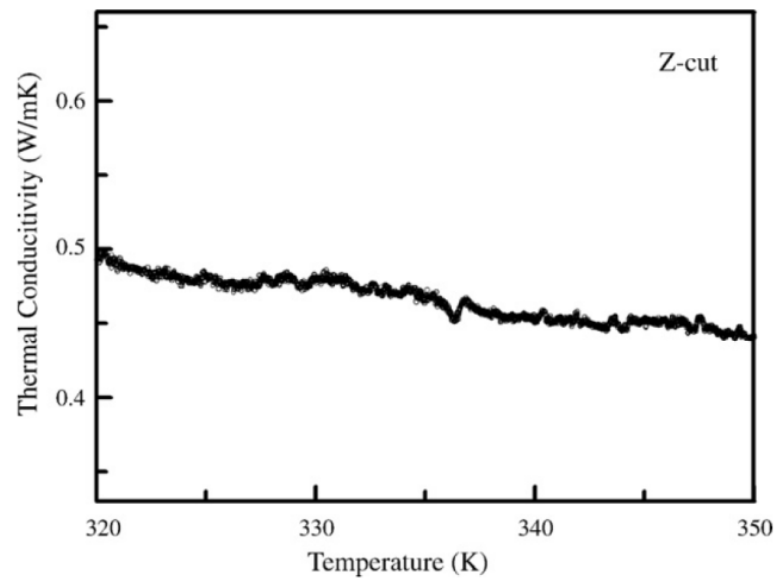
Fig. 3.32. Thermal conductivity of $Sn_2P_2S_6$ crystal in [001] direction [95].

CHAPTER 4

Phase transitions and critical behavior

A complete development of the theory of phase transitions, even if we circumscribe it to the particular case of ferroelectrics, is outside the scope of this PhD Thesis. There are a good number of books, scientific papers, and excellent review papers which deal with this subject written by authorities in this subject [131-150]. Thus, in this chapter we are going to concentrate on the description of the most important elements from the theory which will be used in the following chapters when interpreting and discussing the phase transitions experimentally measured, specially trying to emphasize the applicability of the different models which can be found in literature. This means that we will be concentrating on that part of the theory or on those models which are pertinent when studying the family of ferroelectrics $(Pb,Sn)_2P_2(S,Se)_6$.

4.1. Classical Theory of Phase Transitions for ferroelectric transitions

Landau was the first to introduce the concept of order parameter to describe phase transitions. The order parameter is a magnitude which will be zero above the critical temperature (the one at which the phase transition takes place) and different from zero below: polarization, for instance, in a ferroelectric transition. In a second order/continuous phase transition, the order parameter will change in a continuous way. In these transitions, as opposed to the first order ones, there will be no latent heat and no hysteresis in the variation of the physical variables. Landau proposed to write the thermodynamic potential density with a Taylor expansion series as a function of the order parameter. Taking into account general requirements for stability of phases and state of coexistence of phases, as well as certain symmetry criteria, he proposed the following general form valid for second order phase transitions

$$F = F_0 + \frac{\alpha(T-T_C)}{2}P^2 + \frac{\beta}{4}P^4 + \frac{\gamma}{6}P^6 + \frac{\delta}{2}\left(\vec{\nabla}P\right)^2 + ..., \tag{4.1}$$

where F_0 is the value in the paraelectric phase, α is related to the Curie-Weiss constant, T_C is the transition temperature (critical temperature), β, γ and δ are phenomenological

coefficients which don't depend on temperature and are positive (if β is negative this will indicate a first order phase transition). Some particular values of certain phenomenological coefficients will involve particular phase transitions. For a tricritical point (where three-phase coexistence terminates) $\alpha = 0$ and $\beta = 0$, while for a Lifshitz point $\alpha = 0$ and $\delta = 0$. In ferroelectrics, a Lifshitz point separates two regions in the phase diagram: one with a direct second order phase transition from the paraelectric to the ferroelectric phase and another one in which there is a second order phase transition from the paraelectric phase to an incommensurate one at T_i and then a first order phase transition from the incommensurate phase to the ferroelectric phase at T_C. Eq (4.1) assumes that the phase transition can be described by a one-component order parameter, for simplicity.

The theory also contemplates the possibility of the coupling of the order parameter to some other variables, such as strain, which is useful in the case of uniaxial ferroelectrics, such as [151]

$$F = F_0 + \frac{\alpha(T - T_C)}{2}P^2 + \frac{\beta}{4}P^4 + \frac{\gamma}{6}P^6 + \frac{1}{2}cu^2 + ruP^2, \tag{4.2}$$

where $c=c_{ijkl}$ is the elastic module matrix, $u= u_{ij}$ is the deformation tensor, $r=r_{ijkl}$ is the electrostriction coefficient, and elements of higher order are neglected. This is a short version of the Landau-Khalatnikov potential which includes even more terms [152, 153].

In order to obtain a measurable quantity such as specific heat, the free energy must be minimized with respect to the order parameters (in the first case, polarization P; in the latter, both polarization P and strain u), in order to obtain the equilibrium value of the order parameter in the ferroelectric phase, so that we can obtain for the isobaric heat capacity in the ferroelectric phase

$$C_p = -T\left(\frac{\partial^2 F}{\partial T^2}\right)_P, \tag{4.3}$$

which, applied to eq (4.2), will give

$$C_p = -T\left(\frac{\partial^2 F}{\partial T^2}\right)_P = C_p^0 + \frac{\alpha^2}{2\beta'}\frac{T}{\sqrt{1-4At}}, \tag{4.4 a}$$

where C_p^0 is the heat capacity in the paraelectric phase,

$$\beta' = \beta - \frac{2r}{c^2},$$ (4.4 b)

$$A = \frac{\gamma\alpha}{\beta'^2}$$ (4.4 c)

Thus, the anomalous part of the heat capacity can be expressed as

$$\Delta C_p = \frac{\alpha^2}{2\beta'}\frac{T}{\sqrt{1-4At}}.$$ (4.5)

The comparison of the experimental specific heat anomaly to this last equation by a Lavenberg-Marquardt method, for instance, will allow us to check the appropriateness of the theory extracting at the same time the phenomenological coefficients in the Landau expansion.

This approach (with or without couplings) has been somewhat successful when describing the critical behavior of some ferroelectric materials but it has not happened the same with magnetic materials, for instance (where magnetization plays the role of the order parameter); as the knowledge of the physics of phase transitions increased, the limitations of this theory started to stand out. In a real physical system, as the critical temperature is approached (and the so called reduced temperature $t=(T-T_C)/T_C$ tends to zero), fluctuations of the order parameter start to appear which are more and more relevant as t decreases till they dominate the transition. This is not considered by Landau's theory, where it is assumed that the order parameter is homogeneous throughout the crystal volume, and is the main cause of the deviations from it. Defects also can play a considerable role in ferroelectrics phase transitions whose importance has been considered by some authors.

Theoretical work was developed to extend Landau's approach including first-order fluctuations of the order parameter, with the result that the singularity in specific heat can be written in the form

$$\Delta c_p = \frac{k_B T^2 \alpha^{3/2}}{8\pi\delta^{3/2}}(T-T_C)^{-1/2}; \qquad\qquad \Delta c_p \sim t^{-1/2}.$$ (4.6)

But this has also failed to be proved experimentally in most cases in ferroelectrics. In the case of uniaxial ferroelectrics, the spatially inhomogeneous distributions of the order

parameter are necessarily associated with the appearance of a macroscopic electric field, which can have an influence upon fluctuations. Indeed, the presence of the dipolar-dipolar interaction attenuates the fluctuations effects and a theoretical development which takes this interaction into account leads to the following heat capacity anomaly

$$\Delta c_p = \frac{k_B T^2 \alpha^2}{\sqrt{2}(2\pi)^{3/2} \delta^{3/2} a} \ln\left(\frac{T - T_C}{T_C}\right) ; \qquad \Delta c_p \sim \ln t . \qquad (4.7)$$

This logarithmic correction to the pure Landau theory has proved extremely successful for many uniaxial ferroelectric materials. Another possibility is that the attenuation of fluctuations be small enough so that eq (4.6) could nearly be of application and that only a small logarithmic correction should be introduced; hence, eq (4.6) would turn into

$$\Delta c_p \sim t^{-1/2} |\ln t|^b , \qquad (4.8)$$

with $0.1 < b < 0.33$. This equation is equivalent to having in eq. (4.6) an exponent slightly closer to zero than -0.5.

Finally, the contribution of defects to the anomaly in specific heat in ferroelectrics has also been studied. In general, defects are simply responsible for a rounding of the anomalies in the phase transitions but Isarvediev et al [154-155] demonstrated that in the case of charged defects in ferroelectrics, they can give rise to stronger anomalies as they can induce long-range perturbations of the order parameter. The dependence of the specific heat in this case takes the form

$$\Delta c_p \sim t^{-3/2} . \qquad (4.9)$$

As we will see in section 4.4, sometimes a combination of different mechanisms is needed to properly describe the physics of a phase transition, such as a combination of first order fluctuations and defects, combining equations (4.6) and (4.9) to fit the anomalous part of the specific heat.

An important question when considering the applicability of Landau's extended theory is how close to the transition the fluctuations of the order parameter are extremely relevant so that even the first-order fluctuational correction is not enough and all the equations given above are not fulfilled. The so called Ginzburg's criterium [156] gives the range of reduced temperature out of which the first fluctuational correction

can be used and within which a new approach must be developed. This range is related to another important parameter called the correlation length ξ which represents how far fluctuations of the order parameters are sensed in the sample or, in another way, the size of those fluctuations. Far from the critical temperature ξ is small (and the Landau theory will be valid) but it grows without limit as the critical temperature is approached, either from above or from below, becoming of the order of the size of the sample.

In the case of magnetic systems, the Landau approach has been extremely unsuccessful and that's the main reason why a modern theory of critical behavior was developed from the 1980s which can also be used for the case of ferroelectrics in which the classical theories can not explain their critical behavior.

4.2. Modern Theory of critical behavior. Fluctuations effects

In the near vicinity of a second order phase transition, the specific heat often presents a singularity following the law

$$c_p \sim A^{\pm} \left| \frac{T - T_C}{T_C} \right|^{-\alpha} ; \ c_p \sim A^{\pm} |t|^{-\alpha} \quad (A^- \text{ for } T < T_C, \ A^+ \text{ for } T > T_C) \tag{4.10}$$

But this is not the only physical magnitude with this kind of behavior. In magnetic systems, for instance, the spontaneous magnetization (M_S), the inverse of initial susceptibility (χ_0^{-1}) and the critical isotherm ($M(H)$ at $T=T_C$) fulfill analogous equations with different critical exponents.

$$M_S(T) \ \sim \ |t|^{\beta} \quad (T < T_C), \tag{4.11}$$

$$\chi_0^{-1}(T) \sim \ |t|^{\gamma} \quad (T > T_C), \tag{4.12}$$

$$M(H) \sim \ H^{1/\delta} \quad (T = T_C). \tag{4.13}$$

Scaling analysis theory assesses that all those critical exponents are interrelated [151].

$$\alpha + 2\beta + \gamma = 2; \tag{4.14}$$

$$\delta = 1 + \gamma/\beta. \tag{4.15}$$

Different sets of values of these exponents correspond to different models (which are called universality classes) which have been theoretically developed after a certain expression of the Hamiltonian describing the physical system and using statistical mechanics; the particular values of the exponents have been predicted by different

methods, the most important one being renormalization group theory. [157-159] Fluctuations of the order parameters are fully taken into account even when the correlation length extremely grows, which happens when $t \to 0$. Table 4.1 shows the particular values of the critical exponents and parameters for a mean-field model (which implies long-range order interactions, equivalent to a Landau approach), an isotropic 3 dimensional Heisenberg model, a planar 3 dimensional XY model and a uniaxial 3 dimensional Ising model, referring to the ordering of the spins and the number of spin components needed to describe it. A strong theoretical effort has been developed for magnetic systems (as Landau theory was clearly inadequate to explain the shape of the transitions) but also for many other systems. A full development of all universality classes can be found in several review papers [141-149]. Further experimental efforts using different techniques have also been done from the 1980's in order to check the universality classes to which many magnetic systems belong, with extraordinary success, which opened a new field of research on the study of the critical behavior which is still quite active, as the assignation of any system to a certain universality class gives a deep insight on the physical mechanisms responsible for the particular transition studied.

Table 4.1.

Main universality classes for magnetic systems [157-159]

Universality class	α	β	γ	δ	A^+/A^-
Mean-field Model	0	0.5	1.0	3.0	-
3D-Ising	0.11	0.3265	1.237	4.79	0.53
3D-XY	-0.014	0.34	1.30	4.82	1.06
3D-Heisenberg	-0.115	0.365	1.386	4.80	1.52

Turning our attention to ferroelectrics, a certain number of researchers have also worked theoretically on the different universality classes which might appear depending on the properties of the Hamiltonian used to describe the system as a consequence of the physical mechanisms included in it [141, 142, 161-169]. Apart from specific heat, the equivalent magnitudes to study their critical behavior are the spontaneous polarization P_S and the inverse of susceptibility χ^{-1}.

$$c_p \sim A^{\pm} |t|^{-\alpha} \quad (A^- \text{ for } T < T_C, \ A^+ \text{ for } T > T_C) \tag{4.16}$$

$$P_S(T) \quad \sim \ |t|^{-\beta} \quad (T < T_C), \tag{4.17}$$

$$\chi^{-1}(T) \sim |t|^{\gamma} \quad (T > T_C). \tag{4.18}$$

For which the scaling law

$$\alpha + 2\beta + \gamma = 2, \tag{4.19}$$

is again fulfilled. Table 4.2 contains the universality classes found so far for ferroelectric systems, where the mean field model is again equivalent to the Landau phenomenological model. We would like to emphasize the work done by Folk and coworkers who developed a good part of these universality classes which are appropriate to study the family of uniaxial ferroelectrics $(Pb,Sn)_2P_2(S,Se)_6$ with so complex a phase diagram. [3, 141, 142, 168, 169].

The particular values for the exponents in a certain universality class are sometimes open to debate in literature, depending on the particular mathematical techniques used to obtain it and the order to which the expansions are deployed. For instance, for the Lifshitz class L with m=1 (which is the relevant one for the materials studied in this thesis report), some authors have obtained values for α smaller than 0.25 and closer to 0.2 [170, 171].

Actually, the presence of a Lifsthiz point enhances the fluctuations in the order parameter which will substantially deviate the critical exponents from the mean-field values, and this would lead to the change of the critical exponent of specific heat from α=0 to α=1/4 in systems with short range interactions (L, m=1). On the other hand, fluctuations are strongly suppressed in ferroelectrics with strong dipolar interactions (as it is the case in this family of materials), and these are expressed as a critical exponent α=1/6 (UL, m=1). Another situation in which fluctuations are reduced takes place in the presence of a tricritical point; for uniaxial ferroelectrics in the vicinity of the tricritical Lifshitz point, the critical exponent for specific heat will be α=0.5 with small logarithmic corrections (UTL, m=1).

Table 4.2.

Universality classes for ferroelectric systems for 3 dimensions. S: usual critical point isotropic short-range interaction, U with uniaxial dipolar interactions, T tricritical point, L Lifshitz point. Those exponents with an asterisk * have a logarithmic correction with exponent *x*. *m* is the number of components of the order parameter.

Universality class	α	β	γ	x	Reference
Mean Field model	0	1/2	1		[141]
S	1/6	1/3	$1\frac{1}{6}$	-	[161]
U	0^*	$1/2^*$	1^*	1/3	[162, 163]
T	$1/2^*$	$1/4^*$	1^*	1/3	[164]
UT	1/2	1/4	1	-	[168]
L, m=1	1/4	1/4	$1\frac{1}{4}$	-	[165]
L, m=2	1/3	1/6	$1\frac{1}{3}$	-	[165]
L, m=3	5/12	1/12	$1\frac{5}{12}$	-	[165]
LT, m=1	9/14	1/7	$1\frac{1}{28}$	-	[166, 167]
LT, m=2	31/40	3/80	$1\frac{3}{40}$	-	[166, 167]
UL, m=1	1/6	1/3	$1\frac{1}{16}$	-	[168]
UL, m=2	1/4	1/4	$1\frac{1}{4}$	-	[168]
ULT, m=1	$1/2^*$	$1/4^*$	1^*	1/10	[169]
ULT, m=2	19/48	13/48	$1\frac{1}{16}$	-	[169]

It should be mentioned that there is an equivalent table to Table 4.2 for what is called the Gaussian approximation [141], where fluctuations of the order parameter are not taken into account and where, of course, the exponents have different values to those in Table 4.2 (see Annex 4.1 at the end of this chapter). Any system belonging to those classes would imply that fluctuations are not relevant enough to force the system to deviate from a classical Landau description.

In Table 4.2 the ratio of the critical amplitudes A^+/A^- for specific heat has not been included as they are mathematically very difficult to predict within the framework of the renormalization group theory. But it is also important as it helps to discriminate among universality classes when the critical exponents are too close (compare them in

Table 4.1 for magnetic systems, where they have all been found), as they can be obtained experimentally. Nevertheless, some papers have been devoted to find them for particular universality classes in ferroelectrics and it has been shown that, for the L class (m=1) in first-order approximation, this amplitude is 0.30 and rises up to 0.35 in second-order approximation [172]. On the other hand, in the Gaussian approximation, at a Lifshitz point with long-range interactions this value is 0.25, while if they are neglected, it is increased to 0.42 [173].

Finally, it is worth including here a last comment about equation (4.16). This equation includes only one value for the α parameter and not two different ones (one for the region above the critical temperature and another one below it), as it can be found sometimes in literature. In fact, the full equation which is generally used to fit the experimental curves of specific heat is

$$c_p = B + Ct + A^{\pm} |t|^{-\alpha} \left(1 + E^{\pm} |t|^{0.5} \right), \tag{4.20}$$

where the linear term represents the regular contribution to the specific heat, while the last term represents the anomalous contribution at the second order phase transition. The factor under parenthesis is the correction to scaling that represents a singular contribution to the leading power as known from experiments and theory [174, 175] but which must be small (sometimes there is even no need to include this factor for the fittings). Scaling laws require that there is a unique critical exponent α for both branches and rigorous application states that constant B needs also be the same [176]. These conditions have sometimes been relaxed in literature due to the difficulty of obtaining good fittings to the experimental data with those constraints, but this only makes the interpretation of results more complicated. Strict application of scaling theory must respect these rules.

Finally, it is worth noting that there are several other measurable quantities which can be used to study the critical behaviour in phase transitions as they behave as some of the already described physical variables. A particular case, relevant for this study, is thermal diffusivity D which is related to specific heat by the equation

$$c_p(T) = \frac{K(T)}{\rho D(T)} \; ; \qquad\qquad \frac{1}{D(T)} = \frac{\rho}{K(T)} c_p(T), \tag{4.21}$$

where ρ is the density and K the thermal conductivity of the sample under study, which means that the specific heat and the inverse of the thermal diffusivity will have the same critical behavior in those cases in which thermal conductivity do not present a singularity at the transition, which happens in many cases.

4.3. Critical behavior of commensurate-incommesurate phase transitions

In chapter 3 the phase diagram of the family of ferroelectrics $(Pb,Sn)_2P_2(S,Se)_6$ has been already shown. In the particular case of $Sn_2P_2(S_{1-x}Se_x)_6$ for $0.28 < x < 1$ and $(Pb_xSn_{1-x})P_2Se_6$ for $0 < x < 0.6$, the high temperature phase is paraelectric, the low temperature one is ferroelectric and, in between, there is an intermediate phase. The high temperature phase transition was found to be a structural (commensurate to incommensurate) but continuous one, while the incommensurate to ferroelectric has a first order character. This type of intermediate, incommensurate phase is also present in many other ferroelectric materials such as $NaNO_2$, $(NH_4)_2BeF_4$, K_2SeO_4 ... [177, 178] or in general in the A_2BX_4 materials [179].

The critical behavior of commensurate to incommensurate continuous phase transitions has been theoretically addressed from different points of view and applied to several practical cases. From a classical point of view, as it was clear that there were severe deviations from the Landau theory, Ivanov *et al* [181] developed a method based on the first fluctuational correction to account for those deviations, which is valid for a reduced temperature range $t = (T-T_C)/T_C$ with $t >> G$ (where G is the Ginzburg number expressed in terms of the coefficients of the thermodynamic potential) but not closer to the critical temperature; this method was successfully applied to birefringence measurements in Rb_2ZnBr_4 [182], to NMR data for Rb_2ZnCl_4 [183] or to heat capacity in $SC(NH_2)_2$ [184]. After this model, the experimental specific heat is fitted to the following equations

$$c_p^+ = c_B + \lambda^+(T - T_i)^{-1/2} \qquad\qquad T > T_i; \qquad\qquad (4.22)$$

$$c_p^- = c_B + c_L + \lambda^-\left|T - T_i\right|^{-1/2} \qquad\qquad T < T_i, \qquad\qquad (4.23)$$

where T_i is the critical temperature of the transition, c_B is the regular part of the specific heat, c_L is the specific heat jump at T_i (according to Landau), λ^+ and λ^- are constants

whose ratio is $2\sqrt{2}$ if the order parameter is single-component (Ising-type system) and $\sqrt{2}$ if it has two components (XY-type systems) [185]; the latter is the expected behaviour in structural phase transitions from normal to incommensurate phase. Analogous equations have been used for the first derivative of birefringence with respect to temperature [182].

Renormalization group methods have also been applied to study the universality class to which this kind of transitions could belong, with the result that it is the three dimensional XY (3D-XY) [185], for which the critical exponent is $\alpha = -0.014$ and the ratio of the critical exponents $A^+/A^- = 1.06$ [158]. This model assumes that a two component order parameter is needed to describe the Hamiltonian for the system: in the case of this kind of transition, the order parameter associated with the irreducible representation of the cogroup of the modulation wave vector q is a complex variable; hence the two components [185, 186]. Besides, a strong theoretical effort was performed along the nineties to describe the nuclear-spin-lattice relaxation for quadrupole perturbed magnetic resonance (NMR) in structurally incommensurately modulated crystals, applying it successfully to the particular case of Rb_2ZnCl_4 [187-189]. NMR is also a powerful technique to study the critical behaviour of a transition by means of obtaining the critical parameter β.

The crux of the matter in applying or not a classical view for the commensurate to incommesurate phase transitions lies in the following questions: Is there a non-classical region in which the deviations from the mean field model can be detected? Might there be a crossover region marked by the Ginzburg criterion [3]? Is the non-classical region wide enough to clearly see the 3D-XY behavior? This has been addressed theoretically and also checked with several materials: Kauffmann *et al* [190] worked with an extended renormalization scheme while Wesselinova *et al* [180] used both a self-consistent phonon theory and renormalization group theory and they found that for A_2BX_4 materials there is indeed a wide enough critical region (as wide as 50-60K in Rb_2ZnBr_4, smaller in some other cases) which can be described by the 3D-XY model; this has been experimentally corroborated by NMR measurements. Indeed, from the nineties on, the 3D-XY model has been found to be of application to a few materials

presenting this kind of transition such as K_2SeO_4, Rb_2ZnCl_4 [186, 191], $(ClC_6H_4)_2SO_2$ [192] and betaine calcium chloride dihydrate BCCD [193].

4.4. Critical behavior studies of $(Pb,Sn)_2P_2(S,Se)_6$ prior to this work

4.4.1. $Sn_2P_2S_6$

In general, the uniaxial ferroelectrics with one-component order parameter have a classical mean-field critical behavior as a consequence of the strong suppression of the longitudinal critical fluctuations by the long-range dipolar interactions [194]. However, the critical behavior of $Sn_2P_2S_6$ cannot be explained only by the classical mean-field model; instead, literature shows that different mechanisms must be taken into account such as first-order fluctuations of the order parameter, the presence of charge defects, or the closeness of the system to a Tricritical or Lifshitz point on its phase diagram.

In the first place, ultrasonic investigations performed by Valevichius's research group for $Sn_2P_2S_6$ show that the temperature dependencies of the sound velocity in the ferroelectric phase are well described by the classical Landau theory in terms of mean-field model. In the same work, the dependencies in the paraelectric state have been described by a logarithmic correction of the sort $\Delta V \sim \ln(T\text{-}Tc)$ [195]. Further precise ultrasound studies carried out by Samulionis and coworkers for $Sn_2P_2S_6$ single crystals reveal that in the high-symmetry phase the anomalous part of the ultrasound velocity in the vicinity of the transition is described with a critical exponent $\alpha=0.5$ with a small ($x=0.1$) multiplicative logarithmic correction [196]. This result is in good agreement with the tricritical universality classes theorized by renormalization group theory and supports an idea of closeness to the Tricritical point; the authors suggest that the Uniaxial Lifshitz Tricritical class (ULT m=1 in table 4.2) is of application in this case. They also found that, in the case of the ferroelectric state, the Landau-Khalatnikov model (based on a classical mean-field approach, see section 4.1) is of application to describe the temperature dependence of the ultrasound velocity below the transition point [196]. Say et al. [197] studied the thermal expansion coefficient of $Sn_2P_2S_6$ crystal and they applied equation 4.16 to the ferroelectric phase, finding that the best fitting gave a critical exponent $\alpha=0.5$. From calorimetric investigations Vysochanskii *et al*

[198] obtained that the excessive heat capacity of $Sn_2P_2S_6$ in the paraelectric phase could be well described by two exponential functions $\Delta C_p \sim t^{-0.5}$ in a temperature range of $T>T_0+1K$ and $\Delta C_p \sim t^{-1.5}$ in an interval $T_0<T<T_0+1K$, which correspond to eq.4.6 and eq.4.9, respectively. The first equation contains the fluctuational correction to the Landau approach and the second one the contribution of charged defects. Therefore, they interpreted the heat capacity anomaly in this crystal as defined by "random-field" defects in the immediate closeness to T_0, while far from the transition point it can be explained by first-order fluctuations of the order parameter [198].

Critical analysis of dielectric permittivity for $Sn_2P_2S_6$ single crystal exhibits a slight deviation from the Curie-Weiss law in the paraelectric phase, and was described by the multiplicative logarithmic correction with $b=0.1$: $\chi^{-1} = t\left(\left|ln\, t\right|\right)^b$ (related to eq.4.8), as suggested by Vysochanskii *et al* [199]. In the same publication, a temperature variation of the effective value of the critical index γ_{eff} for dielectric permittivity has been observed (see eq.4.18). This effective value of γ_{eff} is equal to 1 in the paraelectric phase far from the critical point, while approaching the transition temperature it deviates from the classical Curie-Weiss law. This deviation is observed at $T-T_0<10K$ when approaching the critical temperature from above [199].

From a detail analysis of the temperature evolution of the optical birefringence, carried out by Vysochanskii and coworkers [200], it was found that the behavior of the heat capacity in the paraelectric phase was well described by eq.4.8 with a small logarithmic correction ($b=0.1$). In turn, the value of critical index for polarization β was observed to be close to 0.25. These findings agree quite well with the universality class UTL, m=1 (see table 4.2).

In that same paper, the temperature dependence of birefringence in the paraelectric state for $Sn_2P_2S_6$ crystal was also analyzed taking into account the possible superposition of two mechanisms: fluctuations of the order parameter and charged defects influence, which corresponds to a combination of eq. 4.6 and eq. 4.9. The obtained conclusion is that the fluctuational contribution to the critical anomaly is much

bigger than the contribution of defects; however, in the immediate vicinity of the transition ($t \leq 10^{-3}$) the defect contribution becomes predominant [200].

From thermal diffusivity measurements of $Sn_2P_2S_6$ single crystals, Oleaga *et al* found that its ferroelectric phase could be well described within the framework of the Landau model (equation 4.5) while this model fails to describe the temperature dependence of thermal diffusivity in the paraelectric phase. [95] To describe the critical behavior in the vicinity of the transition point in the latter phase, a model taking into account again the superposition of the two aforementioned effects, corresponding to eq.4.6 and eq.4.9, was needed ($\sim A \cdot t^{-0.5} + B \cdot t^{-1.5}$).

4.4.2. $Sn_2P_2(S_{1-x}Se_x)_6$

Owing to the presence of a Lifshitz point on the phase diagram of these ferroelectric compounds it is desirable to divide this section into two parts. The first one will include a review of the critical behavior studies for crystals with concentrations of Se lower than $x \leq 0.28$ (Lifshitz concentration). The second part contains the results obtained for the samples with an atomic percentage of Se exceeding that value. The main reason for this separation is that above the Lifshitz point a second order transition from a paraelectric phase into an incommensurate phase takes place before the ferroelectric one, which happens at a lower temperature (see the phase diagram in section 3.2), whereas for smaller concentrations the transition is directly from the paraelectric state into the ferroelectric one.

a) $Sn_2P_2(S_{1-x}Se_x)_6$, $x \leq x_{LP}$. Vysochanskii *et al* [200] studied the optical birefringence upon changing the chemical composition of $Sn_2P_2(S_{1-x}Se_x)_6$ ferroelectrics for x=0.15, 0.29 and a clear evolution of the anomalous part of the birefringence was observed compare to the undoped sample (x=0). The analysis of this evolution by the combination of two models such as shown in eq. 4.6 and 4.9 ($\sim A \cdot t^{-0.5} + B \cdot t^{-1.5}$) shows that the amplitude *A* of the fluctuational contribution significantly increases when S is replaced by Se, indicating a possible crossover of the critical behavior.

In another work, performing thermooptical investigations near the Lifshitz point (x=0.29), the authors in [198] found that the critical exponent for polarization β to be

equal to 0.20±0.02, which is slightly smaller than the critical index β for a tricritical behavior (0.25). In the same paper, from an analysis of the derivative of birefringence with respect to temperature, the critical exponent α was found to lie within the range 0.4-0.6, which is again close to a tricritical behavior. The authors favored the ULT universality class (see table 4.2) and the lower values of β were explained by the proximity to the tricritical Lifshitz point and a two dimensional modulation state.

Renormalization group theory has been also put to test by Oleaga and coworkers studying thermal diffusivity in $Sn_2P_2(S_{1-x}Se_x)_6$ mixed ferroelectrics [60]. An analysis for samples with Se content of 0, 0.15, 0.20, 0.22, 0.24, 0.26, 0.28, and 0.30 has been performed by making use of the critical equation (4.20), having simultaneously fitted both low and high temperature branches. For crystals doped with 0, 0.15, and 0.2 no meaningful fittings were found, pointing that at those concentrations there is not a clear dominant effect yet (fluctuations, short or long-range dipolar interactions, charged defects…). Concerning the concentrations around the Lifshitz point, from 0.2 up to 0.30, good fittings were obtained, extracting meaningful values of the critical exponent for heat capacity α, which falls within the range of 0.21-0.34. This result supports the universality class L for uniaxial ferroelectrics (see table 4.2 class "L"), indicating that the close presence of the Lifshitz point is more relevant when explaining critical behavior than other effects such as charged defects, first-order fluctuations or closeness to a tricritical point. Moreover, the amplitude ratio A^+ / A^- was found to be in the range 0.42-0.51. This is also close to the theoretically estimated value (0.35) for a Lifshitz system without taking into account strong dipolar interactions. These findings reveal that for selenium concentrations around the Lifshitz point, long-range dipole interactions do not play a significant role and that the critical parameters are close to those of the Lifshitz universality class L.

Finally, critical behavior has also been studied with acoustic measurements: the authors observed that the temperature dependence of the hypersound velocity in a ferroelectric phase for $Sn_2P_2(S_{0.72}Se_{0.28})_6$ crystal is well approximated by a Landau-Khalatnikov approach based on the mean-field model [99].

b) $Sn_2P_2(S_{1-x}Se_x)_6$, $x > x_{LP}$. For the compositions with concentrations exceeding the Lifshitz point, renormalization group theory has predicted that the critical behavior of the second order paraelectric to incommensurate phase transition should correspond to the the 3D-XY universality class, as explained in section 4.3. Unfortunately, the critical study for these compounds is restricted by the physical properties of the incommensurate phase: at most concentrations, the temperature width of this phase is too narrow to allow a clear separation of this transition and the lowest one to the ferroelectric phase (first-order), preventing a proper analysis. So, till present time, the critical behavior of the paraelectric to incommensurate phase transition has only been studied for the pure $Sn_2P_2Se_6$ ferroelectric crystal.

To this end, Maior *et al* obtained the temperature dependence of the thermal expansion coefficient in $Sn_2P_2Se_6$ [201]; they were able to describe the paraelectric phase far enough from the critical point ($t > 10^{-2}$) within the framework of the Landau model including the fluctuational correction, using expressions equivalent to eq. 4.22 and 4.23. But they failed to find a reasonable critical exponent in a closer region and could not relate it to the 3D-XY model.

According to birefringence data published by Vysochanskii and coworkers [202], an analysis of the critical behavior in the incommensurate phase of $Sn_2P_2Se_6$ gives a value of the critical exponent $\beta = 0.35 \pm 0.01$ and this agrees quite well with the theoretical value for the 3D-XY model (β=0.34, see Table 4.1).

Neutron Magnetic Resonance measurements have also been undertaken for $Sn_2P_2Se_6$ with an obtained value of $\beta = 0.45 \pm 0.03$ [203]. This value is in-between the mean-field model and the 3D-Heisenberg class (see Table 4.1). However, an unambiguous answer concerning the appropriateness of the 3D-XY model can only be given after a reliable determination of the critical exponent for specific heat α (as its value differs significantly from one critical model to another, see table 4.1), as well as using experimental data from both sides of the transition.

In order to obtain the critical exponent α, Rizak et al [204] used birefringence data. From the temperature dependence of the derivative of the birefringence in the

paraelectric phase within a temperature range $10^{-3} < t < 10^{-2}$, and using a modified form of equation 4.22, α was found to lie within the range (-0.02, -0.07), which the authors claimed is close to the theoretically predicted value for the 3D-XY model. At temperatures far from the transition $t > 10^{-2}$ a first fluctuation correction to the Landau model was of application (equations 4.22, 4.23), while when approaching T_i for $t < 10^{-3}$, the authors suggested that there is a possible influence of defects.

4.4.3. $(Pb,Sn)_2P_2(S_{1-x}Se_x)_6$

Concerning compounds which contain lead, unfortunately only a few results on critical behavior are reported. Recently, $(Pb_ySn_{1-y})_2P_2S_6$ mixed ferroelectrics have been studied by means of hypersound and ultrasound investigation [107]. Analysis of the temperature dependencies of hypersound velocity for concentrations y=0, 0.2, 0.3, and 0.45 reveal that the anomalies around the second order phase transition are well described by the Landau-Khalatnikov model based on the mean-field approach. The same results have been observed when studying ultrasound velocity. Moreover, from the fitted parameters, the thermodynamic coefficients β and γ in the Landau expansion series (eq.4.1) were extracted. These coefficients are slightly reduced when Pb contents is increased; it is worth noting that all values are positive, indicating a continuous character in the transition in the concentration range under study [107].

The possible influence of defects on the critical anomaly has been tested when replacing Sn by Pb in the cation sublattice and S by Se in the anion sublattice in a low atomic percentage (0.5%), measuring birefringence and using eq.4.6 and eq.4.9 to study the paraelectric phase [200]. This addition has a strong influence on the amplitude of the defect contribution to the critical anomaly, whose value considerably increases. On the other hand, in the same work, the ferroelectric phase was used to extract the critical exponent of the order parameter β, whose value is nearly the same as that of the pure sample.

Annex 4.1

Table.4.3.

Mean-field exponents for different critical points. [141] S: usual critical point isotropic short-range interaction, U with uniaxial dipolar interactions, T tricritical point, L Lifshitz point. m is the number of components of the order parameter.

Universality class	α	β	γ
S	0	1/2	1
U	0	1/2	1
T	1/2	1/4	1
UT	1/2	1/4	1
L, m=1	0	1/2	1
L, m=2	0	1/2	1
L, m=3	0	1/2	1
LT, m=1	1/2	1/4	1
LT, m=2	1/2	1/4	1
LT, m=3	1/2	1/4	1
UL, m=1	0	1/2	1
UL, m=2	0	1/2	1
ULT, m=1	1/4	1/4	1
ULT, m=2	1/4	1/4	1

CHAPTER 5

Experimental results and discussion on Sn(Pb)$_2$P$_2$S$_6$ mixed ferroelectrics

5.1. Introduction

The research problem of this chapter is focused on the left hand side of the general phase diagram (fig.3.7), whose shape is depicted on fig.5.1. As it was previously mentioned in chapter 3, the introduction of Pb^{2+} ions in the cation sublattice of Sn$_2$P$_2$S$_6$ crystal leads to a reduction of the critical temperature of the second order phase transition. This temperature lowering is suggested to be caused by the weakening of the average bond stiffness in the crystal lattice, when Sn ions are substituted by Pb [108]. The nature of this weakening can be related to the difference in atomic radii [109] and electronic structure of Pb and Sn ions. Such changes in crystal lattice might be also reflected somehow in the thermodynamic properties of the crystals, especially around the critical point. So, the aim of this chapter is to thermally characterize (Pb$_x$Sn$_{1-x}$)$_2$P$_2$S$_6$ mixed ferroelectrics in a wide temperature range and present a critical behavior study in the vicinity of the continuous phase transition by means of high resolution thermal diffusivity measurements.
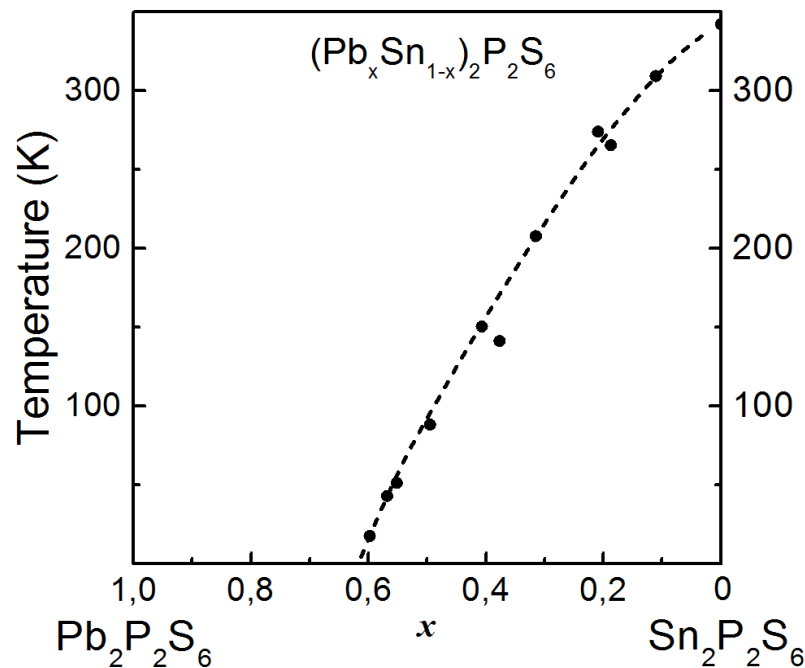
Fig. 5.1. Phase diagram of (Pb$_x$Sn$_{1-x}$)$_2$P$_2$S$_6$ mixed ferroelectrics [205].

5.2. Samples and experimental procedure

Single crystals were grown using two well known methods. The samples with lead concentrations of x=0, 0.1, 0.2, 0.3, 0.45, 0.8, 1 have been grown by vapor-transport method in a quartz tube using SnI_2 as a transport reagent. $Pb_2P_2S_6$ crystal was also grown by crystallization from melt using the Bridgman method. Note that growing procedures were carried out using high-purity elements Sn (99.99%), Pb (99.99%), P (99.999%), S (99.99%) in atomic percentage.

There is no information about the stoichiometric quality and difference between the "real" and "nominal" concentrations. However, according to XPS spectroscopy of $Sn_2P_2S_6$ the atomic concentration on Sn might exceed up to 2% the nominal value [206]. For solid solutions grown by vapor-transport method the real content of Sn and Pb can deviate from the nominal value in less than 0.2% as was shown by atomic adsorption spectroscopy investigations [109].

The crystals were prepared in the form of thin plane-parallel slabs with thickness varying in a range of 300-500 μm. The samples grown by vapor-transport method were cut perpendicular to their (010) crystallographic direction. In the case of the "Bridgman" $Pb_2P_2S_6$ two additional samples were prepared in (100) and (001) directions in order to check the possible thermal anisotropy as has been found for $Sn_2P_2S_6$ [95]. Thermal diffusivity measurements have been carried out using a high-resolution *ac* photopyroelectric calorimeter in the standard back detection configuration using a closed cycle helium cryostat. A detailed description of the experimental setups used during these investigations can be found in chapter 2. Measurements have been performed in two steps: first there was a quick run with a rate of 0.1K/min in order to cover a wide temperature range, and a second step consisted of high-resolution heating/cooling runs around the critical temperature with rates as slow as 20mK/min.

5.3. Experimental results

First of all, thermal diffusivity D was measured as a function of Pb contents in the (010) direction at room temperature (292K). The results are displayed on fig.5.2. It can be seen on the graph that the values are typical for poor thermal conductor materials,

where heat is mainly transported by phonons. The crystal $Sn_2P_2S_6$ possesses a smaller value of D than $Pb_2P_2S_6$. A slight substitution of tin by lead reduces the thermal diffusivity a bit, while further doping of Pb ions increases D up to 0.432 mm^2/s for $x=1$. This rising of D is surely due to the difference between the ionic radii of Pb^{2+} and Sn^{2+} ions, and it is well known that lead has a larger radius than Sn. Therefore, introducing Pb increases the available space for tin ions in $(Pb_xSn_{1-x})_2P_2S_6$ series. Such situation might reduce the intrinsic scattering processes in the crystal and, hence, the phonon mean free path would increase [95].
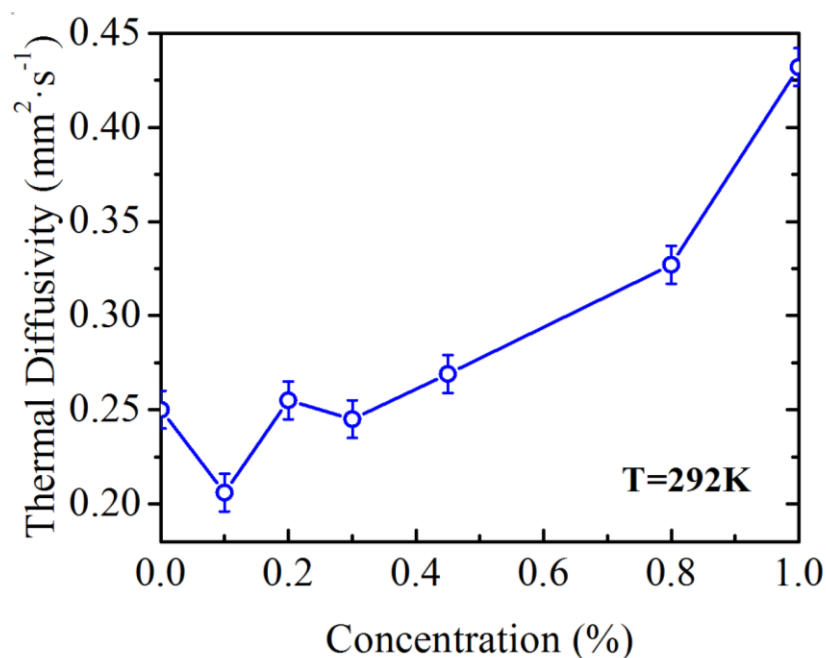
Fig.5.2. Thermal diffusivity of $(Pb_xSn_{1-x})_2P_2S_6$ mixed ferroelectrics along (010) crystallographic direction as a function of Pb contents at room temperature [205].

Fig.5.3 displays the temperature evolution of thermal diffusivity D covering a wide range from 60K up to room temperature. The experimental curves were obtained as a continuous run with a constant variation of temperature in time.
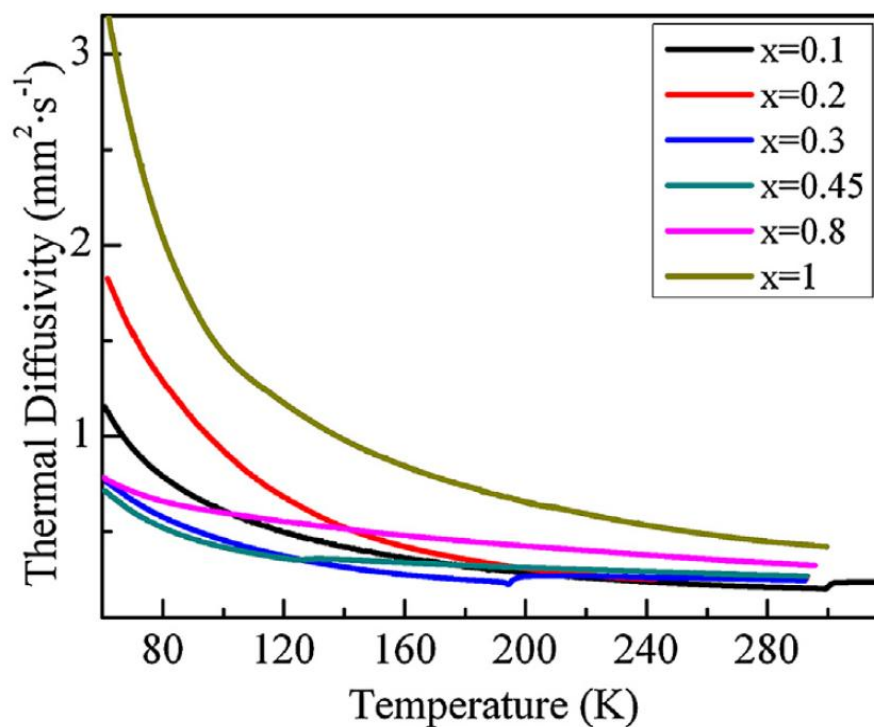
Fig. 5.3. Thermal diffusivity as a function of temperature for (Pb$_x$Sn$_{1-x}$)$_2$P$_2$S$_6$ mixed ferroelectrics [205].

The figure above clearly shows that the general trend is maintained for all samples: thermal diffusivity increases as temperature is lowered. Such behavior is expected to be observed in any material in which phonons are mainly responsible for heat transport, where phonon mean free path rapidly increases with the decrease of temperature. For the concentrations x=0.1, 0.2, 0.3, and 0.45 a dip in the thermal diffusivity curve has been found signaling the presence of the paraelectric to ferroelectric phase transition. Whereas from fig.5.3 it is not clearly seen, fig. 5.4 illustrates those transitions in detail. For all cases the possible presence of hysteresis has been checked by repeating several times the measurement around the transition with rates as low as 20mK/min performed on cooling-heating regimes. No difference between heating and cooling curves was observed confirming the continuous character of the phase transition. In the case of x=0.8 and x=1 the measurements have been performed down to 18K and no transition was found.
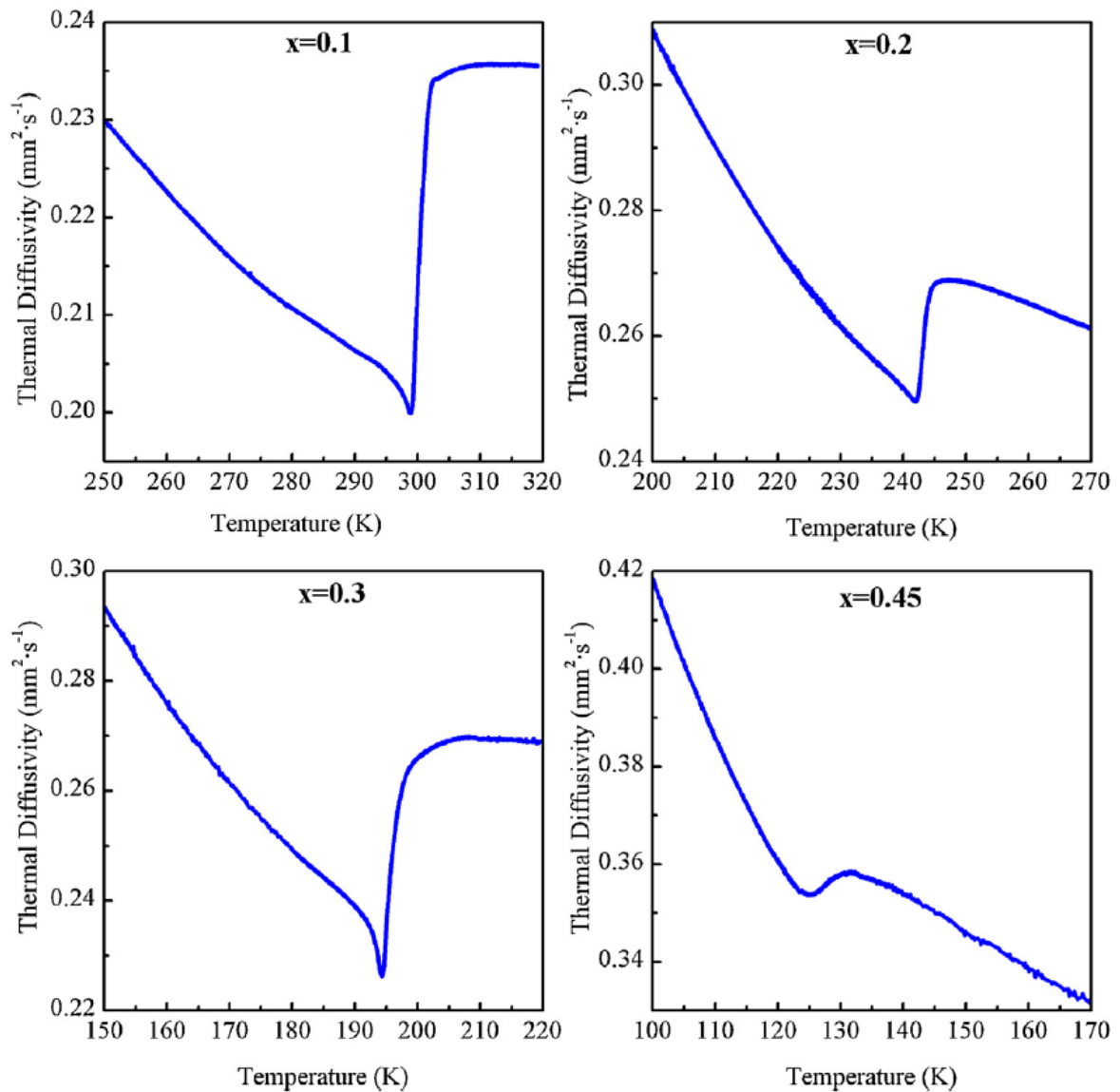
Fig. 5.4. Paraelectric to ferroelectric phase transition temperatures for $(Pb_xSn_{1-x})_2P_2S_6$ mixed compound (x=0.1, 0.2, 0.3, 0.45) [205].

As the crystals possess a monoclinic structure, the possibility of thermal anisotropy has been checked measuring the thermal diffusivity of $Pb_2P_2S_6$ crystals along the three principal crystallographic directions (100), (010) and (001), with a result similar to the one already reported for $Sn_2P_2S_6$ [95]. Analyzing figure 5.5, it can be concluded that heat propagates more easily in (100) direction than along (010), while the (001) falls in between. The same sequence was also observed for $Sn_2P_2S_6$ crystal [95], indicating the presence of a clear thermal anisotropy in this paraelectric phase.
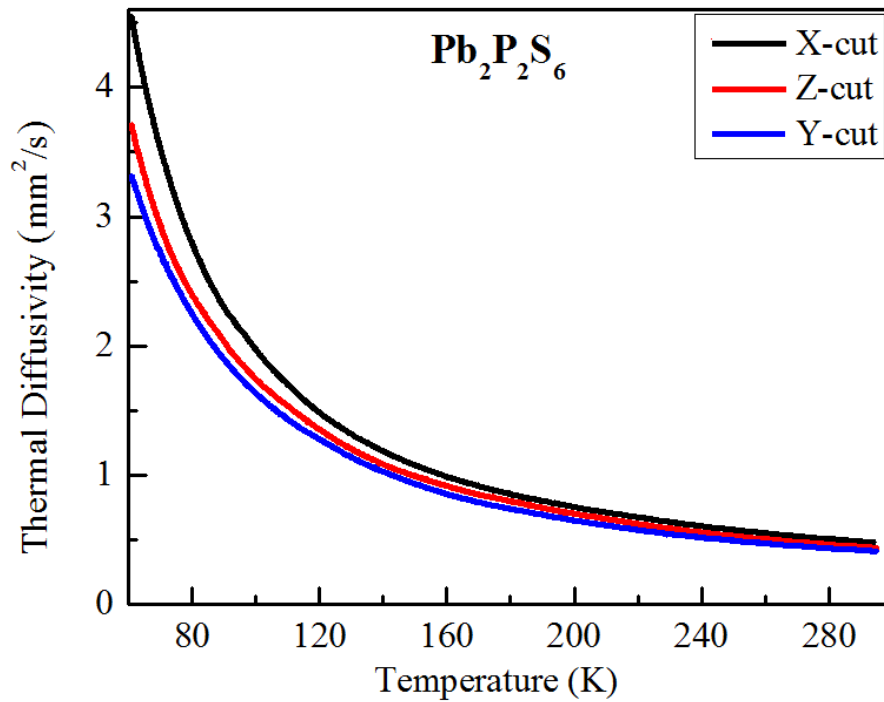
Fig.5.5. Thermal diffusivity as a function of temperature for Pb$_2$P$_2$S$_6$ crystal along its principal crystallographic directions [205].

Moreover, due to the high resolution in fig. 5.5, it is possible to see that the temperature evolution of the thermal diffusivity in the (100) direction increases more rapidly at low temperatures compared to that for (001) and, in particular, for (010) directions. To better distinguish this feature and see how the anisotropy of this monoclinic paraelectric changes with temperature we have performed a normalization which consists of dividing the values of the thermal diffusivities at the same selected temperatures for x-cut and z-cuts over the softest evolution, which takes place for y-cut. As seen from fig. 5.6 in a wide region, from 295K down till about 100K, both normalized diffusivities are practically insensitive to temperature indicating that the thermal anisotropy does not change with temperature. Starting from about 100K for (100) and from about 85K for (001) directions the normalised thermal diffusivity increases. The nature of this increase could be related to the Debye's temperature θ_D, which is about 85K for Pb$_2$P$_2$S$_6$ crystal, according to reference [129]. As known from the solid state physics theory, at the Debye's temperature all the possible internal crystal vibrations, named as phonons, are excited for all crystallographic directions. A further increase in temperature will only enhance their vibration amplitudes, without creating

new modes, thus, having practically no influence on the thermal anisotropy, which is in agreement with what we have on graph 5.6. The interesting situation happens below this specific temperature θ_D, when some of the modes start to be frozen. The freezing of the internal vibrations reduces the probability of collision processes between the phonons, hence, increasing the phonon mean free path and leading to a quicker increase in the thermal diffusivity. This might be a good reason why the thermal diffusivity along (100) direction rises up faster than that for (001) and (010) ones.
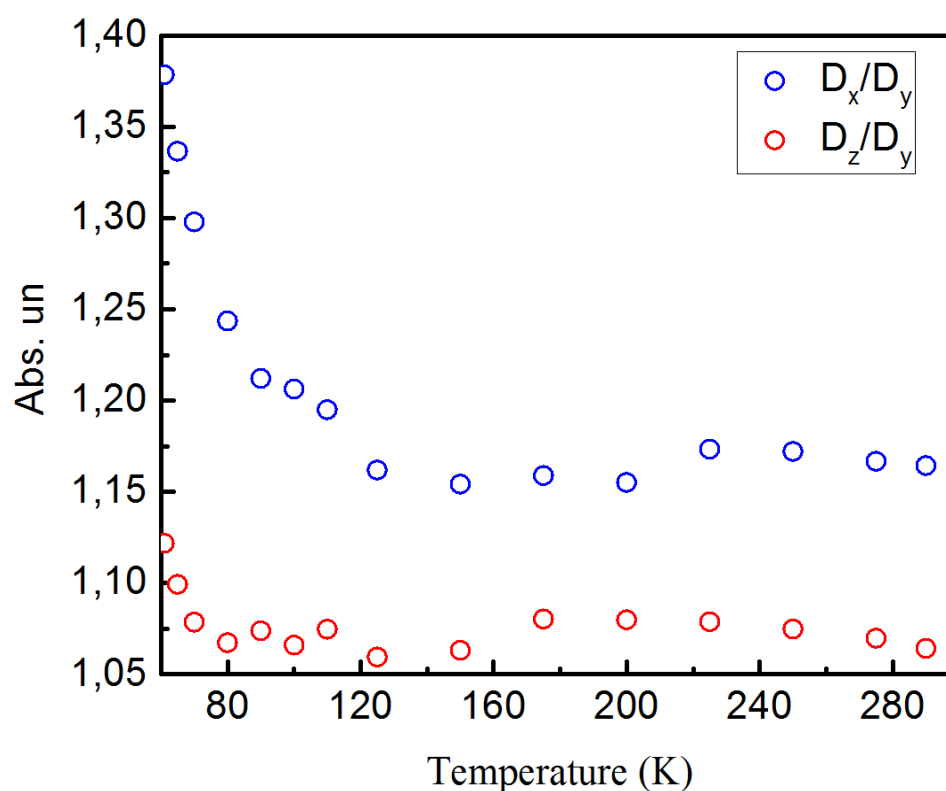
Fig. 5.6. Normalized thermal diffusivity as a function of temperature for x-cut (blue circles) and z-cuts (red circles) of $Pb_2P_2S_6$.

5.4. Discussion on the critical behavior study of the second order phase transition

For the critical analysis the anomalies at T_C of the samples with lead content of $x=0.1$, 0.2 and 0.3 have been studied. In the case of $x=0.45$ the shape is too rounded, which makes it useless for any quantitative treatment. This type of rounding is quite common in heavily doped systems: as Pb ions are introduced in the compound in a high percentage, the disorder and the lattice defects increase noticeably smearing the shape

of the phase transitions. In order to study the critical behavior of the transition, very well defined thermal diffusivity curves have been obtained in the near vicinity of the critical temperatures. As it was explained in a chapter 2, the relation between the thermal diffusivity D and specific heat is c_p: $D = K / \rho c_p$, where K is the thermal conductivity and ρ the density; therefore, the critical behavior of specific heat and the inverse of thermal diffusivity $1/D$ is the same, provided that neither thermal conductivity nor density have significant changes across the transition point, which is the case in these ferroelectric family [95]. To describe the critical behavior at the transition several critical models have been put to test. Thus, the equations used to fit 1/D were written as follows:

a) General mean-field analysis in terms of Landau theory, based on the eq.4.1, for the ferroelectric phases:

$$1/D = B + C(T - T_c) + p_1 \frac{T}{\sqrt{1 - 4p_2(T - T_c)}}, \tag{5.1}$$

where p_1, p_2 are related to the phenomenological coefficients α and β in the Landau expansion series through the relations: $p_1 = a^2 / (2\beta' K)$, $p_2 = \gamma a / (\beta'^2)$. Here and in further models the linear term defined by coefficients B and C represents a regular contribution to the inverse of thermal diffusivity.

b) The modern critical theory that corresponds to eq.4.20, fitting the paraelectric and ferroelectric phases at the same time. It would determine the universality class to which the transition belongs, as has been previously done for $Sn_2P_2(Se_xS_{1-x})_6$ family [60].

$$1/D = B + Ct + A^{\pm} |t|^{-\alpha} \left(1 + E^{\pm} |t|^{0.5}\right), \tag{5.2}$$

where $t = T - T_c / T_c$ is the reduced temperature.

c) In case in which no good fittings could be found with the previous model, we have also studied the paraelectric phase using the following sequence of models:

− First fluctuational correction to the Landau approach, that corresponds to eq.4.6, where the critical exponent α has to be equal to 0.5:

$$1/D = B_1 + C_1 t + A_1 |t|^{-\alpha}. \tag{5.3}$$

− A model based on the eq.4.8, which assumes a possible attenuation of fluctuation effects ($\alpha < 0.5$) in uniaxial ferroelectrics:

$$1/D = B_2 + C_2 t + A_2 |t|^{-0.5} \left| \ln |t| \right|^{b}. \tag{5.4}$$

− A model which contains a superposition of eq. 4.6 and eq. 4.9, taking into account both the contribution of the fluctuation effects and charged defects:

$$1/D = B_3 + C_3 t + A_3 |t|^{-0.5} + D_3 |t|^{-1.5}. \tag{5.5}$$

Let's remind that the critical analysis of acoustic properties such as ultrasound and hypersound velocities of $(Pb_x Sn_{1-x})_2 P_2 S_6$ mixed compounds, obtained by authors in reference [107], reveals that the ferroelectric phase of these crystals could be approximated using the Landau-Khalatnikov model, which is based on a classical mean-field approach. It is interesting to compare the results obtained from the study of the acoustic dynamic properties with one obtained from the analysis of thermal properties such as thermal diffusivity.

As seen from fig.5.7, our fittings performed for samples with Pb content of $x=0.1$, 0.2 and 0.3 are quite good proving that, indeed, the ferroelectric phase of $(Pb_x Sn_{1-x})_2 P_2 S_6$ mixed crystals can be well described by a classical Landau approach in terms of a mean-field model. Besides, the values of the phenomenological coefficients β' and γ calculated from the fittings fall within the range of already published values obtained by means of other techniques [107, 207]. Table 5.1 contains the relevant fitting parameters. When comparing our results with the data reported in reference [107], it can be said that due to the difference in the temperature resolution of the experimental curves, the results obtained from thermal diffusivity measurements have a higher level of confidence. Nevertheless, the general conclusion is practically the same, indicating that the behavior of both physical properties in the ferroelectric phase can be explained in terms of the classical mean-field model.
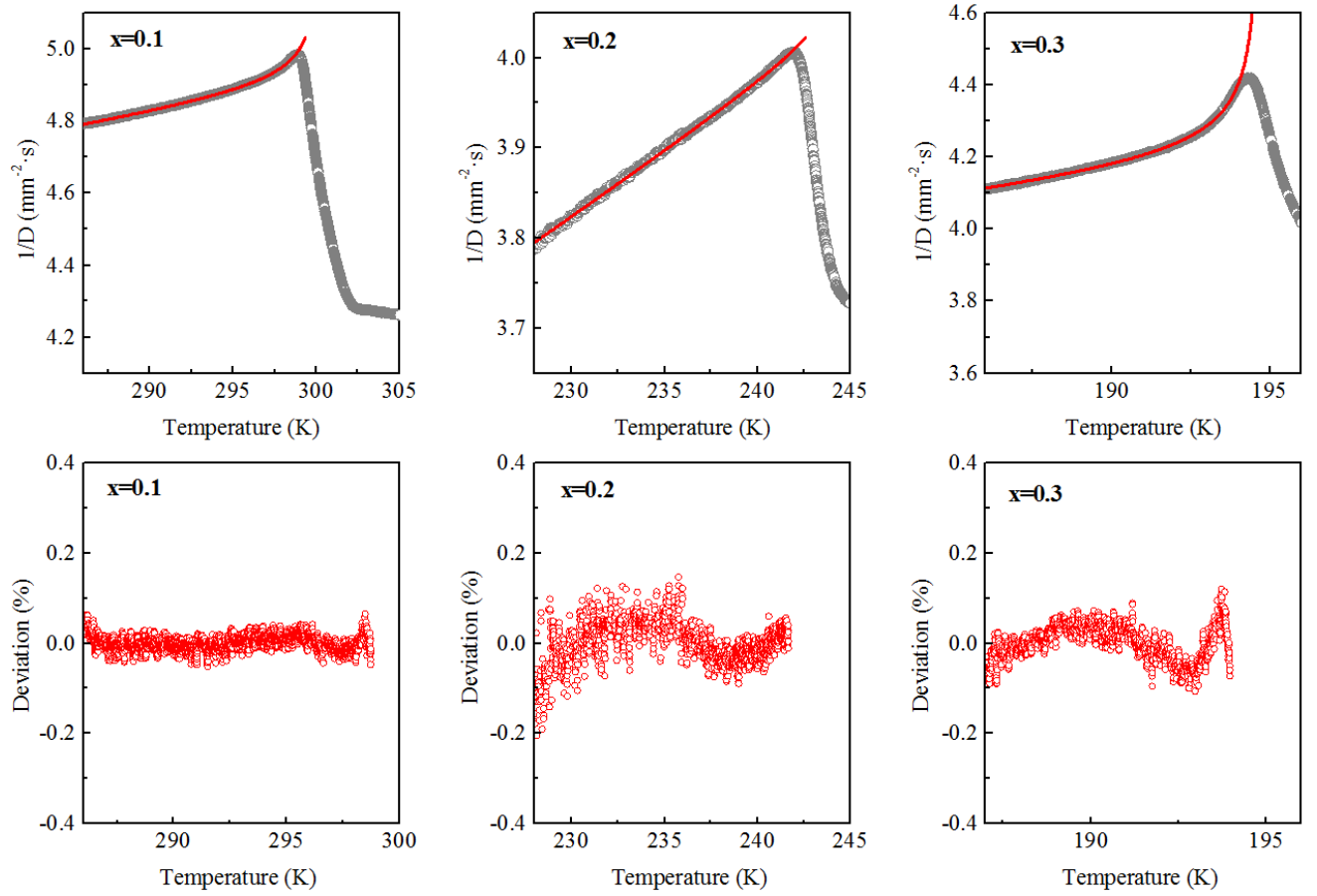
Fig. 5.7. Above: Experimental data for the 1/D as a function of the temperature for x=0.1; 0.2 and 0.3. Red line is the fit by eq.5.1 for the low symmetric phase. Below: Deviation plots corresponding to the fits [205].

Table 5.1.

Results obtained from the fitting by eq.5.1. Here p_1 and p_2 are the adjustable parameters; reduced temperature range t; R^2 is the fitting quality coefficient, β' and γ are coefficients in the Landau expansion eq.4.2 [205].

Parameters	x=0.1	x=0.2	x=0.3
p_1 (s/mm²)	$7.5\times10^{-4} \pm8\times10^{-5}$	$1.26\times10^{-4} \pm7\times10^{-6}$	$4.22\times10^{-3} \pm1.6\times10^{-4}$
p_2 (K⁻¹)	0.41 ± 0.06	0.16 ± 0.05	2.85 ± 0.28
Fitted range, t	$4.4\times10^{-2}-2\times10^{-3}$	$6\times10^{-2}-3.8\times10^{-3}$	$4\times10^{-2}-3.2\times10^{-3}$
R^2	0.9997	0.9992	0.9993
β' (Jm⁵C⁻⁴)	3.1×10^{9}	1.6×10^{10}	4.9×10^{8}
γ (Jm⁹C⁻⁶)	1.6×10^{12}	2.5×10^{13}	4.25×10^{11}

Taking into account both the ferroelectric and the paraelectric phases, eq.5.2 has been applied to the three crystals. For the sample with Pb concentration of 10% the fitting was possible only with huge values of $E^{\pm}$, which goes against the physical

meaning of the correction term in eq.5.2, which must be small. Therefore, this particular result falls out of consideration. In the case of *x*=0.2, a fitting was found with a critical value of $\alpha = -0.07 \pm 0.02$ and acceptable values of the rest of the parameters. For *x*=0.3 the fitting was even better and the critical exponent was equal to $\alpha = -0.04 \pm 0.01$. These two results indicate a tendency to approach the mean-field value, where $\alpha = 0$. This situation means there is a clear change in the critical behavior of the transition as Pb concentration increases. The fits and deviation plots are displayed on the fig. 5.8 while table 5.2 contains the relevant fitting parameters.
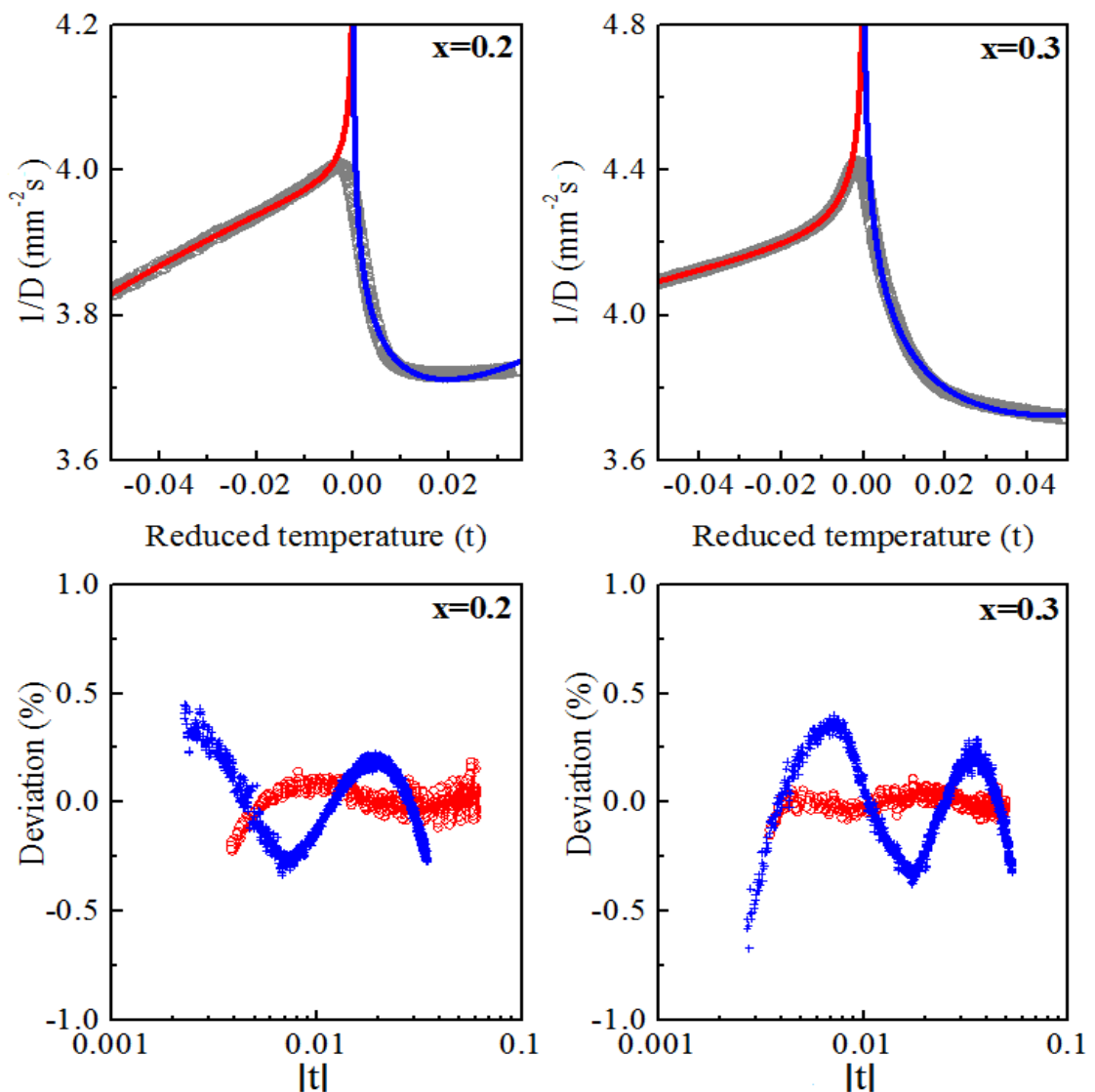
Fig. 5.8. Above: Experimental data for the 1/D as a function of the reduced temperature for *x*=0.2, 0.3. The lines represent the fits using eq. 5.2. Below: Deviation plots corresponding to the fits: blue crosses are for $T > T_c$, red open circles for $T < T_c$ [205].

Since (Pb$_x$Sn$_{1-x}$)$_2$P$_2$S$_6$ mixed ferroelectrics doped with x=0.1 and x=0.2 do not differ much from the undoped Sn$_2$P$_2$S$_6$, their paraelectric phases have also been analyzed checking the applicability of eq. 5.3-5.5. Starting with the sample x=0.1, the fit to eq.5.3 was not possible with critical index α=0.5. The best fitting was obtained with α =0.66, which is higher than theoretically predicted for first order fluctuations. Moreover, this value discards even testing eq.5.4. On the other hand, the fitting of the experimental data to eq.5.5 gave a nice outcome, whose results together with the deviation plots are displayed on fig.5.9. Moreover, the analysis of fitting parameters reveals a ratio D_3/A_3=2.4×10^{-4}, indicating that the contribution of charged defects to the critical anomaly is much smaller than the contribution of fluctuation effects. Nevertheless, the second term in eq.5.5 becomes dominating in the nearest neighborhood of the critical point stressing the importance of the defects role. Note that the same result was obtained by Oleaga and coworkers in publication [95] for undoped Sn$_2$P$_2$S$_6$ crystal, which was not surprising as Pb dopant has been introduced only in a 10% proportion.

Turning now our attention to the sample with x=0.2, the fitting to eq. 5.3 gave a critical exponent of $\alpha = 0.37$, which is too far away from 0.5. Such a low value cannot be corrected simply by a small multiplicative logarithmic correction, as theory predicts, using eq.5.4. That means that the intrinsic fluctuations in the sample are strongly suppressed. So, the next step was to fit using eq.5.5 and it provided rather a good result, even better than the one obtained for x=0.1 (see parameter R^2 in a table 5.2 and deviation plots on fig.5.9), with ratio D_3/A_3=4.3×10^{-4} , indicating an increment of defect influence with respect to the crystal with 10% of Pb content. When Pb is introduced in a higher atomic percentage, the relative influence of defects is enlarged. Note that, in a previously reported paper on the temperature evolution of the birefringence of Sn$_2$P$_2$S$_6$ ferroelectric crystal [200], the authors have also found that the introduction of Pb in a low atomic percentage (0.5%) into its crystal network increases coefficient D$_3$ in eq. 5.5. So, our results follow the same trend, confirming the importance of taking into account the charged defects contribution in the description of the critical anomaly.

In spite of having obtained quite good results for sample *x*=0.3 using the full critical model (eq.5.2) for both phases, eq.5.3-5.5 have been also put to test for the paraelectric one. With eq.5.3 the fit was possible with exponent α=−0.11 (but worse than with eq.5.2), while the two other models (eq.5.4 and 5.5) did not give good fittings.
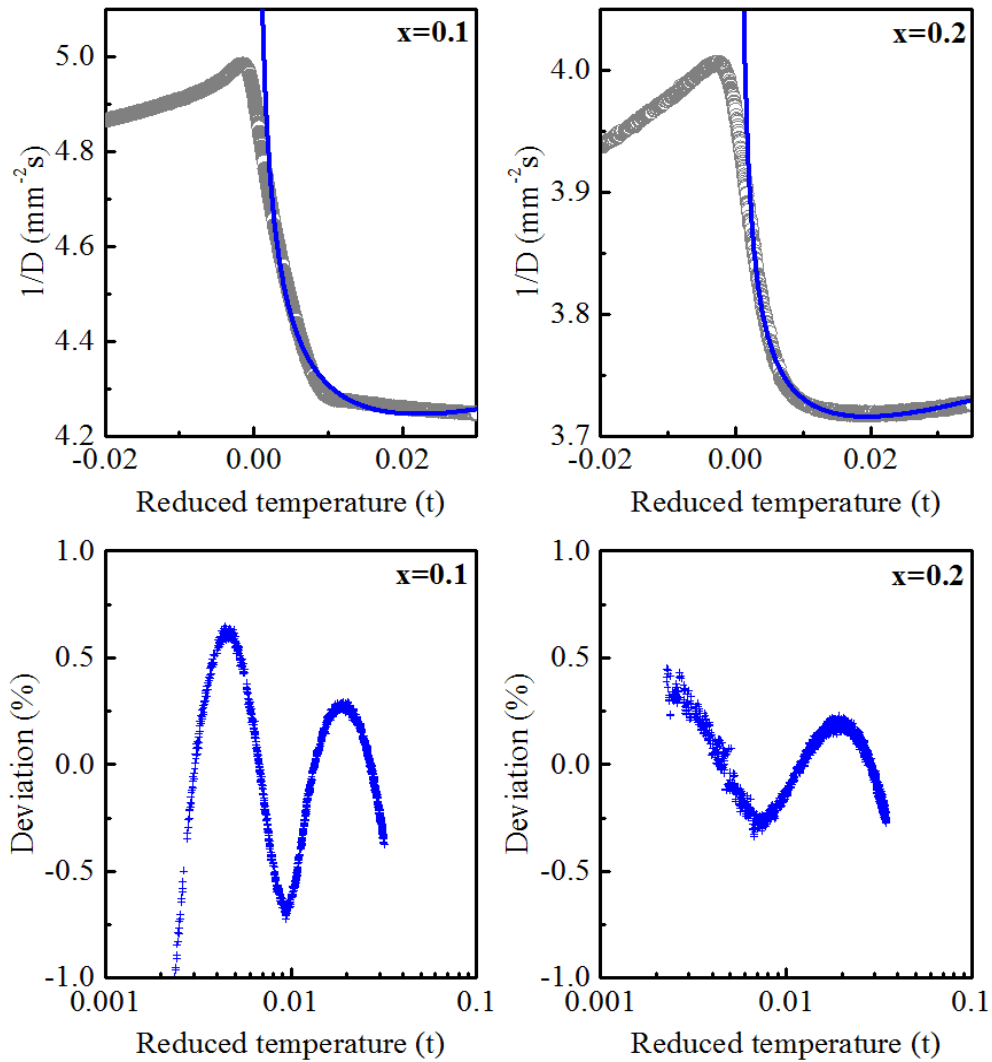
Fig. 5.9. Above: Experimental data for the inverse of thermal diffusivity (grey circles) for (Pb$_x$Sn$_{1-x}$)$_2$P$_2$S$_6$ crystals together with their fits to eq.5.5 (blue lines). Below: Deviation plots corresponding to the fittings, presented in percentage [205].

All these findings give a clear picture on how critical behavior changes when Pb ions are introduced in the cation sublattice of Sn$_2$P$_2$S$_6$ ferroelectric. In all cases the ferroelectric phase can be well described by the classical Landau model but this might be due to the fact that we can not get too close to the critical temperature on that side of

the phase transition, so we can not see the influence of the possible fluctuations of the order parameter and their enhancement or attenuation by some other mechanisms.

Table 5.2.

Results of fitting procedure for samples x=0.1, x=0.2 and x=0.3. Only the sensible fits are included in the table, which contains their relevant parameters, such as critical index α, fitted range t, fitting quality coefficient R^2, and adjustable fitting parameters $A^{\pm}$, A_1, A_3 and D_3 [205].

Model	Parameters	x=0.1	x=0.2	x=0.3
Eq.5.2	A^+ (s/mm^2)		0.76±0.27	4.38±0.81
	A^- (s/mm^2)		0.77±0.28	4.32±0.81
	α		-0.07±0.02	-0.04±0.01
	t for T>T$_C$		3.5×10^{-2}–2.3×10^{-3}	5.3×10^{-2}–2.7×10^{-3}
	t for T<T$_C$		6.0×10^{-2}–3.8×10^{-3}	7.4×10^{-2}–3.4×10^{-3}
	R^2		0.997	0.999
Eq.5.3	A_1 (s/mm^2)	0.014±0.002	0.043±0.005	
	α	0.66±0.02	0.369±0.015	
	t for T>T$_C$	3.2×10^{-2}–2.7×10^{-3}	3.5×10^{-2}–2.3×10^{-3}	
	R^2	0.979	0.986	
Eq.5.5	A_3 (s/mm^2)	0.0292±7×10^{-4}	0.0119±2×10^{-4}	
	D_3 (s/mm^2)	7.06×10^{-6}±9.6×10^{-7}	5.11×10^{-6}±2.5×10^{-7}	
	D_3/A_3	2.4×10^{-4}	4.3×10^{-4}	
	t for T>T$_C$	3.2×10^{-2}–2.7×10^{-3}	3.5×10^{-2}–2.3×10^{-3}	
	R^2	0.977	0.992	

At low atomic percentage of dopands (x=0.1), the behavior in the vicinity of T$_c$ is practically the same as for the undoped sample, where a combination of several competing mechanisms is needed to describe the anomaly in the paraelectric phase. On the one hand, the nearness to a Lifshitz point enhances the fluctuations of the order parameter while on the other one, the nearness to a tricritical point reduces them. Besides, point defects are responsible for inducing long-range perturbations of the order parameter. The combination of all of them is needed to take into account a clear deviation from a mean field model, which has been discarded by the appropriate fittings.

An interesting event happens when Pb content is increased: for the sample doped with x=0.2 a clear evolution starts, because its critical behavior can be explained by two models. The first one, obtained by only fitting the paraelectric phase, is a combination

of the first fluctuational correction together with the contribution of charged defects (eq.5.5), similarly to x=0.1. The second model is the one which takes into account both phases at the same time (eq. 5.2) whose fitting gave a critical index $\alpha = -0.07$, which is close to the mean-field one. Finally, if Pb ions are introduced in a proportion of x=0.3, a very nice fitting of both phases to eq.5.2 gives a critical parameter $\alpha = -0.04$, which is even closer to the mean field model (α=0), while it was not possible to fit it to any model with had any relation to the nearness to Lifshitz or tricritical points or the contribution of point defects. This result implies that the sample with x=0.3 behaves as a common uniaxial ferroelectric, where long range interactions are dominating. Thus, comparing the critical studies for these three samples, a clear evolution from a non mean-field behavior to it has been observed, when Sn ions are substituted by Pb ones in $(Pb_xSn_{1-x})_2P_2S_6$ mixed ferroelectrics up to x=0.3.

5.5. Conclusions

The thermal diffusivity of $(Pb_xSn_{1-x})_2P_2S_6$ ferroelectric family has been measured in a wide temperature range, observing the typical behavior of poor thermal conductive materials, where phonons are predominant in heat propagation. Thermal anisotropy has been confirmed for $Pb_2P_2S_6$ paraelectric crystal with monoclinic structure. The second order character of the transition has been proved for samples with Pb content of x=0.1, 0.2, 0.3 and 0.45. The evolution of critical behavior when introducing Pb ions has been observed. There is a crossover from a non-mean field behavior at x=0.1 (the first fluctuational correction and the contribution of charged defects must be taken into account) to a mean-field one at x=0.3 (long-range interactions are predominating).

CHAPTER 6

Experimental results and discussion on (Pb$_x$Sn$_{1-x}$)$_2$P$_2$Se$_6$ mixed ferroelectrics

6.1. Introduction

This chapter is focused on the third and last part of the general phase diagram (fig.3.7). After chapter 3, it is established that the substitution of Sn by Pb atoms in (Pb$_x$Sn$_{1-x}$)$_2$P$_2$Se$_6$ series leads to a decrease in the temperature of both the paraelectric to incommensurate (T$_i$) and the incommensurate to ferroelectric (T$_c$) phase transitions. At the same time, the temperature width of the incommensurate phase considerably increases [3]. Such ion replacing also alter the shape of the anomalies at critical temperatures T$_i$ and T$_c$, which become more smeared around the phase transitions when Pb is introduced in the crystal lattice. The question we are interested in is: how the introduction of Pb dopands into (Pb$_x$Sn$_{1-x}$)$_2$P$_2$Se$_6$ mixed crystals (whose state diagram after ref. [94, 109] is displayed on fig.6.1) will affect the thermal properties and the critical behavior in the neighborhood of the second order phase transition at T$_i$ (paraelectric to incommensurate).

Thus, the aim of this chapter is to thermally characterize the family (Pb$_x$Sn$_{1-x}$)$_2$P$_2$Se$_6$ measuring thermal diffusivity in a wide temperature range (from 30K to room temperature), studying the character of the different phase transitions as well as the critical behavior of the continuous ones.

6.2. Samples characterization

Single semiconductor crystals (Pb$_x$Sn$_{1-x}$)$_2$P$_2$Se$_6$ with monoclinic crystalline structure [76] were grown by a vapor-transport method in a quartz tube using SnI$_2$ as a transport reagent. The nominal concentrations of Pb were as follows x=0, 0.05, 0.1, 0.2, 0.47, 0.8 and 1. The crystals were prepared in three groups. The first one comprises x=0 and 1. Thin plane parallel slabs (300-500μm) were cut and polished in the monoclinic symmetry plane perpendicular to (010) direction, so their absolute values could be compared with to the ones reported in [205]. Second group includes the samples with x=0.05, 0.2, and 0.47. The growth of these mixed solid solutions turned out to be more difficult; hence, small and brittle crystals were obtained. Finally, the crystals with Pb

concentrations of x=0.1 and 0.8 were grown in order to extend the concentration series. When preparing thin plane parallel slabs with Pb contents of x=0.05, 0.1, 0.2, and 0.47, it was not possible to obtain their surfaces in a direction perpendicular to (010) but only to the (100) one. In particular, for one crystal (Pb$_{0.8}$Sn$_{0.2}$)$_2$P$_2$Se$_6$ was even impossible to find any principal direction; as a consequence, the sample was prepared to measure only the effective value of thermal diffusivity. The crystalline quality has been checked by X-ray measurements, which was very good save for the sample with x=0.8, which had an evident worse quality than the rest of the crystals.
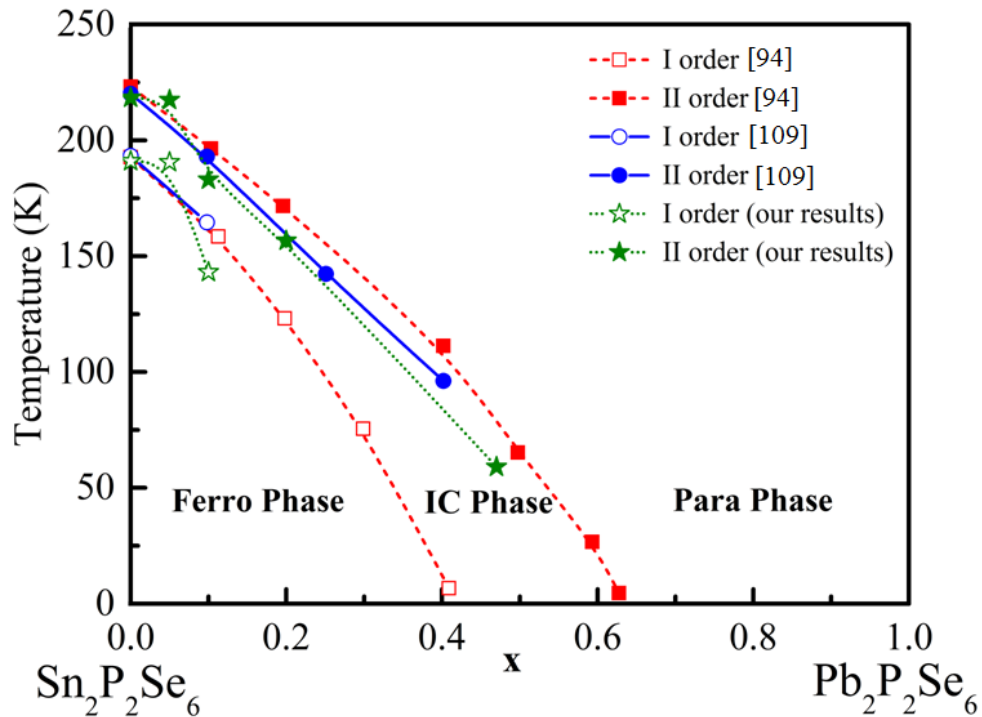
Fig. 6.1. Phase diagram for (Pb$_x$Sn$_{1-x}$)$_2$P$_2$Se$_6$ mixed ferroelectrics after references [94, 109] together with data obtained from our thermal diffusivity measurements [60, 208, 209]. The solid symbols present the second order transition from the paraelectric phase to the incommensurate one. Empty symbols indicate the first order transition from the incommensurate to ferroelectric phase. Lines are just guides for the eye.

6.3. Experimental results

Thermal diffusivity (*D*) curves for lead/sulfur-selenium mixed compounds in a temperature range from 30K till room temperature are presented in fig.6.2. As explained in a section 2, in samples x=0 and 1 *D* was measured along (010) crystallographic direction while in samples x=0.05, 0.1, 0.2 and 0.47 it was measured along the (100) direction. Note that for x=0.8 an effective thermal diffusivity has been obtained. Since

the thermal anisotropy for these materials is well established [205, 95, 127] and thermal diffusivity as well as thermal conductivity are higher in the (100) direction than in the (010) one, the two curves for x=0 and x=1 will have a higher value in the (100) direction than what is shown in fig.6.2, being above the rest of the curves at room temperature. This behavior has already been observed when comparing thermal diffusivity curves in the three directions at room temperature for Sn$_2$P$_2$S$_6$ [95] and Pb$_2$P$_2$S$_6$ (see figure 5.5 in chapter 5 and [205]).
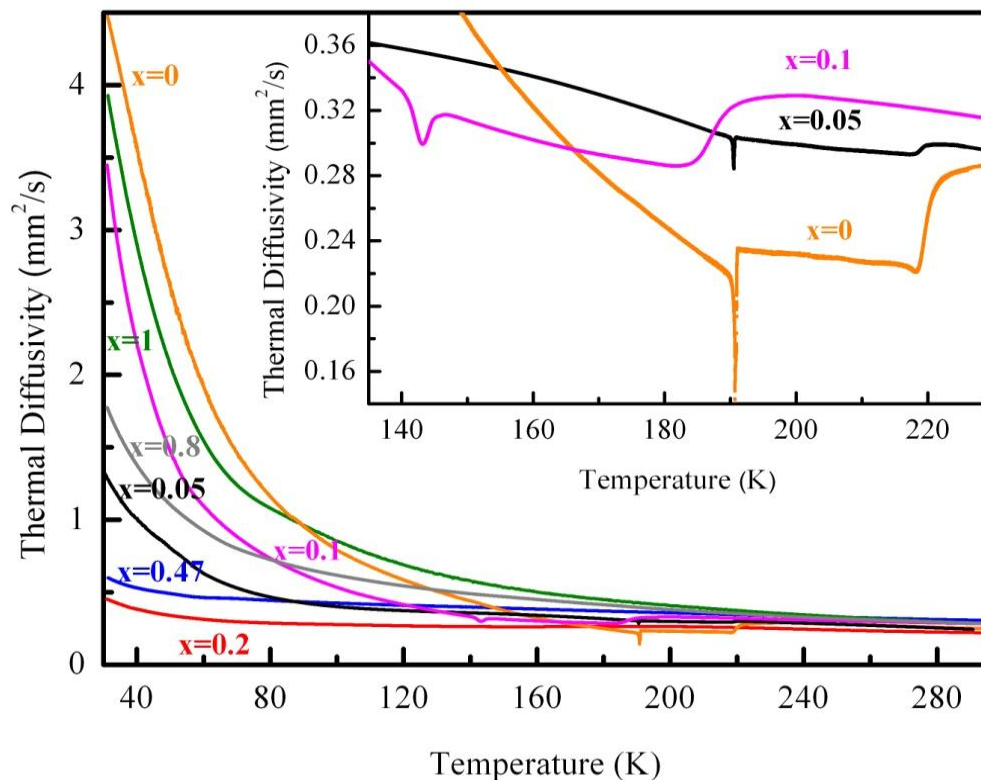
Fig.6.2. Temperature evolution of our thermal diffusivity data for (Pb$_x$Sn$_{1-x}$)$_2$P$_2$Se$_6$ crystals [208].

As seen from fig.6.2 the general trend is maintained in all curves and thermal diffusivity increases with decreasing temperature. The same has been observed in the case of (Pb$_x$Sn$_{1-x}$)$_2$P$_2$S$_6$ ferroelectrics (see fig 5.3 in chapter 5 and [205]), confirming their thermal insulator behavior, where phonons are responsible for the heat transport. The increase of *D* for the mixed compounds at lower temperatures is slowlier than that for undoped crystals. This can be explained by the presence of two different species (Pb and Sn) with different sizes (Pb^{2+} ionic radius is larger than that for Sn^{2+}) in the cation sublattice for mixed compositions. As a consequence, both atoms share the same space

available for them, distorting the crystalline lattice and, in turn, reducing the phonon mean free path.

Dips have been observed superimposed on the curves for samples x=0, 0.05, 0.1, 0.2, and 0.47 indicating the presence of phase transitions (fig.6.2). The first order transition from the incommensurate to the ferroelectric phase has been detected only on the crystals with concentrations x=0, 0.05, and 0.1; they can be seen in the inset of fig 6.2 (lower temperature transitions) and are presented in detail in fig.6.3. As seen from the latter figure, there is a clear hysteresis indicated not only by the difference of the critical temperature on high resolution (10mK/min) heating and cooling runs but also by the difference in shape between them, confirming the discontinuous character of the transition. It is worth noting that the temperature difference is increased when Pb is introduced in a higher atomic percentage. This is in agreement with data reported by Vysochanskii and coworkers obtained by means of light transmission measurements [94].
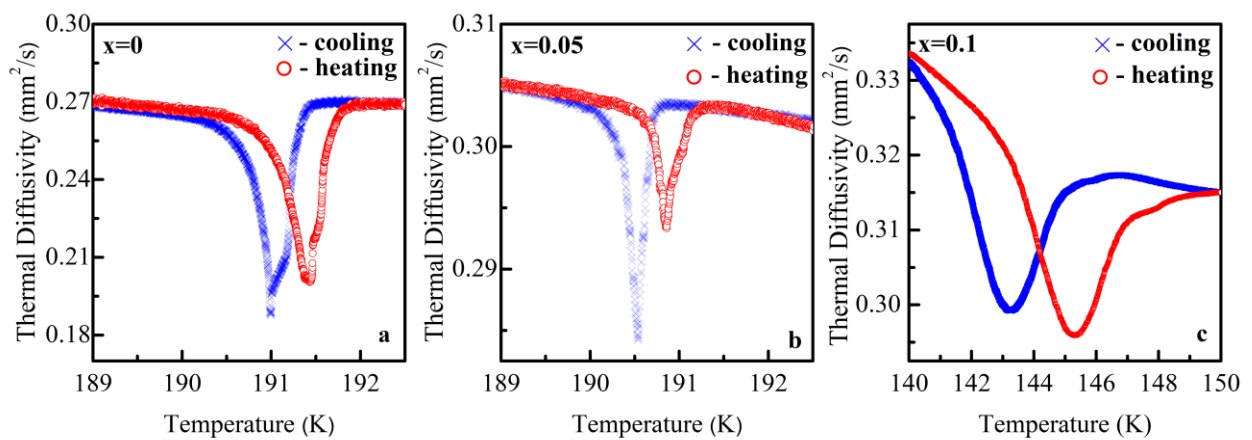
Fig. 6.3. Thermal diffusivity as a function of temperature for(Pb$_x$Sn$_{1-x}$)$_2$P$_2$Se$_6$. First order transition: (a) x=0; (b) x=0.05 and (c) x=0.1.

The continuous paraelectric to incommensurate phase transition has been detected in the samples with lead concentrations of x=0, 0.05, 0.1, 0.2, and 0.47. As they can not be well appreciated in fig.6.2, fig 6.4 illustrates them in detail, confirming that the increase of Pb concentration induces an expanding smearing of the anomaly at T$_i$. First, the anomaly becomes less marked at low dopant concentration (x=0.05) with respect to the pure crystal. Then, starting with x=0.1 to x=0.2, the transition becomes more

"extended" in temperature. Note that the vertical scale for x=0.2 is extremely shallow compared to the one for x=0.
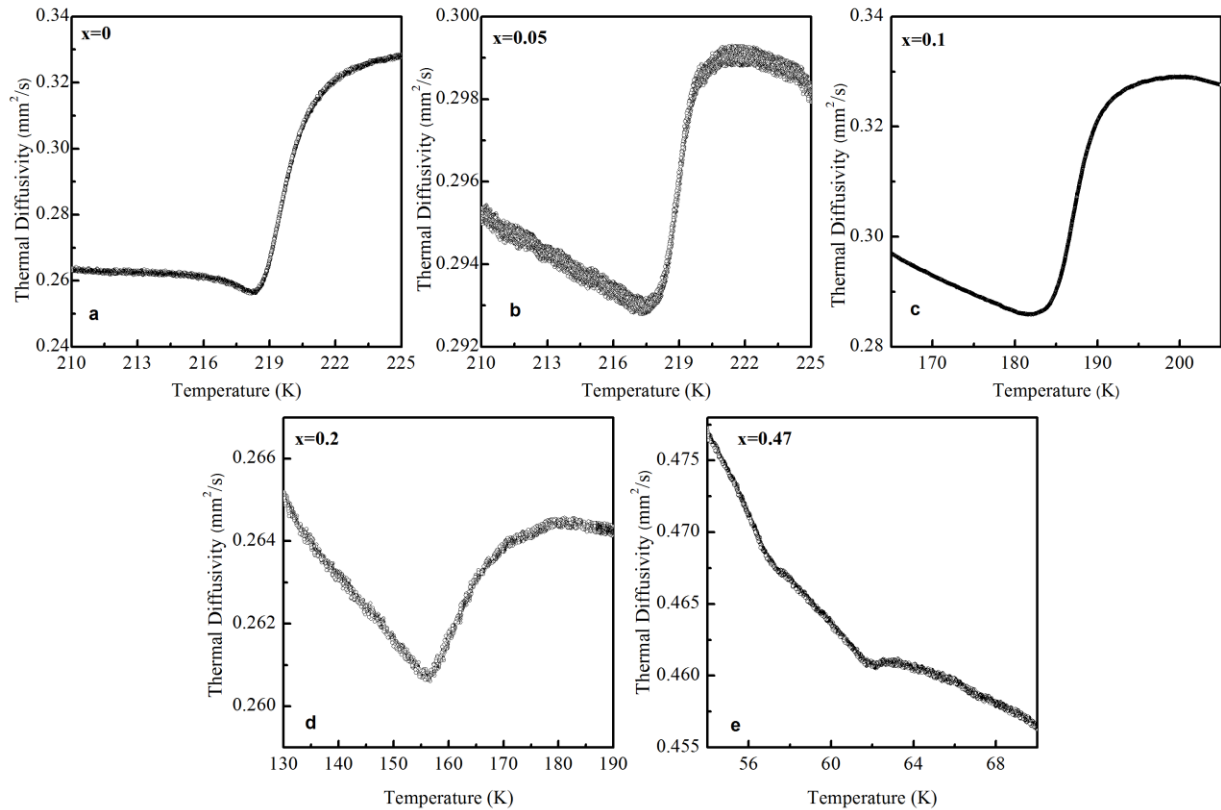
Fig. 6.4. Thermal diffusivity as a function of temperature for$(Pb_xSn_{1-x})_2P_2Se_6$. Second order transition: (a) x=0; (b) x=0.05; (c) x=0.1; (d) x=0.2; (f) x=0.47.

Further increasing of Pb contents to x=0.47 leads to even a stronger smearing of the transition (fig.6.3.e). Nevertheless, two distinct changes in the slope of the thermal diffusivity curve are seen, separated by about 7K. These two points probably indicate the starting and finishing points of the phase transition. Note that the continuous transition at x=0.47 is even more "suppressed" than that at x=0.2, meaning that transition itself is dissolved at higher Pb content. For the samples doped with x=0.8 and x=1 the measurement has been performed down to 30K and no transition of any kind was found in any of them. The continuous character of the transitions displayed on fig.6.3 has been checked out by repeating slow heating and cooling runs several times. No hysteresis is hinted, neither by the difference in critical temperature nor in the shapes of the thermal diffusivity curves. The resulting phase transition temperatures which have been observed in this work are also plotted on fig.6.1. As can be seen, there

is some discrepancy between data reported by different authors [94, 109] and our results. As it is well known, the precise position of any phase transition depends heavily on the stoichiometry of the particular sample, which is a question of the growing procedure. This could be the reason for the temperature discrepancies of the transitions, since the authors in [94, 109] have worked with different samples than us.

6.4. Critical behavior

Regarding the critical analysis, we have used as fitting variable the inverse of the thermal diffusivity, since it behaves as specific heat in the critical region (see the previous chapter for the justification), using eq.5.2 based on the modern critical theory and fitting both branches of the phase transition at the same time.

$$1/D = B + Ct + A^{\pm} |t|^{-\alpha} \left(1 + E^{\pm} |t|^{0.5} \right). \tag{6.1}$$

Unfortunately, only the thermal diffusivity dips for x=0, 0.05 and 0.1 are useful to retrieve meaningful information. In particular, the sample doped with 10% of Pb is probably the limiting case for which such a quantitative study can be performed, since for x=0.2 the shape of the anomaly is too rounded.

The results of the fitting are shown in fig.6.5, together with the corresponding deviation plots, which signal the deviation of the fitted curves from the experimental data. The relevant fitted parameters are gathered in table 6.1. As seen from the table, the critical index α as well as the ratio of the critical coefficients A^+/A^- for all three samples x=0, 0.05 and 0.1 are in good agreement with the 3D-XY model (theoretical value for α=-0.014 and ratio A^+/A^-=1.06), as predicted by renormalization group theory (see chapter 4, section 4.3). This model assumes that a two component order parameter is needed to describe the Hamiltonian for the system, as was aforementioned. The quality of the fittings is confirmed by the high coefficient of determination R^2 (for an ideal fit R^2=1).

It is worth noting that the critical behavior analysis of (Pb$_x$Sn$_{1-x}$)$_2$P$_2$Se$_6$ family had been previously undertaken only for the undoped Sn$_2$P$_2$Se$_6$ crystal, measuring optical birefringence [202, 204] or neutron magnetic resonance (NMR) [203]. Moreover, in those publications only one phase of the transition has been considered, the paraelectric

one for birefringence and the incommensurate one for NMR. Bear in mind that our results have been obtained simultaneously fitting both low and high temperature branches of the critical anomaly. Our fits have also been performed under the strictest theoretical conditions described in section 4.2, which is the only way to retrieve valuable information on the appropriate universality class. In this respect, the results obtained from our thermal diffusivity measurements accompanied with the findings reported in [202, 203, 204] give us a clear picture, indicating that the continuous paraelectric to incommensurate phase transitions at x=0, 0.05 and 0.1 add up to the list of the 3D-XY universality class.
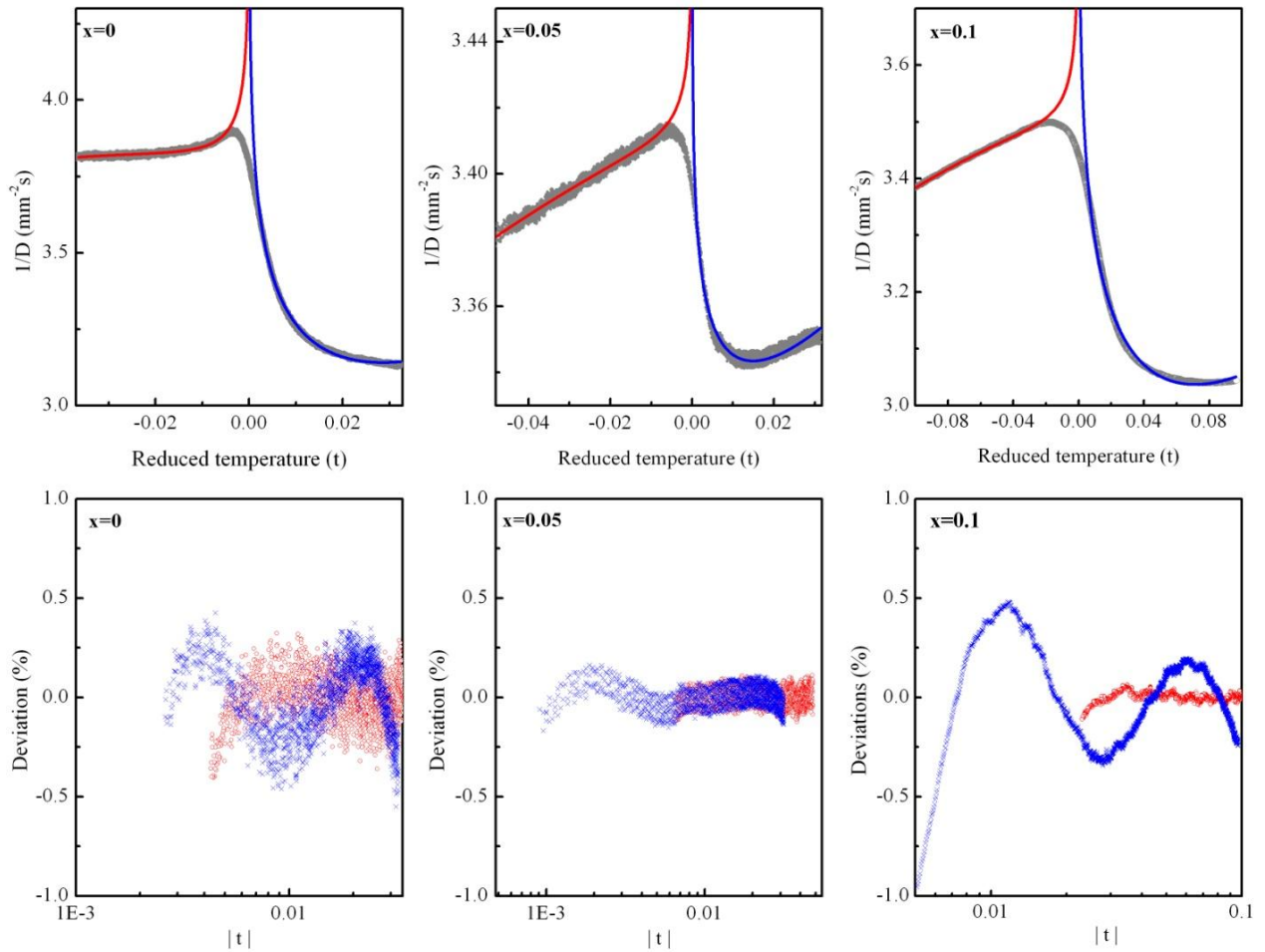
Fig.6.5. Above: Experimental data (circles) for the inverse of thermal diffusivity as a function of the reduced temperature t = (T-T_C)/T_C for $(Pb_xSn_{1-x})_2P_2Se_6$ ferroelectrics. The lines represent the fits to eq. 6.1, fitting both branches at the same time. Below: Deviation plots corresponding to the fits shown above. Open circles are for T < T_C and crosses for T > T_C.

Table 6.1.

Results of the fitting of the inverse of thermal diffusivity using eq. 6.1. The relevant fitting parameters are shown together with the fitted range in reduced temperature units $t=(T-T_C)/T_C$ as well the quality of the fitting through the coefficient of determination R^2.

Parameters	x=0	x=0.05	x=0.1
α	-0.019 ± 0.008	-0.026 ± 0.018	-0.018 ± 0.007
A^+/A^-	1.00	1.03	0.99
Fitted range for $T > Tc$	$2.6\times10^{-3}\text{-}3.2\times10^{-2}$	$9.1\times10^{-4}\text{-}3.1\times10^{-2}$	$5.07\times10^{-3}\text{-}9.63\times10^{-2}$
Fitted range for $T < Tc$	$4.3\times10^{-3}\text{-}3.6\times10^{-2}$	$6.4\times10^{-3}\text{-}4.8\times10^{-2}$	$2.21\times10^{-2}\text{-}1.05\times10^{-1}$
R^2	0.999	0.995	0.999

6.5. Conclusions

The thermal diffusivity in (Pb$_x$Sn$_{1-x}$)$_2$P$_2$Se$_6$ mixed ferroelectrics has been measured in a range from 30K till room temperature using an ac photopyroelectric calorimeter. A temperature evolution typical for thermally insulating materials has been observed. The structural first order transition from the ferroelectric to the incommensurate phase has been detected for samples with Pb contents of x=0, 0.05 and 0.1 and its hysteresis checked. In turn, the continuous paraelectric commensurate to incommensurate phase transition has been observed for x=0, 0.05, 0.1, 0.2, and 0.47. The critical behavior of this transition has been studied for x=0, 0.05 and 0.1. The critical parameters obtained from the analysis allow to attribute these three transitions to the 3D-XY universality class. The samples doped with x=0.8 and x=1 do not show any transition in the full temperature range of study (30K to room temperature).

CHAPTER 7

Experimental results and discussion on $Sn_2P_2S_6$ doped with Ge, Sb, Te

7.1. Introduction

Isovalent doping can significantly modify the physical properties of a material. Concerning $Sn_2P_2S_6$ − like crystals, a significant property is ferroelectricity. The nature of that effect comes from the stereochemical activity of the electron lone pair $(5s^2)$ of Sn atoms in the cation sublattice, which is determined by a hybridization with P_2S_6 molecular electronic levels $(3p^4)$. As a result of those electronic orbital interactions a spontaneous polarization appears [115, 210, 211]. In this chapter we consider the influence of isovalent atom substitutions on the ferroelectric properties of $Sn_2P_2S_6$ crystal, which presents a second order ferroelectric to paraelectric phase transition at about 337K. At the same time, it is also interesting to study the evolution of its critical behavior in the neighborhood of the transition, when Sn is replaced by Ge, or P by Sb or S by Te in the crystal lattice. This might give relevant information about the influence and contribution of the different species to the physical mechanisms responsible for the critical anomaly.

7.2. Samples and measuring procedure

Single crystals of $Sn_2P_2S_6$ doped with Ge, Sb and Te atoms were grown by a vapour-transport method in a quartz tube using SnI_2 as a transport reagent. The synthesis of the starting material in the polycrystalline form has been carried out using high-purity elements Sn (99.99%), P (99.999%), S (99.99%), Ge (99.999%), Sb (99.999%), Te (99.99%), the numbers in parenthesis representing the atomic percentage. The nominal content of dopants, given in atomic percentage, is as follows: Ge: 3%, 5%; Sb: 0.5%, 1%, 2% and Te: 1%, 2%. Depending on the particular doping the samples present different color: for Ge it is a light orange, while for Sb and Te the color is light red and light brown, respectively.

For thermal diffusivity investigations the crystals have been prepared in the form of thin plane-parallel slabs with faces perpendicular to the (001) crystallographic direction and thickness in a range of 0.500-0.530 mm. The experimental setup and

measuring procedure used during the study have been the same as those used in chapters 5 and 6, complying with all the theoretical requirements needed. The only difference has been the use of another cryostat. Since the temperatures of interest for these materials falls out of the working regime of a closed cycle He cryostat (20-320K), a liquid nitrogen bath cryostat has been employed (78-400K).

7.3. Experimental results

Thermal diffusivity as a function of temperature has been measured for all doped samples in a range of 295-395K. The experimental curves are presented on fig.7.1.-7.3. To better compare and visually see the influence of each dopant (Ge, Sb and Te) the previously measured thermal diffusivity for the pure $Sn_2P_2S_6$ along its (001) direction [95] has been also included in fig. 7.1-7.3. For all curves a dip superimposed on the typical evolution with temperature signals the presence of a second order phase transition from the initial high temperature paraelectric phase to the low temperature ferroelectric one. As seen from graphs 7.1-7.3 the three dopants alter the original shape of the transition but in a different way.

Introducing Ge atoms into the cation sublattice of $Sn_2P_2S_6$ crystal increases the critical temperature. From the initial value of $T_C = 336.2$ K for the undoped sample, it rises up to 346.1K at 3% Ge and then to 349.2K for the nominal Ge content of 5% (fig.7.1). An increase of the transition temperature had already been observed by Maior and coworkers [212] measuring the temperature evolution of the piezoelectric and pyroelectric coefficients but with less resolution. It should be pointed out, that the dip of the transition becomes sharper as Ge is introduced at higher atomic percentage.
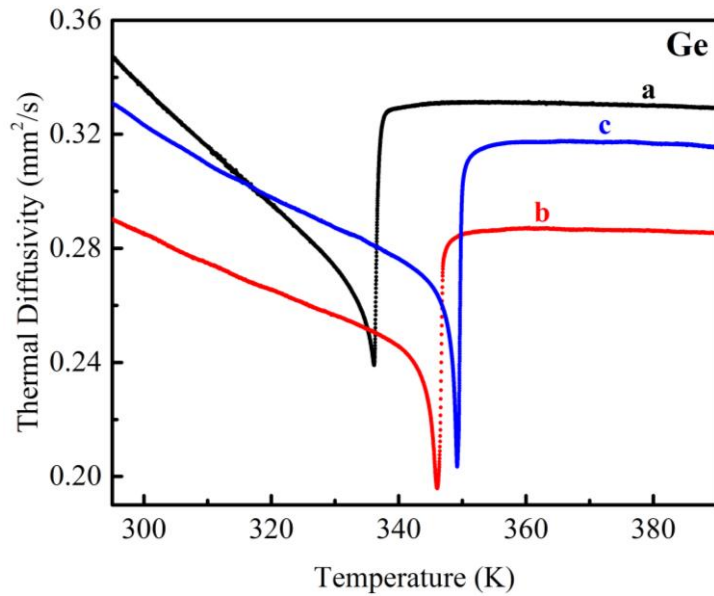
Fig. 7.1. Thermal diffusivity in the (001) direction as a function of temperature for $Sn_2P_2S_6$ doped with Ge: (a) pure $Sn_2P_2S_6$ [95]; (b) $Sn_2P_2S_6$+3%Ge; (c) $Sn_2P_2S_6$+5%Ge.

On the contrary, Sb atoms, which are isovalent to P in the anion sublattice, provoke a slight downward shift in the critical temperature. But the effect is much smaller compared to the influence of Ge atoms. At the same time, the transition is broadened and the shape of the anomaly at T_C is more rounded. For the samples doped with Sb of 1% and 2% the position of the transition temperature is practically the same but the general evolution of *D(T)* dependence is altered (see fig. 7.2).
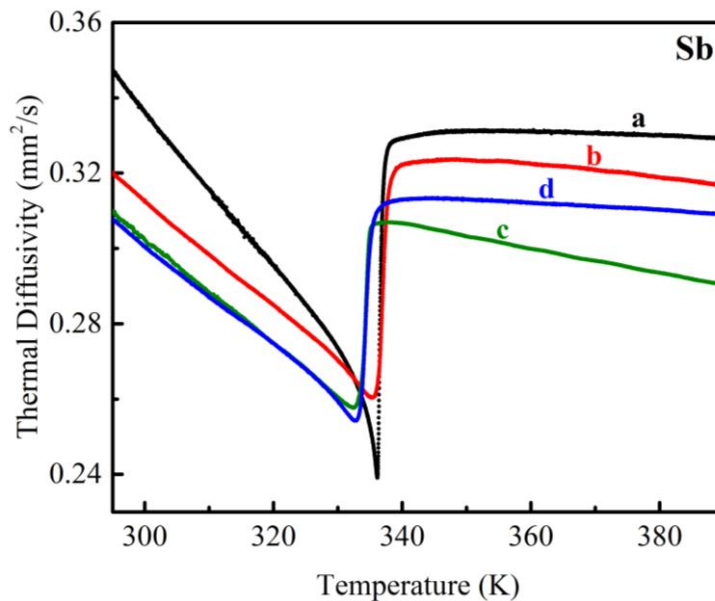
Fig. 7.2. Thermal diffusivity in the (001) direction as a function of temperature for $Sn_2P_2S_6$ doped with Sb: (a) pure $Sn_2P_2S_6$ [95]; (b) $Sn_2P_2S_6$+0.5%Sb; (c) $Sn_2P_2S_6$+1%Sb; (c) $Sn_2P_2S_6$+2%Sb.

Concerning the substitution of S by Te, there is just a minor variation in the critical temperature between the undoped crystal and the doped ones (1%, 2%, see fig.7.3). As seen from the graph, in the case of Te the shapes of the anomalies are more similar to the undoped ones than in the case of Ge and Sb. Roughly, we can say there is only a vertical extension of the dip at 1% of Te and a compression for the 2% doped sample compared to the pure $Sn_2P_2S_6$.
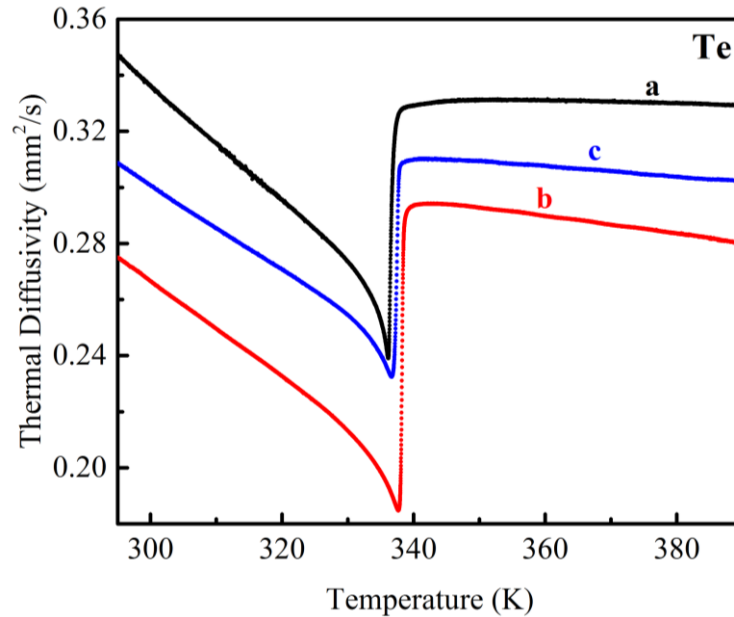
Fig. 7.3. Thermal diffusivity in the (001) direction as a function of temperature for $Sn_2P_2S_6$ doped with Te: (a) pure $Sn_2P_2S_6$ [95]; (b) $Sn_2P_2S_6$+1%Te; (c) $Sn_2P_2S_6$+2%Te.

For all cases the continuous character of the transitions has been confirmed by the lack of a temperature hysteresis performing slow heating-cooling runs (20-25mK/min). There was also no difference in the shape of the anomalies on heating and cooling regimes.

It is worth noting that there is one common feature among fig.7.1-7.3. For all three cases the absolute value of the thermal diffusivity is reduced at "low" dopant contents while a further doping increase leads to a rise in thermal diffusivity, but always smaller than the one for the undoped sample. Moreover, the absolute value of D is quite low for all samples and fall within the range of poor thermal conductors, where phonons play the main role in heat transport. It is quite common that, in thermal insulators, small additions of dopant reduce the phonon mean free path due to the disorder introduced while from a certain atomic percentage up there is a relative increment, as it happens

with these crystals. This feature has also been observed when studying the thermal diffusivity at room temperature for $(Pb_xSn_{1-x})_2P_2S_6$ mixed compounds (fig.5.2), where doped samples had a lower values than the undoped ones [205]. The possible reason for a low thermal diffusivity for $Sn_2P_2S_6$ − like ferroelectrics at room temperature is the low mean group velocity of their short-wave acoustic phonons and the small phonon mean free path, which is comparable to the unit cell size of these crystals [127].

7.4. Influence on the ferroelectricity

Let's discuss the influence of the particular dopant on the ferroelectric properties of $Sn_2P_2S_6$ crystal. As the spontaneous polarization in this material is attributed to the stereoactivity of the Sn atoms in the cation sublattice, we will first consider the influence of Ge. As seen from fig. 7.1, the transition itself becomes sharper and it is shifted to higher temperatures with the increased addition of Ge. As stated in ref. [211], the origin of the ferroelectricity lies in the hybridization of the electronic orbitals of the cation Sn^{2+} ($5s^2$) and $P_2S_6^{4-}$ (3p) anion sublattices and it heavily depends on the energy distance between their electronic state levels. Thus, the isovalent atoms entering the stereoactive cation sublattice will change this hybridization affecting the ferroelectric properties. Thus, the introduction of Ge ($4s^2$) instead of Sn ($5s^2$) reduces the energy difference between the electronic states responsible for the hybridization, and as a consequence the ferroelectric state can be stable at higher temperatures. Exactly the opposite effect has been observed when Sn is replaced by Pb. Because of the larger energy distance between Pb ($6s^2$) and $P_2S_6^{4-}$ (3p) electronic states the hybridization becomes weaker, disfavoring the ferroelectricity, which is reflected in the lowering of the transition temperature and the smearing in the shape of the critical anomaly (see fig.5.4 in chapter 5).

Turning our attention to $Sn_2P_2S_6$ doped with Sb, it is clear from fig.7.2 that there is some broadening of the transition and a slight reduction in the critical temperature. Both the broadening and the decrease in temperature T_C suggest a slight disfavor of the ferroelectricity. As stated in ref. [211], the contribution of the P_2S_6 clusters to the ferroelectricity, whose acentricity is mainly reflected in the deformation of the charge

distribution along the P-P bonds, is much smaller than the contribution of Sn atoms. The isovalent replacement of P by Sb atoms with larger atomic radius modifies the position of the energy levels at the top of valence band [213], which could be related to the slight disfavor of ferroelectricity.

Finally, as seen from fig. 7.3 the Te atoms practically do not alter the position of the critical temperature, keeping the similar features in the shape of the anomalies. It could be said that there is a very slight favoring of the ferroelectricity. The effect of Te on the electronic orbitals has been also studied by XPS [213] with the conclusion that there is a strong hybridization with P and S orbitals near the top of the valence band but with a very slight influence on the Sn^{2+} lone pair, thus having very little influence on the stereoactivity. Hence, the results we have obtained are not surprising when Te substitutes non-ferroactive S atoms in the crystal lattice.

7.5. Critical behavior

The phase transition has been quantitatively analyzed in all samples to study the evolution of the critical behavior with doping. The models put to test have been the same ones as exposed on chapter 5, for the same reasons. Therefore, the inverse of thermal diffusivity *1/D* has been fitted by theoretical models corresponding to the equations 5.1-5.5.

The first equation used has been the classical Landau approach in terms of general mean-field model taking into account the possible coupling of polarization to strain (eq. 5.1), applied to the ferroelectric phase and that we reproduce here for the sake of clarity.

$$1/D = B + C(T-T_c) + p_1 \frac{T}{\sqrt{1-4p_2(T-T_c)}},\qquad(7.1)$$

with $p_1 = a^2/(2\beta'K)$, $p_2 = \gamma a/(\beta'^2)$. In all cases the fits were quite good indicating, that, indeed, the temperature evolution of the inverse of the thermal diffusivity in the low temperature phase of these doped ferroelectrics can be nicely described by a Landau model. Moreover, depending on the particular dopant (Ge, Sb or Te), there is some variation in the phenomenological parameters in the Landau expansion β' and γ obtained

from the fitting coefficients. We can compare them with the obtained ones for the pure sample using the same technique by Oleaga *et al* [95]. Both β' and γ are reduced with an increase of germanium content, the first maintaining the positive sign, which confirms the second order character of the transition (see table 7.1). This reduction is due to the fact that the transition becomes sharper. The introduction of Sb instead of P in $Sn_2P_2S_6$ crystal lattice also alters the values of the phenomenological Landau parameters (Table 7.1), with the difference that the phenomenological coefficient β' is slightly decreased and γ is heavily reduced when compared with the pure sample (Table 7.1). The reduction in β' is related to the broadening of the transition. Finally, the introduction of Te atoms slightly increases both coefficients β' and γ but, in all, they do not differ much from those of the undoped $Sn_2P_2S_6$.

Table 7.1.

Results of the fitting using the Landau model (eq. 7.1). The columns show the adjustable parameters p_1 and p_2, the fitted range in reduced temperature units $t=(T-T_C)/T_C$, the coefficient of determination R^2, as well as the calculated phenomenological parameters in the Landau expansion β' and γ. The values for $Sn_2P_2S_6$ are extracted from ref [95].

Sample	p_1 (s/mm^2)	p_2 (K^{-1})	Fitted range	R^2	β'(Jm^{5}C^{-4})	γ(Jm^{9}C^{-6})
$Sn_2P_2S_6$	3.321×10^{-3} $\pm4\times10^{-6}$	0.0512 ±0.0002	3.2×10^{-2}-2.0×10^{-3}	0.9922	6.1×10^{8}	2.3×10^{10}
3% Ge	0.0185 ±0.0044	10.02 ±4.23	3.1×10^{-2}-1.4×10^{-3}	0.9994	1.6×10^{8}	1.6×10^{10}
5% Ge	0.0111 ±0.0008	4.49 ±0.45	2.7×10^{-2}-9.1×10^{-4}	0.9994	2.5×10^{7}	1.7×10^{9}
0.5% Sb	0.018 ±0.006	0.0037 ±0.0008	4.2×10^{-2}-1.9×10^{-3}	0.9990	1.6×10^{8}	5.9×10^{7}
1% Sb	0.026 ±0.008	0.0015 ±0.0003	6.6×10^{-2}-3.3×10^{-3}	0.9996	1.1×10^{8}	1.1×10^{8}
2% Sb	0.017 ±0.005	0.0044 ±0.0008	3.5×10^{-2}-3.0×10^{-3}	0.9996	1.7×10^{8}	7.8×10^{7}
1% Te	3.67×10^{-3} $\pm2.1\times10^{-4}$	0.105 ±0.005	2.8×10^{-2}-8.6×10^{-4}	0.9999	7.8×10^{8}	4.0×10^{10}
2% Te	2.54×10^{-3} $\pm2.5\times10^{-4}$	0.093 ±0.009	3.6×10^{-2}-1.3×10^{-3}	0.9999	1.1×10^{9}	7.3×10^{10}

All the fits to eq. 7.1 performed for the samples $Sn_2P_2S_6$+3%Ge, $Sn_2P_2S_6$+5%Ge, $Sn_2P_2S_6$+0.5%Sb, $Sn_2P_2S_6$+1%Sb, $Sn_2P_2S_6$+2%Sb, $Sn_2P_2S_6$+1%Te and $Sn_2P_2S_6$+2%Te together with the corresponding deviation plots are displayed on figures 7.4-7.6. Additionally, table 7.1 contains all the relevant fitting parameters related to the eq. 5.1 such as the fitted range, adjustable parameters p_1 and p_2, coefficient of determination R^2 and phenomenological Landau parameters β' and γ.

Now let's turn our attention to the paraelectric phase. The first model we have tested has been a first fluctuation correction to the Landau approach corresponding to eq. 5.3, where critical exponent α has to be -0.5. Unfortunately, for all doped samples no good fits to eq.5.3 were found, indicating that the first order fluctuation of the order parameter is not enough on its own to describe the critical behavior of the inverse of the thermal diffusivity in the immediate vicinity of the transition. We have also allowed the critical exponent to deviate from -0.5 in the fittings with Eq 5.3, to see if the model which takes into account the possible attenuations of the fluctuation effects caused by long-range dipole interactions could be of application. Eq 5.4 corresponds to this model and introduces a small multiplicative logarithmic correction $\left| \ln |t| \right|^b$. But the fittings were very bad and the values of α deviated strongly from -0.5 (both to bigger and smaller values, depending on the samples), which definitely ruled out this model, with or without a logarithmic correction.

After this, the next model tested has been the combination of two mechanisms: the fluctuation effects and the possible contribution of charged defects, which corresponds to eq.5.5:

$$1/D = B_3 + C_3 t + A_3 |t|^{-0.5} + D_3 |t|^{-1.5} . \tag{7.2}$$

The helpful information that can be retrieved from the eq. 7.2 is the ratio of the coefficients D_3/A_3, which indicates the relative importance of the charged defects (D_3) with respect to the first order fluctuations (A_3). In particular, this model was of application when describing the critical behavior of the pure $Sn_2P_2S_6$ uniaxial ferroelectric [95]. As the samples under study do not differ much from the pure sample, it was necessary to test if this model could be also valid now. Indeed, for all doped

samples, good fits to eq. 7.2 were found. The fitted curves together with the corresponding deviation plot are displayed on fig.7.4-7.6. All the relevant fitting parameters are collected in table 7.2. As can be seen from that table, there is also some correlation between those critical ratios depending on the particular type of dopant.

Table 7.2.

Results of the fitting procedure using eq. (5.5). In each case the relevant fitting parameters are shown together with the fitted range in reduced temperature units $t=(T-T_C)/T_C$ as well the quality of the fitting through the coefficient of determination R^2. The values for $Sn_2P_2S_6$ are extracted from ref [95].

Sample	Fitted range	R^2	A_3 (s/mm^2)	D_3 (s/mm^2)	D_3/A_3
$Sn_2P_2S_6$	2.7×10^{-2}-6.8×10^{-4}	0.981	3.25×10^{-3} $\pm6\times10^{-4}$	1.62×10^{-5} $\pm1\times10^{-7}$	5.0×10^{-3}
3% Ge	2.5×10^{-2}-5.3×10^{-4}	0.966	7.10×10^{-4} $\pm2.15\times10^{-4}$	1.60×10^{-5} $\pm2\times10^{-7}$	2.3×10^{-2}
5% Ge	2.9×10^{-2}-7.2×10^{-4}	0.985	6.15×10^{-4} $\pm1.65\times10^{-4}$	2.83×10^{-5} $\pm2\times10^{-7}$	4.6×10^{-2}
0.5% Sb	3.2×10^{-2}-1.9×10^{-3}	0.988	4.06×10^{-3} $\pm8.1\times10^{-4}$	5.45×10^{-5} $\pm1.0\times10^{-6}$	1.3×10^{-2}
1% Sb	3.6×10^{-2}-1.2×10^{-3}	0.953	1.63×10^{-3} $\pm2.7\times10^{-4}$	2.52×10^{-5} $\pm3\times10^{-7}$	1.6×10^{-2}
2% Sb	3.6×10^{-2}-2.8×10^{-3}	0.987	5.59×10^{-3} $\pm8.9\times10^{-4}$	9.95×10^{-5} $\pm1.5\times10^{-6}$	1.8×10^{-2}
1% Te	2.0×10^{-2}-5.8×10^{-4}	0.967	2.07×10^{-3} $\pm2.0\times10^{-4}$	1.10×10^{-5} $\pm1\times10^{-7}$	5.3×10^{-3}
2% Te	2.3×10^{-2}-6.9×10^{-4}	0.952	2.99×10^{-3} $\pm6.7\times10^{-4}$	1.77×10^{-5} $\pm4\times10^{-7}$	5.9×10^{-3}

In the case of Ge impurities, this ratio is increased from 5.0×10^{-3} in the undoped crystal [95] to 2.3×10^{-2} and 4.6×10^{-2} in the samples doped with 3% and 5% Ge, showing how the introduction of Ge atoms in the crystal lattice increases the importance of the charged defects mechanism in the vicinity of the transition compared to the case of the pure sample. For Sb atoms there is also an increase of D_3/A_3 ratio, but smaller than in the case of Ge. It rises up from an initial value of 5.0×10^{-3} to 1.3×10^{-2} for 0.5% Sb, 1.6×10^{-2} for 1% Sb and finally 1.8×10^{-2} for 2% Sb. Finally, when studying the critical behavior by fitting to eq. 7.2 for Te-doped samples, only minor variations of the ratio D_3/A_3 have been found. There is just a slight increase from 5.0×10^{-3} to 5.3×10^{-3} for 1%

Te and 5.9×10^{-3} for 2% Te. Nevertheless, the values for doped samples are very close to the undoped one indicating that the introduction of Te atoms in low atomic percentages does not alter the critical behavior as it happens with Sb and in particular with Ge atoms. Thus, we can say that Ge is the dopant which introduces the strongest changes in the critical ratio D_3/A_3.

It is worth noting that an effort has also been done to fit both high and low temperature branches simultaneously under the modern criteria for critical behavior, using eq. 5.2, trying to attribute a particular universality class out of the ones presented in chapter 4 for ferroelectric materials. Unfortunately, no proper fits were found in any case and that's why they are not shown in this report.
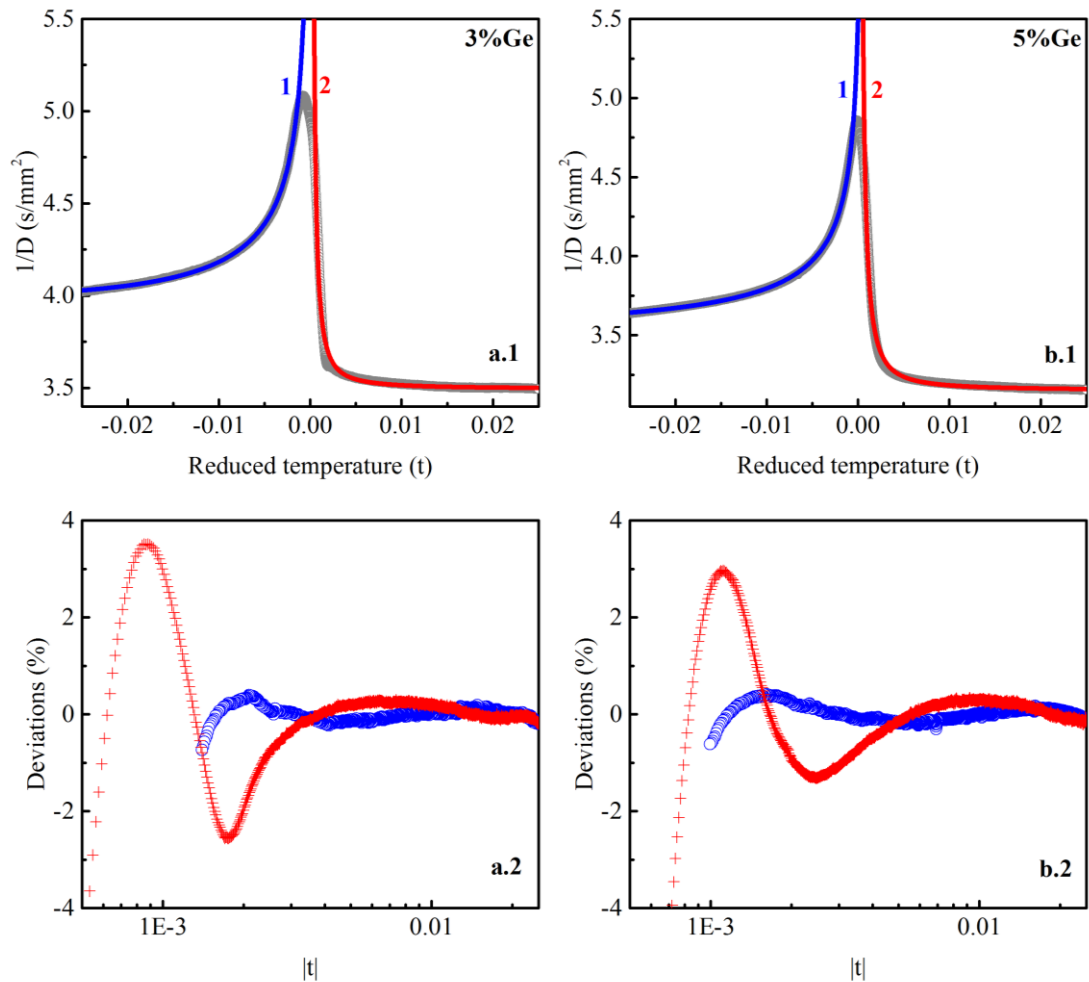
Fig. 7.4. Above: Experimental data (circles) for the inverse of thermal diffusivity as a function of the reduced temperature for Sn$_2$P$_2$S$_6$+3%Ge (a.1) and Sn$_2$P$_2$S$_6$+5%Ge (b.1). The lines marked as (1) represent the fits to eq. (7.1) for the ferroelectric phases while the ones marked as (2) represent the fits to eq. (7.2) for the paraelectric phases. Below: Deviation plots corresponding to the fits shown above. Open circles are for $T < T_C$ and crosses for $T > T_C$.
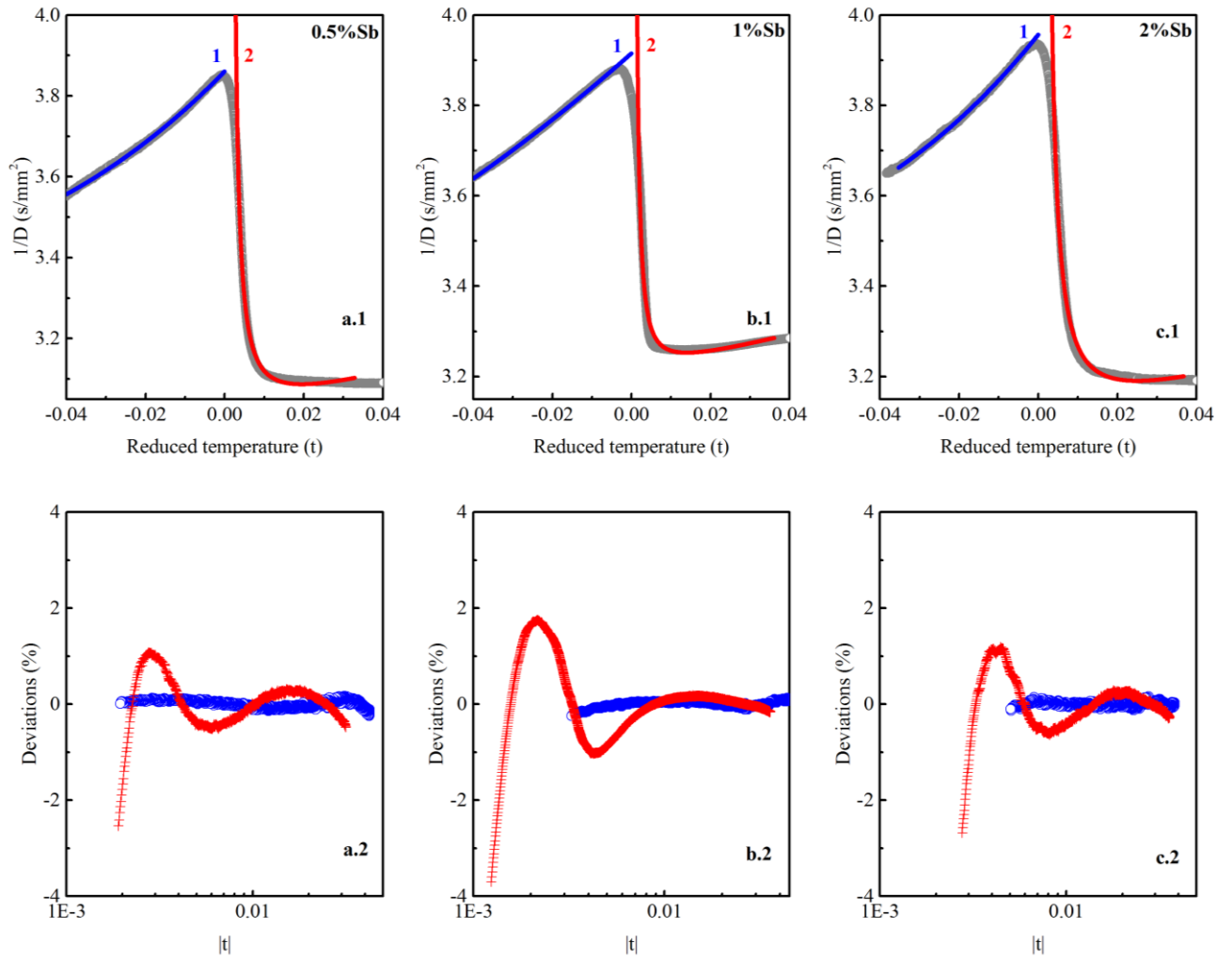
Fig. 7.5. Above: Experimental data (circles) for the inverse of thermal diffusivity as a function of the reduced temperature for Sn$_2$P$_2$S$_6$+0.5%Sb (a.1), Sn$_2$P$_2$S$_6$+1%Sb (b.1), Sn$_2$P$_2$S$_6$+2%Sb (c.1). The lines marked as (1) represent the fits to eq. (7.1) for the ferroelectric phases while the ones marked as (2) represent the fits to eq. (7.2) for the paraelectric phases. Below: Deviation plots corresponding to the fits shown above. Open circles are for $T < T_C$ and crosses for $T > T_C$.
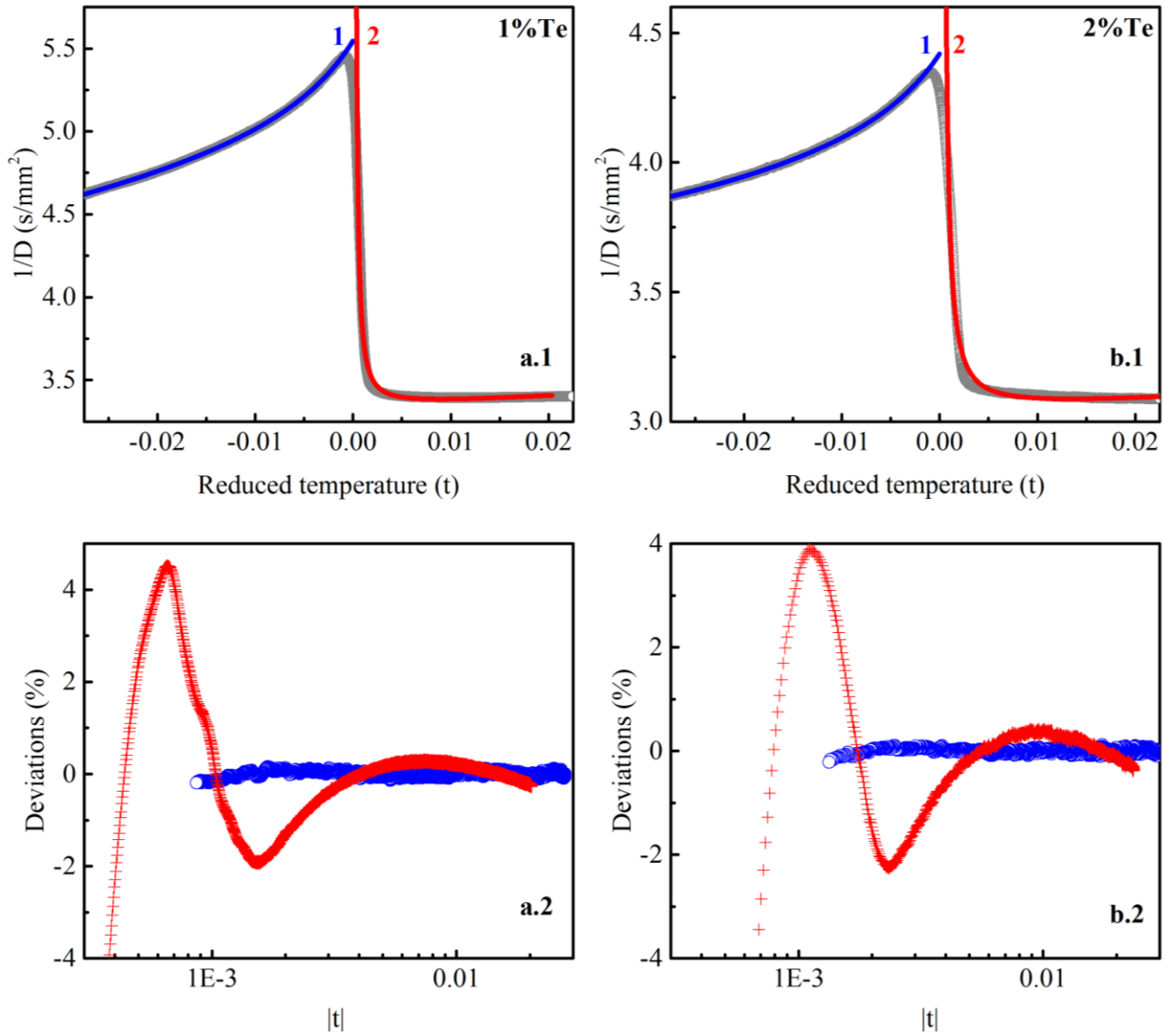
Fig. 7.6. Above: Experimental data (circles) for the inverse of thermal diffusivity as a function of the reduced temperature for $Sn_2P_2S_6+1\%Te$ (a.1) and $Sn_2P_2S_6+2\%Te$ (b.1). The lines marked as (1) represent the fits to eq. (7.1) for the ferroelectric phases while the ones marked as (2) represent the fits to eq. (7.2) for the paraelectric phases. Below: Deviation plots corresponding to the fits shown above. Open circles are for $T < T_C$ and crosses for $T > T_C$.

7.6. Conclusions

The temperature evolution of the thermal diffusivity in the neighbourhood of the second order ferroelectric phase transition has been measured in the poor conductive uniaxial ferroelectric $Sn_2P_2S_6$ crystal independently doped with isovalent Ge, Sb and Te atoms using *ac* photopyroelectric calorimetry in the back configuration. It was found that Ge dopant strongly improves the stereoactivity, caused by the strengthening of the sp^2 electronic levels hybridization, increasing the transition temperature. Sb atoms affect

in a smaller scale but in an opposite manner, disfavoring the ferroelectricity (shifting the transition to little bit lower temperatures) while Te has practically no influence at the studied concentrations. The critical behavior for all dopants has been studied via the inverse of the thermal diffusivity. In all cases the ferroelectric phase can be well described by classical Landau model in terms of a mean-field approach. On the contrary, for the description of the paraelectric phase it is necessary to take into account fluctuation effects of the order parameter accompanied together with the possible contribution of the charged defects, ruling out a mean-field description. From the quantitative analysis it was found that the relative importance of the charged defects mechanism is stronger in the samples doped with Ge than in those doped with Sb, while Te impurities have practically no influence on the critical behavior and the samples containing it behave very close to the undoped $Sn_2P_2S_6$ crystal.

CHAPTER 8

Experimental results and discussion on $Sn_2P_2(S_{0.72}Se_{0.28})_6$ doped with Pb and Ge. In search of a tricritical Lifshitz point

8.1. Introduction

The uniaxial ferroelectric family $(Sn_{1-y}Pb_y)_2P_2(S_{1-x}Se_x)_6$ is quite an interesting physical system, which allows a comprehensive study of a series of multicritical points which appear on the (T, p, x, y) phase diagram. In chapter 3 we have already discussed some theoretical predictions and experimental data related to the possible existence of special multicritical points such as Lifshitz, tricritical, Lifshitz tricritical, and a virtual Lifshitz tricritical point. The locations of a tricritical point and a Lifshitz point have already been well established (see chapter 3, section 3.2.5). On the other hand, two others (a Lifshitz tricritical and a virtual Lifshitz tricritical) have been theorized but not experimentally confirmed by any research group yet.

In this work we try to localize experimentally a tricritical Lifshitz point on the (T, x, y) state diagram taking into account two dopants (x and y). To be able perform this type of research we have studied the well known crystal with a Lifshitz point $Sn_2P_2(S_{0.72}Se_{0.28})_6$, which has been additionally doped with Pb or Ge atoms. As known from previous chapters, only these species have a strong influence on the stereoactivity of the $Sn_2P_2S_6$ crystal, which is reflected in the phase transition temperature shift. The most intriguing question is: could, indeed, Pb or Ge isovalent dopants change the character of the phase transition starting from the Lifshitz point LP?

To answer this question we will carefully investigate the changes in the character of the transition in the samples using low temperature rate measurements of the thermal diffusivity. The experimental results will be discussed within the theoretical models taking into account the features of the three-well local potential for fluctuations of the order parameter. Additionally, we will analyze the evolution of the critical behavior using the renormalization group calculations and focusing our attention on the possible appearance of a Lifshitz Tricritical universality class.

8.2. Samples and measuring procedure

The vapour-transport method has been used to obtain the single ferroelectric crystals $Sn_2P_2(S_{0.72}Se_{0.28})_6$ additionally codoped with 5% Pb, 8% Pb and 5% Ge in atomic percentage. The samples were grown in an evacuated quartz tube using I_2 as a transport agent. The synthesis of the starting material in the polycrystalline form was carried out using high-purity elements Sn (99.99%), P (99.999%), S (99.99%), Se (99.99%), Pb (99.99%) and Ge (99.999%), also in atomic percentage. The required amount of Sn, P, S, Se, Pb or Ge was placed into the quartz tube for further homogenization at 650 C during one week. After that, the recrystallization by vapor transport between hot zone at 650 C and cool zone at 630 C has taken three days. In the next stage, the cool zone was cleaned by heating and further this zone has been cooled to 615 C and kept at this temperature till the appearance of a visually observed crystal nucleus. From this moment the single crystal growth was started with a duration of nearly one month. At finish of growth process the hot zone of quartz tube was absolutely clean, what gives evidence about full mass transport and growth of the single crystal with the required stoichiometry.

Due to the electronic properties of Ge this type of dopant can be introduced into the crystal lattice of $Sn_2P_2(S_{0.72}Se_{0.28})_6$ only up to a certain percentage [211] while Pb atoms can completely substitute Sn ones. The crystalline quality has been checked by X-ray diffraction technique. All three samples show well defined sharp diffraction lines confirming their good crystal quality. No additional phases were found. The same equipment has been employed to orient the samples studied. The two crystals doped with Pb and the one doped with Ge were oriented in the [001] and [100] crystallographic directions, respectively.

The physical variable we have measured is thermal diffusivity D retrieved by means of a high resolution ac photopyrocalorimetry technique. The detailed description of the experimental setup used can be easily found in the previous chapters of the present thesis. We just want to emphasize that during this study the lowest temperature variations were as slow as 2.5 mK/min. This was necessary to precisely detect the possible temperature hysteresis while performing heating/cooling runs and detect a

change in the phase transition character. Similar temperature rates have been used by Oleaga, et.al, in order to detect the change in the character of the phase transition in $Sn_2P_2(S_{1-x}Se_x)_6$ ferroelectric family at Se content from x=0 up to x=1 [60]. Fig. 8.1 contains the difference in the position of the critical temperature in heating and cooling runs as a function of the temperature rate for concentrations close to the Lifshitz point x=0.28 presented in that paper. This figure will help us while discussing the experimental data obtained in this work.
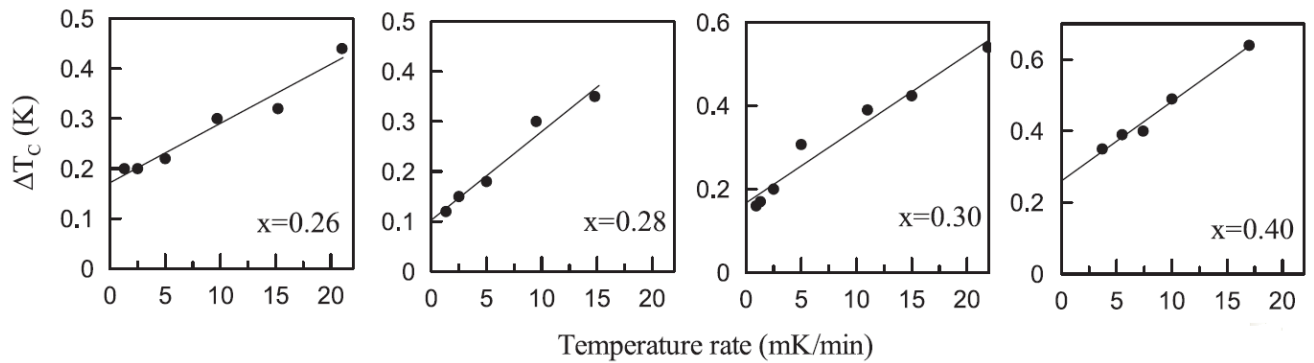
Fig. 8.1. Hysteresis study (difference in the position of the critical temperature in heating and cooling runs as a function of the temperature rate) for $Sn_2P_2(S_{1-x}Se_x)_6$ mixed ferroelectrics near the Lifshitz concentration; x=0.28 is the crystal with a Lifshitz point LP [60].

8.3. Experimental results and critical behavior

The temperature evolution of the thermal diffusivity D in the neighborhood of T_C for the three samples is presented on fig. 8.2. To better compare our experimental curves with the undoped $Sn_2P_2(S_{0.72}Se_{0.28})_6$ and to see the differences among the anomalies, we also show the published thermal diffusivity data for $Sn_2P_2(S_{1-x}Se_x)_6$ (fig. 8.3) for $0 \leq x \leq 0.3$ [60]. The introduction of Pb into the crystal lattice reduces the critical temperature from an initial value of 281.31 K for $Sn_2P_2(S_{0.72}Se_{0.28})_6$ (see fig.8.3) down to 259.12 K and 251.96 K for the samples doped with 5% and 8% Pb, respectively (fig.8.2, curves 1, 2). This happens due to the changes in the hybridization of the electronic orbitals of the cation and anion sublattices: when Pb substitutes Sn the hybridization becomes weaker, reducing the transition temperature. It is worth noting that the dip which marks the transition is broadened and smeared at higher Pb contents with respect to $Sn_2P_2(S_{0.72}Se_{0.28})_6$ crystal. A similar behavior has been observed in (Sn₁.

$_x$Pb$_x$)$_2$P$_2$S$_6$ [205]. On the other hand, Ge dopant affects in an opposite manner enhancing the total stereoactivity of the crystal. The critical temperature is shifted upwards to 284 K (fig.8.2, curve 3). The anomaly keeps its sharpness, but the shape is slightly broadened with respect to the Lifshitz concentration. A similar influence of Ge atoms has been found when studying the thermal diffusivity in Sn$_2$P$_2$S$_6$ doped with Ge [214].
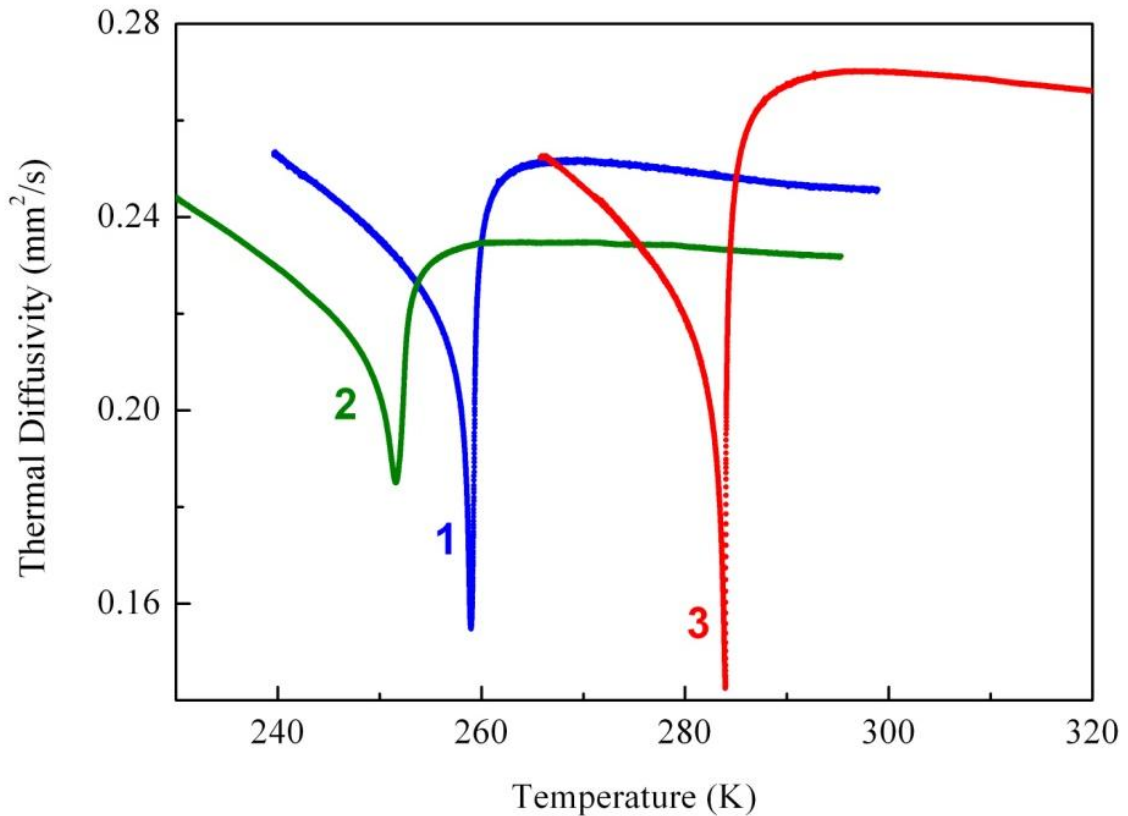
Fig. 8.2. Thermal diffusivity as a function of temperature in the vicinity of T_C for Sn$_2$P$_2$(S$_{0.72}$Se$_{0.28}$)$_6$ doped with 5% Pb, 8% Pb and, 5% Ge (curves 1, 2 and 3, respectively).

The character of the three transitions was checked in detail investigating a possible temperature hysteresis. For each sample, heating and cooling runs were performed with decreasing rates of 20, 10, 5, 2.5 mK/min. The results are displayed on fig 8.4.
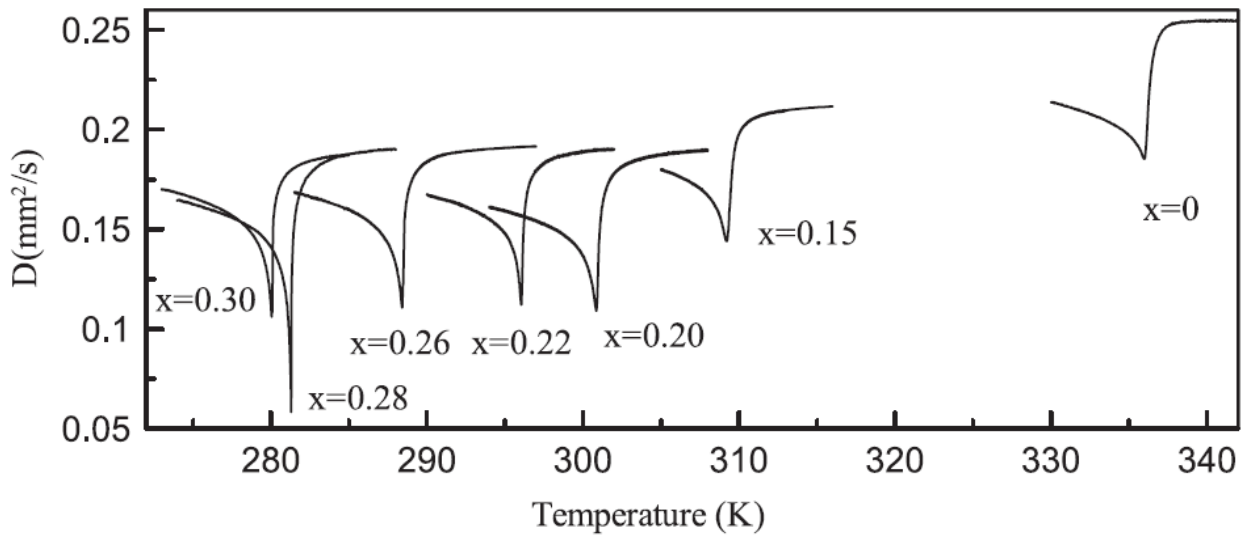
Fig. 8.3. Thermal diffusivity as a function of temperature for the $Sn_2P_2(S_{1-x}Se_x)_6$ family near a Lifshitz point [60].
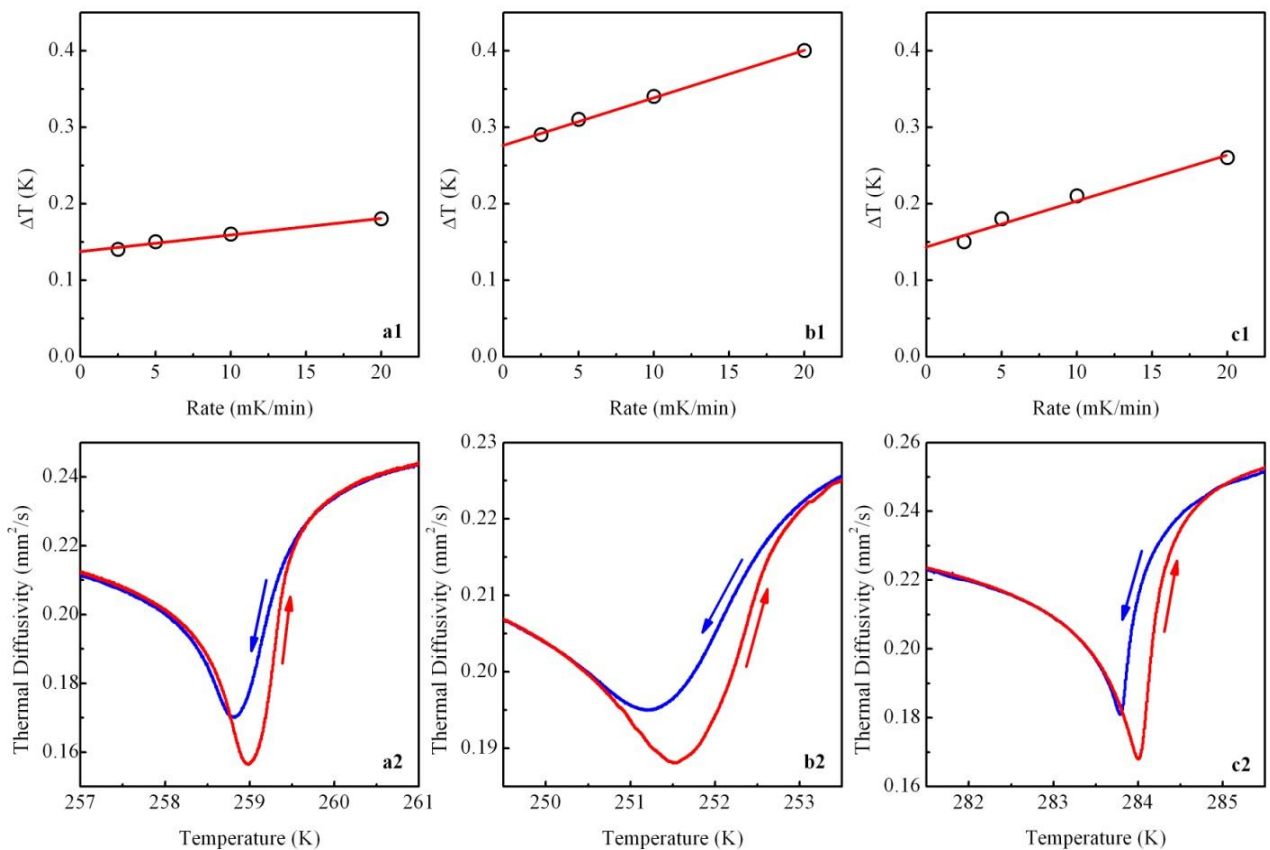
Fig. 8.4. Thermal hysteresis. Above: Difference in the critical temperature in heating and cooling runs as a function of temperature rate; the circles are the experimental values, the straight lines the linear fittings. Below: Shape of the thermal diffusivity curves on heating and cooling for a temperature rate of 10 mK/min. Labels are as follows: a1 and a2 are for $Sn_2P_2(S_{0.72}Se_{0.28})_6$ doped with 5% Pb, b1 and b2 with 8% Pb, c1 and c2 with 5% Ge.

The samples doped by 5% Pb and 5%Ge show similar asymptotic behavior with intersection point about of 0.14 K on the vertical axis (fig.8.4 *a*, *c*). This value is quite close to the one obtained for Sn$_2$P$_2$(S$_{0.72}$Se$_{0.28}$)$_6$ [60], which is about 0.1K (see fig. 8.1 at *x*=0.28). This means the transitions are in the verge of changing their character to first order. Moreover, we have not found a perfect superposition of the shapes at heating/cooling runs, as it happens in the case of a clear second order phase transition. In the case of 8%Pb, the value of the temperature hysteresis is twice larger than in the two previous samples and it is about 0.28 K (fig. 8.4 *b*). Note, that a similar hysteresis was observed in Sn$_2$P$_2$(S$_{0.6}$Se$_{0.4}$)$_6$ crystal (see fig. 8.1 at *x*=0.4) [60], for which the character of the phase transition has already crossed the border between the second and first order types. These data give a hint that a tricritical point has been crossed.

In order to ascertain which kind of tricritical point is present here, we have used the renormalization group theory analysis and investigated the evolution of the universality class from the Lifshitz one obtained for Sn$_2$P$_2$(S$_{0.72}$Se$_{0.28}$)$_6$ [60]. It is worth noting that the best way to discriminate among universality classes is monitoring the critical index α, which describes the specific heat anomaly near the continuous phase transition. The benefit of this exponent with respect to other critical indices such as β (related to the spontaneous polarization) and γ (related to the inverse of dielectric susceptibility) is that α changes more from one universality class to another one (see table 4.2 in chapter 4). Moreover, to obtain β and γ only one branch is involved, while to rigorously obtain α it is necessary to consider both branches of the transition (below and above T_C), which makes it more reliable.

As was shown in previous chapters of this thesis, instead of specific heat the inverse of thermal diffusivity *1/D* can be successfully used in a critical behavior analysis in this family of ferroelectrics. Thus, according to the theory, to extract the value of the critical exponent α, well defined experimental curves obtained for Sn$_2$P$_2$(S$_{0.72}$Se$_{0.28}$)$_6$+5%Pb and Sn$_2$P$_2$(S$_{0.72}$Se$_{0.28}$)$_6$+5%Ge have been fitted to the following equation, which is based on eq. 4.20.

$$1/D = B + Ct + A^{\pm} |t|^{-\alpha} \left(1 + E^{\pm} |t|^{0.5}\right), \qquad (8.1)$$

where *t* is the reduced temperature, which is defined as $t = (T - T_C)/T_C$.

　　　The fits have not been performed for the sample with 8%Pb as the transition in this case is already a first order type. In the fitting procedure we focus our attention on the possible appearance of universality classes where tricriticality takes place, such as a Tricritical T (α=0.5 with small logarithmic correction), Uniaxial Tricritical UT (α=0.5), Tricritical Lifshitz LT (α=9/14) and Uniaxial Lifshitz tricritical ULT (α=0.5 with another logarithmic correction) [3].

　　　The results of the theoretical fitting for 5%Pb and 5%Ge accompanied with their corresponding deviation plots are depicted on fig.8.5. The fitting parameters $A^{\pm}$, *B*, *C*, $E^{\pm}$ and α together with their errors are collected in table 8.1. In the same table we have also included the temperature range *t* fitted and the determination coefficient R^2, which represents the quality of the fits. As seen from the graph both fits are very good, which is also confirmed by the high determination coefficient R^2 (R^2=1 the case for perfect fit) and the deviation plots. The values of the critical exponent α are 0.64 and 0.25 for 5%Pb and 5%Ge, respectively. In the first case, the value agrees with $\alpha_{theoretical}$=0.64, which corresponds to the Lifshitz Tricritical LT universality class while the second one coincides with Lifshitz class L ($\alpha_{theoretical}$=0.25). The ratio of the critical parameters A^+/A^- is 0.63 and 0.49, respectively.
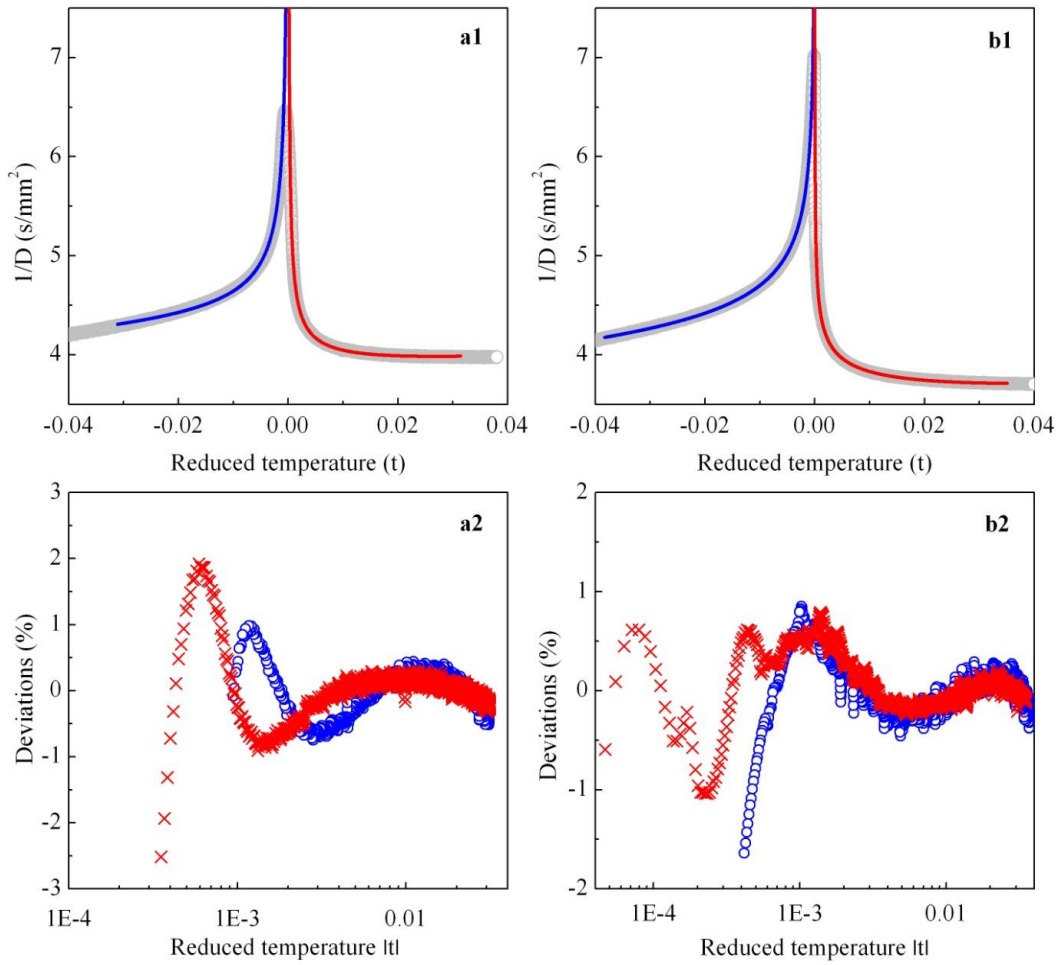
Fig. 8.5. Above: Experimental data (circles) for the inverse of thermal diffusivity as a function of the reduced temperature for $Sn_2P_2(S_{0.72}Se_{0.28})_6$ doped with 5% Pb (a.1) and with 5%Ge (b.1). The continuous lines represent the fits to Eq. (8.1). Below: Deviation plots corresponding to the fits shown above. Open circles are for $T < T_C$ and crosses for $T > T_C$.

Table. 8.1.

Result of the fitting of the inverse of thermal diffusivity $1/D$ using Eq. (8.1). The parameters (α, A^+, A^+/A^-, T_C, B, C, $E^{\pm}$) are shown together with the fitted range and the coefficient of determination R^2.

Parameters	5%Pb	5%Ge
α	0.638 ± 0.006	0.252 ± 0.001
A^+, s/mm^2	0.0140 ± 0.0008	0.269 ± 0.004
A^+/A^-	0.631 ± 0.001	0.493 ± 0.005
T_C, K	259.122 ± 0.001	283.995 ± 0.001
Fitted range |t|, $T > Tc$	3.54×10^{-4} - 3.14×10^{-2}	4.69×10^{-5} - 3.50×10^{-2}
Fitted range |t|, $T < Tc$	9.45×10^{-4} - 3.11×10^{-2}	4.18×10^{-4} - 3.83×10^{-2}
B, s/mm^2	3.85 ± 0.02	2.84 ± 0.01
C, s/mm^2	2.89 ± 0.05	2.98 ± 0.04
E^+	-3.8 ± 0.7	1.23 ± 0.06
E^-	9.5 ± 0.9	0.87 ± 0.01
R^2	0.9988	0.9997

8.4. Discussion

Such a complicated phenomenon as a multicritical point on the state diagram of any material needs a strong theoretical basement. In literature there are several publications which explain the possible presence of different high-order points on the (T, p, x, y) state diagram of $(Sn_{1-y}Pb_y)_2P_2(S_{1-x}Se_x)_6$ mixed compounds.

To explain the appearance of a tricritical points in this ferroelectric family we consider some theoretical models related to this phenomenon. It has been recently shown that a macroscopic model for $Sn_2P_2S_6$ developed with an *ab-inito* effective-Hamiltonian approach based on a three-well shape of the local potential can explain its dynamic and thermodynamic properties in a wide temperature range [115]. This model allows predicting a specific heat anomaly with features comparable to the experimentally observed ones [215]. Later, it has also been proposed that the shape of this local potential can be related to the Blume-Emery-Griffiths model (BEG), where pseudospins can have values -1, 0 and +1. This approach has been used to quantitatively explain the influence of Pb atoms on the ferroelectric properties while they substitute Sn in the $(Sn_{1-y}Pb_y)_2P_2S_6$ series [107]. Moreover, a combination of the BEG and the axial-next-nearest-neighbour Ising model (ANNNI) has been used to predict a possible location of a Tricritical Lifshitz point TCLP in a system with a three-well local potential. According to these predictions the Lifshitz points line should terminate in a high-order TCLP while external pressure is applied [216]. This model also implies that the continuous phase transition at $T_C \approx 337$ K in $Sn_2P_2S_6$ should change its character under compression. As was shown in chapter 3 the TCP in $Sn_2P_2S_6$ has been experimentally proven on (T, p) and its coordinates are $p \approx 0.4$ GPa, $T \approx 250$ K [105]. Under mechanical compression the stereoactivity of $Sn_2P_2S_6$ is reduced due to the three-well local potential surface flattening. This leads to the critical temperature decrease till the TCP is reached, where the transition changes its character from second-order to first order.

Additionally, if Pb is introduced instead of Sn to obtain $(Sn_{1-y}Pb_y)_2P_2S_6$ the stereoactivity is also reduced due to the electronic hybridization weakening [216]. This is caused by the larger energy distance between the ferroactive electron lone pair of Pb

$(6s^2)$ and the molecular orbital of the anion sublattice, with respect to the Sn $(5s^2)$ ones. Pb atoms play the role of the so-called "chemical pressure", additionally creating strong random-field defects. This situation has been successfully described by BEG model taking into account the random field influence. According to the explanation given by this theoretical approach, the phase transition in $(Sn_{1-y}Pb_y)_2P_2S)_6$ series must change its character as the critical temperature decreases. Also, the shape of the anomaly at T_C should be more smeared due to the influence of the random field defects created by Pb atoms [216, 217]. At S substitution by Se the critical temperature is also shifted downwards but the effect is much smaller than that of Pb. Moreover, there is no phase transition shape smearing [60], which means the random field is less relevant than in the case of Pb doping.

Taking into account the influence of both species (Pb as well as Se) and all the theoretical predictions written above, it can be expected that a tricritical Lifshitz point would be achieved if Pb atoms are introduced into the crystal lattice of $Sn_2P_2(S_{0.72}Se_{0.28})_6$. Thus, the critical temperature lowering should lead to a crossover from a Lifshitz point LP to a tricritical Lifshitz point TCLP.

The experimental results obtained in this work strongly support this hypothesis. Let's consider the fits performed in more detail. From $Sn_2P_2(S_{0.72}Se_{0.28})_6+0\%Pb$ to $Sn_2P_2(S_{0.72}Se_{0.28})_6+5\%Pb$ the critical index α changes from 0.34 (close to L universality class $\alpha \approx 0.25$) to 0.64 (LT class $\alpha_{theoretical} \approx 0.64$). The fits performed have quite a good quality with very small errors in the fitting parameters (see table 8.1) and small deviations, which are presented as a percentage on fig.8.5 *a*. The universality classes T and UT are discarded as their critical values are 0.5 (with logarithmic correction) and 0.5, respectively. This means, indeed, that the transition in $Sn_2P_2(S_{0.72}Se_{0.28})_6+5\%Pb$ is related to a Lifshitz point. We have also checked the possibility of fitting the experimental curves to two other classes: UL (uniaxial dipole-dipole interactions are relevant, $\alpha_{theoretical} \approx 1/6$) or UTL ($\alpha_{theoretical} \approx 0.5$ with another logarithmic correction) but all trials failed. Thus, we can say that the dipolar interactions in this transition are not as relevant as the order parameter fluctuations, which, in turn, are caused by presence of a Lifshitz point. Additionally, we have calculated the ratio of the critical

parameters $A^+/A^- = 0.63$ for $Sn_2P_2(S_{0.72}Se_{0.28})_6 + 5\%Pb$, but that value is theorized in literature only for the Lifshitz class L, which falls within the range of 0.30-0.35 [172], not for LT, UL or UTL. For $Sn_2P_2(S_{0.72}Se_{0.28})_6$ the ratio A^+/A^- was found to be 0.42 [60]. New theoretical developments are needed to know if the value that we have obtained is sensible or not.

Another evidence which supports the idea that we passed along a tricritical point is the fact that the phase transition in $Sn_2P_2(S_{0.72}Se_{0.28})_6 + 8\%Pb$ is first order as shown by the hysteresis study (fig.8.4 *b*) while the sample doped with 5%Pb is on the verge of changing the transition character. Besides, both transitions for 5%Pb and 8%Pb are more and more smeared with respect to the undoped sample, confirming the theoretical predictions given by BEG-model with random field influence created by the impurities.

Finally, turning our attention to the crystal doped with 5%Ge, it is seen that Ge has an opposite effect to that caused by Pb atoms. There is a slight upwards shift in the critical temperature (of about 2.7 K) compared to the undoped $Sn_2P_2(S_{0.72}Se_{0.28})_6$ sample [60]. This is caused by the electronic hybridization strengthening, which takes place with the addition of Ge. The transition itself keeps similar features (shape, hysteresis value) to the ones shown in $Sn_2P_2(S_{0.72}Se_{0.28})_6$. Moreover, the critical exponent obtained coincides perfectly well with the Lifshitz universality class L and the critical ratio A^+/A^- = 0.49 is slightly higher than that of $Sn_2P_2(S_{0.72}Se_{0.28})_6$ A^+/A^- = 0.42 [60]. The quality of the fitting was extremely good (see both table 8.1 and fig 8.5 *b*). Thus, we can say that doping with Ge does not provoke any changes in the character of the transition and that the critical behavior of the transition is maintained, belonging to the Lifshitz class.

8.5. Conclusions

The location of a tricritical Lifshitz point TCLP has been experimentally defined for $(Sn_{0.95}Pb_{0.05})_2P_2(S_{0.72}Se_{0.28})_6$ solid solution at T_C = 259.12 K, fulfilling all the predictions provided by BEG-model with random field. The theory says that Lifshitz points line must terminates in a TCLP at phase transition temperature decreasing. This can be realized by mechanical pressure or by addition of chemical dopants. Besides, the chemical dopants can produce random field defects, smearing the anomaly at T_C. This is

exactly what we have if Pb is introduced in a crystal with the Lifshitz concentration. The hysteresis study confirms that the samples with 5%Pb and 5%Ge are on the verge of changing the transition character while the crystal doped by 8%Pb has already crossed the border, confirming that there is a clear first order transition. Besides, the fittings performed show that the ferroelectric transition in $(Sn_{0.95}Pb_{0.05})_2P_2(S_{0.72}Se_{0.28})_6$ belongs to the Lifshitz Tricritical LT class as the critical index α is exactly the same as the theoretically predicted one $\alpha = 0.64$. On the other hand, the introduction of Ge increases the critical temperature, which was 281.31 K for $Sn_2P_2(S_{0.72}Se_{0.28})_6$, to 284 K for $Sn_2P_2(S_{0.72}Se_{0.28})_6$+5%Ge due to the strengthening of the stereoactivity. There is no change in the critical behavior as the Lifshitz class L is maintained for this sample, because the critical index $\alpha = 0.25$.

CHAPTER 9

Origin of ultra-low thermal conductivity in $Sn(Pb)_2P_2S(Se)_6$ ferroelectric crystals

9.1. Introduction

Nowadays an enormous attention is dedicated to searching possible ways which allow minimizing the lattice thermal conductivity of semiconductors [218, 22]. This challenge is one of the crucial problems for thermoelectric applications, where waste of heat can be converted into useful electricity. Thus, understanding the nature of sources producing a thermal resistance in crystalline solids can give new ideas in manufacturing prospective thermoelectric materials. To sort out this problem we discuss some peculiarities about the low thermal conductivity of $Sn(Pb)_2P_2S(Se)_6$-like ferroelectrics. We explain the effect of different mechanisms of anharmonicity on the shape of the thermal conductivity curves considering at the same place the features occurring on the state diagram of phosphorouss chalcogenide family studied. In spite of the fact that our materials are not thermoelectric, the physical interpretation of the results is of great importance and can serve as a good basement for further researches. Besides, the experimental data together with the theoretical support presented in the chapter will provide a quite complete picture about heat propagation in $Sn(Pb)_2P_2S(Se)_6$ compounds. This will also help to better understand the origin of the electron-phonon interaction processes taking place in this type of crystals.

$Sn(Pb)_2P_2S(Se)_6$ system is a very suitable candidate to perform such a broad study. In the first place, this is due to the complex shape of the phase diagram where three different phases (paraelectric, incommensurate and ferroelectric) are separated by first and second order transition lines as well as by multicritical points (see fig. 3.7). Remember that the ferroelectric phase in $Sn_2P_2S_6$ is associated with the transverse (TO) polar soft optic mode near the Brillouin zone center [219, 220]. The incommensurate phase appearance in the more covalent $Sn_2P_2Se_6$ is related to the linear interaction of the soft transverse optic (TO) branch with the longitudinal acoustic (LA) and the transverse acoustic (TA) branches [220, 99]. For the lead containing crystals $Pb_2P_2S_6$ and $Pb_2P_2Se_6$ the paraelectric state is stabilized down to lowest temperatures [107, 221]. This provides an interesting comparison among the parent compounds $Sn_2P_2S_6$, $Pb_2P_2S_6$, $Sn_2P_2Se_6$,

$Pb_2P_2Se_6$ along a wide temperature range. Secondly, this family allows obtaining a whole set of stable solid solutions $(Pb_ySn_{1-y})_2P_2S_6$, $(Pb_ySn_{1-y})_2P_2Se_6$ and $Sn_2P_2(Se_xS_{1-x})_6$, giving an opportunity to study the influence of mass fluctuation effects on the thermal conductivity behavior. Thirdly, the three-well landscape of the local potential of $Sn_2P_2S_6$ [115] is sensitive to Sn by Pb substitution or to a presence of isovalent alien dopants and also to the temperature changes. As a result, the shape of the central and side wells depths can be heavily modified producing new channels for anharmonicity.

Recently it was shown that, in addition to the Sn^{2+} $5s^2$ stereoactive lone pair, the charge disproportionation of phosphorous ions $P^{4+} + P^{4+} \leftrightarrow P^{3+} + P^{5+}$ is also involved in the valence fluctuations creating the $Sn_2P_2S_6$ paraelectric phase instability in the considered crystals [222]. Thus, the lone pair electrons relaxations together with the valence fluctuations determine a strong lattice anharmonicity which is characterized by a high value of the Grüneisen parameter: using acoustic data, it has been determined to be $\gamma = 1.52$ for $Pb_2P_2S_6$ and $\gamma = 1.36$ for the paraelectric phase of $Sn_2P_2S_6$ [223, 108].

All these peculiarities about the structural, electronic and chemical features of these chalcogenide ferroelectrics have led to presenting an illustrative analysis of a high lattice anharmonicity in connection with electron instability studying the temperature evolution of the thermal conductivity curves.

9.2. Samples and experimental results

According to the scope of this thesis, a set of samples was selected as representatives of the right hand side and left hand side of the phase diagram (fig. 3.7). The full list of them is as follows: $(Pb_ySn_{1-y})_2P_2S_6$ series with y=0, 0.1, 0.2, 0.3, 0.45, 0.8 and 1; $(Pb_ySn_{1-y})_2P_2Se_6$ series with y=0, 0.1, 0.2, 0.47, 0.8 and 1. We have also studied two germanium doped crystals: $Sn_2P_2S_6+5\%Ge$ and $Pb_2P_2S_6+2\%Ge$.

The thermal conductivity dependencies for all samples studied were calculated using the constitutive eq. (9.1) by mixing our measured thermal diffusivity D data with heat capacity C_p published in literature [100, 224, 109, 125, 225].

$$k = C_p D. \qquad (9.1)$$

One important comment has to be mentioned in here. In the calculation procedure only the background of heat capacity was considered avoiding the region of the critical anomaly occurrence. This is caused by the fact that the techniques, rates, and samples used to measure both thermal variables were different. Thus, the exact position and shapes of the anomalies (where there were any) did not coincide in the thermal diffusivity and heat capacity curves. This is why the dips in thermal conductivity dependencies presented below should be considered as "artifacts" whose form is mainly caused by having combined the full thermal diffusivity data with the background heat capacity. Luckily, our analysis is not focused on the region close to the phase transition but, instead, we are interested in the wide temperature evolution.

Figure 9.1 displays the temperature evolution of both thermal diffusivity D as well as thermal conductivity k for the four parent compounds in a wide temperature range. From the left panel it is clearly seen that the diffusivity dependencies steadily grow on cooling showing a typical thermal insulator behavior. In the paraelectric phases the pair of crystals Pb$_2$P$_2$S$_6$, Pb$_2$P$_2$Se$_6$ have a slightly higher thermal diffusivity with respect to their Sn containing analogues. At low temperatures the opposite happens for the ferroelectric state of Sn$_2$P$_2$S$_6$ and Sn$_2$P$_2$Se$_6$, where the value of D exceeds those for the paraelectric phases in Pb$_2$P$_2$S$_6$ and Pb$_2$P$_2$Se$_6$. Also, the more covalent Pb$_2$P$_2$Se$_6$, Sn$_2$P$_2$Se$_6$ present a lower thermal diffusivity than that of Pb$_2$P$_2$S$_6$ and Sn$_2$P$_2$S$_6$.

Now we turn our attention to the thermal conductivity curves (fig. 9.1 right panel). For Pb$_2$P$_2$S$_6$ and Pb$_2$P$_2$Se$_6$ in the paraelectric phase and for Sn$_2$P$_2$S$_6$ and Sn$_2$P$_2$Se$_6$ in the ferroelectric one the dependencies decrease on heating according to the usual Eiken law behavior where $k \sim T^n$ (our exponents falls within the range of -0.8 to -1.2). This confirms a predominant contribution of the three-phonon scattering processes to heat exchange above the Debye temperature, which has the following values: $\Theta_D \approx 85$ K for Pb$_2$P$_2$S$_6$, $\Theta_D \approx 55$ K for Pb$_2$P$_2$Se$_6$, $\Theta_D \approx 83$ K for Sn$_2$P$_2$S$_6$ and $\Theta_D \approx 74$ K for Sn$_2$P$_2$Se$_6$ after [224, 100, 226]. At high temperatures $T \gg \Theta_D$ in the paraelectric phase for all extreme compounds the thermal conductivity deviates to constant values. At low temperatures inside the ferroelectric phase the conductivity is higher for the Sn-containing crystals than in the Pb$_2$P$_2$S$_6$ and Pb$_2$P$_2$Se$_6$ samples.

Within the incommensurate phase in $Sn_2P_2Se_6$ between $T_c \approx 193$ K and $T_i \approx 221$ K the thermal conductivity reveals almost a flat behavior reaching the lowest value among all four extreme compounds. Note that a similar value has been previously found by Rizak *et. al.* for $Sn_2P_2Se_6$ glassy material [127]. This fact demonstrates that the minimal thermal conductivity k_{min} is successfully observed for the investigated crystals. In the incommensurate phase with a modulation period of near 14 unit cells [220] the folding of the Brillouin zone can create additional phonon scattering centers producing an effective suppression of the thermal conductivity. At lowest temperatures near 40K the maximum value of about 6 W/m K was found for $Sn_2P_2S_6$ ferroelectric phase while the minimal one of about 1.7 W/m K was observed for $Pb_2P_2Se_6$ crystal.
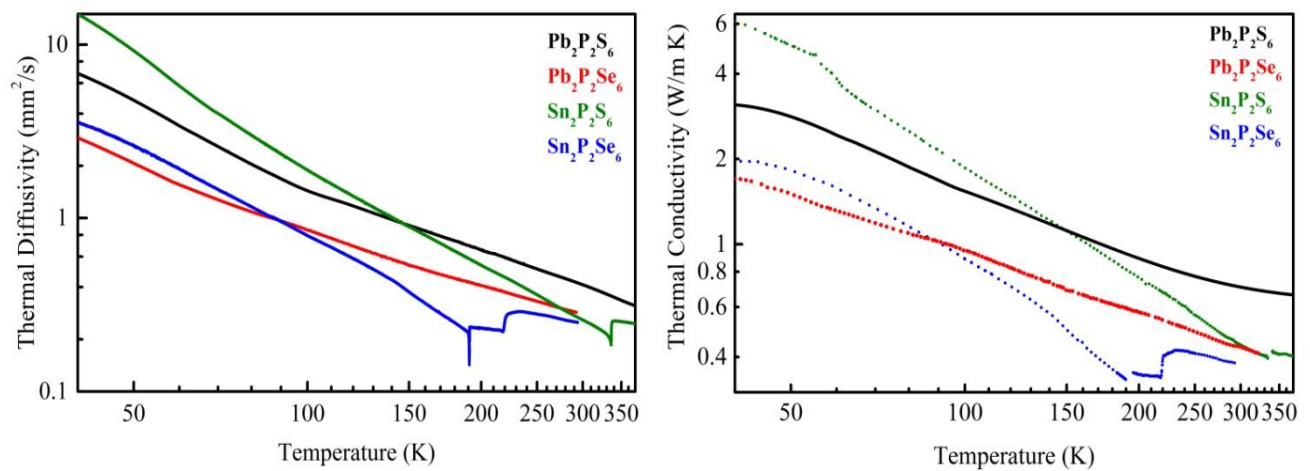
Fig. 9.1. Double logarithmic scale of the thermal diffusivity (left panel) and the thermal conductivity (right panel) as a function of temperature for $Pb_2P_2S_6$, $Pb_2P_2Se_6$, $Sn_2P_2S_6$ and $Sn_2P_2Se_6$ crystals.

In the mixed compositions $(Pb_ySn_{1-y})_2P_2S_6$ and $(Pb_ySn_{1-y})_2P_2Se_6$ the $k(T)$ dependencies are drastically altered (fig. 9.2, 9.3). The measured thermal diffusivity curves have already been presented in chapter 5 (fig. 5.3) for $(Pb_ySn_{1-y})_2P_2S_6$ mixed compounds and in chapter 6 (fig. 6.2) for $(Pb_ySn_{1-y})_2P_2Se_6$ system. There is a big contrast between the pure and the doped crystals due to the mass fluctuations which induce additional phonon scattering. Especially this is clearly demonstrated at low temperatures, approximately below 100K, in the middle of the concentration interval (y $\approx$ 0.5) where the thermal conductivity is lowered several times reaching almost 0.5 W/m K for both sulfide and selenide series (fig. 9.2, 9.3, 9.4). Concerning the high temperature region (above 250K) there are no significant changes in thermal

conductivity. Here, obviously, the crystal lattice anharmonicity is so strong that additional phonon scattering mechanism by atom mass fluctuations does not play a relevant role.
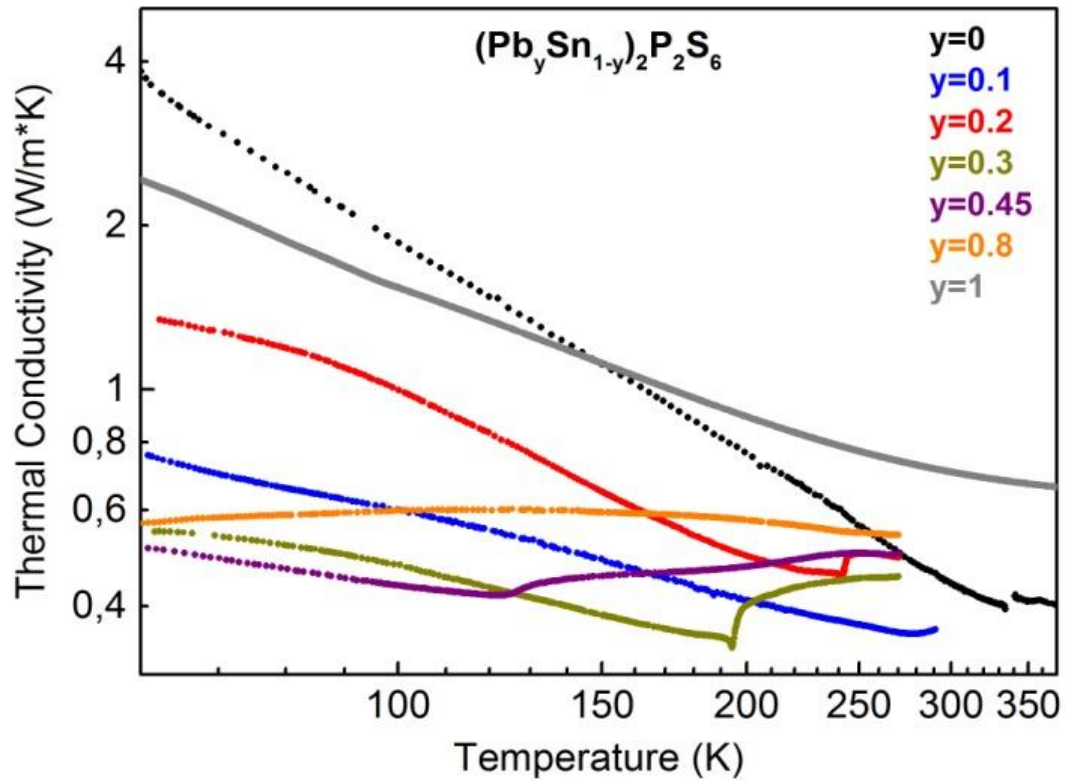
Fig. 9.2. Temperature dependence of thermal conductivity for $(Pb_ySn_{1-y})_2P_2S_6$ crystals, in log-log scale.

An interesting thermal conductivity behavior has been observed for $(Pb_ySn_{1-y})_2P_2Se_6$ with lead content of $y=0.2$ (fig. 9.3). This crystal reveals a very broad temperature minimum of $k(T)$, which is located near the paraelectric to incommensurate phase transition ($T_i \approx 160K$). Also a wide minimum is observed close to the paraelectric-ferroelectric transition in $(Pb_ySn_{1-y})_2P_2S_6$ at $y=0.45$ ($T_0 \approx 125K$). The most uncommon behavior of the conductivity has been found for the selenide mixed crystals doped with $y=0.2$ and $y=0.47$. For these two samples the dependencies present a soft decrease on cooling which is similar to the temperature evolution of the glassy $Sn_2P_2Se_6$ [127] (fig. 9.3). These peculiarities are related to the heat capacity regular behavior together with the temperature change of the phonon group velocity for the heat transferring lattice vibrations characterized by thermal diffusivity and also their lifetimes.
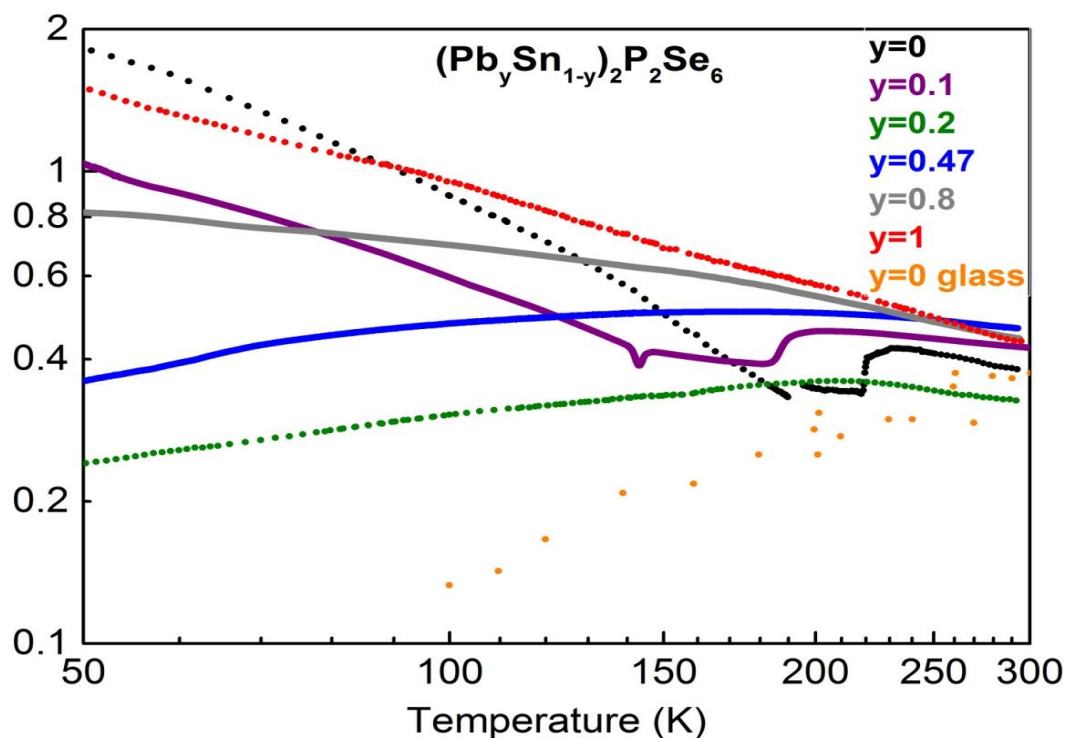
Fig. 9.3. Temperature dependence of thermal conductivity for $(Pb_ySn_{1-y})_2P_2Se_6$ crystals, in log-log scale. Data for $Sn_2P_2Se_6$ glassy are taken from [127].
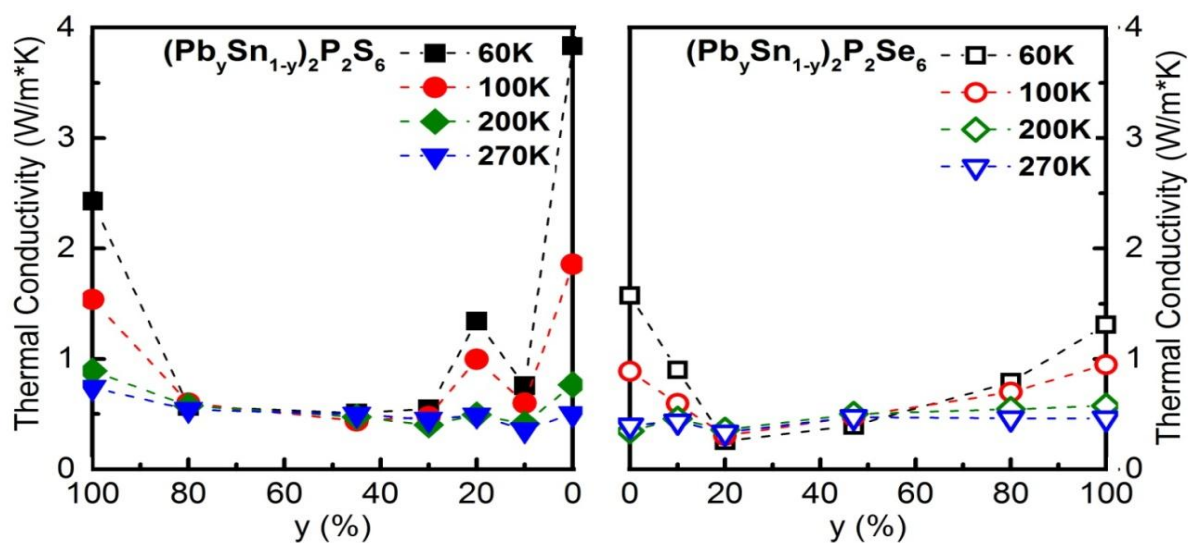
Fig. 9.4. Composition dependence of thermal conductivity for $(Pb_ySn_{1-y})_2P_2S_6$ and $(Pb_ySn_{1-y})_2P_2Se_6$ crystals at different temperatures.

Lastly, we have checked the possible influence of Ge impurities on the thermal properties of $Sn_2P_2S_6$ ferroelectric and $Pb_2P_2S_6$ paraelectric crystals (fig. 9.5). It was found that Ge dopants steadily increase the thermal diffusivity as well as thermal conductivity of $Pb_2P_2S_6$ on cooling. Near 40K the doped sample reaches the maximum

value of about 5 W/m K in thermal conductivity (see fig. 9.5) while the pure sample at the same temperature shows about 3 W/m K. On the other hand, germanium atoms have virtually no influence on both transport thermal properties in the ferroelectric phase of $Sn_2P_2S_6$ (fig. 9.5).
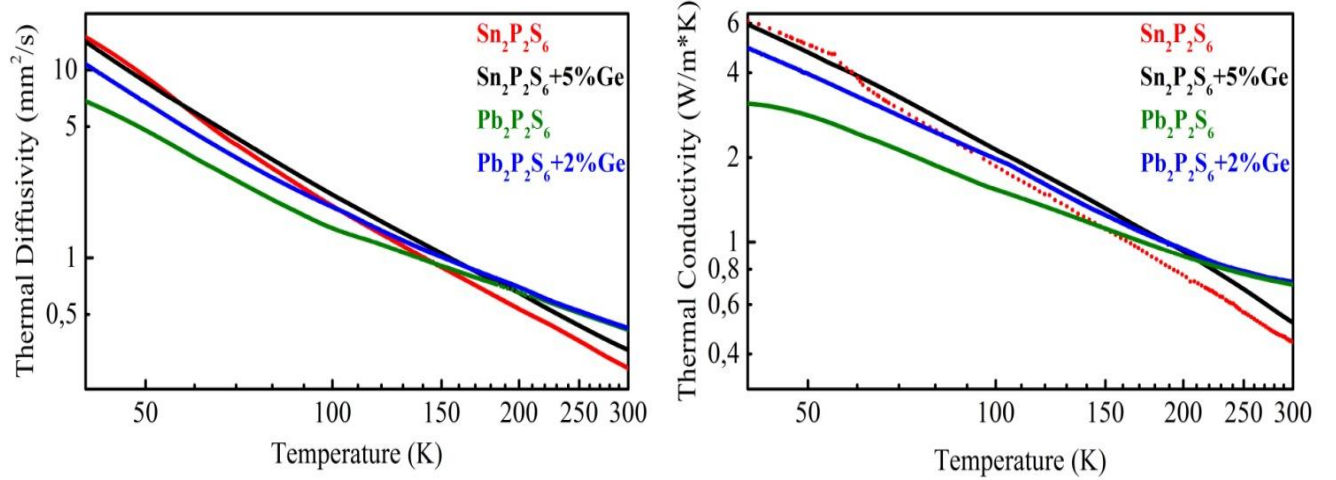
Fig. 9.5. Temperature dependence of thermal diffusivity (left panel) and thermal conductivity (right panel) for nominally pure $Pb_2P_2S_6$ and $Sn_2P_2S_6$ crystals in comparison with data for $Pb_2P_2S_6$ and $Sn_2P_2S_6$ crystals doped with Ge.

9.3. Discussion

In the first place, let's try to explain the ultralow thermal conductivity experimentally obtained for the crystalline structures of $Sn(Pb)_2P_2S(Se)_6$ system. To estimate the lowest possible thermal conductivity limit for this type of materials we use what is known as the "amorphous limit" for crystals or minimum thermal conductivity [227]:

$$k_{min} = \left(\frac{\pi}{6}\right)^{1/3} k_B n^{2/3} \sum_i \upsilon_i \left(\frac{T}{\theta_i}\right)^2 \int_0^{\theta_i/T} \frac{x^3 e^x}{\left(e^x - 1\right)^2} dx. \tag{9.2}$$

Where the summation is over three (two transverse and one longitudinal) sound modes with velocities υ_i, θ_i is the Debye temperature for each mode $\theta_i = \upsilon_i (\hbar/k_B)(6\pi^2 n)^{1/3}$, n is the density of atoms, and k_B is the Boltzmann constant.

Thus, taking into account the values of sound velocities $\upsilon_{LA} = 2760$ m/s, $\upsilon_{TA1} = 1830$ m/s and $\upsilon_{TA2} = 1690$ m/s for $Sn_2P_2Se_6$ crystal [3] the calculated curve of the minimum value of thermal conductivity is presented on fig. 9.6. We have selected this crystal not

at random as it is possible to compare this theoretical prediction with experimental data available for $Sn_2P_2Se_6$ glassy material. Besides, $Sn_2P_2Se_6$ crystal reveals the lowest conductivity among all parent compounds at high temperatures (see fig. 9.1). As seen from the graph near 300 K the curve saturates reaching 0.4 W/m K and coincides with the value for $Sn_2P_2Se_6$ glassy (fig. 9.3). Consequently, for all four extreme compounds at room temperature, the lowest thermal conductivity is reached. This, in turn, means that the phonon mean free path l achieves its minimal length which is comparable with the unit cell size ($l \approx 10$–20 Å). This estimation also shows that "hoping" thermal conductivity is reached instead of heat transport by propagating phonons.
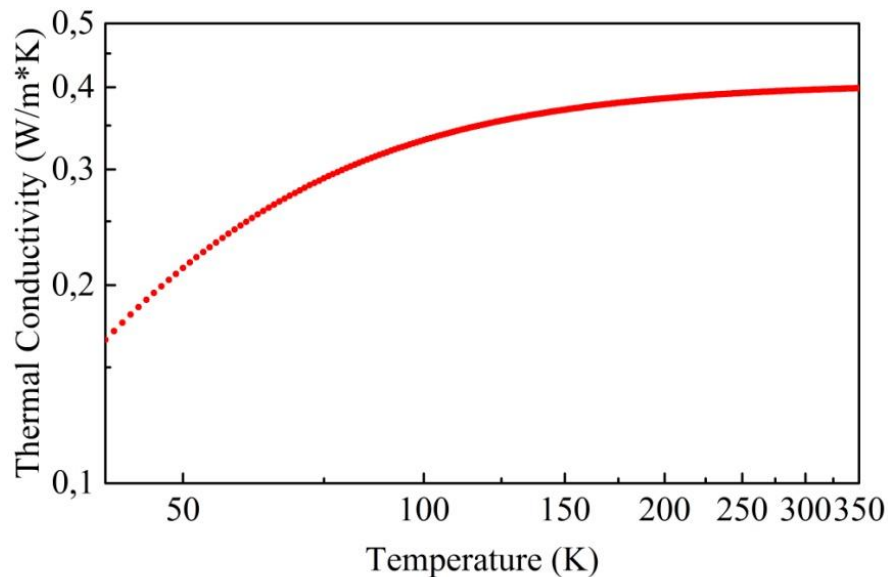
Fig. 9.6. Calculated dependence for minimal value of thermal conductivity in $Sn_2P_2Se_6$ crystal.

Let's now discuss the temperature evolution of the experimentally obtained curves regarding the physical mechanisms which are responsible for the thermal resistance and also for the anharmonicity of the crystal lattice in $Sn(Pb)_2P_2S(Se)_6$ system.

In the first place, a strong lattice anharmonicity is observed by means of neutron scattering measurements performed for $Sn_2P_2S_6$ and $Sn_2P_2Se_6$ [219, 220], shown by a temperature dependent coupling of the soft optic branches with the longitudinal and transverse acoustic branches in a wide reciprocal space of the Brillouin zone, associated with the phase transitions. This coupling is also pronounced in ultrasound and hypersound attenuation investigations [9].

Secondly, the experimental data about phonon anharmonicity in the paraelectric phase of Sn$_2$P$_2$S$_6$ type crystals could be interpreted considering the phase transitions mechanisms based on the BEG model for systems with local three-well potential for the order parameter (spontaneous polarization) fluctuations [3, 107, 115, 228]. The side wells are deeper than the central one in the case of the stereoactive Sn^{2+} cation sublattice. For lead containing compounds, because of the weakened Pb^{2+} stereoactivity, the central well in the local three-well potential is the deepest one [221, 212]. Here also the P^{4+} + P^{4+} ↔ P^{3+} + P^{5+} valence fluctuations could be important for electron- phonon interaction [221]. The thermal conductivity experimental curves correlate fairly well with the state diagram. At low temperatures the ferroelectric phase lattice dynamics are not perturbed by electron lone pair relaxations because the pseudospins with highest probability are placed in the side well with lowest energy. On the contrary, on heating above 250K, the probability of finding a pseudospin in a central well increases and lone pair relaxations contribute to the growth of the lattice anharmonicity. Such picture correlates with the observed rise of thermal conductivity on cooling for Sn$_2$P$_2$S$_6$ crystal, whose $\kappa(T)$ dependence grows above that of the Pb$_2$P$_2$S$_6$ crystal (fig. 9.1). A similar rise of $\kappa(T)$ for Sn$_2$P$_2$Se$_6$ relative to the one for Pb$_2$P$_2$Se$_6$ is observed on cooling as well.

Let's now turn our attention to the mixed compounds. For selenide crystal with $y=0.2$ a minimum of k is attained close to $T_i \approx 160$ K (≈ 0.3 W/m K) (see fig. 9.3) which is lower than the minimum attained for the (Pb$_y$Sn$_{1-y}$)$_2$P$_2$S$_6$ sample with y = 0.45 near T_0 ≈ 125 K (≈ 0.45 W/m K) (see fig. 9.2). Such comparison evidently demonstrates a much stronger softening of the heat transferring phonons group velocity in selenide mixed compound as a result of the coupling between the soft optic and acoustic branches related to the transition into the IC phase. Besides, this effect has an electronic nature: a more covalent chemical bounding in the selenide compounds enforces that coupling associated with the modulated IC phase appearance [220, 99]. It is worth to emphasize one aspect. Comparing the slopes and absolute values of the experimentally observed $k(T)$ dependencies (fig. 9.2 and 9.3) with those of the calculated minimum value for Sn$_2$P$_2$Se$_6$ (fig. 9.6), it is found that among all samples (Pb$_{0.2}$Sn$_{0.8}$)$_2$P$_2$Se$_6$ crystal possesses the most similar behavior to the latter theoretical curve (fig. 9.7). For both

curves the thermal conductivity increases with temperature (this only happens in the samples doped with intermediate concentrations) and with a not too different trend, especially in the temperature range from 60K to about 165K, where the incommensurate phase appears for the doped (Pb$_{0.2}$Sn$_{0.8}$)$_2$P$_2$Se$_6$. In this mixed compound the thermal conductivity is maximally suppressed. This tells us that the strong coupling of optic and acoustic phonon branches that provokes the IC phase, together with mass fluctuations, can heavily reduce the thermal conductivity of the crystalline semiconductors.
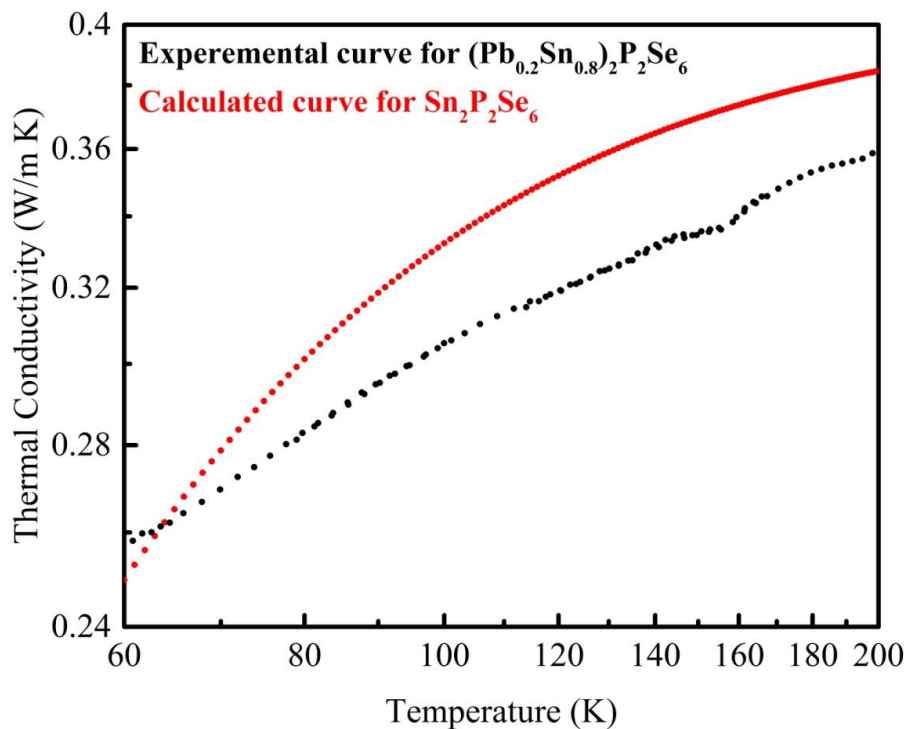
Fig. 9.7. Experimental thermal conductivity curve for (Pb$_{0.2}$Sn$_{0.8}$)$_2$P$_2$Se$_6$ (black dots) and minimum calculated value for Sn$_2$P$_2$Se$_6$ using eq. 9.1 (red dots).

Lastly, the influence of the strongly stereoactive Ge cations can be easily interpreted. While Ge is introduced into the crystal matrix of Sn$_2$P$_2$S$_6$ the local potential does not change its shape and the side wells remain deeper than the central one; thus, there is no influence on the anharmonicity. In the case of the paraelectric Pb$_2$P$_2$S$_6$, where the central well of the local potential is the deepest, the germanium impurities change this picture, surely inducing a deeper side well and thus reducing the anharmonicity, which leads to a rise of the thermal conductivity.

9.4. Conclusions

By mixing heat capacity and thermal diffusivity, the temperature evolution of thermal conductivity has been analyzed for Sn(Pb)$_2$P$_2$S(Se)$_6$ semiconductor ferroelectrics. An ultralow conductivity near 0.5 W/m K is observed for parent compounds near room temperature in the paraelectric phase. The origin of the strong lattice anharmonicity in Sn$_2$P$_2$S$_6$ is related to the relaxations of the 5s^2 electron lone pairs of Sn^{2+} together with P^{4+} + P^{4+} ↔ P^{3+} + P^{5+} valence fluctuations in the anionic sublattice. At lower temperatures the ferroelectric Sn$_2$P$_2$S$_6$ and Sn$_2$P$_2$Se$_6$ crystals exceed their lead containing analogous because the relaxations of Sn^{2+} lone pair are frozen.

In the mixed (Pb$_y$Sn$_{1-y}$)$_2$P$_2$S$_6$ and (Pb$_y$Sn$_{1-y}$)$_2$P$_2$Se$_6$ compounds a clear evidence of mass fluctuation has been observed with a result that thermal conductivity is reduced till about 0.5 W/m K near 50K. At high temperatures above 250 K this effect does not play a significant role. The lowest *k(T)* values have been found for (Pb$_{0.2}$Sn$_{0.8}$)$_2$P$_2$Se$_6$ crystal, in which the mass fluctuations effect, together with the presence of the IC phase caused by strong between optic and acoustic phonon branches, heavily suppress the thermal conductivity.

The introduction of alien ferroactive Ge^{2+} atoms considerably increases the thermal conductivity of the Pb$_2$P$_2$S$_6$ paraelectric sample at low temperatures near 50K and virtually do not create changes on the thermal conductivity dependence of Sn$_2$P$_2$S$_6$ ferroelectric crystal. This is related to the changes (or absence of them) in the shape of the well potential caused by Ge.

CONCLUSIONS

In this summary of the thesis, the author would like to stress the important results obtained in the study of the thermal properties and the critical behavior of the second order phase transitions of $Sn(Pb)_2P_2S(Se)_6$ by means of *ac* photopyroelectric calorimetry:

• The influence of Pb atoms in $(Sn_{1-y}Pb_y)_2P_2S_6$ series with y=0, 0.1, 0.2, 0.3, 0.45, 0.8 and 1 is reflected as a strong downward shifting of the critical temperature with a simultaneously anomaly shape smearing. It was found that the thermal diffusivity is higher in the extreme compounds than in the mixed ones. This can be explained by distortions of the crystal lattice caused by the fact that Sn and Pb atoms share the same space available for them, which leads to a phonon mean-free path reduction. Also, thermal anisotropy was confirmed in the monoclinic $Pb_2P_2S_6$ paraelectric with the conclusion that heat propagation is favored in the (100) direction. A critical behavior study has been performed for the samples with y = 0.1, 0.2, 0.3 and compared with the results obtained for the undoped sample. To properly describe the situation in samples with $y = 0$ and 0.1 it is necessary to use a model in which both order parameter fluctuations and contribution of the charged defects are accounted for. In the case of $y = 0.3$, a very good fit was found for both phases with a critical index close to 0, meaning the sample behaves as a common uniaxial ferroelectric. The crystal with y = 0.2 is an intermediate case in which the predominance of the long-range perturbations is not settled yet as it happens in $y = 0.3$. Thus, we can conclude that introduction of Pb provokes an evolution of the critical behavior from non mean-field at $y = 0$ and 0.1 to a mean-field one $y = 0.3$. There is no change in the character of the transition.

• In the case of $(Sn_{1-y}Pb_y)_2P_2Se_6$ mixed ferroelectrics, Pb also reduces the temperature of the continuous and discontinuous transitions. At the same time, the thermal hysteresis of the first order transition increases as well the width of the incommensurate phase existence. Two transitions have been detected for samples with Pb content of y = 0, 0.05 and 0.1 while in the crystals with y = 0.2 and 0.47 we have only found the continuous paraelectric to incommensurate phase transition. Thermal diffusivity rises up with temperature lowering due to a phonon mean-free path increase.

A critical behavior study has been carried out for the continuous transition at $y = 0$, 0.05 and 0.1 within the frame of renormalization group theory. The critical exponents obtained are in good agreement with the theoretically predicted 3D-XY model for that kind of transition. This means that the Hamiltonian describing the dynamics of the system at the anomaly has to contain a two components order parameter.

• The investigation of $Sn_2P_2S_6$ doped with Ge, Sb and Te has established that each dopant affects the ferroelectricity in quite a different way. Thus, the introduction of Ge enhances the total ferroelectricity, Sb atoms slightly reduce it and Te virtually has no influence on it. This is caused by changes in the electronic orbitals hybridization between the cation and the anion sublattices provided by the introduction of the alien atoms. The results of the critical behavior analysis show that for all doped samples the ferroelectric phase is well approximated by the classical Landau model, while to describe the paraelectric one it is necessary to take into account the combined contributions of charged defects and order parameter fluctuations. The same combination of models has been observed for the undoped sample. No appropriate fits to any other possible universality class were found. The relevant importance of the charged defects is higher for the sample doped with Ge atoms with respect to the pure $Sn_2P_2S_6$ crystal. For the ones doped with Sb this importance is smaller. Lastly, Te doping only slightly increases the critical parameters, but in all they are close to those obtained for the undoped sample.

•An equivalent study on $Sn_2P_2(S_{0.72}Se_{0.28})_6$ independently doped with 5% Pb, 8%Pb and 5%Ge has been performed and the changes from the undoped sample have been compared with the theoretical predictions given by the Blue-Emery-Griffiths model with random field. The critical index $\alpha = 0.64$ obtained for $Sn_2P_2(S_{0.72}Se_{0.28})_6+5\%Pb$ coincides perfectly well with the one predicted by renormalization group theory for the Lifshitz Tricritical class ($\alpha_{theor} = 0.64$). All other universality classes such as Uniaxial Lifshitz Tricritical, Uniaxial Tricritical and Tricritical have been discarded by the fact that it was impossible to obtain any proper fit. The sample $Sn_2P_2(S_{0.72}Se_{0.28})_6+8\%Pb$ already reveals a first order transition. On the other side, an introduction of 5%Ge changes neither the character of the transition nor

the critical behavior from the one observed in the undoped $Sn_2P_2(S_{0.72}Se_{0.28})_6$. Their critical exponents $\alpha = 0.25$ and $\alpha = 0.34$, respectively, are close to the Lifshitz class ($\alpha_{theor} = 0.25$). Besides, the results agree with a Blue-Emery Griffiths model with random field. The model says that three-well local potential flattening caused by a decrease of the transition temperature can lead to the appearance of a Tricritical point. In our case the anomaly has been shifted from initial 281.31K for $Sn_2P_2(S_{0.72}Se_{0.28})_6$ down to 259.12K for $Sn_2P_2(S_{0.72}Se_{0.28})_6+5\%Pb$. Thus, the experimental data confirms the appearance of the Lifshitz tricritical point in the $(Sn_{1-y}Pb_y)_2P_2(S_{1-x}Se_x)_6$ solid compounds. Its coordinates have been found as follows: $T_{LTP} = 259.12$ K, $x = 0.28$ and $y = 0.05$.

•A complete analysis of the thermal conductivity of $Sn(Pb)_2P_2S(Se)_6$ system has been performed taking into account the features of their composition-temperature phase diagram. The ultra-low thermal conductivity (about 0.5 W/m K) in the high-temperature centrosymmetric phase of $Sn_2P_2S_6$ crystal is due to a strong lattice anharmonicity. This is caused by the relaxations of the $5s^2$ electron pairs of Sn^{2+} together with valence fluctuations related to $P^{4+} + P^{4+} \leftrightarrow P^{3+} + P^{5+}$ charge disproportionation in the anionic $(P_2S_6)^{4-}$ subgroup of the crystal unit cell. In the case of $Pb_2P_2S(Se)_6$ the smaller stereoactivity of the $6s^2$ electrons lone pairs of Pb^{2+} cations determines the growth of thermal conductivity on cooling in the paraelectric phase. At low temperatures inside the ferroelectric phase the $k(T)$ curve of $Sn_2P_2S_6$ exceeds the one for $Pb_2P_2S_6$ paraelectric crystal, because of freezing of the electron lone pair relaxations of Sn^{2+} cations. At low temperatures the same happens with Se-containing compositions. Substitution of S by Se in $Sn_2P_2S_6$ induces the incommensurate phase appearance between the paraelectric and ferroelectric phases and increases the coupling of the soft optic and acoustic branches in a wide region of wave vectors space. This effectively lowers the thermal conductivity. Besides, the conductivity of the more covalent $Sn_2P_2Se_6$ and $Pb_2P_2Se_6$ crystals is lower with respect to their sulfur analogues.

In the case of $(Pb_ySn_{1-y})_2P_2S_6$ and $(Pb_ySn_{1-y})_2P_2Se_6$ mixed compositions the mass fluctuations create additional phonon scattering centers, which heavily suppress the thermal conductivity. Especially, this effect is pronounced at low temperatures (near

60K) for the middle of Pb concentrations (about $y \approx 0.5$) for both selenide and sulfide crystals. Besides, $(Pb_{0.2}Sn_{0.8})_2P_2Se_6$ reveals the lowest $k(T)$ dependence among all samples studied due to a combination of the mass fluctuation in the crystal matrix together with the IC phase existence.

Partial substitution of Sn and Pb in sulfide crystals by strongly ferroactive Ge atoms steadily increases the thermal diffusivity as well the thermal conductivity of $Pb_2P_2S_6$ paraelectric. The maximal difference between nominally pure (3.1 W/m K) and doped (4.9 W/m K) samples is reached at lowest temperature near 40K. In case of $Sn_2P_2S_6$ ferroelectric the introduction of Ge have virtually no influence on the general evolution of $D(T)$ and $k(T)$.

BIBLIOGRAPHY

1. M. Aggarwal, A. Batra, P. Guggilla, M. Edwards, B. Penn, J. Currie, Jr. / *Pyroelectric Materials for Uncooled Infrared Detectors: Processing, Properties, and Applications* // Marshall Space Flight Center, MSFC, Alabama 35812, 2010. – P. 88.

2. Y.Xu / *Ferroelectric Materials and Their Applications* // England, North-Holland, London, 1991. – P. 391.

3. Yu. Vysochanskii, T. Janssen, R. Currat, R. Folk, J. Banys, J. Grigas, V. Samulionis / *Phase transitions in ferroelectric phosphorous chalcogenide crystals* // University Publishing House, Vilnius, 2006. – P. 456.

4. S. Gevorgian / *Ferroelectrics in Microwave Devices, Circuits and Systems* // Springer-Verlag London, 2009. – P. 396.

5. L. Mitoseriu; J.M. Gregg; M. Alguero / *Nanoscale Ferroelectrics and Multiferroics: Key Processing and Characterization Issues and Nanoscale Effects* // John Wiley & Sons Ltd, West Sussex, United Kingdom, 2016. – P. 997.

6. Handbook / *Advances in Ferroelectrics* // Edited by A.P. Barranco, InTech, 2012. – P. 542.

7. D.P. Almond and P.M. Patel / *Photothermal Science and Techniques* // Chapman & Hall, London, 1996. – P. 241.

8. H.S. Carslaw and J.C. Jaeger / *Conduction of Heat in Solids* // Oxford University Press, Oxford, 1959. – P. 526.

9. M. Necati Özışık / *Heat Conduction* // John Wiley & Sons Inc., 1980. – P. 687.

10. I. Prigogine / *Thermodynamics of Irreversible Processes, 3rd edition* // Wiley-Intersience, New York, 1968. – P. 147.

11. A. Salazar / *Energy propagation of thermal waves* // European Journal of Physics, 2006. – V. 27. – № 1. – P. 1349-1355.

12. A. Mandelis, L. Nicolaides, Y. Chen / *Structure and the Reflectionless / Refractionless Nature of Parabolic Diffusion-Wave Fields* // Physical Review Letters, 2001. – V. 87. – 020801.

13. E. Marín, J. Marín and R. Hechavarría // *Hyperbolic heat diffusion in photothermal experiments with solids* // Journal de Physique IV France, 205. – V. 125– P. 365-368.

14. E. Marin / *On the wave treatment of the conduction of heat in photothermal experiments with solids* // European Journal of Physics, 2007. – V. 28. – P. 429-445.

15. E. Marin / *Escuchando la luz: breve historia y aplicaciones del efecto fotoacústico* // Lat. Am. J. Phys. Educ., 2008. – V. 2. – №2. – P. 209-215.

16. J. Scales and R. Snieder / *What is a wave?* // Nature, 1999. – V. 401. – P. 739-740.

17. J.A. Balderas-Lopez and A. Mandelis / *Self-consistent photothermal techniques: Application for measuring thermal diffusivity in vegetable oils* // Review of Scientific Instruments, 2003. – V. 74. – P. 700-702.

18. C. Cattaneo / *A form of heat conduction equation whic h eliminates the paradox of instantaneous propagation* // Comptes Rendus, 1958. – V. 247. – P. 431-433.

19. M. Massot / *Desarrollo y aplicación de la calorimetría fotopiroeléctrica al estudio de transiciones de fase*: PhD thesis: 3.04.2009 // Bilbao, Spain, 2008. – P. 137.

20. Yu. Popik / Physics of semiconductors // Uzhgorod: TOB "IBA", 2014. – P. 820.

21. O. Delaire et. al. / *Giant Anharmonic Phonon Scattering in PbTe* // Nature Materials, 2011. – V. 10. – P. 614-619.

22. C. W. Li, J. Hong, A. May, D. Bansal, S. Chi, T. Hong, G. Ehlers, O. Delaire / *Orbitally driven giant phonon anharmonicity in SnSe* // Nature Physics, 2015. – V. 11. – P. 1063-1069.

23. M. Nielsen, V. Ozolins, J. Heremans / *Lone pair electrons minimize lattice thermal conductivity* // Energy Environ. Sci., 2013. – V. 6. – P. 570-578.

24. D. Morelli, V. Jovovic, J. Heremans / *Intrinsically Minimal Thermal Conductivity in Cubic I-V-VI$_2$ Semiconductors* // Phys. Rev. Letters, 2008. – V. 101. – P. 035901.

25. S. Lee, K. Esfarjani, T. Luo, J. Zhou, Z. Tian, G. Chen / *Resonant bonding leads to low lattice thermal conductivity* // Nature Communications, 2014. – V. 5. – P. 3525.

26. L. Aggarwal, A. Banik, S. Anand, U. Waghmare, K. Biswas, G. Goutam Sheet / *Local ferroelectricity in thermoelectric SnTe above room temperature driven by competing phonon instabilities and soft resonant bonding* // Journal of Materiomics, 2016. – V. 2. P. 196-202.

27. J. Hong, O. Delaire / *Electronic instability and anharmonicity in SnSe* // arXiv:1604.07077v1 [cond-mat.mtrl-sci] 2016.

28. G. Snyder, E. Toberer / *Complex thermoelectric materials* // Nature Materials, 2008. – V. 7. – P. 105-114.

29. Z. Tian, J. Garg, K. Esfarjani, T. Shiga, J. Shiomi, G. Chen // *Phonon conduction in PbSe, PbTe, and PbTe$_{1-x}$Se$_x$ from first-principles calculations* // Phys. Rev. B, 2012. – V. 85. – P. 184303.

30. H. Wang, A. Charoenphakdee, K. Kurosaki, S. Yamanaka, G. Snyder / *Reduction of thermal conductivity in PbTe:Tl by alloying with TlSbTe$_2$* // Phys. Rev. B, 2011. – V. 83. – P. 024303.

31. K. Shalimova / *Physics of semiconductors* // Moscow: Энергия, 1976. – P. 390.

32. L. Stilbans / *Physics of semiconductors* // Moscow: Советское радио, 1967. – P. 452.

33. A. Salazar / *On thermal diffusivity* // European Journal of Physics, 2003. – V. 24. – P. 351-358.

34. J. Thoen, G. Cordoyiannis, and C. Glorieux / *Investigations of phase transitions in liquid crystals by means of adiabatic scanning calorimetry* // Liquid Crystals, 2009. – V. 36. – P. 669-684.

35. H. Yao, K. Ema, and C.W. Garland / *Nonadiabatic scanning calorimeter* // Review of Scientific Instruments, 1998. – V. 69. – P. 172-178.

36. P.F. Sullivan and G. Seidel / *Steady-state ac-temperature calorimetry* // Physical Review, 1968. – V. 17. – № 3. – P. – P. 679-685.

37. C.W. Garland / *High-resolution ac calorimetry and critical behavior at phase transitions* // Thermochimica Acta, 1985. – V. 88. – P. 127-142.

38. N.O. Birge and S.R. Nagel / *Specific-heat spectroscopy of the glass-transition* // Physical Review Letters, 1985. – V. 54. – P. 2674-2677.

39. C.C. Huang, J.M. Viner, and J.C. Novack / *New experimental-technique for simultaneously measuring thermal-conductivity and heat-capacity* // Review of Scientific Instruments, 1985. – V. 56. – P. 1390-1393.

40. A. Mandelis and M.M. Zver / *Theory of photopyroelectric spectroscopy of solids* // Journal of Applied Physics, 1985. – V. 57. – P. 4421-4430.

41. U. Zammit, M. Marinelli, F. Mercuri, S. Paoloni, F. Scudieri / *Perspective: photopyroelectric effects and pyroelectric measurements: "Invited review article: photopyroelectric calorimeter for the simultaneous thermal, optical, and structural characterization of samples over phase transitions"* // Review of Scientific Instruments, 2011. – V. 82. – № 12. – 121101.

42. S.N. Lang / *Pyroelectricity: from ancient curiosity to modern imaging tool* // Physics Today, 2005. – V. 58. – № 8. – P. 31-36.

43. M. Chirtoc and G. Mihailescu / *Theory of the photopyroelectric method for investigation of optical and thermal materials properties* // Physical Review B, 1989. – V. 40. – P. 9606-9617.

44. D. Dadarlat, M. Chirtoc, C. Nematu, R.M. Candea, D. Bicanic / *Inverse photopyroelectric detection method* // Physica Status Solidi A-Applied Research, 1990. – V. 121. – № 2. – P. 231-234.

45. A. Salazar / *On the influence of the coupling fluid in photopyroelectric measurements* // Review of Scientific Instruments, 2003. – V. 74. – № 1. – P. 825-827.

46. A. Salazar, A. Oleaga / *Overcoming the influence of the coupling fluid in photopyroelectric measurements of solid samples* // Review of Scientific Instruments, 2012. – V. 83 – № 1. – 014903.

47. S. Delenclos, M. Chirtoc, A. Sahraoui, C. Kolinsky, J. Buisine / *Assessment of calibration procedures for accurate determination of thermal parameters of liquids and their temperature dependence using the photopyroelectric method* // Review of Scientific Instruments, 2002. – V. 73. – № 7. – P. 2773-2780.

48. M. Marinelli, U. Zammit, F. Mercuri, R. Pizzoferrato / *High-resolution simultaneous photothermal measurements of thermal parameters at a phase-transition with the photopyroelectric technique* // Journal of Applied Physics, 1992. – V. 72, – № 3. – P. 1096-1100.

49. D. Dadarlat, A. Frandas / *Inverse photopyroelectric detection of phase-transitions* // Applied Physics A-Materials Science & Processing, 1993. – V. 57. – № 3. – P. 235-238.

50. A. Hadj Sahraoui, S. Longuemart, D. Dadarlat, S. Delenclos, C. Kolinsky, and J. M. Buisine / *The application of the photopyroelectric method for measuring the thermal*

parameters of pyroelectric materials // Review of Scientific Instruments, 2002. – V. 73. – №7. – P. 2766-2772.

51. M.O. Sonnaillon, R. Urteaga, F.J. Bonetto / *Random Sampling in High-Frequency Digital Lock-In Amplifiers* // XI Reunión de trabajo en procesamiento de la Información y Control, Rio Cuarto Cordoba, 2005.

52. A. Salazar, A. Oleaga / *On the piezoelectric contribution to the photopyroelectric signal* // Review of scientific instruments, 2005. – V. 76. – №3. – 034901.

53. M. Marinelli, F. Mercuri, U. Zammit, P. Pizoferrato / *The influence of the coupling fluids and of the pyroelectric transducer on low-temperature photopyroelectric studies* // Applied Physics A-Materials Science & Processing, 1991. – V. 52. – №3. – P. 115-118.

54. E.H. Bentefour, C. Glorieux, M. Chirtoc, J. Thoen / *Characterization of pyroelectric detectors between 170 and 300 K using the photopyroelectric technique* // Review of Scientific Instruments, 2003. – V. 74. – №1. – P. 811-813.

55. S. Longuemart, A. Hadj Sahraoui, D. Dadarlat, S. Delenclos, C. Kolinsky, J. Biusine / *Study of thermal parameter temperature dependence of pyroelectric materials* // Review of Scientific Instruments, 2003. – V. 74. – №1. – P. 805-807.

56. A. Oleaga, V. Shvalya, A. Salazar / *Transport thermal properties of $LiTaO_3$ pyroelectric sensor from 15 K to 400 K and its application to the study of critical behavior in $EuCo_2As_2$* // International Journal of Thermophysics, 2016. – V. 37. – №1. – 4.

57. M. Chirtoc, D. Dadarlat, D. Bicanic, J.S. Antoniow, M. Egée / *Progress in Photothermal and Photoacoustic Science and Technology*, edited by A. Mandelis and P. Hess // SPIE, Bellingham, Washington, 1998. – Vol. 3. – P. 476.

58. D. Dadarlat and C. Neamtu / *Detection of molecular associations in liquids by photopyroelectric measurements of thermal effusivity* // Measurement Science and Technology, 2006. – V. 17. – №12. – P. 3250-3254.

59. D. Dadarlat, C. Neamtu, M. Streza, R. Turcu, I. Craciunescu, D. Bica and L. Vekas / *High accuracy photopyroelectric investigation of dynamic termal parameters of FeO*

and CoFeO magnetic nanofluids // Journal of Nanoparticle Research, 2008. – V. 10. – №8. – P. 1329-1336.

60. A. Oleaga, A. Salazar, A. Kohutych, Yu. Vysochanskii / *Critical behavior near the Lifshitz point in $Sn_2P_2(S_{1-x}Se_x)_6$ ferroelectric semiconductors from thermal diffusivity measurements* // Journal of Physics-Condensed Matter, 2011. – V. 23. – №8. – 025902.

61. D. Dadarlat / *Photothermal calorimetry of liquids; recent development and applications* // Laser Physics, 2009. – V. 19. – №6. – P. 1330-1339.

62. D. Dadarlat, M.N. Pop, M. Streza, S. Longuemart, M. Depriester, A. Hadj Sahraoui and V. Simon // *Combined FPPE-PTR calorimetry involving TWRC technique. Theory and mathematical simulations* // International Journal of Thermophysics, 2010. – V. 31. – №11-12. – P. 2275-2282.

63. D. Dadarlat, M. Pop, V. Tosa, S. Longuemart, A. Hadj Sahraoui, P. Hus / *On the photopyroelectric investigation of thermal effusivity of solids. Amplitude vs. phase in the FPPE-TWRC configuration* // Optoelectronics and Advanced Materials, 2010. – V. 4. – №11. – P. 1775-1778.

64. D. Dadarlat, M. Streza, M.N. Pop, V. Tosa, S. Delenclos, S. Longuemart and A. H. Sahraoui / *Photopyroelectric calorimetry of solids* // Journal of Thermal Analysis and Calorimetry. 2010. – V. 101. – №1. – P. 397-402.

65. K. Strzalkowski / *Characterization of thermal properties of $Cd_{1-x-y}Zn_xMg_ySe$ mixed crystals by means of photopyroelectric and infrared imaging techniques* // Materials Science and Engineering B, 2014. – V. 184. – P. 80-87.

66. K. Strzalkowski, M. Streza, D. Dadarlat and A. Marasek / *Thermal characterization of II-VI binary crystals by photopyroelectric calorimetry and infrared lock-in thermography* // Journal of Thermal Analysis and Calorimetry, 2015. – V. 119. – №2. – P. 1469-1469.

67. A. Salazar, A. Oleaga, V. Shvalya, E. Apinaniz / *Improved thermal effusivity measurements of solids using the photopyroelectric technique in the front configuration* // International Journal of Thermal Sciences, 2016. – V. 100. – P. 60-65.

68. M. Massot, A. Oleaga, A. Salazar, D. Prabhakaran, M. Martin, P. Berthet and G. Dhalenne / *Critical behaviour of CoO and NiO from specific heat, thermal conductivity,*

and thermal diffusivity measurements // Physical Review B, 2008. – V. 77. – №13. – 134438.

69. Y.A. Çengel / *Heat Transfer: A practical Approach* // McGraw-Hill, Boston, 2003. – P. 932.

70. L.R. Touloukian, R.W. Powell, C.Y. Ho and M.C. Nicolasu / *Thermophysical Properties of matter, Thermal conductivity* // IFI/Plenum, New York, 1970. – V. 1 and 2.

71. L.R. Touloukian, R.W. Powell, C.Y. Ho and M.C. Nicolasu / *Thermophysical Properties of matter, Thermal Diffusivity* // IFI/Plenum, New York, 1973. – Vol. 10. – P. 670.

72. *CRC Handbook of Chemistry and Physics, 78th edition* / edited by D.R. Lide. Chemical Rubber Corp., Boca Raton, FL, 1997. – P. 2447. – ISBN 0-8493-0478-4.

73. A. Hadj Sahraoui, S. Longuemart, D. Dadarlat, S. Delenclos, C. Kolinsky and J.M. Buisine / *Analysis of the photopyroelectric signal for investigating thermal parameters of pyroelectric materials* // Review of Scientific Instruments, 2003. – V. 74. – №1. – P. 618-620.

74. W. Koechner / *Solid-State Laser Engineering* // Springer-Verlag, New York, 1976. – P 620.

75. G. Dittmar, H. Shafer / *Die Struktur des Di-Zinn-Hexathiohypo-diphosphats Sn2P2S6* // Zs. Natturforsch., 1974. – V. 296. – № 5 – 6. – P. 312-317.

76. C. Carpentie, R. Nitsche / *Vapour growth and crystal data of the thio (seleno) – hypodiphosphates Sn2P2S6, Sn2P2Se6, Pb2P2S6, Pb2P2Se6 and their mixed crystals* // Mat. Res. Bull., 1974. – V. 9. – № 4. –P. 401-410.

77. Yu. Voroshilov, Yu. Vysochanskii, A. Grabar, M. Potorii, I. Pritz, V. Rizak, L. Seykovskaya, V. Slivka, A. Yatsenko / *Peculiarities of structure and phase transitions in crystals Sn(Pb)$_2$P$_2$S(Se)$_6$* // Ukr. Fiz. Zh., 1990. – V. 35. – № 1. – P. 71-75.

78. Yu. Voroshilov, M. Potorii, L. Seykovskaya, A. Yatsenko, I. Pritz / *Crystal-structure of Sn$_2$P$_2$Se$_6$* // Kristallografiya, 1988. – V. 33. – № 5. – P. 1282-1283.

79. B. Scott, M. Pressprich, R. Willet, D. Cleary / *High temperature crystal structure and DSC of Sn2P2S6* // Solid State Chem., 1992. – V. 96. – № 2. – P. 294-300.

80. A. Gomonnay, A. Grabar, Yu. Vysochanskii, A. Belyaev, V. Machulin, M. Gurzan and V. Slivka / *The splitting of phase transitions in ferroelectric solid solutions of $Sn_2P_2(Se_xS_{1-x})_6$* // Fiz. Tv. Tela, 1981. – V. 23. – № 12. – P. 3602-3606.

81. T. Barsamian, S. Khasanov, V. Shekhtman, Yu. Vysochanskii and V. Slivka / *Incommensurate phase in proper ferroelectric $Sn_2P_2Se_6$* // Fiz. Tv. Tela, 1985. – V. 27. – № 11. – P. 3327-3331.

82. T. Barsamian, S. Khasanov, V. Shekhman / *Diffraction analysis of incommensurate phases in crystals of quasi-binary system $Sn_2P_2(S_{1-x}Se_x)_6$* // Ferroelectrics, 1993. – V. 138. – № 1. – P. 63-77.

83. R. Israel, R. Gelder, J. Smits, P. Beurskens, S. W. H. Eijt, T. Rasing, H. van Kempen, M. Maior, S. Motrija / *Crystal structures of di-tin-hexa(seleno)hypodiphosphate, $Sn_2P_2Se_6$, in the ferroelectric and paraelectric phase* // Z. Kristallographie, 1998. – V. 213. – P. 34-41.

84. R. Enjalbert, J. Galy, Yu. Vysochanskii, A. Ouedraogo, P. Saint-Gregoire / *Structural study of the ferroelectric instability in $Sn_2P_2Se_6$* // Eur. Phys. J. B., 1999. – V. 8. – P. 169-177.

85. R. Becker, W. Brockner, H. Schäfer // *Kristallstruktur und Schwingungsspektren des Di-Blei- Hexathiohypodiphosphates $Pb_2P_2S_6$* // Z. Naturforsch., 1983. – V. 38. · № 8. – P. 874-879.

86. I. Prits, M. Potorii, Y. Voroshilov / *Phase equilibria in the Pb-P-S(Se) systems*. Soviet Progress in Chemistry (translated from Ukrainskii Khimichnii Zhurnal), 1989. – V. 55. – № 2. – P. 25-27

87. Pierre Villars, Material Phases Data System (MPDS), CH-6354 Vitznau, Switzerland (ed.) SpringerMaterials $Pb_2P_2S_6$ ($PbPS_3$ ht) Crystal Structure. *http://materials.springer.com/isp/crystallographic/docs/sd_1010592.*

88. Pierre Villars, Material Phases Data System (MPDS), CH-6354 Vitznau, Switzerland (ed.) SpringerMaterials $Pb_2P_2Se_6$ ($PbPSe_3$) Crystal Structure. http*://materials.springer.com/isp/crystallographic/docs/sd_1006625#.*

89. R. Nitshe / *Crystal growth of metal-phosphorus-sulfur compounds by vapor transport* // Mat. Res. Bull., 1970. – V. 5. – № 6. – P. 419-424.

90. Yu. Vysochanskii, V. Slivka, Yu. Voroshilov / *The model of phase transitions in Sn$_2$P$_2$S$_6$ ferrosemiconductor and their lattice dynamics* // Fiz. Tverd. Tela, 1979. – V. 21. – № 8. – P. 2402-2408.

91. M. Major, B. Koperles, B. Savchenko, M. Gurzan, O. Morozova, N. Korda / *The heat capacity and linear expansion of crystals Sn$_2$P$_2$(Se$_x$S$_{1-x}$)$_6$ in the field of phase transitions* // Fiz. Tver. Tela, 1983. – V. 25. – P. 214-223.

92. A. Gomonnay, A. Grabar, Yu. Vysochanskii, A. Belyaev, V. Machulin, M. Gurzan, V. Slivka / *The splitting of phase transitions in ferroelectric solid solutions of Sn$_2$P$_2$(Se$_x$S$_{1-x}$)$_6$* // Fiz. Tverd. Tela, 1981. – V. 23. – № 12. –P. 3602-3606.

93. K. Moriya K. Iwauchi, M. Ushida, A. Nakagawa, K. Watanabe, S. Yano, S. Motojima and Yo Akagi / *Dielectric Studies of Ferroelectric Phase Transitions in Pb$_{2x}$Sn$_{2(1-x)}$P$_2$S$_6$ Single Crystals* // Journal of the Phys. Society of Japan, 1995. – V. 64. – № 5. – P. 1775-1784.

94. Yu. Vysochanskii, M. Gurzan, M. Maior, S. Motrja, S. Perechinskii, M. Potorii, L. Salo, M. Khoma, V. Slivka, Yu. Vorosilov / *Concentration dependencies of temperatures and character of phase transitions in (Pb$_y$Sn$_{1-y}$)$_2$P$_2$S$_6$ and (Pb$_y$Sn$_{1-y}$)$_2$P$_2$Se$_6$* // Phys. Solid State, 1985. – V. 23. – № 3. – P. 858-864.

95. A. Oleaga, A. Salazar, M. Massot, and Yu. M. Vysochanskii / *Thermal diffusivity and critical behaviour of uniaxial ferroelectric Sn$_2$P$_2$S$_6$* // Thermochim. Acta, 2007. – V. 459. № 1-2. – P. 73-79.

96. T. Barsamian, S. Khasanov, V. Shekhtman, Yu. Vysochanskii, V. Slivka / *Incommensurate phase in proper ferroelectric Sn$_2$P$_2$Se$_6$* // Ferroelectrics, 1986. – V. 67. – № 1. – P. 47-54.

97. Yu. Vysochanskii, A. Molnar, M. Khoma / *Influence of defects and conductivity on the phase transitions and the domain structure properties in ferroelectric-semiconductors Sn$_2$P$_2$S(Se)$_6$* // Ferroelectrics, 1999. – V. 223. – № 1. – P. 19-26.

98. M. Maior, B. Kopereles, Yu. Vysochanskii, M. Gurzan / *Phase transitions in crystals Sn$_2$P$_2$S$_6$* // Fiz. Tv. Tela, 1984. – V. 26. – № 3. – P. 690-695.

99. A. Kohutych, R. Yevych, S. Perechinskii, V. Samulionis, J. Banys, Yu. Vysochanskii / *Sound behavior near the Lifshitz point in proper ferroelectrics* // Phys. Rev. B, 2010. – V. 82. – P. 054101(1)-054101(10).

100. K. Moriya, H. Kuniyoshi, K. Tashita, Y. Ozaki, S. Yano, T. Matsuo / *Ferroelectric Phase Transitions in $Sn_2P_2S_6$ and $Sn_2P_2Se_6$ Crystals* // Journal of the Physical Society of Japan, 1998. – V. 67. – № 10. –P. 3505-3511.

101. K. Rushchanskii, A. Molnar, R. Bilanych, R. Yevych, A. Kohutych, Yu. Vysochanskii, V. Samulionis, J. Banys / *Observation of nonequilibrium behavior near the Lifshitz point in ferroelectrics with incommensurate phase* // Phys. Rev. B, 2016. – V. 93. – № 1. – P. 014101(1)-014101(12).

102. A. del Campo, T. W. B. Kibble, and W. H. Zurek / *Causality and non-equilibrium second-order phase transitions in inhomogeneous systems* // Journal of Physics: Condensed Matter, 2013. – V. 25. – № 40. – P. 404210(1)-404210(10).

103. T. Kibble, G. Volovik / *On phase ordering behind the propagating front of a second-order transition* / Journal of Experimental and Theoretical Physics Letters, 1997. – V. 65. – № 1. – P. 102-107.

104. O. Anderson, O. Chobal, I. Rizak and V. Rizak / *Tricritical Lifshitz point in the temperature-pressure-composition diagram for $(Pb_ySn_{1-y})_2P_2(Se_xS_{1-x})_6$ ferroelectrics* // Physical Review B. 2009. – V. 80. – № 17. – P. 174107(1)- 174107(5).

105. Yu. Vysochanskii, A. Kohutych, V. Kityk, V. Zadorozhna, M. Khoma, and A. Grabar / *Tricritical behavior of $Sn_2P_2S_6$ ferroelectrics at hydrostatic pressure* // Ferroelectrics, 2010. – V. 399. – P. 83-88.

106. Yu. Vysochanskii, M. Gurzan, M. Mayor, S. Motrya, M. Potoriy, L. Salo, M. Khoma. Yu. Voroshilov, V.Slyvka / *Concentration dependencies of temperatures and character of phase transitions in $(Pb_ySn_{1-y})_2P_2S_6$ and $(Pb_ySn_{1-y})_2P_2Se_6$* // Fiz. Tverd. Tela, 1984. – V. 27. – P. 858-864.

107. K. Rushchanskii, R. Bilanych, A. Molnar, R. Yevych, A. Kohutych, S. Perechinskii, V. Samulionis, J. Banys, Yu. Vysochanskii / *Ferroelectricity in $(Pb_ySn_{1-y})_2P_2S_6$ mixed crystals and random field BEG model* // Phys. Status Solidi B, 2016. – V. 253. – № 2. – P. 384-391.

108. R. Bilanych, R. Yevych, A. Kohutych, S. Perechinskii, I. Stoika, Yu. Vysochanskii / *Elastic properties of $(Pb_ySn_{1-y})_2P_2S_6$ solid solutions* // Central European Journal of Physics, 2014. – V. 12. – № 9. – P. 611-614.

109. K. Moriya, T. Yamada, K. Sakai, S. Yano, S. Baluja, T. Matsuo, I. Pritz, Yu. Vysochanskii / *Ferroelectric phase transitions in $Pb_{2x}Sn_{2(1-x)}P_2Se_6$ system* // Journal of Thermal Analysis and Calorimetry, 2002. – V. 70. – №2. – P. 321-328.

110. K. Moriya, T. Yamada, S. Baluj, T. Matsuo, I. Pritz, Yu. Vysochanskii // Low-temperature thermal properties of $Pb_2P_2Se_6$ and $Pb_{1.424}Sn_{0.596}P_2Se_6$ // Thermochimica Acta, 2003. – V. 43. – № 2. – P. 153-160.

111. I. M. Rizak, V. M. Rizak, M. I. Gurzan, S. I. Perechinskii, Yu. Vysochanskii, V. Yu. Slivka // *Lifshitz points line on the state diagram $(Pb_ySn_{1-y})_2P_2(Se_xS_{1-x})_6$* // Ukr. Fiz. J., 1993. – V. 38. – № 5. – P. 67-70.

112. M. Major, S. Molnar, Yu. Vysochanskii, M. Gurzan, P. van Loosdrecht, P. van der Linden, H. van Kempen / *New dielectric material for low temperature thermometry in high magnetic fields* // Applied Physics Letters, 1993. – V. 62. – № 21. – 2646-2648.

113. M. Maior, S. Molnar, Yu. Vysochanskii, V. Slivka, T. Rasing, P. H. M. Van Loosdrecht, H. van Kempen / *Freezing of the incommensurate modulation dynamics in $(Pb_ySn_{1-y})_2P_2Se_6$* // Phys. Rev. B, 1995. – V. 51. – № 14. – 9325-9328.

114. M. Maior, S. Wiegers, Th. Rasing, S. Eijt, F. Penning, Yu. Vysochanskii, S. Motrja and H. van Kempen / *Low temperature properties of incommensurate ferroelectrics $(Pb_ySn_{1-y})_2P_2Se_6$* // Ferroelectrics, 1997. – V. 202. – P. 139-148.

115. K. Z. Rushchanskii, Yu. M. Vysochanskii, D. Strauch / *Ferroelectricity, nonlinear dynamics and relaxation effects in monoclinic $Sn_2P_2S_6$* // Phys. Rev. Lett., 2007. – V. 99. – № 20. – P. 207601(1)-207601(4).

116. M. Blume, V. Emery, R. Griffiths / *Ising model for lambda transition and phase separation in He-3-He-4 mixtures* // Phys. Rev. A, 1971. – V. 4. – № 3. – 1071-1077.

117. Yu. M. Vysochanskii, M. M. Mayor, V. M. Rizak, V. Yu. Slivka, M. M. Khoma / *The tricritical Lifshitz point on the phase diagram of $Sn_2P_2(Se_xS_{1-x})_6$ ferroelectrics* // Sov. Phys. JETP, 1989. – V. 68. – № 4. – 782-787.

118. A. G. Slivka, E. I. Gerzanich, P. P. Guranich, V. S. Shusta, V. M. Kedyulich / *Phase transitions in $Sn_2P_2S_6$ ferroelectric under high pressures* // Condens. Matter. Phys., 1999. – V. 2. – № 3. – P. 415-420.

119. E. I. Gerzanich / *Optical properties of $A_2^{IV}B_2^{V}C_6^{VI}$ ferroelectrics-semiconductors: the effect of temperature and hydrostatic pressure* // Ukr. J. Phys. Opt., 2008. – V. 9. – № 3. – P. 129-163.

120. P. Ondrejkovic, M. Kempa, Yu. Vysochanskii, P. Saint-Grégoire, P. Bourges, K.Z. Rushchanskii, J. Hlinka / *Neutron scattering study of ferroelectric $Sn_2P_2S_6$ under pressure* // Phys. Rev. B, 2012. – V. 86. – № 22. – 224106-(1)-224106-(8).

121. B. Zapeka, M. Kostyrko, I. Martynyuk-Lototska, R. Vlokh / *Critical behaviour of $Sn_2P_2S_6$ and $Sn_2P_2(Se_{0.28}S_{0.72})_6$ crystals under high hydrostatic pressures* // Phil. Mag., 2015. – V. 95. – № 4. – P. 382-393.

122. P. Ondrejkovic, M. Guennou, M. Kempa, Y. Vysochanskii, G. Garbarino, J. Hlinka / *An x-ray scattering study of $Sn_2P_2S_6$: absence of incommensurate phase up to 1 GPa* // J. Phys.: Condens. Matter, 2013. – V. 25. – № 11. – P. 115901-115901.

123. A. Falicov, A. Nihat Berker / *Tricritical and Critical End-Point Phenomena under Random Bonds* // Phys. Rev. Lett., 1996. – V. 76. – № 23. – P. 4380-4383.

124. I. M. Rizak, V. M. Rizak, Yu. M. Vysochanskii, M. I. Gurzan, V. Yu. Slivka / *Tricritical Lifshitz point in phase diagram of $(Pb_ySn_{1-y})_2P_2(Se_xS_{1-x})_6$ ferroelectrics* // Ferroelectrics, 1993. – V. 143. – P. 135-141.

125. V. Rizak, I. Rizak, M. Gurzan, K. Al'-Shoufi, Yu. Vysochansky and V. Slivka / *Thermal properties of $(Pb_ySn_{1-y})_2P_2(Se_xS_{1-x})_6$ crystals with tricritical Lifshitz point on a phase diagram* // Ferroelecrics, 1995. – V. 168. – P. 39-53.

126. Yu. Vysochanskii, M. Mayor, V. Slivka, M. Gurzan / *Influence of cation and anion replacing on anomalous hysteresis of dielectric susceptibility in crystals $Sn_2P_2S_6$* // Fiz.Tv. Tela, 1985. – V. 27. – № 5. – P. 1560-1562.

127. V. Rizak, K. Al'-Shoufi, I. Rizak, A. Bokotey, Yu. Vysochanskii and V. Slivka / *Thermal conduction of $Sn(Pb)_2P_2S(Se)_6$ like compounds* // Ferroelecrics, 1997. – V. 197. – P. 167-175.

128. O. Mys, I. Girnyk, A. Grabar, I. Martynyuk-Lototska, M. Kostyrko, R. Vlokh / *Thermal expansion of $Pb_2P_2Se_6$ crystals* // Ukr. J. Phys. Opt., 2013. – V. 14. – № 4. – P. 219-224.

129. R. Bilanych / PhD Thesis: "*Anharmonicity of the lattice dynamic and characteristics of dipole ordering in chalcogenide crystals*" // Ukraine. – Uzhgorod. – 2015. – P. 162.

130. K. Al'-Shufi, V. Rizak, I. Rizak, I. Pritz, Yu. Vysochanskii, V. Slivka / *Thermal conductivity of ferroelectric $Sn_2P_2S_6$ in the temperature range 4,2–370 K* // Phys. Solid State, 1993. – V. 35. – № 8. – P. 1055-1057.

131. H. E. Stanley / Handbook "*Introduction to Phase Transitions and critical phenomena*"/ Oxford University Press. – Oxford, 1971. – P. 328.

132. N. Goldenefeld / Handbook "*Lectures on Phase Transitions and the renormalization group theory*" // Westview Press, 1992. – P. 420.

133. J. J. Binney, N. J. Dowrick, A. J. Fisher, M. E. J. Newman / Handbook "*The theory of critical phenomena*" // Oxford University Press Inc. – New York, 2002. – P. 480.

134. I. Herbut / Handbook "*A modern approach to critical phenomena*" // Cambridge University Press. – New York, 2007. – P. 224.

135. D. I. Uzunov / Handbook "*Introduction to the Theory of Critical Phenomena*" // World Scientific Publishing Co. – Singapore, 2010. – P. 673.

136. J. M. Yeomans / Handbook "*Statistical Mechanics of Phase Transitions*" / Oxford University Pres. – Oxford, 1992. – P. 168.

137. S. Ma / Handbook "*Modern Theory of Critical Phenomena*" // Westview Press, 2000. – P. 561.

138. C. Domb, J. L. Lebowitz // Handbook "*Phase Transitions and Critical Phenomena*" // Academic Press. – San Diego, 1992. – P. 245.

139. B. A. Strukov, A. P. Levanyuk / Handbook "*Ferroelectric Phenomena in crystals*" // Springer-Verlag Berlin Heidelberg, 1998. –P. 313.

140. A. P. Levanyuk, A. S. Sigov / Handbook "*Defects and structural phase transitions*" // Gordon and Breach Science Publishers. – Amsterdam, 1988. – P. 222.

141. R. Folk / *Multicritical behavior in ferroelectrics* // Phase Transitions: A Multinational Journal, 1999. – V. 67. – № 4. – P. 645-666.

142. R. Folk, G. Moser / *Critical dynamics: a field-theoretical approach* // J. Phys A: Math Gen., 2006. – V. 39, № 24. – P. R207-R313.

143. B. Halperin, P. Hohenberg / *Generalization of scaling laws to dynamical properties of a system near its critical point* // Phys. Rev. Lett., 1967. – V. 19. – № 12. – P. 700-703.

144. B. Halperin, P. Hohenberg, E. Siggia / *Renormalization-group treatment of critical dynamics of superfluid-helium, isotropic antiferromagnet, and easy-plane ferromagnet* // Phys. Rev. B, 1976 . – V. 13. – № 3. – P. 1299-1328.

145. P. Hohenberg, B. Halperin / *Theory of dynamic critical phenomena* // Rev. Mod. Phys., 1977. – V. 49. – № 3. – P. 435-479.

146. L. Kadanoff, W. Götze, D. Hamblen, R. Hecht, E. Lewis, V. Palciauskas, M. Rayl, J. Swift / *Static phenomena near critical points - theory and experiment* // Rev. Mod. Phys., 1967. – V. 39. – № 2. – P. 395-431.

147. M. E. Fisher / *Renormalization group in theory of critical behavior* // Rev. Mod. Phys., 1974. – V. 46. – № 4. – P. 597-616.

148. E. Frey, F. Schwabl / *Critical-dynamics of magnets* // Adv. Phys., 1994. – V. 43. – № 5. – 577-683.

149. A. Pelisseto, E. Vicari / *Critical phenomena and renormalization-group theory* // Phys. Rep., 2002. – V. 368. – № 4. – P. 549-727.

150. H. E. Stanley / *Scaling, universality, and renormalization: Three pillars of modern critical phenomena* // Rev. Mod. Phys., 1999. – V. 71. – № 2. – P. 358-366.

151. M. M. Khoma, A. A. Molnar, Yu. Vysochanskii / *The mean-field analysis of $Sn_2P_2(Se_xS_{1-x})_6$ thermodynamical properties in the paraelectric, incommensurate and ferroelectric phases* // J. Physical Studies, 1998. – V. 2. – № 4. – P. 524-535.

152. L. Landau, I. Khalatnikov / *On the anomalous absorption of sound near a second order phase transition point* // Dokl. Akad. Nauk SSSR, 1954. – V. 96. – P. 469-472.

153. J. Alberts, E. Balashova, A. Klopperpieper, V. Lemanov, H. Muser, A. Sherman / *Ultrasonic study of deuterated betaine phosphate crystals* // Ferroelectrics, 1990. – V. 108. – P. 357-362.

154. A. Isaverdiyev, N. Lebedev, A. Levanyuk, A. Sigov / *Influence of defects on the properties of uniaxial ferroelectrics near the lifshitz point* // Fiz. Tverd. Tela, 1989. – V. 31. – P. 272-274.

155. A. Isaverdiev, N. Lebedev, A. Levanyuk, A. Sigov / *Influence of defects on the properties of uniaxial ferroelectrics near the lifshitz point* // Ferroelectrics, 1991. – V. 117. – P. 135-139.

156. V. L. Ginzburg / *Some remarks on phase transitions of the second kind and the microscopic theory of ferroelectric materials* // Soviet physics-solid state, 1961. – V. 2. – № 9.– P. 1824-1834.

157. R. Guida, J. Zinn-Justin / *Critical exponents of the N -vector model* // J. Phys. A: Math Gen., 1998. – V. 31. – № 40. – P. 8103-8121.

158. M. Campostrini, M. Hasenbusch, A. Pelisseto, P. Rossi, E. Vicari / *Critical behavior of the three-dimensional XY universality class* // Phys. Rev. B, 2001. – V. 63. – № 21. – 214503.

159. M. Campostrini, M. Hasenbusch, A. Pelisseto, P. Rossi, and E. Vicari / *Critical exponents and equation of state of the three-dimensional Heisenberg universality class* // Phys. Rev. B, 2002. – V. 65. – № 3 – P. 144520.

160. M. Hasenbusch / *Universal amplitude ratios in the three-dimensional Ising universality class* // Phys. Rev. B, 2010. – V. 82. – № 17. – P. 174434.

161. K. Wilson, M. Fisher / *Critical Exponents in 3.99 Dimensions* // Phys. Rev. Lett., 1972. – V. 28. – № 4. – P. 240-243.

162. A. Aharony / *Critical Behavior of Magnets with Dipolar Interactions. V. Uniaxial Magnets in d Dimensions* // Phys. Rev. B, 1973. – V. 8. – № 7. – P. 3363-3370.

163. E. Brezin, J. Zinn-Justin / *Critical behavior of uniaxial systems with strong dipolar interactions* / Phys. Rev. B, 1976. – V. 13. − № 1. – P. 251-254.

164. F. Wegner, E. Riedl / *Logarithmic corrections to the molecular-field behavior of critical and tricritical systems* // Phys. Rev. B, 1973. – V. 7. − № 1. – P. 248-256.

165. R. M. Hornreich, M. Luban, S. Shtriktman / *Critical Behavior at the Onset of k-Space Instability on the λ Line* // Phys. Rev. Lett., 1975. – V. 35. − № 25. – P. 1678-1681.

166. R. Dengler / *Renormalization group calculation of the critical exponents for the lifshitz tricritical point* / Phys. Lett., 1985. – V. 108A. − № 5. – P. 269-271.

167. A. Aharony, E. Domany, R.M. Hornreich / *Renormalization-group analysis of Lifshitz tricritical behavior* / Phys. Rev. B, 1987. – V. 36. − № 4. – P. 2006-2013.

168. R. Folk, G. Moser */ Lifshitz points in uniaxial ferroelectrics* / Phys. Rev. B, 1993. – V. 47. − № 21. – P. 13992-13997.

169. A. Abdel-Hadif, R. Folk / *Tricritical Lifshitz point in uniaxial ferroelectrics* // Phys. Rev. B, 1996. – V. 54. − № 6. – P. 3851-3860.

170. H.W. Diehl and M. Shpot / *Critical behavior at m-axial Lifshitz points: Field-theory analysis and ε-expansion results* / Phys. Rev. B, 2000. – V. 35. − № 25. – P. 1678-1681.

171. Z. Mo and M. Ferer / *Three-dimensional axial next-nearest-neighbor Ising model: A series investigation* / Phys. Rev. B, 1991. – V. 43. − № 13. – P. 10890-10904.

172. I. Nasser, A. Abdel-Hady, R. Folk */ Specific-heat amplitude ratio near a Lifshitz poin.* // Phys. Rev. B, 1997. – V. 56. − № 1. – P. 154-160.

173. I. Nasser / *Exactly solvable model for the specific-heat amplitude ratio with uniaxial dipolar interaction* // Phys. Rev. B, 1999. – V. 60. − № 5. – P. 2983-2986.

174. M. Marinelli, F. Mercuri, U. Zammit, R. Pizzoferrato, F. Scudieri, D. Dadarlat / *Photopyroelectric study of specific heat, thermal conductivity, and thermal diffusivity of Cr_2O_3 at the Néel transition* // Phys. Rev. B., 1994. – V. 49. − № 14. – P. 9523-9532.

175. A. Kornblit, G. Ahlers / *Heat capacity of EuO near the Curie temperature* // Phys. Rev. B, 1975. – V. 11. − № 7. – P. 2678-2688.

176. G. Ahlers, A. Kornblit / *Universality of the specific heat of Heisenberg magnets near the critical temperature* // Phys. Rev. B, 1975. – V. 12. − № 5. – P. 1938-1946.

177. S. Hoshino and H. Motegi / *X-ray study on the phase transition of $NaNO_2$* // Jap. J. Appl. Phys., 1967. – V. 6. − № 6. – P. 708-718.

178. M. Iizumi and K. Gesi / *Incommensurate phase in $(ND_4)_2BeF_4$* // Solid St. Commun., 1977. – V. 22. − № 1. – P. 37-39.

179. M. Iizumi, J.D. Axe, G. Shirane and K. Shimaoka / *Structural phase transformation in K_2SeO_4* // Phys. Rev. B, 1977. – V. 15. − № 9. – P. 4392-4411.

180. J. Wesselinowa, D. Michel, H. Braeter, N. Plakida, J. Petersson, G. Völkel / *Width of the critical region at incommensurate phase transitions* // Phys. Rev. B, 2003. – V. 68. − № 22. – P. 224109.

181. N. Ivanov, A. Levanyuk, S. Minyukov, J. Kroupa and J. Fousek / *Temperature dependence of birefringence in Rb_2ZnBr_4: Discussion of "critical" behaviour* // Ferroelectrics, 1989. – V. 96. − № 1. – P. 83-86.

182. N. Ivanov, A. Levanyuk, S. Minyukov, J. Kroupa and J. Fousek / *The critical temperature dependence of birefringence near the normal-incommensurate phase transition in Rb_2ZnBr_4* // J. Phys.: Condens. Matter, 1990. – V. 2. − № 26. – P. 5777-5786.

183. A. Fajdiga, T. Apih, J. Dolinsek, R. Blonc, A. Levanyuk, S. Minyukov and D. Ailion / *Thermal fluctuations and NMR spectra of incommensurate systems* // Phys. Rev. Lett., 1992. – V. 69. − № 18. – P. 2721-2724.

184. S. Kallaev, I. Kamilov, A. Aliev, S. Abdulvagidov, A. Amirova and A. Batdalov / *Critical Behavior of the Heat Capacity in the Region of the Incommensurate Phase Transition of $C(NH_2)_2$ Crystals* // Inter. J. Thermophys., 2005. – V. 26. − № 2. – P. 471-477.

185. R. Cowley and A. Bruce / *The theory of structurally incommensurate systems. I. Disordered-incommensurate phase transitions* // J. Phys. C: Solid State Phys., 1978. – V. 11. − № 17. – P. 3577-3590.

186. Z. Chen / *Analysis of the specific-heat anomalies of K_2SeO_4 and Rb_2ZnCl_4 near the normal-incommensurate phase transition* // Phys Rev. B, 1990. – V. 41. − № 13. – P. 9516-9518.

187. R. Walisch, J. Petersson, D. Schüssler, U. Häcker, D. Michel and J. Perez-Mato // *Dynamics in incommensurate phases studied by NMR: Theory and relaxation*

measurements on Rb^{87} satellites in Rb_2ZnCl_4 // Phys. Rev. B, 1994. – V. 50. − № 22. – P. 16192-16204.

188. K. Holzer, J. Petersson, D. Schüler, R. Walisch, U. Häcker and D. Michel / *Critical Dynamics above the Incommensurate Phase Transition of Rb_2ZnCl_4 Studied by NMR* // Europhys. Lett., 1995. – V. 31. − № 4. – P. 213-218.

189. P. Mischo, F. Decker, U. Häcker, K. Holzer, J. Petersson and D. Michel / *Low-Frequency Phason and Amplitudon Dynamics in the Incommensurate Phase of Rb_2ZnCl_4* // Phys. Rev. Lett., 1997. – V. 78. − № 11. – P. 2152-2155.

190. B. Kaufmann, F. Schwabl and U. Täuber / *Critical dynamics at incommensurate phase transitions and NMR relaxation experiments* // Phys. Rev. B, 1999. – V. 59. − № 17. – P. 11226-112443.

191. R. Walisch, J. Perez-Mato and J. Petersson / *NMR determination of the nonclassical critical exponents β and β^- in incommensurate Rb_2ZnCl_4* // Phys. Rev. B, 1989. – V. 40. − № 16. – P. 10747-10752.

192. A. Taye, D. Michel and J. Petersson / *35 Cl nuclear magnetic resonance study of critical fluctuations in bis (4-chlorophenyl) sulphone [$(ClC_6H_4)_2SO_2$]* // Phys. Rev. B, 2002. – V. 66. − № 17. – P. 174102.

193. K. Holzer, J. Petersson, D. Schüler, R. Walisch, U. Häcker and D. Michel / *NMR evidence for universal nonclassical critical behavior of incommensurately modulated crystals* // Phys. Rev. Lett., 1993. – V. 71. − № 1. – P. 89-92.

194. J. Hlinka, R. Currat, M. de Boissieu, F. Livet and Yu. Vysochanskii / *Two-length-scale behavior near the ferroelectric phase transition of $Sn_2P_2S_6$* // Phys. Rev. B, 2005. – V. 71. − № 5. – P. 052102.

195. V. Valevichius, V. Samulionis and V. Skritskij / *Orientational dependence of ultrasonic velocity near the phase transition in $Sn_2P_2S_6$ single crystals* // Ferroelectrics, 1988. – V. 79. − № 1. – P. 225-228.

196. V. Samulionis, J. Banys, Yu. Vysochanskii and A. Grabar / *The Critical Behaviour of Ultrasonic Velocity at a Second-Order Phase Transition in $Sn_2P_2S_6$ Single Crystals* // Phys. Stat. Sol. B, 1999. – V. 215. − № 2. – P. 1151-1156.

197. A. Say, O. Mys, A. Grabar, Yu. Vysochanskii and R.Vlokh / *Thermal expansion of $Sn_2P_2S_6$ crystals* // Phase transition, 2009. – V. 82. − № 7. – P. 531-540.

198. Yu. Vysochanskii, S. Perechinskii, V. Rizak and I. Rizak / *Critical behaviour of uniaxial $Sn_2P_2S(Se)_6$ ferroelectrics* // Ferroelectrics, 1993. – V. 143. − № 1. – P. 59-66.

199. Yu. Vysochanskii, A. Molnar, A. Horvat and Yu. Nakonechnii */ Phase transitions in the vicinity of the lifshitz point in ferroelectric-semiconductors* // Ferroelectrics, 1995. – V. 170. − № 1. – P. 249-256.

200. Yu. Vysochanskii, V. Mitrovcij, A. Grabar, S. Perechinskii, S. Motrja and J. Kroupa / *Birefringence investigations of the $Sn_2P_2(Se_xS_{1−x})_6$ uniaxial ferroelectrics behaviour near the lifshitz point* // Ferroelectrics, 2000. – V. 237. − № 1. – P. 193-200.

201. M. Maior, P. van Loosdrecht, H. van Kempen, T. Rasing, S. Molnar and S. Motrij / *Fluctuation effects on the thermal expansion of the incommensurate crystal $Sn_2P_2Se_6$* // J. Phys. Condens. Matter, 1993. – V. 5. − № 33. – P. 6023-6028.

202. Yu. Vysochanskii, A. Grabar, N. Dovka / *Manifestation of the fluctuation effects in the vicinity of the tricritical Lifshitz point in $Sn_2P_2(Se_xS_{1-x})_6$* // Izv. AN USSR, Ser. Fiz., 1991. – V. 55. − № 3. – P. 606-611.

203. S. W. H. Eijt, "*Structure and Dynamics of Type II Incommensurate crystals. A study of the $Sn_2P_2Se_6$*" (Dr. Thesis, Nijmegen 1997).

204. I. Rizak, V. Rizak, S. Perechinskii, Yu. Vysochanskii and V. Slivka / *Critical behavior of birefringence of $Sn_2P_2Se_6$ in vicinity of phase transition from paraelectric to incommensurate phase* // Fiz. Tverd. Tela, 1992. – V. 34. − № 12. – P. 3709-3712.

205. V. Shvalya, A. Oleaga, A. Salazar, A. Kohutych, Yu. Vysochanskii / *Critical behavior study of ferroelectric semiconductors $(Pb_xSn_{1−x})_2P_2S_6$ from thermal diffusivity measurements* // Thermochimica Acta, – 2015. – V. 617. – № 10 – P. 136-143.

206. J. Grigas, E. Talik, V. Lazauskas, Yu. Vysochanskii, R. Yevych, M. Adamiec, V. Nelkinas / *X-ray photoelectron spectroscopy of $Sn_2P_2S_6$ crystals* // Condensed Matter Physics, – 2008. – V. 11. – № 3(55) – P. 473-482.

207. Yu. Vysochanskii, V. Rizak, I. Rizak, M. Gurzan, V. Slivka / *Heat capacity of ferroelectric solid solutions of $(Pb_ySn_{1-y})_2P_2S_6$ and $(Pb_ySn_{1-y})_2P_2Se_6$* // Ukr. Phys. J., – 1992. – V. 37. – № 13 – P. 1745-1750.

208. V. Shvalya, A. Oleaga, A. Salazar, A. Kohutych, Yu. Vysochanskii / *Thermal diffusivity and 3D-XY critical behavior of ferroelectric semiconductors $(Pb_xSn_{1-x})_2P_2Se_6$* // Journal of Physics and Chemistry of Solids, – 2016. – V. 88. – P. 78-84.

209. V. Shvalya, A. Oleaga, A. Salazar, A. Kohutych, Yu. Vysochanskii / *Thermal characterization and critical behavior study of $(Pb_xSn_{1-x})_2P_2Se_6$* // Ferroelectrics (accepted for publication 2016).

210. Yu. Vysochanskii, K. Glukhov, K. Fedyo, R. Yevych / *Charge transfer and anharmonicity in $Sn_2P_2S_6$ ferroelectrics* // Ferroelectrics, – 2011. – V. 414. – № 1 – P. 30-40.

211. K. Glukhov, K. Fedyo, J. Banys, Yu. Vysochanskii / *Electronic Structure and Phase Transition in Ferroelectic $Sn_2P_2S_6$ Crystal* // Int. J. Mol. Sci., – 2012. – V. 13. – № 11 – P. 14356-14384.

212. M. Maior, M. Gurzan, S. Molnar, I. Prits, Yu. Vysochanskii / *Effect of germanium doping on pyroelectric and piezoelectric properties of $Sn_2P_2S_6$ single crystal* // IEEE transactions on ultrasonics, ferroelectrics, and frequency control. – 2000. – V. 47. – № 4. – P. 877-880.

213. J. Grigas, E. Talik, K. Glukhov, K. Fedyo, I. Stoika, M. Gurzan, I. Prits, A. Grabar, Yu. Vysochanskii / *XPS of Impurities Influence on Electronic Structure of $Sn_2P_2S_6$ Ferroelectrics* // Ferroelectrics, – 2011. – V. 418. – № 1 – P. 134-142.

214. V. Shvalya, A. Oleaga, A. Salazar, I. Stoika, Yu. Vysochanskii / *Influence of dopants on the thermal properties and critical behavior of the ferroelectric transition in uniaxial ferroelectric $Sn_2P_2S_6$* // Journal of Materials Science, – 2016. – V. 51. – № 17 – P. 8156-8167.

215. R. Yevich, Yu. Vysochanskii / *Tripple well potential and macroscopic properties of $Sn_2P_2S_6$ ferroelectrics near phase transition* // Ferroelectrics, – 2011. – V. 412. – № 1 – P. 38-44.

216. T. Tomé, R. Salinas / *Modulated phases and chaotic behavior in a spin-1 Ising model with competing interactions* // Phys Rev. A, – 1989. – V. 39. – № 4 – P. 2206-2213.

217. A. Falicov, A. Nihat Berker / *Tricritical and critical end-point phenomena under random bonds* // Phys. Rev. Lett., – 1996. – V. 76. – № 23 – P. 4380-4383.

218. J. Skelton, L. Burton, S. Parker, A. Walsh, C. Kim, A. Soon, I. Tanaka / *Anharmonicity in the high-temperature Cmcm phase of SnSe: soft modes and three-phonon interactions* // arXiv:1602.03762v2 [cond-mat.mtrl-sci] (2016)

219. S. Eijt, R. Currat, J. Lorenzo, P. Saint-Gregoire, B. Hennion, Yu. Vysochanskii / *Soft modes and phonon interactions in $Sn_2P_2S_6$ studied by inelastic neutron scattering* // Eur. Phys. J. B, – 1998. – V. 5. – № 2 – P. 169-178.

220. S. Eijt, R. Currat, J. Lorenzo, P. Saint-Gregoire, S. Katano, T. Janssen, B. Hennion, Yu. Vysochanskii / *Soft modes and phonon interactions in $Sn_2P_2Se_6$ studied by inelastic neutron scattering* // J. Phys.: Cond. Matt., – 1998. – V. 10. – № 22 – P. 4811-4844.

221. R. Yevych, V. Haborets, M. Medulych, A. Molnar, A. Kohutych, A. Dziaugys, J. Banys, Yu. Vysochanskii / *Valence fluctuations in $Sn(Pb)_2P_2S_6$ ferroelectrics* // arXiv:1605.02367v1 [cond-mat.mtrl-sci] (2016).

222. Yu. Vysochanskii, M. Medulych, A. Molnar, K. Glukhov, A. Dziaugys, J. Banys, R. Yevych, M. Maior // *Chemical bonding and polarons in $Sn_2P_2S(Se)_6$ ferroelectrics* // Ferroelectrics, – 2014. – V. 462. – № 1 – P. 117-128.

223. A. Kohutych, R. Yevych, S. Perechinskii, Yu. Vysochanskii / *Acoustic attenuation in ferroelectric $Sn_2P_2S_6$ crystals* // Cent. Eur. J. Phys., – 2010. – V. 8. – № 6 – P. 905-914.

224. K. Moriya, T. Yamada, S. Baluya, T. Matsuo, P. Pritz, Yu. Vysochanskii / *Low-temperature thermal properties of $Pb_2P_2Se_6$ and $Pb_{1.424}Sn_{0.596}P_2Se_6$* // Thermochimica Acta, – 2003. – V. 403. – № 2. – P. 153-160.

225. S. Il'kovic, M. Reiffers, V. Seben, K. Sterbakova, V. Burger, L. Parma, O. Chobal, I. Rizak, V. Rizak / *High Temperature Magnetic and Thermal Properties of $(Pb_ySn_{1-y})_2P_2S_6$ Chalcogenides* // Acta Polonica A, – 2012. – V. 122. – № 1. – P. 12-14.

226. D. Baltrunas, K. Mazeika, Yu. Vysochanskii, A. Grabar, V. Slivka / *Mossbauer spectroscopy of the phase transitions in the ferroelectric system $Sn(Pb)_2P_2S(Se)_6$* // Ferroelectrics, – 1995. – V. 165. – № 1. – P. 359-368.

227. D. Cahill, S. Watson, R. Pohl / *Lower limit to the thermal conductivity of disordered crystals* / Phys. Rev. B, – 1992. – V. 46. – № 10. – P. 6131-6140.

228. Yu. Vysochanskii, A. Molnar, R. Yevych, K. Glukhov, M. Medulych / *Ferroelectricity and polarons in $Sn_2P_2S_6$ crystals* // Ferroelectrics, – 1995. – V. 440. – № 1. – P. 31-41.

SUMMARY IN SPANISH / RESUMEN EN CASTELLANO

"Influencia de dopantes isovalentes en el comportamiento crítico y las propiedades térmicas dinámicas de cristales ferroeléctricos Sn(Pb)$_2$P$_2$S(Se)$_6$"

Esta tesis doctoral se ha realizado en el marco de un acuerdo de cotutela internacional entre la Uzhgorod National University, Uzhgorod, Ucrania y la Universidad del País Vasco-Euskal Herriko Unibertsitatea, habiendo realizado el estudiante Vasyl Shvalya una estancia en la UPV/EHU de 23 meses (aproximadamente la mitad del período total) con el soporte económico de la Unión Europea a través del programa ERASMUS MUNDUS ACTIVE.

Los primeros 4 capítulos de la memoria son capítulos que contextualizan el trabajo experimental que se describe en los capítulos 5 al 9. El capítulo 1 contiene una descripción general de los procesos de transferencia de calor, introduciendo las definiciones de las variables térmicas que se van a manejar en la memoria. El capítulo 2 describe con todo detalle las técnicas experimentales utilizadas y su fundamento teórico. La técnica básica utilizada ha sido calorimetría fotopiroeléctrica y en todos los casos se han utilizado monocristales de alta calidad para los estudios. El capítulo 3 contiene el estado del arte de las propiedades físicas de la familia ferroeléctrica estudiada y el capítulo 4 desarrolla la teoría del comportamiento crítico de transiciones de fase continuas (segundo orden), empezando por la teoría clásica de Landau y las correcciones aplicadas a la misma con el fin de considerar fenómenos tales como fluctuaciones del parámetro de orden, presencia de interacciones dipolares fuertes, contribución añadida de defectos cargados, etc. Se describen los límites de esta teoría clásica y se pasa a describir la teoría moderna del comportamiento crítico, basada en el desarrollo de los hamiltonianos que incluyan las interacciones relevantes en la transición y la obtención por diferentes métodos (el más relevante de los cuales es la teoría de grupos de renormalización) del comportamiento singular de diferentes variables físicas, como el calor específico o la difusividad térmica. Se obtienen así las

diferentes clases de universalidad, donde cada una tiene un conjunto particular de exponentes críticos, susceptibles de ser evaluados experimentalmente. Así, una vez que obtengamos las curvas experimentales, las ajustaremos a los diferentes modelos teóricos con el fin de extraer conclusiones sobre los mecanismos físicos relevantes en la transición. La magnitud experimental utilizada para dichos ajustes ha sido en todos los casos el inverso de la difusividad térmica, cuyo comportamiento crítico es análogo al del calor específico en estos materiales.

El propósito del estudio ha sido, en primer lugar, investigar la evolución de las propiedades térmicas de la familia ferroeléctrica $Sn(Pb)_2P_2S(Se)_6$ en un muy amplio rango de temperaturas, estudiando el comportamiento crítico de las transiciones de fase continuas (segundo orden) que aparecen en su diagrama de fases, centrándonos especialmente en la influencia de la sustitución de Sn por Pb en las soluciones sólidas $(Sn_{1-y}Pb_y)_2P_2S_6$ and $(Sn_{1-y}Pb_y)_2P_2Se_6$. Con este propósito, se ha procedido a la medida de la difusividad térmica de ambas familias $(Sn_{1-y}Pb_y)_2P_2S_6$ and $(Sn_{1-y}Pb_y)_2P_2Se_6$ desde baja temperatura (30-40K) hasta temperatura ambiente o superior, según los casos, verificando la anisotropía de dicha propiedad térmica debida a la estructura monoclínica de los monocristales. En el caso de la familia $(Sn_{1-y}Pb_y)_2P_2S_6$ (capítulo 5) se han identificado las transiciones de fase (todas continuas) que van siendo frustradas a medida que se incrementa el contenido de Pb, hasta que anula por completo la transición ferroeléctrica para $y > 0.45$. Se ha estudiado el comportamiento crítico de las mismas considerando la teoría clásica de Landau (campo medio), las posibles desviaciones a la misma teniendo en cuenta fluctuaciones del parámetro de orden, las posibles atenuaciones de estas fluctuaciones debidas a fuertes interacciones dipolares y/o la contribución de defectos cargados, comparando los resultados con las diferentes clases de universalidad. La conclusión ha sido que existe un crossover desde la muestra con $y = 0.1$ hasta la muestra con $y = 0.3$. En la primera, el comportamiento crítico de la fase paraeléctrica se puede describir con una combinación de la corrección de fluctuaciones de primer orden y la contribución de defectos cargados (por lo tanto, un comportamiento alejado del campo medio descrito por la teoría clásica pura de Landau) mientras que en la última es suficiente considerar interacciones de largo alcance (campo

medio) para su descripción. En todos los casos las fases ferroeléctricas sí siguen el modelo de Landau. No ha sido posible encontrar correlación con las clases de unversalidad derivadas de la teoría moderna de comportamiento crítico al no poder realizar un único ajuste a las dos fases al mismo tiempo con dicho modelo. Las ecuaciones utilizadas para los ajustes en cada caso están descritas con todo detalle en el capítulo 4.

El capítulo 6 contiene el estudio equivalente de la familia $(Sn_{1-y}Pb_y)_2P_2Se_6$ donde la principal diferencia estriba en que, sin plomo, existen dos transiciones; desde la fase paraeléctrica de alta temperatura se pasa a una inconmensurable (segundo orden) para luego pasar, a más baja temperatura, a una fase ferroeléctrica con una transición de primer orden. En este caso, se han identificado las transiciones de primer orden en las muestras con dopaje y=0, 0.05, 0.1 a través del estudio de la histéresis: comportamiento asintótico de la posición de la temperatura crítica en subida o bajada en función de la velocidad de cambio de la temperatura así como de la diferencia en la forma de la transición. Se han localizado transiciones de segundo orden de la fase paraeléctrica a la inconmensurable en y = 0, 0.05, 0.1, 0.2, 0.47 de las cuales se han podido ajustar las tres primeras (las dos últimas se manifiestan sólo por leves alteraciones sobre el fondo de difusividad térmica). La teoría de grupos de renormalización afirma que esta transición particular debe ser descrita con un parámetro de orden con dos componentes y que la clase de universalidad a la que debe pertenecer es la 3D-XY (lo que ha sido experimentalmente verificado en muy pocas ocasiones a pesar de que este tipo de transición se da en muchos ferroeléctricos). Los ajustes realizados con las 3 muestras han concluido que, efectivamente, esta transición pertenece a dicha clase de universalidad. Por último, indicar que en las muestras con y = 0.8, 1 no se ha encontrado ninguna transición de fase.

En el capítulo 7 se estudia la influencia de otros dopantes (Ge, Sb, Te) en las propiedades ferroeléctricas, térmicas y comportamiento crítico de $Sn_2P_2S_6$. Ge sustituye al Sn, Sb al P y Te al S. Se discute cómo esas sustituciones (que se han realizado independientemente y no combinadas) alteran las hibridaciones de los niveles electrónicos del material responsables de las propiedades ferroeléctricas del mismo. La

presencia de Ge incrementa fuertemente la estereoactividad ya que refuerza la hibridación de los niveles sp^2, lo que se revela en un notable incremento de la temperatura de la transición así como en un anomalía más marcada. Sb tiene un efecto contrario al del Ge pero es mucho más débil (la temperatura crítica se reduce ligeramente) mientras que Te no tiene prácticamente ninguna influencia. En lo que se refiere al comportamiento crítico en comparación con el de $Sn_2P_2S_6$, de nuevo puede ser descrito por teoría clásica pura (modelo de Landau) en su fase ferroeléctrica, con ligeras variaciones en los coeficientes fenomenológicos del potencial termodinámico; la fase paraeléctrica, en cambio, sí es descrita por la teoría clásica pero teniendo en cuenta una combinación del efecto de fluctuaciones de primer orden del parámetro de orden junto con la presencia de defectos cargados. Se discute el cambio en el peso relativo de una u otra contribución.

En el capítulo 8 se presenta el estudio de la consecución de un punto de Lifshitz tricrítico en el diagrama de fase de esta familia ferroeléctrica a partir de la concentración donde se da el punto de Lifshitz $Sn_2P_2(S_{0.72}Se_{0.28})_6$. Hay estudios previos sobre la consecución de puntos tricríticos aplicando presión mecánica en $Sn_2P_2S_6$ o dopado e incluso se ha teorizado que podría encontrarse en el diagrama de fase (T, p, x, y) de la familia $(Pb_ySn_{1-y})_2P_2(S_{1-x}Se_x)_6$ pero sin llegar a encontrarlo experimentalmente. Además, del modelo Blue-Emery-Griffiths (BEG) con influencia de campos al azar (random field influence) se infiere que se debería poder alcanzar un punto tricrítico a menor temperatura que en el caso del punto de Lifshitz $Sn_2P_2(S_{0.72}Se_{0.28})$ (se teoriza en torno a 250 K) y las singularidades en la transición deberían estar redondeadas, tanto más cuando ya cambie el carácter de la transición. Es bien conocida la equivalencia entre presión mecánica y presión química (dopaje) en la evolución de los diagramas de fase por lo que este trabajo se ha centrado en obtener dicho punto tricrítico añadiendo dopantes que tengan un efecto claro y conocido en la estereoactividad del material, como son Pb (que la frustra) y Ge (que la refuerza). Así, se ha dopado $Sn_2P_2(S_{0.72}Se_{0.28})$ con 5% Pb, 8% Pb y 5% Ge (independientemente en cada caso) y se ha estudiado el carácter de cada transición (con un detallado estudio de la histéresis) y el comportamiento crítico de las de segundo orden; lo relevante de este último estudio es

que existen clases de universalidad relacionadas con los puntos de Lifshitz y puntos tricríticos en su diferentes combinaciones. El estudio ha revelado que con 5% Pb se alcanza un punto Lifshitz tricrítico (el exponente crítico coincide perfectamente con la clase de universalidad del mismo nombre) mientras que con 5% Ge sigue perteneciendo a la clase Lifshitz. Además, en el caso del 5% Pb, se cumplen las previsiones del modelo BEG acerca de las características y posición de la singularidad. La transición con 8% Pb es claramente primer orden.

Por último, en el capítulo 9, se realiza un estudio general de análisis de las propiedades térmicas de $Sn(Pb)_2P_2S(Se)_6$ desde 30K hasta en torno a temperatura ambiente con el fin de analizar el papel de los fonones en la propagación del calor. Se utilizan las medidas de difusividad térmica descritas en los capítulos anteriores y se combinan con valores de calor específico presentes en literatura para obtener la conductividad térmica, obteniendo valores ultrabajos de la misma para determinadas concentraciones. Se discute este comportamiento considerando la influencia de diversos mecanismos físicos que pueden ser el origen del crecimiento de la anarmonicidad de la red en estos cristales, tales como la interacción de fonones acústicos y ópticos, fluctuaciones de masa en la red cristalina, relajación de pares aislados de electrones. Por último, se analiza también el cambio en dicha anarmonicidad al codopar con Ge.

Este trabajo de investigación ha dado lugar a 7 publicaciones en revistas del Journal Scitation Index y una octava está en proceso de revisión. Además, se han presentado seis comunicaciones en congresos internacionales y otras dos en nacionales.